



Atomic-level Electron Microscopy of Metal and Alloy Electrocatalysts

Deiana, Davide

Publication date:
2014

Document Version
Publisher's PDF, also known as Version of record

[Link back to DTU Orbit](#)

Citation (APA):
Deiana, D. (2014). *Atomic-level Electron Microscopy of Metal and Alloy Electrocatalysts*. Technical University of Denmark.

General rights

Copyright and moral rights for the publications made accessible in the public portal are retained by the authors and/or other copyright owners and it is a condition of accessing publications that users recognise and abide by the legal requirements associated with these rights.

- Users may download and print one copy of any publication from the public portal for the purpose of private study or research.
- You may not further distribute the material or use it for any profit-making activity or commercial gain
- You may freely distribute the URL identifying the publication in the public portal

If you believe that this document breaches copyright please contact us providing details, and we will remove access to the work immediately and investigate your claim.

Atomic-level Electron Microscopy of Metal and Alloy Electrocatalysts

Ph.D. dissertation by

Davide Deiana

November 2014

*Center for Electron Nanoscopy
Technical University of Denmark*

Abstract

This thesis presents the application of transmission electron microscopy techniques towards the characterisation of novel metal nanoparticle catalysts. Two main subjects have been covered: first, the sintering-resistance behaviour of monomodal mass-selected Pt cluster catalysts have been studied by means of *ex situ* Scanning Transmission Electron Microscopy (STEM) in combination with *in situ* indirect nanoplasmonic sensing. Secondly, electron microscopy imaging and spectroscopy have been used for the characterisation of novel metal alloy nanoparticle electrocatalysts for the Oxygen Reduction Reaction (ORR) and for the electrochemical production of hydrogen peroxide. This has been done in the context of an extensive investigation including electrochemical measurements, theoretical calculations, and surface science studies.

Pt cluster catalysts of selected mass have been deposited on different flat surfaces and exposed to different sintering conditions. *Ex situ* STEM imaging has been used to monitor the variation of the particle dimensions through the analysis of particle area distributions. Clusters with a monomodal size distribution exhibited intrinsic sintering resistance on different supports and under different reaction conditions, in contrast to cluster with broader and bimodal size distributions. The reason for the stability has been assigned to the suppression of the Ostwald ripening mechanism. In Ostwald ripening, mass transport from small particles to bigger ones is driven by the difference in their chemical potential. By mass-selecting the clusters, sharp and narrow particle distributions are achieved and the driving force for Ostwald ripening mechanism is eliminated.

Pt_xY and Pt_xGd nanoparticles exhibit electrochemical activity among the most active catalysts for the ORR, more than 5 times higher activity compared to the best commercial Pt nanoparticles. Furthermore, they both retain more than

60% of the activity after accelerated ageing tests and they still perform more than 3 times better than Pt. By employing STEM X-ray Energy Dispersive Spectroscopy (EDS) spectrum imaging, the elemental distribution of the Pt_xY , before and after the electrochemical tests, has been determined. A core-shell structure is formed after the ORR chemical treatment, with an alloyed core embedded by a ~ 1 nm Pt-rich shell, due to the segregation of the Y from the first few atomic layers of the particle and its dissolution into the electrolyte. The formed Pt-rich shell prevents further dissolution of the rare earth metal protecting the alloyed core.

Pt–Hg and Pd–Hg have been identified by Density Functional Theory (DFT) calculations as promising candidates for the electrochemical production of hydrogen peroxide H_2O_2 . The active surface is predicted to be formed by reactive Pt or Pd atoms surrounded by more inert Hg atoms. Electrochemical measurements on the two catalysts have shown performance exceeding the current state-of-the-art in both forms of extended surface and nanoparticles. Electron microscopy has been used to elucidate the structure and composition of the nanoparticle alloys to confirm the theoretical predictions. In Pt–Hg nanoparticles, EDS spectroscopy has indicated the presence of both elements on single particles, although high-resolution imaging has shown particles where pure Pt was the only matching structure. In the case of Pd–Hg, a core-shell structure has been found, with a pure Pd core and a Pd-Hg shell. Through atomic resolution STEM, the structure of the alloy in the shell of different particles has been revealed, showing the formation of an ordered alloy structure.

Resume

Denne afhandling præsenterer anvendelsen af transmissionselektronmikroskopi teknikker til karakteriseringen af hidtil ukendte metalliske nanopartikelkatalysatorer. To hovedemner er blevet undersøgt: Først blev sintring-modstandsevns opførsel for monomodale masseselektrede Pt klynge katalysatorer undersøgt med ex situ Skannende Transmissions Elektron Mikroskopi (STEM), dette i kombination med in situ nanoplasmonisk detektion. Dernæst blev elektron mikroskopi afbildning samt spektroskopi anvendt til, at karakterisere nye metallegerings nanopartikelkatalysatorer til oxygen reduktions reaktionen (ORR), samt til den elektrokemiske produktion af hydrogenperoxid. Dette blev gjort som et led i en større studie med elektrokemiske målinger, teoretiske beregninger samt overfladefysik studier.

Masseselektrede Pt klynge katalysatorer blev deponeret på forskellige flade substrater og udsat for forskellige sintringsbetingelser. Ex situ STEM billeder er blevet brugt til at monitorere variationen af partikeldimensioner gennem analyse af partikelareal fordelinger. Klynger med monomodal størrelsesfordeling udviste en iboende modstandsevne over for sintring på forskellige substrater og under forskellige reaktionsbetingelser, i kontrast til klynger med bredere størrelsesfordelinger og bimodale størrelsesfordelinger. Ved Ostwald ripening, drives massetransporten fra mindre til større partikler af forskellen i de kemiske potentialer. Ved at masseselektre klyngerne kan der opnås veldefinerede og smalle partikeldistributioner og drivkraften for Ostwald ripening mekanismen elimineres.

Pt_xY og Pt_xGd nanopartikler udviser en elektrokemisk aktivitet blandt de mest aktive katalysatorer for ORR, mere end fem gange højere aktivitet sammenlignet med de bedste kommercielle Pt nanopartikler. Ydermere bibeholder de

begge mere end 60% af deres aktivitet efter accelererede aldringstests, og de er stadig mere end tre gange bedre end Pt. Ved at bruge STEM røgten Energi Dispersiv Spektroskopi (EDS) spektrum afbildning, blev elementfordelingen af Pt_xY bestemt, før og efter elektrokemiske tests. Efter den kemiske ORR behandling dannes der en kerne-skal struktur, med en legeringskerne og en Pt-rig skal på ~ 1 nm, dette skyldes Y segregering fra de første få atomlag i partiklen og den efterfølgende opløsning i elektrolytten. Den dannede Pt-rige skal forhindre yderligere opløsning af det sjældne jordart metal.

Pt-Hg og Pd-Hg er blevet identificeret ved Densitets Funktional Teori (DFT) beregninger som lovende kandidater til den elektrokemiske produktion af hydrogenperoxid H_2O_2 . Den aktive overflade er bestemt til at være aktive Pt og Pd atomer omgivet af inaktive Hg atomer. Elektrokemiske målinger på de to katalysatorer har vist en aktivitet højere end for de kendte katalysatorer både for makroskopiske krystaller og nanopartikler. Elektron mikroskopi er blevet brugt til at kaste lys over strukturen og kompositionen af nanopartikel legringerner for at bekræfte de teoretiske forudsigelser. For Pt-Hg nanopartikler har EDS spektroskopi indikeret tilstedeværelsen af begge elementer i individuelle partikler, selvom højopløste billeder har vist partikler hvor en ren Pt struktur har været det eneste kandidat. For Pd- Hg blev en kerne-skal struktur fundet, med en ren Pd kerne og en Pd-Hg skal. Gennem atomar opløst STEM blev strukturen af legeringen i skallen af flere forskellige partikler afdækket, og dannelsen af en ordnet legeringsstruktur påvist.

Acknowledgement

This project was carried out at the Center for Electron Nanoscopy of the Technical University of Denmark (DTU Cen) in the period between November 2011 and November 2014 under the supervision of Senior Researcher Thomas Willum Hansen and Professor Jakob Birkedal Wagner. A part of the experimental measurements was performed at the Interdisciplinary Center for Electron Microscopy (CIME) at EPFL, Switzerland. The scientific staff at CIME is gratefully acknowledged for their support.

This work is the result of a strong collaboration among different universities and several research groups at DTU. I would like to thank the DTU colleagues at the Department of Physics in the group of Ifan Stephens and Ib Chorkendorff (CINF), in particular to Arnau, Federico, Patricia, Amado, Paolo, Brian and Elisa for the fantastic collaboration established between Cen and CINF. Thanks to Florian Schweinberger, Kristina Wettergren and Christoph Langhammer from TUM and Chalmers University for the great work done together. Thanks to Quentin for the help at CIME.

Special thanks to my supervisors Jakob and Thomas, for their invaluable and constant support throughout the three years of my PhD. It has been a great honour to work with them. Thanks to all my colleagues and friends at Cen for the great time we had together in the most stimulating and easygoing environment. To the members of the moka club: keep calm and drink (real) good coffee! Such a great environment could not be possible without a great director, Andy Burrows. I express him my sincere thanks for his help and support, especially in the very tough times. Huge thanks to Willie, not only for the countless times he saved me at the microscope (especially on weekends!), but mostly for the great

friendship developed with him and his family.

Special thanks to my flatmate, officemate and brotherly friend Diego for the countless nights out, travels, the endless discussions on perovskites and a lot of other funny stuff. Thanks to Manuel for being the great person and friend you are. Thanks to all my friends in Denmark, you are too many to be listed here, so you know who you are! I have had the greatest experience of my life here with you.

The greatest thanks to my family, Tonino, Maria, Daniela and Simone, for their unconditional love and support. This thesis is dedicated to them.

List of publications

Included papers

Paper 1

High Sintering Resistance of Size-Selected Platinum Cluster Catalysts by Suppressed Ostwald Ripening.

Kristina Wettergren, Florian F. Schweinberger, **Davide Deiana**, Claron J. Ridge, Andrew S. Crampton, Marian D. Rötzer, Thomas W. Hansen, Vladimir P. Zhdanov, Ueli Heiz, and Christoph Langhammer. *Nano Letters*, 14(10): 5803-5809, September 2014.

Contribution: Aberration-corrected STEM is employed for the *ex situ* study of mass-selected Pt nanoclusters of different size exposed to sintering conditions. Particle area distributions are extracted from the STEM micrographs to obtain an insight on the sintering-resistance behaviour shown by monomodal mass-selected clusters.

Paper 2

Mass-selected nanoparticles of Pt_xY as model catalysts for oxygen electroreduction.

Patricia Hernandez-Fernandez, Federico Masini, David N. McCarthy, Christian

E. Strebel, Daniel Friebel, **Davide Deiana**, Paolo Malacrida, Anders Nierhoff, Anders Bodin, Anna M. Wise, Jane H. Nielsen, Thomas W. Hansen, Anders Nilsson, Ifan E.L. Stephens and Ib Chorkendorff. *Nature Chemistry*, 6: 732-738, July 2014.

Contribution: The morphology, structure, size distribution and local composition of highly active Pt_xY nanoparticle catalysts is revealed by employing aberration-corrected (S)TEM, electron energy-loss spectroscopy and X-ray energy dispersive spectroscopy. The high stability over extended electrochemical ageing tests of these alloy nanoparticles on a carbon film support is shown with identical-location TEM measurements. By combining STEM-EDS spectrum imaging and EXAFS measurements, strain effects are identified as the reason for the enhanced activity.

Paper 3

Exploring the phase space of time of flight mass selected Pt_xY nanoparticles.

Federico Masini, Patricia Hernandez-Fernandez, **Davide Deiana**, Christian E. Strebel, David N. McCarthy, Anders Bodin, Paolo Malacrida, Ifan E.L. Stephens and Ib Chorkendorff. *Physical Chemistry Chemical Physics*, Advance Article, DOI: 10.1039/C4CP02144D, July 2014.

Contribution: Transmission electron microscopy is used to verify the morphology and size distribution of time-of-flight mass-selected nanoparticles of different composition produced in a magnetron sputtering cluster source through a gas aggregation technique.

Paper 4

The enhanced activity of mass-selected Pt_xGd nanoparticles for oxygen electroreduction.

Amado Velázquez-Palenzuela, Federico Masini, Anders F Pedersen, María Escudero-Escribano, **Davide Deiana**, Paolo Malacrida, Thomas W Hansen, Daniel Friebel, Anders Nilsson, Ifan E.L. Stephens, Ib Chorkendorff. *Accepted*.

Contribution: New highly active and stable Pt-Gd alloy nanoparticles of different size are studied by means of (S)TEM in order to determine their structure, morphology and size distribution. Through identical location TEM, the high stability on the carbon film support is shown after extended electrochemical treatments.

Paper 5

Enabling direct H₂O₂ production through rational electrocatalyst design.

Samira Siahrostami, Arnau Verdaguer-Casadevall, Mohammadreza Karamad, **Davide Deiana**, Paolo Malacrida, Björn Wickman, María Escudero-Escribano, Elisa A. Paoli, Rasmus Frydendal, Thomas W. Hansen, Ib Chorkendorff, Ifan E. L. Stephens and Jan Rossmeisl. *Nature Materials*, 12: 1137-1143, November 2013.

Contribution: The structure and composition of novel Hg-Pt nanoparticle electrocatalysts for H₂O₂ production is revealed by means of aberration-corrected TEM and STEM X-ray energy dispersive spectroscopy.

Paper 6

Trends in the Electrochemical Synthesis of H₂O₂: Enhancing Activity and Selectivity by Electrocatalytic Site Engineering.

Arnau Verdaguer-Casadevall, **Davide Deiana**, Mohammadreza Karamad, Samira Siahrostami, Paolo Malacrida, Thomas W. Hansen, Jan Rossmeisl, Ib Chorkendorff, and Ifan E. L. Stephens. *Nano Letters*, 14(3):1603-1608, January 2014.

Contribution: State-of-the-art Hg-Pd nanoparticle electrocatalyst for H₂O₂ production are analysed by means of aberration-corrected STEM and STEM-EDS spectrum imaging. A core-shell structure is revealed, with a pure Pd core surrounded by a Pd-Hg ordered alloy shell.

Other papers

Paper 7

Oxygen evolution on well-characterized mass-selected Ru and RuO₂ nanoparticles.

Elisa A. Paoli, Federico Masini, Rasmus Frydendal, **Davide Deiana**, Christian Schlaup, Mauro Malizia, Thomas W. Hansen, Sebastian Horch, Ifan E. L. Stephens and Ib Chorkendorff. *Chemical Science*, September 2015.

Contribution: The morphology and particle area distributions of mass-selected Ru nanoparticles of different sizes is studied by means of aberration-corrected STEM imaging.

Paper 8

***Tentative title:* Determination of core-shell structures by STEM-EDS in nanoparticle electrocatalysts for oxygen reduction.**

Tentative authors: Davide Deiana, Arnau Verdaguer-Casadevall, Federico Masini, Ifan E. L. Stephens, Ib Chorkendorff, Jakob B. Wagner and Thomas W. Hansen.
In preparation, based on Section 5.2.3 and 6.2.2 of this thesis.

Contents

1	Introduction	1
1.1	Description of the thesis	3
2	Nanoparticle Electrocatalysts	5
2.1	Catalysis in low temperature fuel cells	5
2.2	Sintering mechanism	7
2.3	Alloys of Pt for the Oxygen Reduction Reaction	9
2.4	Rare earth Pt alloys	11
2.5	ORR towards H ₂ O ₂	13
3	Electron Microscopy	17
3.1	Transmission Electron Microscopy	18
3.2	Scanning Transmission Electron Microscopy	20
3.3	Electron Energy-Loss Spectroscopy	23
3.4	Energy Dispersive X-Ray Spectroscopy	25
3.4.1	EDS quantification	27
3.5	Electron microscopes	29
3.6	Complementary techniques	30
4	Sintering resistance of Pt cluster catalysts	33
4.1	Synthesis of mass-selected Pt clusters	33
4.2	<i>In situ</i> INPS experiment	35
4.3	<i>Ex situ</i> STEM experiments	37
4.3.1	<i>Ex situ</i> experiment at harsher conditions	39
4.3.2	Conclusion	40
5	Nanoparticle alloy catalysts for the oxygen reduction reaction	43
5.1	Synthesis of mass-selected alloy nanoparticle catalysts	43

5.2	Mass-selected Pt-Y alloy nanoparticles	44
5.2.1	Morphology	44
5.2.2	Catalytic activity and stability	45
5.2.3	Electron spectroscopy	51
5.3	Mass-selected Pt-Gd alloy nanoparticles	63
5.3.1	Morphology	63
5.3.2	Catalytic activity and stability	63
5.4	Enhanced activity of Pt alloys	69
6	Nanoparticle alloy catalysts for H₂O₂ production	73
6.1	Pt-Hg alloy nanoparticles	73
6.2	Pd-Hg alloy nanoparticles	77
6.2.1	Spectroscopy studies and elemental distribution	81
6.2.2	High-resolution STEM	83
6.2.3	Summary	85
7	Conclusions and Outlook	89
A	Appendix	93
	Bibliography	99
	Included papers	111

Introduction

Low temperature fuel cells represent a potentially zero emission alternative to traditional combustion power sources. Nonetheless, they are yet not competitive with traditional systems. The major limitation of this technology is the intrinsic high cost of the rare and precious platinum metal employed to catalyse the electrochemical reactions at the electrodes of the fuel cell. Particularly, due to its slow kinetics, the Oxygen Reduction Reaction (ORR) at the cathode requires high loadings of Pt to be driven and accounts for the majority of the efficiency losses in the fuel cell. State-of-the-art low temperature fuel cells employ Pt nanoparticles supported on high surface area carbon cathodes. The long-term stability of the catalyst is challenged by the harsh oxidising conditions of the ORR and dissolution of the metal, detachment from the support and *sintering* contribute in further lowering the efficiency of the fuel cells. Particularly, sintering is an undesired process in which some particles of the catalyst grow in dimension while other disappear, resulting in a net loss of active surface area.

In a collaborative approach, this PhD project aims to address the problem of I) rational designing of sintering-resistant catalytic systems and II) finding novel, highly active catalysts for the oxygen reduction reaction to be implemented in low temperature proton exchange membrane fuel cell (PEMFC) cathodes. The former has been accomplished in collaboration with Chalmers University of Technology and the TUM – Technical University of Munich, while the latter is the result of a collaboration with two research centres at the Department of

Physics at DTU, CINF - Center for Individual Nanoparticle Functionality and CAMD - Center for Atomic-scale Material Design.

Conducted on model mass-selected Pt clusters of less than 100 atoms supported on Si-based flat surfaces, the sintering experiments have consisted in imaging these clusters *ex situ*, before and after exposure to high temperatures and different ambient conditions. The resistance towards sintering of the clusters has been studied through the analysis of the particle distributions extracted from the electron micrographs. High angle annular dark field scanning transmission electron microscopy (HAADF-STEM) has been the technique of choice due to the strong Z-dependence of the image contrast. Heavy metals such Pt distinctly appear on light Si-based substrates. Although, imaging the supported clusters with dimension close to and below the single nanometre required the employment of state-of-the-art equipment. For this reason, the imaging has been performed in a probe spherical aberration-corrected transmission electron microscope, where a resolution below 1 Ångström can be achieved.

Alloying Pt with inexpensive and abundant materials is a promising way to decrease the cost of the ORR catalyst in PEMFCs. Y and Gd alloyed with Pt have been predicted, synthesised and then tested, in form of extended surface electrodes, as being both active and stable ORR catalysts. In order to be used as real catalysts, the alloys have been synthesised in form of nanoparticles, showing great electrocatalytic performances. To understand the reason for the high catalytic activities of the nanoparticles, the structure and the composition at the local level need to be revealed. For this reason, transmission electron microscopy has played an essential role in the characterisation of the alloy nanoparticles. As the harsh conditions of the ORR changes the elemental distribution of the catalyst, STEM X-ray energy dispersive spectroscopy (EDS) spectrum imaging has been employed to study the change in chemical composition of the nanoparticles after being subjected to catalytic tests and prolonged ageing tests.

In the same research framework of theoretical calculations/synthesis/characterisation of novel catalysts for the ORR in fuel cells technology, new alloys for the oxygen electroreduction to hydrogen peroxide (H_2O_2) have also been studied. Hg-based nanoparticles have been predicted and tested as highly active and stable systems for the reduction of oxygen to H_2O_2 . In order to provide insights on the high activity and confirm the theoretical predictions, high-resolution electron microscopy imaging and EDS spectroscopy have been employed to determine the structure and chemical compositions of promising Pt–Hg and Pd–Hg nanoparticle catalysts.

1.1 Description of the thesis

Chapter 2 briefly introduces the working principle of PEMFCs and the oxygen reduction reaction. Sintering is shortly described as well as the alloying effect on the electrocatalysts for the ORR. In Chapter 3 the basics of electron microscopy and related spectroscopy are shortly covered. The microscopes used in this project are also listed. The chapter contains also a short description of the XPS technique since XPS data will be frequently compared with electron spectroscopy one.

Chapter 4 is based on the work published in the Paper 1 attached to this thesis and describes the sintering experiments on model Pt clusters. In addition to the *ex situ* microscopy analysis, the *in situ* INPS experiment is outlined.

In Chapter 5 the experimental results of newly discovered nanocatalysts for the ORR are reported. The electron microscopy results of two studied systems, Pt_xY and Pt_xGd nanoparticles, are explained in relation to the electrochemical activities and results of complementary techniques. Analogously, Chapter 6 shows the experimental results of the Pt-Hg and Pd-Hg nanoparticle catalysts for the reduction of oxygen to H₂O₂. Part of the electron microscopy work of Chapter 5 and 6 is found in the Papers 2-6 attached to this thesis.

Nanoparticle Electrocatalysts

2.1 Catalysis in low temperature fuel cells

Fuel cells technology represents one of the most promising solution for clean energy production and conversion. A fuel cell is an electrochemical device that convert chemical energy to electrical energy. Among the different types of fuel cells, Proton Exchange Membrane Fuel Cells (PEMFCs) are considered one of the most promising alternatives to traditional power sources, especially to combustion engines used in the automotive sector due to their high power density and low operating temperature [1]. In a PEMFC, hydrogen is combined with oxygen to produce electrical energy and water via the overall reaction

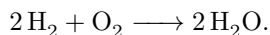


Figure 2.1 illustrates the working principle of a PEMFC. Hydrogen as fuel is oxidised to protons at the anode of the cell. The membrane in the central part of the cell, separating the two reactions, conduces only protons from the anode to the cathode while the electrons are collected into an external circuit, producing electricity. The protons reach the cathode and produce water by reacting with oxygen and the electrons.

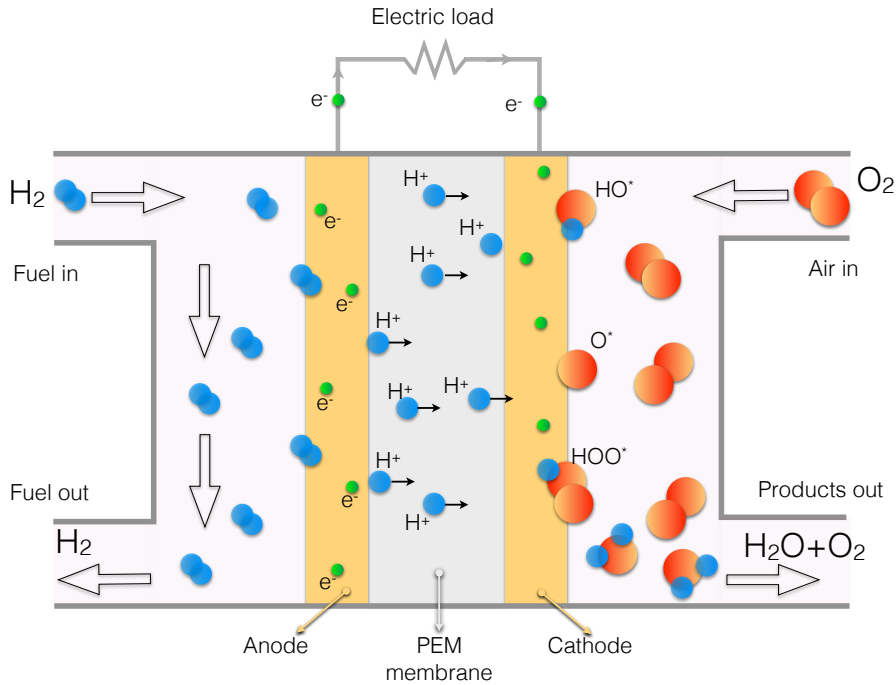


Figure 2.1: Working principle of a PEMFC.

At present, the high cost of the fuel cells system itself limits the widespread of PEMFC technology [2, 3]. The reason for the high cost is related to the materials required to catalyse the Hydrogen Oxidation Reaction at the anode (HOR) and the Oxygen Reduction Reaction (ORR) at the cathode [4], that are both based on the rare and expensive metal platinum (Pt), typically in the form of supported nanoparticles. If we consider to replace the combustion engine of a typical vehicle, ~ 100 kW, with a fuel cell-based engine, by using the state-of-the-art PEMFCs technology an amount of ~ 50 g of Pt would be necessary to drive both HOR and ORR reactions [1]. For comparison, such quantity exceeds the current level of Pt used in a catalytic converter by more than an order of magnitude, a level precluding the usage of PEMFCs at large scale [5]. A realistic implementation of this technology requires the Pt loading to be reduced at least of a factor of 10 [4, 6].

Pt is a rare metal and none of more abundant catalysts have been found both sufficiently active and stable for replacing it. Non-Pt metal catalysts are generally unstable under the harsh conditions of the PEMFCs [7]. Under strong acidic conditions of the cathode, even Pt is subjected to degradation phenomena such

as dissolution, sintering and detachment from the support [6, 8, 9]. Although present in both anode and cathode, the Pt content at the cathode is almost ten times higher compared with that of anode: this is due to the five orders of magnitude slower kinetics of the ORR compared to the HOR, making the ORR the major source of efficiency loss in a fuel cell [3]. For this reason most efforts have been focused on finding new catalysts with improved ORR performance. One promising way to achieve this goal is to alloy Pt with a cheaper and more abundant metal.

2.2 Sintering mechanism

Sintering is an undesired phenomenon common to a wide range of heterogeneous catalysis reactions. It is the mechanism in which a supported metal catalyst, in nanoparticulate form, experiences a growth in the size of the nanoparticles during the reaction, with a consequent loss in surface area and therefore activity. It is one of the most important deactivation mechanisms in industrial chemical processes where elevated temperatures are commonly used.

Sintering of supported metal nanoparticles is agreed to occur via two operative mechanisms: *particle migration and coalescence* and *Ostwald ripening*. Figure 2.2 shows the schematics of the two sintering processes: both are driven by the minimisation of the total energy of the particles. An extensive description of the sintering mechanisms can be found in the work of T.W. Hansen [10].

In a metal nanoparticle the atoms are not stable in fixed position, but move around the particle surface. This movement can induce a Brownian motion of the entire nanoparticle, allowed by a weak particle-interaction support. When two particles meet, they will coalesce and become one bigger particle. In the Ostwald ripening, atoms from small particles are detached and transported to big particles, through diffusion on the support surface or the vapor phase, due to their difference in surface energy. The chemical potential of a metal particle is described by the Gibbs-Thompson equation

$$\mu(r) = \mu_0(\infty) + \frac{2\gamma_m V_m}{r} \quad (2.1)$$

with r the radius of the particle, $\mu_0(\infty)$ is the chemical potential of the bulk, γ_m the surface free energy of the metal particle and V_m its molar volume. Due to the inverse proportionality of μ with r , the difference in chemical potential between small and large particles creates a driving force for the growth of the large particles at the expenses of the small ones.

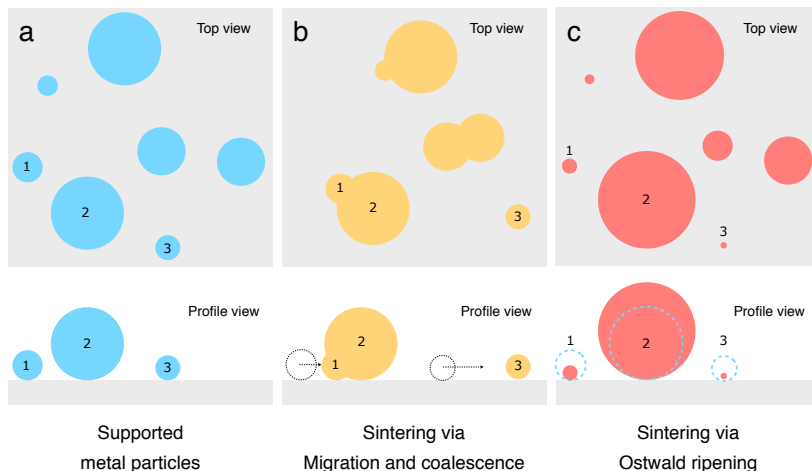


Figure 2.2: Schematics of *Particle migration and coalescence* and *Ostwald ripening* sintering mechanisms of supported metal catalysts (top-view and side-view). Three particles are labelled for an easier identification. **a:** Particles at the initial stage. **b:** Particles migrate on the support and coalesce when they meet (particle 1 and 2). **c:** In the Ostwald ripening mass transport occurs from small particles to big ones due to chemical potential differences.

Sintering has been extensively studied through the analysis of Particle size distributions (PSDs). Theoretically, the two sintering mechanisms described above can be distinguished by the shape of the PSD. With particle coalescence, the larger particles are expected to rise in number and a "tail" towards larger particles is formed, leading to a log-normal shaped size distribution. In contrary, in Ostwald ripening the PSD is shifted to higher values with a sharp cut-off and presents a tail towards small particles. However, it has been proven that PSD shapes should not be used to rule out one sintering mechanism with respect to the other. Datye *et al* [11] have studied the particle size distribution in the sintering of metallic Pd and Pt nanoparticles at high temperature and different atmospheric conditions. Even if Ostwald ripening was the observed mechanism, the PSDs in their experiments were in contradiction with the theoretical PSD models. *In situ* TEM has given a strong impetus to the sintering studies in the last years [12]. Simonsen *et al*, through time-resolved TEM imaging, have monitored the sintering of Pt nanoparticles supported on Al_2O_3 in low pressure synthetic air at 650°C , revealing Ostwald ripening to be the leading mechanism [13]. Benavidez *et al* also found Ostwald ripening to be the dominant sintering process by studying, via continuous imaging in an environmental TEM, Pd nanoparticles supported on carbon and Pt nanoparticles on SiO_2 at different environment conditions [14]. In their review, Hansen *et al* [15] have ex-

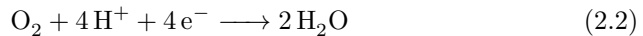
amined the recent results of metal nanoparticle sintering at high temperatures, showing dominant Ostwald ripening to be the cause of rapid activity decay in the first phase of the sintering process [15].

The growth of particles is also a reason of activity loss in PEMFCs, where temperatures are far below with respect to the ones used in industrial conditions. The durability of the catalyst during PEMFC operation is still a key challenge for the development of long-lifetime low temperature fuel cells. Shao-Horn and Ferreira have dedicated many studies to the degradation mechanism of carbon supported Pt nanoparticles in fuel cells cathode electrodes, where the metal is present in high concentrations to catalyse the sluggish ORR [8, 16, 17]. The catalyst typically consist of nanoparticles with diameter in the range of 2-5 nm in order to obtain a high surface area per unit of Pt mass. There is a general consensus in the literature that the particle growth in PEMFCs cathodes occurs mainly via electrochemical Ostwald ripening [18], a process involving the transport of neutral Pt species via a coupled process of Pt ion transport through the prevailing medium and electrons transferred through the carbon support [8, 18-21].

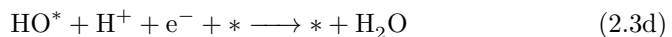
In theory, if the catalyst is formed by particles with the same size, the Ostwald ripening is not supposed to occur, should a sufficient interaction with the support be provided to avoid particle migration. In Chapter 4 of this thesis, this prediction is experimentally investigated on model Pt cluster catalysts.

2.3 Alloys of Pt for the Oxygen Reduction Reaction

The ORR involves a total transfer of four protons and four electrons in the so-called *direct four-electron reduction* [22]



Equation 2.2 represents the overall reaction, while the detailed pathway involves different intermediates:



where HOO^* , O^* and HO^* are adsorbed intermediates bound to the active site through oxygen and $*$ is the active site on the catalyst surface. Density Functional Theory (DFT) have been extensively used in the last decade to study the ORR mechanism, providing the values of chemical potentials and adsorption energies of the different intermediates [22]. The ORR activity is related to the binding energy of the reaction intermediates HOO^* , O^* , HO^* that scale linearly with each other [23,24]. The activity can then be described by the HO^* binding energy at the surface. DFT calculations on model surfaces have shown that an optimal catalyst for the ORR should have HO^* surface binding energy ~ 0.1 eV weaker compared to that of Pt(111) [22,25].

Alloying Pt with other metals is the common approach for tuning the surface binding energy. Late transition metals such as Cu, Ni, Fe and Co alloyed with Pt have been the subject of many studies since they show promising ORR activities [26,27]. In this kind of systems, the surface is composed of a Pt layer protecting the alloy [26]: the non-noble metals are in fact unstable under the acidic conditions of PEMFCs and they dissolve from the surface into the electrolyte by *dealloying*. The improved activity of such systems compared to pure Pt is originated by the alteration of the electronic and geometric structure of the surface, resulting in an energy shift of the d-band center of the Pt atoms and consequently affecting the binding energy of the reaction intermediates. This alteration can occur via *ligand* or *strain* effects [28]. Ligand effects are induced by a short-range electronic interaction of the surface Pt atoms with the atoms of the alloying metal in adjacent position to the surface. Geometric effects are induced by a long-range geometric lattice strain of the surface induced by a mismatch in the lattice parameters between the Pt alloy substrate and the outermost surface layer. The two effects coexist in most of the real systems, although in some cases the improved activity has been associate to a single effect [24,29].

The considerations made so far have been experimentally probed and confirmed mainly on large extended surfaces like single crystals or polycrystalline alloys, where it is easier to connect experimental results to the theoretical predictions. Unfortunately, this kind of samples are far from being suitable for real implementations in PEMFCs due to their high costs and low power densities. These limitations impose the use of large catalytic surface area, usually achieved by nanostructuring the catalyst. Pt nanoparticles supported on high surface area carbon (Pt/C) are in fact the currently used catalyst in fuel cells. When using nanoparticles, additional parameters need to be considered. The size of the particles starts to play an important role in the activity as the number of active sites at the surface and their specific activity depend on particle diameter. Nanoparticulate catalysts are improved by optimising their *mass activity*, defined as the ORR current at a given potential (the activity) per mass of precious metal. De-

creasing the particle size could in principle improve the mass activity since the surface-mass ratio increases and, consequently, the number of possible active sites on the surface (per mass of catalyst) would also increase. The drawback is that reducing the nanoparticle size increases the number of under-coordinated sites, and the coordination influences the specific activity [30]. In the case of Pt, these sites (such steps, kinks and edges) bind the ORR intermediates too strongly: this makes HO^* more difficult to be removed from the surface (equation 2.3d), with the consequence of lowering the overall ORR activity [25]. This size effect on the catalyst results in a mass activity peak for Pt at a particle diameter around 3 nm [8, 31].

Nanoparticle alloys of Pt and late transition metals have been studied extensively due to their enhanced ORR activities compared to pure Pt [32–34]. Analogously to their extended surface counterparts, where dealloying creates a surface layer of pure Pt on top of the alloy substrate, the dealloying process in the nanoparticles forms a *core-shell* structure where the non-noble metal is leached out from the surface. The result is an alloyed core encased in a Pt-rich shell [29, 35, 36].

The shell thickness is an important parameter controlling the activity of the nanoparticles since it determines the ligand and geometry effects applied by the alloyed core to the outermost surface layer. An increasing shell thickness would decrease the influence of both effects on the surface and therefore their impact on the activity enhancement. Thicker shells would bring the activity of the alloyed particles closer to the one of pure Pt particles.

Preserving the enhanced activity is also crucial for a promising Pt alloy nanoparticle catalyst. The critical parameter is the stability of the alloy under the operating conditions of the fuel cell. The dealloying process is in the main reason of degradation of bimetallic Pt nanoparticles, where the non-noble metal segregates to the surface and subsequently dissolves [37].

2.4 Rare earth Pt alloys

In the quest for highly active and stable catalysts, Nørskov, Rossmeisl and co-workers have employed DFT calculations to conduct a screening study in order to find new Pt alloys for the oxygen reduction reaction. The screening looked for Pt alloys with generic transition metals forming a Pt overlayer and binding the HO^* intermediate around 0.1 eV weaker than pure Pt. Stability was taken into account by selecting alloys with enthalpy of formation as negative as possible. This should in fact provide kinetic stability to prevent dealloying in

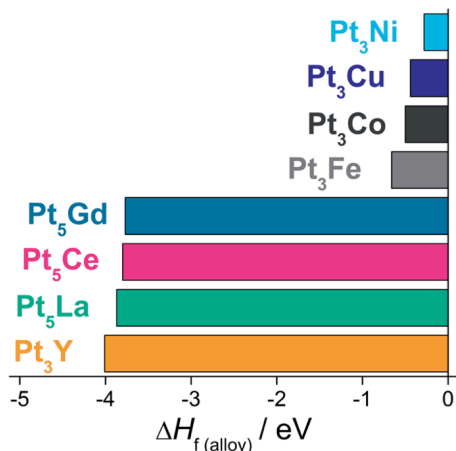


Figure 2.3: Experimental enthalpies of formation per formula unit. Image from [39].

ORR conditions. Pt₃Y was identified as a potential catalyst both active and stable for ORR [38]. Successive experiments on a polycrystalline surface have confirmed the high activity compared to polycrystalline Pt [4]. In light of the promising results of Pt-Y alloys and following the same scheme, the screening has been extended also to lanthanide metals. The most promising candidates were Pt₅La, Pt₅Ce, Pt₅Gd. Together with Pt₃Y, they all have an exceptionally negative heat of formation, as shown in Figure 2.3. Pt alloys with late transition metals such Pt₃Co, Pt₃Cu and Pt₃Ni have less negative heat of formation, making it a possible reason for their tendency to degrade through dealloying. In fact, experimental results on polycrystalline Pt₅La, Pt₅Ce and Pt₅Gd confirmed their high activity and exceptional stability for the ORR [39, 40].

As stated before, the next necessary step towards a commercialisation of the newly discovered alloys into fuel cells is their synthesis in nanoparticulate form. In addition, the synthesis process needs to be compatible for large scale production. The main obstacle for alloys of Pt with elements such Y, La, Gd is concealed in their high reactivity and tendency to form oxide compounds, which is why a suitable fabrication method is still missing. This thesis reports the electron microscopy study of the most promising catalysts for ORR, Pt-Y and Pt-Gd for the first time in form of mass-selected nanoparticles, both synthesised with a physical method based on the gas aggregation technique.

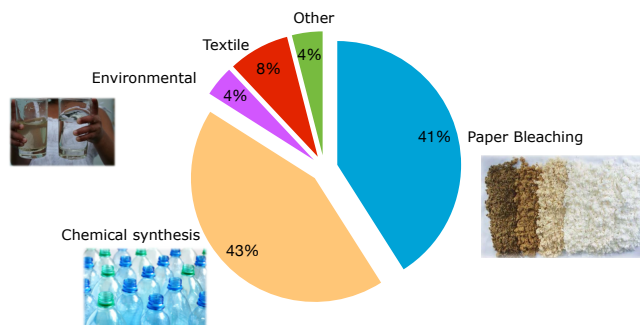


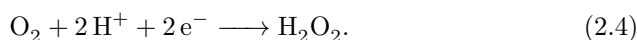
Figure 2.4: Current consumption of H_2O_2 in Europe [42].

2.5 ORR towards H_2O_2

As described in the previous sections, PEMFCs requires highly active catalysts for promoting the direct 4-electron reduction reaction (Equation 2.2)



In aqueous solutions the oxygen reduction may occur via a parallel pathway, the *2-electron reduction* [23] of oxygen to hydrogen peroxide H_2O_2



H_2O_2 is an undesirable product in power generating fuel cells since it reduces the performance by affecting their durability [41]. Consequently, the appropriate catalysts need to be highly selective toward the 4-electron reduction. On the other hand, the 2-electron reaction (Equation 2.4) can be employed in an electrochemical device where H_2O_2 is the desired reaction product. In this case, the appropriate catalyst would enhance the 2-electron pathway reaction. There is indeed a great interest in producing H_2O_2 efficiently since is one of the most commonly produced chemicals. Its current global production reaches 3 Mtons /year [42] with a forecast of 4.67 Mtons /year by 2017 [43, 44]. As illustrated in Figure 2.4, chemical synthesis and pulp/paper bleaching account for the majority of the european consumption of H_2O_2 and over 60 % of worldwide demand [42, 45]. Its use as bleaching agent allows the replacement of chlorine-based products in the chemical processes, lowering the impact on the environment. Furthermore, H_2O_2 decomposes in water and oxygen, making it one of the cleanest oxidants.

At present, hydrogen peroxide is produced via the anthraquinone process, a complex batch synthesis method run in large scale plants involving the sequential hydrogenation and oxidation of anthraquinone molecules requiring significant energy input [42]. This production process has inherent disadvantages: the energy inefficiency and the generation of waste make it not environmental friendly. In addition, transport and handling of concentrated volumes of hydrogen peroxide are not without hazards, further increasing its costs. Other synthesis methods have therefore been explored with the aim of creating a more decentralized infrastructure with small-scale production sites closer to the consumption points.

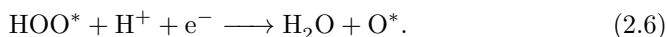
Hydrogen peroxide can be synthesised directly from its elements H_2 and O_2 through a catalytic reaction [46–48]. Au–Pd based catalysts are the most active for this process [49–51]. As anticipated, H_2O_2 can also be produced via electroreduction of O_2 in an electrochemical device of similar concept of a fuel cell or an electrolyser, where the two reactive gases are kept separated. In this way, the careful handling of hydrogen and oxygen away from the explosive regime is completely avoided.

By producing H_2O_2 in a fuel cell, hydrogen is oxidised at the anode while oxygen is reduced to hydrogen peroxide at the cathode and the energy released during the reaction would be, in principle, recovered as electric energy. When H_2O_2 is produced in an electrolyser, water can substitute hydrogen as proton source at the anode. If the device is coupled with renewable energy sources (like solar or wind) they can serve as a way of energy storage.

As already mentioned, the major limitation of such electrochemical devices resides on the slow kinetics of the ORR at the cathode. Therefore, in order to be industrially competitive, the electrochemical synthesis of H_2O_2 requires a highly active, selective and stable catalyst. The overall 2-electron oxygen reduction (Equation 2.4) takes place in two steps:



where $*$ is the active site and HOO^* the adsorbed intermediate at the catalyst surface. The catalyst has to promote the reaction 2.5b at the expenses of the parallel, undesirable reaction step



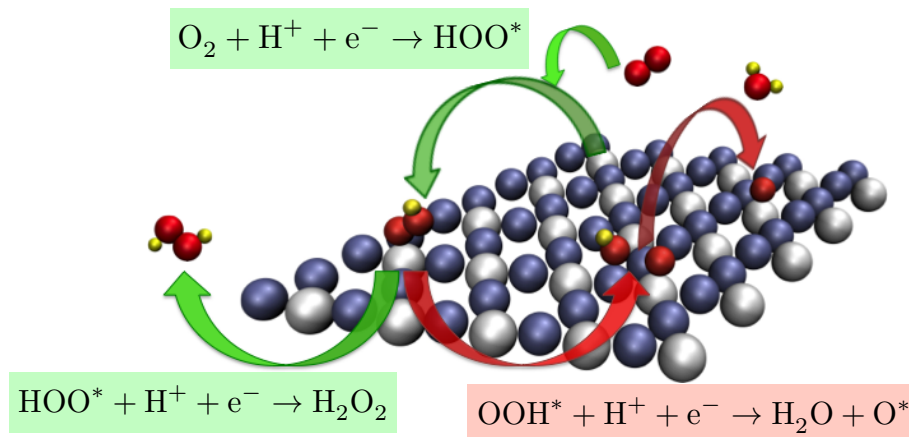


Figure 2.5: Reactions occurring on a PtHg_4 (110) model surface. Green arrows indicate the desired reaction pathway, while red arrows indicate the competitive, undesired reaction.

The catalytic activity is related to the binding energy of the reaction intermediate HOO^* while the selectivity towards the production of H_2O_2 is dictated by the catalyst's ability to dissociate HOO^* by breaking the O–O bond. In fact, if HOO^* is separated into O^* and HO^* , water formation (equation 2.6) is then preferred. An active and selective catalyst has to lower the energy barrier for the reaction 2.5 and minimise the intermediate HOO^* dissociation, i.e. raise the energy barrier for O–O splitting. This can be achieved by tuning the geometry of the reactive sites on the catalyst surface. In the highly active Pd–Au alloy catalysts for example, the active sites consist of isolated reactive atoms (Pd) [50]. Pd atoms are surrounded by less reactive ones (Au) that are unable to break the O–O bond.

With this idea, Density Functional Theory has been employed to identify new possible catalysts that could satisfy the requirements of activity, selectivity and stability. DFT calculations have been used for a screening study in search for new alloy catalysts for the electrochemical production of H_2O_2 . The screening has been performed within alloys with optimized binding energy for the HOO^* intermediate and high stability against dissolution in the reactive conditions [52]. The calculations results have indicated different metal alloys as potential candidates. Each of the alloy surfaces presents an active site where the atom of the reactive metal, such as Pt or Pd, is surrounded by atoms of the more inert element, such as Au and Hg. Among all the potential alloys discovered by the screening, PtHg_4 (110) and Pd_2Hg_5 (001) alloy surfaces have been found to be the most promising ones [52, 53].

Figure 2.5 shows a representation of the oxygen reduction reactions on a PtHg₄ (110) model surface. The grey and blue spheres represent Pt and Hg atoms, respectively. The isolated Pt atoms are the active sites where the HOO* intermediate is adsorbed. The geometry of the surface prevents the competitive pathway of HOO* reduced to H₂O + O* (red arrows in Figure 6.6), allowing high selectivity towards H₂O₂ production.

On the basis of the DFT findings, subsequent electrochemical experiments have been conducted on extended polycrystalline PtHg₄ and Pd₂Hg₅ electrodes to measure the activity for the oxygen reduction to H₂O₂ [52, 53] confirming the theoretical predictions: the two alloys have shown superior ORR activity towards hydrogen peroxide production. Following the encouraging results obtained on extended surfaces, the alloys have been synthesised in the more technologically appealing form of nanoparticles. In this thesis, the electron microscopy study of newly discovered Pt–Hg and Pd–Hg nanoparticle electrocatalysts is presented.

CHAPTER 3

Electron Microscopy

Nanoparticle catalysts are characterized with a wide range of complementary techniques such as XRD, XPS, EXAFS, XANES [54]. Although extremely powerful, these techniques provide values averaged on the whole sample and do not provide local information of the single particles. In order to obtain a local characterisation with a resolution down to the scale of the nanoparticle diameters, a technique such as electron microscopy becomes necessary.

In this thesis, transmission electron microscopy (TEM) and related spectroscopies have been employed for the study of catalytic nanoparticles. In this chapter a brief description of the TEM is given, as well as a short description of the related spectroscopic techniques. The studied catalysts were also characterised by other complementary techniques that have provided information to be correlated with the TEM results. They have been performed by other researchers as will be specified in the results sessions in the next chapters. Details are available in the published articles attached to this thesis.

3.1 Transmission Electron Microscopy

A transmission electron microscope has many analogies with an optical microscope. In an optical microscope the light source illuminates a specimen and the transmitted light is then manipulated by a series of optical lenses to form a magnified image. Optical lenses can be shaped with such high accuracy that aberrations can be neglected and do not affect the resolution of the light-optical instrument. The resolution is limited by diffraction, and is defined by the Rayleigh formula

$$\delta = \frac{0.61\lambda}{\mu \sin \beta}$$

where μ is the refractive index of the viewing medium and β the semiangle of collection. With a large aperture lens and considering air as the viewing medium, we can approximate the term $\mu \sin \beta \approx 1$. For green light $\lambda = 550$ nm, the best possible resolution δ is about 300 nm. It is clear that optical microscopes do not provide sufficient resolution to observe the matter at the *nanoscale* (below 100 nm).

In a TEM an electron-transparent sample is illuminated with high energy electrons generated by an electron gun (by thermionic effect or field emission) and accelerated by an applied voltage. The electrons transmitted through the specimen are projected onto the image plane to form a two-dimensional image.

Electrons are quantum particles and possess a De Broglie wavelength λ related to their momentum p :

$$\lambda = \frac{h}{p}$$

where h is Planck's constant. When accelerated by a voltage V , electrons acquire a kinetic energy that must be equal to the potential energy

$$eV = \frac{1}{2}m_0v^2$$

and since the particle momentum $p = m_0v$, the electron wavelength can be expressed in function of the accelerating voltage

$$\lambda = \frac{h}{\sqrt{2m_0eV}}. \quad (3.1)$$

Common accelerating voltages in TEM microscopes span from 80 kV to 300 kV. At such energies, the electrons enter in the relativistic regime, therefore the

equation 3.1 is corrected with a relativistic factor assuming the form

$$\lambda = \frac{h}{\sqrt{2m_0eV \left(1 + \frac{eV}{2m_0c^2}\right)}}. \quad (3.2)$$

Typical wavelengths are 3.35 pm for 120 kV, 2.51 pm for 200 kV and 1.97 pm for 300 kV accelerating voltages.

Electrons are charged particles and their trajectories can be modified with Lorenz forces. In the TEM the electron beam generated by the gun is controlled by a series of electromagnetic lenses vertically aligned and forming the microscope column. When the electron passes through a lens, its trajectory is modified by the electromagnetic field generated by a current circulating in the lens. Therefore, the strength of the lens is controlled by adjusting the current running through its internal coils. This allows focus and magnification adjustments without moving the lenses, differently from the optical microscope. Despite this advantage, electromagnetic lenses are far from being perfect. In fact, the generated field is not uniform: electrons entering the lens at different distances from the optical axis are focussed differently. The effect is that a single point of the object is projected not into a single point in the image plane but into a disk. This effect is known as *spherical aberration*, and is the main one limiting the resolution in a TEM. High-end microscopes can nowadays compensate the spherical aberration with additional, more complex lenses (aberration correctors) to achieve higher resolutions.

In TEM the specimen is illuminated by a parallel coherent electron beam that passes through it. The image is formed by collecting transmitted electrons through an objective lens (and its aperture) centred around the optical axis as depicted in Figure 3.1. Electrons can be transmitted undeflected or scattered at different angles by interacting with the sample. If they are scattered at angles higher than the objective aperture semi-angle α , they are intercepted by the objective aperture and do not contribute to form the image, while unscattered electrons will not be stopped. In this case, a *bright-field* image is formed. Alternatively, the objective aperture can be displaced in order to select and transmit electrons scattered at particular angles, and a *dark-field* image is formed.

When travelling through the specimen, electrons interact in different ways with the sample's material. For this reason, different contrast mechanisms are possible in the TEM. *Mass-thickness* contrast is the result of incoherent elastic scattering of electrons (Rutherford scattering). In this process the scattering cross section is a function of both the atomic number Z and the thickness of the sample. Heavy-atom and/or thicker regions of the specimen scatter the electrons at higher angles (i.e. more electrons will be deviated at an angle greater

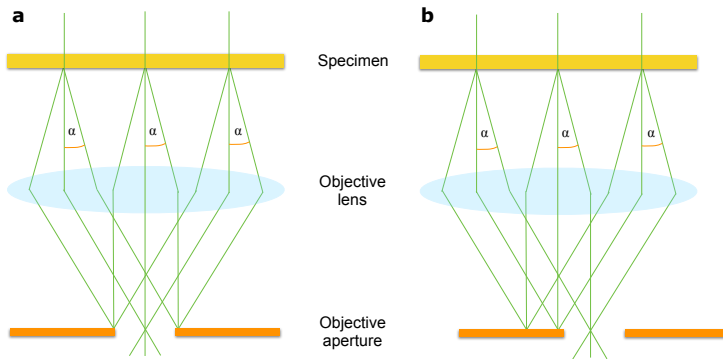


Figure 3.1: **a:** Formation of a bright-field image and **b:** Dark-field image. α is the objective aperture semi-angle.

than the objective aperture semi-angle α in Figure 3.1-a) that are subsequently intercepted by the objective aperture as shown in Figure 3.2, thus making those regions appear darker.

Diffraction contrast is also generated by elastic scattering of electrons but results from coherent Bragg scattering by lattice planes of the crystalline sample oriented at specific (Bragg, θ_B) angles relative to the incident beam, as shown in Figure 3.3. When $2\theta_B$ exceeds the semi-angle α of the objective aperture, the crystalline area will appear dark in the image. Finally, *phase contrast* arises from the interference of the diffracted beams and the incident beam in crystalline specimens (Figure 3.4). The phase variation is related to the projected potential of the specimen along the optical axis, and is translated in a contrast variation in form of fringes carrying the information on the lattice periodicity of the crystal. For this reason phase contrast is at the basis of atomic resolution TEM.

3.2 Scanning Transmission Electron Microscopy

In scanning transmission electron microscopy (STEM) a convergent electron probe is illuminating the specimen instead of a parallel beam like in TEM [55]. In STEM the image is formed by rastering the probe across the region of interest of the specimen and measuring the intensity of the transmitted beam as a function of the probe position. Analogously to TEM, bright-field and dark-field images can be formed by selecting the transmitted electrons at different scattering angles. Figure 3.5 shows the different collected electrons as a function of

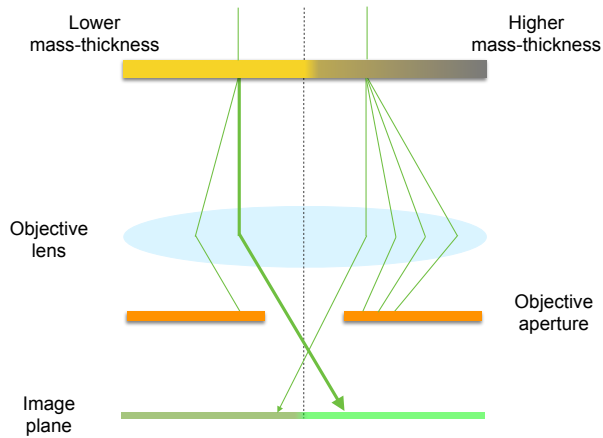


Figure 3.2: Mass-thickness contrast formation. The electron scattering from different regions of the thin specimen is shown. In low mass-thickness areas (left) only few electrons are scattered and stopped by the aperture while many undeflected ones reach the image plane, making the region appear bright. In high mass-thickness areas (right) more electrons are scattered and consequently intercepted by the aperture: the regions appear dark.

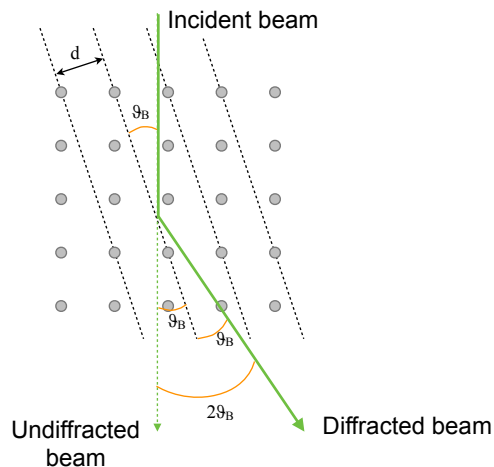


Figure 3.3: Schematics of electron diffraction from atomic planes. θ_B is the Bragg's angle and d is the interplanar distance.

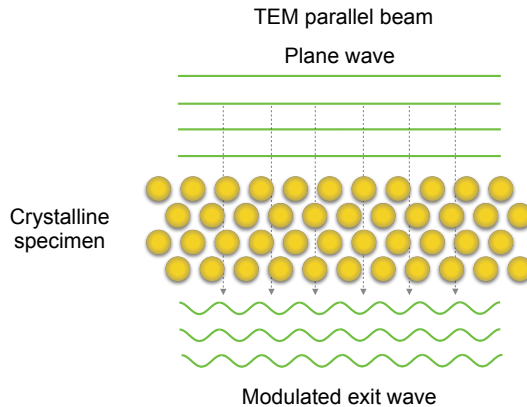


Figure 3.4: Schematics of phase contrast formation. The coherent TEM beam illuminates the crystalline sample as a plane wave. At the crystal exit surface, the transmitted electron wave carries information about the crystal potential, projected in the direction of the incident beam.

the scattering angle.

Bright-field STEM images are formed collecting the direct beam and scattered electrons at small angles (diffracted electrons) through the bright-field detector. Electrons scattered through higher angles (between 10 mrad and 50 mrad) are used to form a dark-field image and are collected by an annular dark-field (ADF) detector. Regions with higher mass-thickness will then appear brighter. *Z-contrast* is the name given to high-resolution (atomic) mass-thickness contrast imaging, where single-atom (or column of atoms) scattered electrons are collected. A high-angle annular dark field (HAADF) detector is employed for *Z-contrast* imaging, where only the electrons deflected by pure elastic incoherent scattering are collected. Typically, HAADF-detectors collect the electrons scattered at angles larger than 50 mrad (θ_1 in Figure 3.5). In this way Bragg diffraction effects are avoided and the contrast is not influenced by the orientation of the specimen, but solely dependent on the atomic number Z (with an exponential dependency $\sim Z^{1.7}$) and the thickness. *Z-contrast* images are also referred as HAADF images.

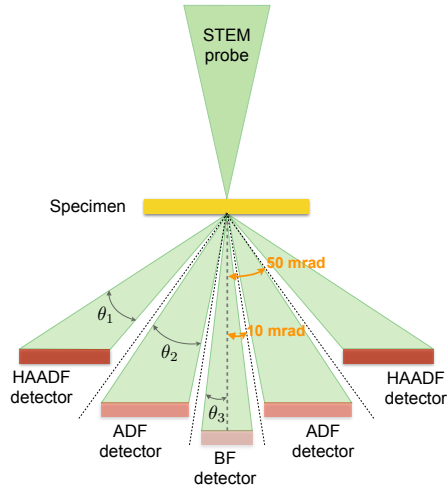


Figure 3.5: The electron probe in STEM is rastered across the specimen. Scattered electrons collected at different angles provide different image contrast. The HAADF detector collects electrons scattered at more than 50 mrad (θ_1), the ADF detector from 10 mrad to 50 mrad (θ_2). For the BF detector, θ_3 is less than 10 mrad.

3.3 Electron Energy-Loss Spectroscopy

Electron energy-loss spectroscopy (EELS) analyses the energy distribution of the electrons transmitted through the specimen [56]. In TEM, the high energy electrons transmitted through the specimen can either emerge unaffected or interact with it. This interaction can lead to different scattering phenomena and in a part of the initial energy of the incoming electrons is transferred to the specimen. When an incident electron approaches the nucleus of an atom, the large electrostatic field generated by the nuclear charge causes the electron to be deflected elastically through a large angle (Rutherford scattering) with no appreciable loss of energy. Inelastic scattering is the result of the electrostatic interaction between the fast incident electrons and the electronic cloud of the atom. The result is the excitation of an atomic electron to a higher energy level and different scenarios are possible as depicted in Figure 3.6.

Inner shell electrons can undergo a transition from their ground state to an unoccupied state above the Fermi level only if they absorb an amount of energy equal to (or larger) than the binding energy. Due to conservation of energy, the same amount of energy is lost by the incident electron. The vacancy left by the exited electron is then filled by an electron in an outer shell that undergoes a downward energy transition, liberating the excess energy in the form of X-rays

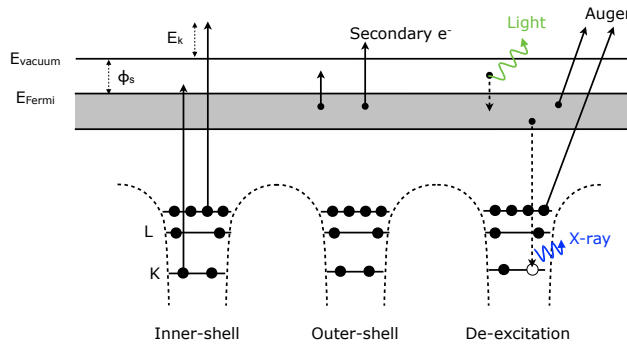


Figure 3.6: Energy excitation and relaxation processes.

or as kinetic energy of another atomic electron (Auger emission). Outer shell electrons can also be excited by the incident fast electron to a higher energy level. If the absorbed energy is sufficient to reach the surface and the final state of the transition is above the vacuum level, the excited electron can be emitted as a secondary electron. Outer shell scattering may also take the form of a many-atom excitation of the specimen called *plasmon* excitation, where valence electrons are excited in a collective oscillation (plasmon resonance). The basic requirement for plasmon excitation is that the participating electrons share their energy: this condition is fulfilled by electrons in delocalised states, such as the valence states in metals.

An EELS spectrum is produced separating the transmitted electrons according to their kinetic energy, showing the number of electrons (intensity) as a function of their energy-loss suffered in the interaction with the specimen. Different regions can be identified in the EELS spectrum. Around zero energy-loss an intense peak represents the electrons transmitted without transferring energy and remaining undeflected after going through the specimen. This peak is named zero-loss peak, and includes also electrons that suffered energy loss under the detection limit. The region below ~ 50 eV is named low-loss region, where the scattering from outer shell electrons, such as plasmons, is generally visible as a peak. The rest of the spectrum, the core-loss region, contains the features representing the inner shell excitations that usually take the form of edges occurring at the ionization thresholds, i.e. approximately the binding energy of the corresponding atomic shell. These edges provide a direct elemental identification since the binding energy of the inner shells is characteristic of the atomic species.

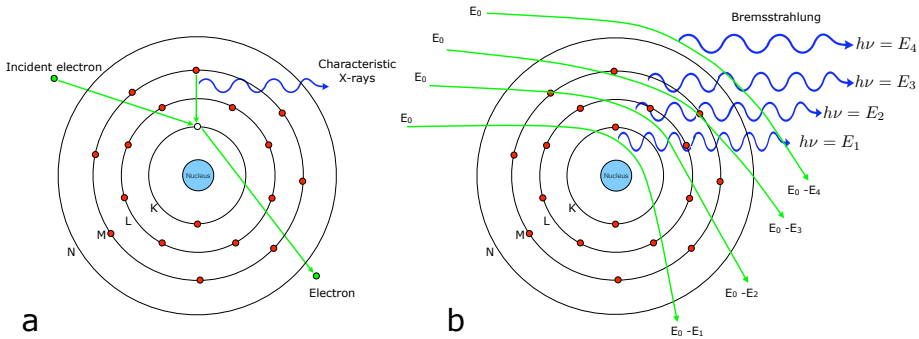


Figure 3.7: Electron-atom X-ray generation interactions. **a-** Characteristic X-rays and **b-** Bremsstrahlung radiation.

3.4 Energy Dispersive X-Ray Spectroscopy

X-Ray energy dispersive spectroscopy (usually referred as EDX, XEDS or EDS) analyses the energy distribution of the X-Rays generated by the interaction of the high energy electrons with the analysed specimen. As briefly outlined in the previous section, inner shell electrons can absorb enough energy to ionize the atoms in the specimen (the ionization energy) and characteristic X-Rays are isotropically emitted in the relaxation process [57].

The primary electrons may also be inelastically scattered by the electrostatic field of the nuclei losing some of the energy in the form of X-rays called Bremsstrahlung radiation. Since any amount of energy-loss is possible (up to the energy of the incoming electrons and depending on the strength of the interaction) the Bremsstrahlung radiation presents a continuous energy distribution. The final spectrum of the X-rays coming out of the specimen is then composed of a continuous background formed by Bremsstrahlung X-rays with superimposed characteristic X-rays peaks. X-rays in the TEM are collected by EDS detectors positioned closed to the specimen in the microscope column. A typical configuration is depicted in Figure 3.8. Si(Li) detectors are still the most common in TEM and STEM EDS analysis, but they are gradually being replaced by Si-drift detectors (SDD) due to their improved performance.

X-rays EDS is a powerful technique especially when used in combination with STEM. In fact, the electron probe can easily be moved around the specimen and the local chemical information coming from the different selected features in the specimen can be easily acquired. Nonetheless, the EDS sensitivity in STEM is severely limited by mainly two factors: the small interaction volume and

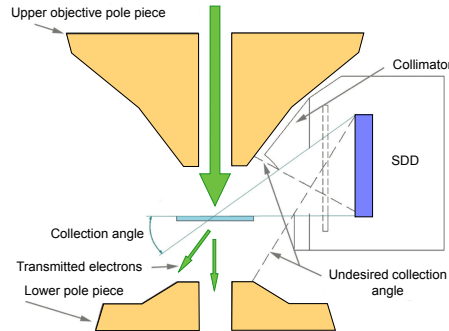


Figure 3.8: Schematics of typical EDS detector/pole piece geometry in the TEM column.

the microscope-detector configuration. The electron probe excites a very small volume of matter in electron-transparent samples and, consequently, the number of generated X-rays from the beam-specimen interaction is very small. The geometry of the system affects the EDS analysis since it influences the fraction of the characteristic X-rays collected. An important parameter characterising the EDS detector is the collection angle, that is the solid angle subtended by the active area of the detector at the analysis point of the specimen. Detectors are usually oriented towards the specimen to maximise the solid angle that can be expressed as $\Omega = A/d^2$, with A the active area of the detector and d the distance from the analysis point to the detector [58]. Typical solid angle values range from 0.15 sr to ~ 0.3 sr out of the 4π sr X-ray emission sphere. Such small values of Ω lower the detection efficiency to very low numbers (1-3 %), therefore X-ray spectra of small specimens require long acquisition times. Other parameters are important to maximise the efficiency of the detection, such as the elevation angle, the sample holder geometry etc. Field emission guns (FEG) in STEM microscopes has led to a huge improvement in the available beam current densities even with very small electron probes [59]. For EDS this translates to a higher amount of photons generated per volume unit and a high count rate is then achievable. The compact design of new SDD detectors has allowed new detector-microscope geometries to be proposed in the past years [60,61]. FEI has recently integrated four SDD detectors in the conventional TEM geometry symmetrically placed around the optical axis close to the sample area. In this way a total solid angle of 0.9 sr has been achieved, with an average 4-fold improvement on the count rate with respect to standard Si-Li detectors [62].

EDS point analysis is a standard procedure in STEM-EDS. The probe is left stationary on points of interest of the specimen and X-rays are collected for an appropriate amount of time depending on sample stability, contamination and beam damage. EDS Spectrum Imaging (SI) is an extension of the point analysis

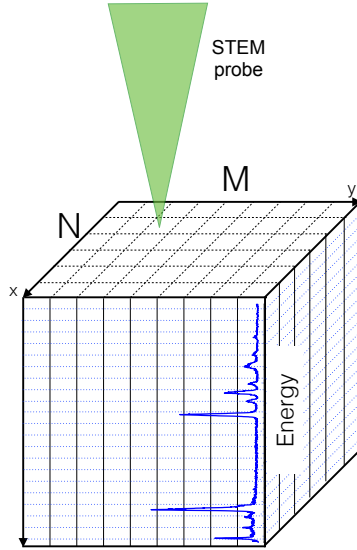


Figure 3.9: Schematics of the spectrum imaging acquisition in STEM. For each pixel in the $N \times M$ grid, a full EDS spectrum is acquired.

where the X-rays are used to form an image with a 2-dimensional chemical information. The probe is scanned on a $N \times M$ pixels matrix drawn on the STEM image of specimen and for each pixel a full EDS spectrum is acquired. The result is a 3-dimensional data cube with the electron image on the $x - y$ plane and the X-rays energy along z as depicted in Figure 3.9.

3.4.1 EDS quantification

Characteristic X-ray peaks in the EDS spectrum can also be used to obtain a quantitative analysis of the specimen under study. In bulk materials, the concentration of an element C_i in the specimen generates a certain amount of characteristic X-rays. Castaing proposed that using a known standard of the same element with a certain concentration $C_{(i)}$, the concentration C_i could be calculated following the relation

$$\frac{C_i}{C_{(i)}} = K \frac{I_i}{I_{(i)}} \quad (3.3)$$

where I_i is the X-rays intensity emerging from the specimen and $I_{(i)}$ is the measured intensity emerging from the standard. K is a sensitivity factor taking

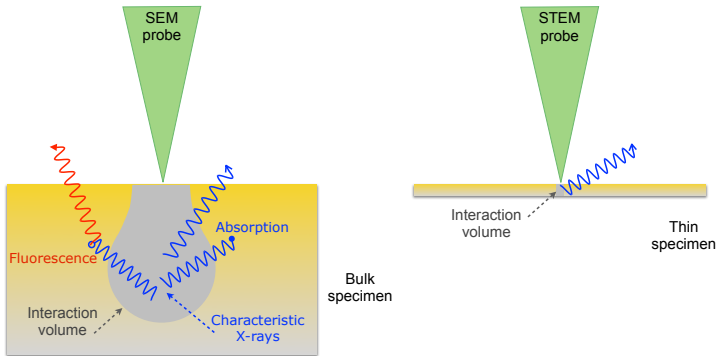


Figure 3.10: Volume interactions in a bulk specimen (left) and an electron-transparent specimen (right). In thin specimens STEM-EDS the absorption and fluorescence are commonly neglected.

into account the difference between the generated and measured X-ray intensities for the standard and specimen. Three parameters contribute to K :

- The atomic number Z
- The absorption of X-rays within the specimen A
- The X-ray fluorescence within the specimen F .

Figure 3.10 shows the *interaction volume* from where the X-rays are generated by the electron beam/specimen interaction.

In bulk samples, typically analysed in a scanning electron microscope (SEM), the X-rays are generated from a large volume, and the absorption of an X-ray emitted from another atom within the specimen is not unlikely. The absorption decreases the total amount of X-rays that can be collected from the X-ray detector. Fluorescence within the sample occurs when characteristic X-rays from a heavier element can ionise atoms of lighter elements instead of escaping from the sample. This causes an increment of the total X-rays detected from the light element, while the number from the heavier element decreases. Therefore, in bulk specimen analysis absorption and fluorescence need to be taken into account. The atomic number correction (Z) depends on the average atomic numbers of the specimen, and takes into account the electron back-scattering and the electron stopping power effects. The correction procedure is often referred as ZAF correction [63].

In STEM the specimen is an electron-transparent sample. Due to the reduced interaction volume, corrections for absorption and fluorescence can be neglected and only the Z correction needs to be performed. This approximation is named *thin-film criterion*. For a thin specimen the quantification can be simplified by measuring the intensities of different elements simultaneously in the EDS spectrum with the *Cliff-Lorimer ratio* method [64]. In a specimen composed of two elements A and B , their compositions C_A and C_B (defined usually as weight%, mass% or atomic%) can be determined from their corresponding characteristic X-ray intensity, above the background, I_A and I_B as

$$\frac{C_A}{C_B} = k_{AB} \frac{I_A}{I_B} \quad (3.4)$$

avoiding the measurement of data from standard samples. k_{AB} is the Cliff-Lorimer sensitivity factor. k factors can be determined experimentally [57] or theoretically [63], depending on the necessary accuracy. k factors depend on many parameters among which are the detector efficiency, ionization cross section, fluorescence yield, microscope parameters and are usually integrated in the EDS analysis software.

3.5 Electron microscopes

The electron microscopy results reported in this project have been obtained by data collected in three different microscopes, two FEI Titan TEMs located in the Center for Electron Nanoscopy at DTU (Lyngby, Denmark) and an FEI Osiris TEM at the Interdisciplinary Center for Electron Microscopy - EPFL (Lausanne, Switzerland).

Titan E-Cell 80-300ST TEM is a 300 kV monochromated FEG (S)TEM equipped with a CESCOR C_s spherical aberration corrector for the objective lens. The microscope has been used for high-resolution bright-field images acquired via a Gatan 894 2Kx2K UltraScan 1000 CCD camera. This microscope is also equipped with a differential pumping system for *in-situ* studies at different gas environments.

Titan Analytical 80-300ST TEM is a 300 kV monochromated FEG (S)TEM equipped with a CESCOR C_s spherical aberration corrector for the condenser lens, optimised for STEM imaging. The microscope have been used for high-resolution HAADF-STEM images acquired via a FISCHIONE HAADF detector,

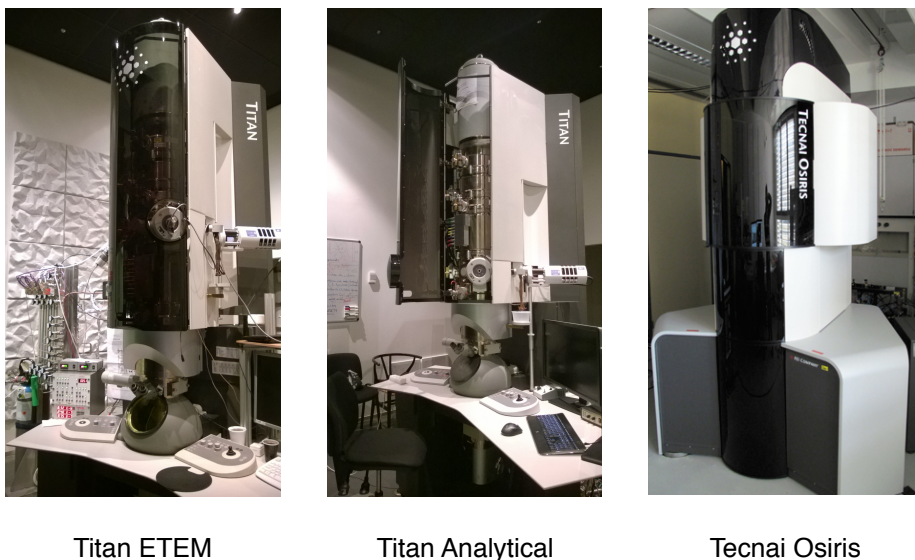


Figure 3.11: The two Titan at DTU Cen and the Tecnai Osiris at CIME-EPFL transmission electron microscopes.

STEM-EDS analysis with a Oxford Instrument X-Max SDD EDS detector attached to the microscope column and STEM-EELS analysis with a Gatan 865 Tridiem energy filter.

Tecnai Osiris 80-200 (S)TEM is a 200 kV FEG (S)TEM microscope optimised for STEM-EDS analysis. The microscope is equipped with four windowless Super-X SDD EDS Bruker detectors with a total collection angle of 0.9 sr. The STEM-EDS spectrum images presented in this thesis have been acquired with this electron microscope.

3.6 Complementary techniques

X-Ray Photoelectron Spectroscopy (XPS)

XPS is a spectroscopy technique widely used in surface science [54]. It provides elemental composition information as well as the chemical bonding state of the elements composing the surface of the analysed specimen. XPS is based on the

photoelectric effect where electrons are emitted from an atom due to absorption of photons (X-rays). If the energy of the photon $h\nu$ absorbed by the atom is higher than the binding energy E_b and the work function of the material ϕ , an electron is emitted (Figure 3.6). The kinetic energy E_k of the ejected electron is then a function of the initial binding energy (characteristic of the chemical element). An XPS spectrum reports the distribution of kinetic energies of the emitted electrons calculated from the equation

$$E_k = h\nu - E_b - \phi.$$

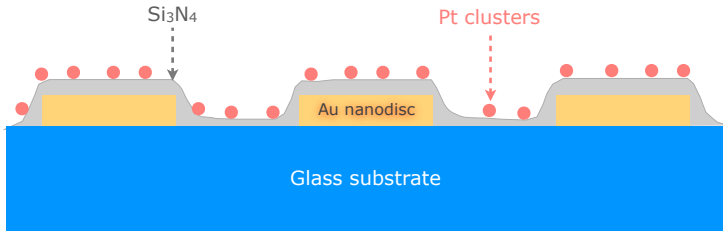
XPS is a surface-sensitive technique since the emitted electrons interact strongly with the material itself with a typical mean free path ranging from 5 Å to 20 Å, so only electrons emitted from atoms close to the surface can be collected.

Sintering resistance of Pt cluster catalysts

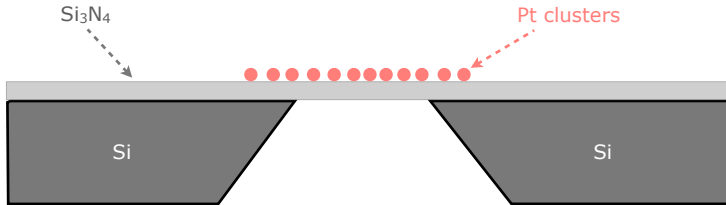
As mentioned in Chapter 2, sintering by Ostwald ripening causes a loss of active surface area of catalysts during chemical processes. Since the driving force for this mechanism has its origin on the different chemical potential and curvature of the nanoparticles, a catalyst presenting particles with identical size should in theory not experience Ostwald ripening, provided that they are sufficiently stable on the support and therefore do not migrate at the selected temperature. Mass transport between particles is most likely still happening but with a net flux equal to zero, therefore no particle growth is expected to occur. This assumption is here experimentally verified. By employing model size-selected Pt clusters, the sintering resistance of the metal catalysts exposed to relevant condition is tested by means of *in situ* indirect nanoplasmonic sensing (INPS) and *ex situ* scanning transmission electron microscopy (STEM) [Paper 1].

4.1 Synthesis of mass-selected Pt clusters

Four samples with different particle distribution have been synthesised in a laser ablation cluster source [65]. By using such a cluster source it is possible to synthesise specimens with a narrow size distribution peaked at the desired



(a) INPS chip design. Gold nanodiscs are placed onto a glass slide and a Si_3N_4 substrate is subsequently deposited. Pt clusters are then soft-landed on the chip.



(b) Schematics of the Si_3N_4 TEM window. Pt clusters are soft-landed on the electron transparent region of the film.

Figure 4.1: INPS chip (a) and TEM window (b) schematics.

size. The details of the deposition can be found in the synthesis section of the Paper 1 attached to this thesis and a full description of the synthesis setup is found in [66]. For the *ex situ* STEM experiments, the Pt clusters have been soft-land deposited on flat amorphous Si_3N_4 TEM windows. For the *in situ* INPS experiments, the clusters have been deposited on INPS sensor chips [67]. As shown in Figure 4.1, INPS sensor chips are constituted of a glass slide support ($15 \times 15 \text{ mm}^2$) where an array of gold nanodiscs is deposited on top of it via mask colloidal lithography. The nanodiscs have a diameter of 80 nm and height of 20 nm. The glass substrate and the Au discs are then covered with a thin dielectric Si_3N_4 layer (10 nm) onto which the Pt clusters are soft-land deposited. The Si_3N_4 layer is needed to recreate the same surface conditions of the TEM windows, allowing for a direct comparison.

The different samples consist of:

- Unselected $Pt_{n>53}$: a broad distribution of Pt cluster sizes is created by simply avoiding the size-selection during the deposition, although a minimum number of 53 Pt atoms per cluster is still retained due to the synthesis conditions [66];

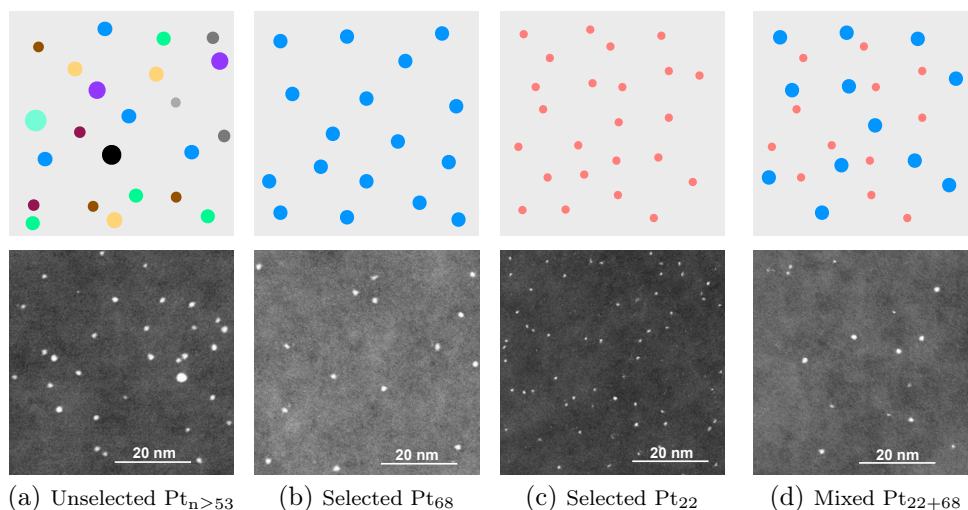


Figure 4.2: Schematic representation (top) and corresponding HAADF-STEM micrographs (bottom) are shown for the different Pt clusters.

- Mass-selected Pt_{68} : a monomodal distribution of 68 atoms Pt clusters is created;
- Mass-selected Pt_{22} : a monomodal distribution of 22 atoms Pt clusters is created;
- Mixed Pt_{22+68} : a bimodal distribution is created by mixing the two different mass-selected clusters with a 1:1 ratio.

Figure 4.2 shows a schematic representation of the four different types of the as-prepared clusters together with representative HAADF-STEM images. The clusters (assumed with a spherical shape [66, 68, 69]) are colour-coded according to their size. For the unselected sample a variety of sizes are deposited, while the selected Pt_{68} and Pt_{22} consist of well defined and uniform clusters. In the mixed sample Pt_{22+68} , both 22 and 68 atoms clusters are deposited.

4.2 *In situ* INPS experiment

The resistance towards sintering of the Pt clusters has been tested *in situ* under inert atmosphere at high temperature using a Insplorion X1 flow-reactor INPS

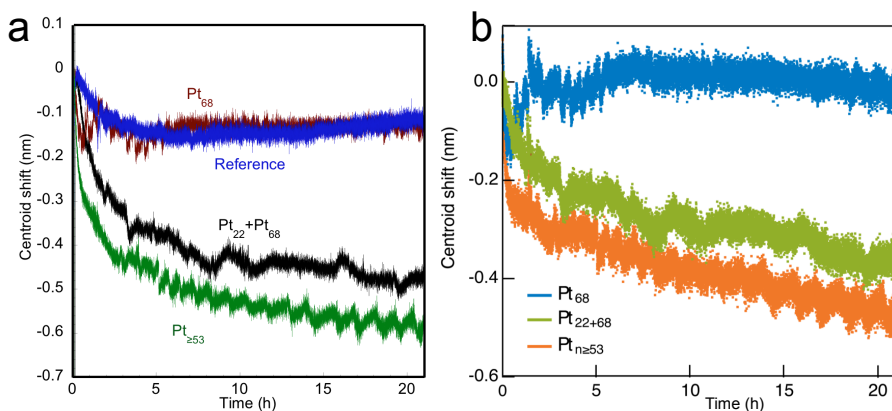


Figure 4.3: **a:** Raw INPS data for a reference chip without particles (blue) and for chips with different deposited cluster sizes. **b:** Reference-subtracted INPS centroid shift for the different samples.

platform [67, 70]. Both INPS chips and TEM windows have been treated simultaneously to ensure the same treatment to all the samples. For each sintering experiment, the reactor has been pre-heated to 453 K and the samples inserted and left under isothermal conditions for 21 h in Ar flow of 200 mL min^{-1} . The INPS platform allows to monitor the sintering kinetics in real time by exciting a localised surface plasmon resonance (LSPR) [70] in the Au disks of the INPS chips through illumination with low power polychromatic light. The plasmon frequency is dependent to the local environment, that is the density of the particles and their size. A negative shift in the INPS signal frequency indicates that sintering occurs [71]. During the INPS experiment, the maximum light extinction wavelength of the LSPR (denoted as centroid) is recorded through a fiber-coupled spectrometer.

Figure 4.3 shows the INPS centroid shift vs. sintering time, for the Pt_{68} , Pt_{22+68} and $Pt_{n \geq 53}$ clusters in Ar at 453 K. Figure 4.3-a represents the raw INPS data, where the blue line is the measurement of a blank chip with no particles deposited. This serves as a reference that is subtracted from the cluster's curves to obtain the curves in Figure 4.3-b.

For the size-selected Pt_{68} clusters the INPS centroid shift signal is stable along the 21 h treatment. The instability registered at the initial stage is due to temperature equilibration and desorption of volatile species from the surface of the cold sample inserted in the hot reactor. In contrary, the mixed Pt_{22+68} and the unselected $Pt_{n \geq 53}$ clusters show a clear negative centroid shift towards

shorter wavelength as function of sintering time, indicating that sintering occurs.

4.3 *Ex situ* STEM experiments

To give a clear picture of the sintering process occurred during the thermal treatment and strengthen the INPS measurements, *ex situ* STEM imaging before and after the treatment has been performed. As previously mentioned, samples with the same amount and size of clusters of the INPS chips were prepared by depositing the Pt clusters onto Si_3N_4 TEM windows. The TEM samples have been exposed to the same sintering conditions as the INPS chips since they have been treated in parallel inside the reactor. HAADF-STEM has been employed as imaging technique in the FEI Titan Analytical at 300 kV accelerating voltage. Due to the atomic-number dependence of the HAADF signal, this technique has been the favourite choice to image the very small heavy-metal Pt particles on the selected substrate. HAADF-STEM micrographs of the samples were acquired before and after the sintering treatment and the corresponding particle area distributions extracted. For the Pt clusters studied here, the measure of the projected area is preferred to the commonly used particle diameter since the influence of the different isomer structures on the diameter of the clusters is stronger than for bigger particles [69].

Figure 4.4 shows the particle area distribution histograms of the different analysed samples before and after the sintering treatment. The as-prepared histogram of the unselected clusters shows a broad particle area distribution, where the area spans in range $\sim 1 \text{ nm}^2$ to 4 nm^2 . The size-selected and mixed samples show the sign of the mass selection, with narrow monomodal area distributions for the Pt_{68} and Pt_{22} clusters and a bimodal distribution for the mixed Pt_{22+68} clusters.

In the $Pt_{n>53}$ sample, the number of large area clusters increases at the expense of small area clusters after the sintering treatment. If particle migration and coalescence occurred, the number of clusters would decrease, but this is not the case. In fact, the measurement of the cluster coverage (number of clusters per unit of support area) reported in Table 4.1 indicates that the particle density stays constant through the sintering treatment. These results suggest then Ostwald ripening as the main sintering mechanism, where the bigger particles grow at the expenses of the small ones. In fact, Ostwald ripening is characterised (at early stage) by a constant particle density while in particle migration and coalescence the density always decreases. As seen from the INPS centroid shift (Figure 4.3), the mass-selected Pt_{68} clusters show a high-sintering resistance at 453 K, with only very small changes detected in the area distribution histogram.

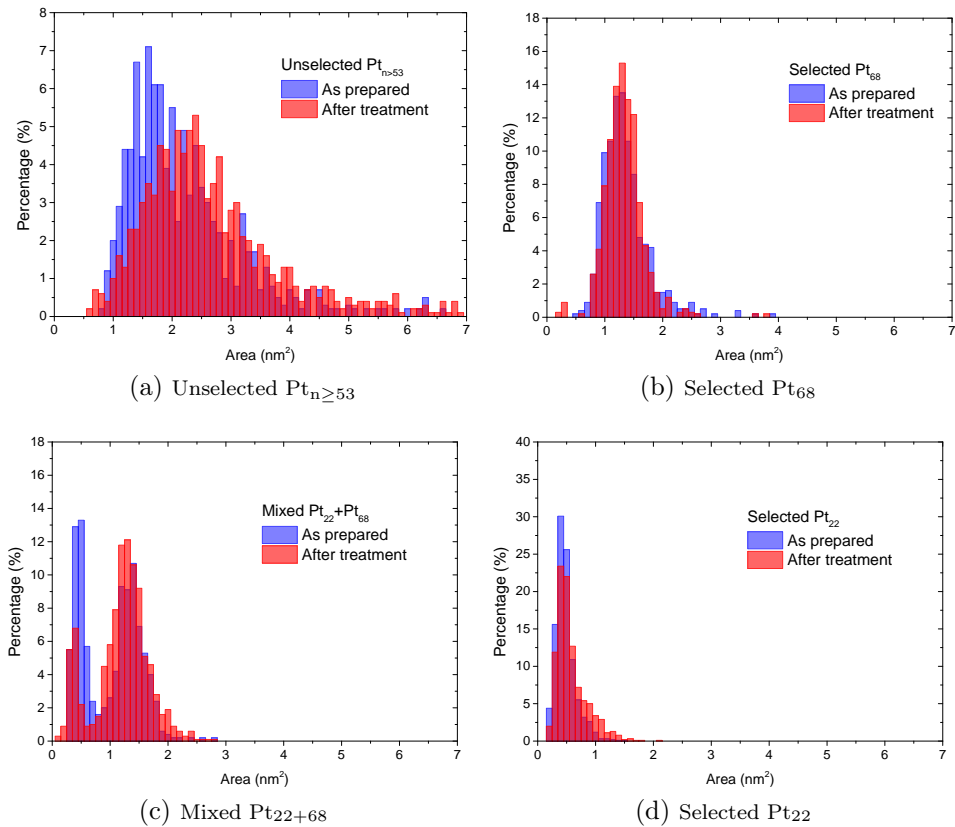


Figure 4.4: Particle area distribution histograms of the different clusters extracted from the HAADF-STEM micrographs before (blue) and after (red) the sintering treatment.

Table 4.1: Cluster coverage for the different samples.

Sample	Coverage as-prepared (clusters/nm ²)	Coverage after treatment (clusters/nm ²)
Unselected Pt _{n≥53}	0.004	0.004
Selected Pt ₆₈	0.003	0.003
Mixed Pt ₂₂₊₆₈	0.003	0.003
Selected Pt ₂₂	0.016	0.017

The result of Ostwald ripening is also observed in the mixed Pt_{22+68} sample: the peak of the 22-atom clusters clearly drops and shifts towards smaller areas, while the larger clusters around the 68-atom clusters increase in number. A constant coverage is also observed for the mixed sample. To completely exclude the migration of the 22-atom clusters as the cause of the observed sintering in the mixed Pt_{22+68} sample, a mass-selected sample of only Pt_{22} with high coverage (5 times the coverage of the other three systems) has been tested and the *ex situ* experiment results are shown in Figure 4.4d. Even the small Pt_{22} clusters show stability towards sintering.

The results obtained from the particle area distribution histograms clearly show that monomodality is a key factor for suppressing Ostwald ripening, with single-size clusters not sintering at the applied conditions.

4.3.1 *Ex situ* experiment at harsher conditions

The rate of sintering depends strongly on the operating temperature. The temperature at which the particles become mobile depends on many factors such as the morphology of the support surface, the size of the particles, the ambient pressure etc. Nevertheless, the melting point of the metal is a key parameter since the diffusion of the atoms in the particles becomes higher as the temperature increases and gets closer to the melting point. The Hüttig and Tammann temperatures give a general indication of about where diffusion becomes important. They are directly related to the melting point of the metal with the semi-empirical relations $T_H = 0.3T_{melting}$ and $T_T = 0.5T_{melting}$ [72]. They indicate the temperature at which the atoms of the surface (T_H) and atoms of the bulk (T_T) become mobile.

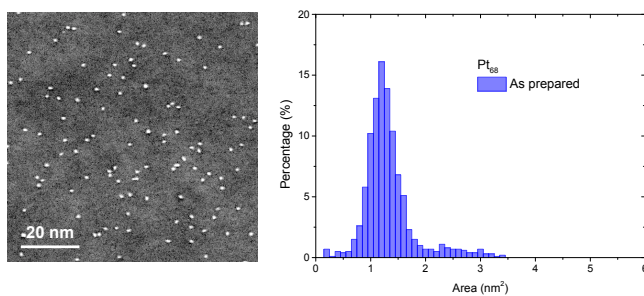
The conditions applied to the samples studied here are quite harsh for such small clusters. For bulk Pt $T_{melting} = 2028$ K so $T_H \approx 600$ K. The melting

point decreases with the dimension of the particles [69] and is expected to be sensibly lower for small nanoclusters with less than 100 atoms [73, 74]. To further challenge the sintering resistance of the mass-selected Pt_{68} clusters, the sample has been exposed to a harsher environment, that is, the hydrogen oxidation reaction conditions. In addition, a 4 times higher coverage with respect to the previous samples has been used in order to decrease the interparticle distance. The clusters have been deposited on a SiO_2 sputter-deposited TEM window with an amorphous structure as a first attempt to probe the effect of the support on the rate of sintering. The sample has then been heated up to 533 K at 6 K min^{-1} and cooled down to room temperature in a reactant mixture of $[H_2]/([H_2] + [O_2]) = 0.45$ and total concentration of 4% at 1 bar, with the catalyst under oxidising sintering conditions [70]. The heating/cooling cycle has been repeated 5 times in a reactant flow rate of 1 L min^{-1} . In addition, the hydrogen oxidation reaction is highly exothermic with $\Delta H = -250\text{ kJ mol}^{-1}$. Therefore, the actual temperature of the clusters during the reaction is expected to be higher than 533 K. The *ex situ* particle area distributions of the clusters before and after sintering are shown in Figure 4.5, together with representative HAADF-STEM images.

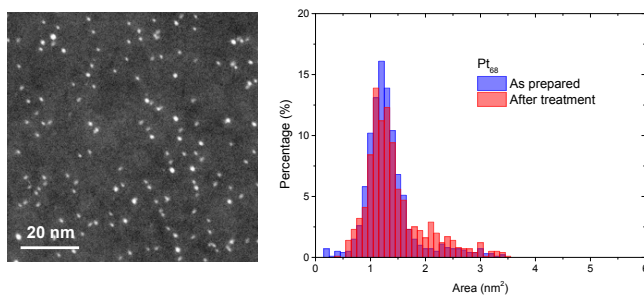
In the as-prepared sample (Figure 4.5a), an additional peak at higher areas is visible. This corresponds to the double mass clusters always formed in mass-selected cluster source samples [75]. In this case, the double mass peak results more pronounced due to the higher coverage with respect to the samples previously studied. By analysing the post-treatment area distribution histogram (Figure 4.5b), a small Oswald ripening effect is visible, with Pt_{68} clusters depleted and an increased number of larger ones. Nevertheless, the particles show good resistance towards sintering despite the high surface coverage and the harsher reaction conditions, and sintering could probably be suppressed (on the time scale under investigation) by eliminating the double mass clusters.

4.3.2 Conclusion

With the combination of *in situ* INPS and *ex situ* STEM experiments, the sintering resistance of monomodal, mass-selected Pt catalyst clusters has been demonstrated on two different supports, Si_3N_4 and SiO_2 , at high temperature and atmospheric pressure in Ar. The clusters resulted resistant towards sintering also at the harsher conditions, that is the hydrogen oxidation reaction conditions. The reason for the sintering resistance is identified in the suppression of the Ostwald ripening driving force, that is the difference in the chemical potential between clusters of different size. This is achieved via mass-selecting the catalyst clusters, obtaining a monomodal size distribution. It is important to stress that the sintering resistance is not confined to the small sizes (less than



(a) As prepared Selected Pt₆₈. Coverage 0.0013 clusters/nm².



(b) After treatment Pt₆₈. Coverage 0.0014 clusters/nm²

Figure 4.5: Particle area distribution histograms of the Pt₆₈ clusters extracted from the HAADF-STEM micrographs before (a) and after (b) the hydrogen oxidation reaction condition. Representative images of the sample are shown.

100 atoms) of the clusters studied here since has its ground on the physics of the sintering mechanism and is therefore generic. Hence, larger nanoparticles with a monomodal distribution are expected to show sintering resistance. This is particularly important in real catalytic systems where metal nanoparticles in the range of several nanometres are employed.

Nanoparticle alloy catalysts for the oxygen reduction reaction

5.1 Synthesis of mass-selected alloy nanoparticle catalysts

The synthesis of Pt-M (M=Y, Gd) alloys in the form of nanoparticles is challenging. The main issue with these materials is related to the high affinity to oxygen of the rare earth elements and their particularly negative standard reduction potential. Chemical or electrochemical synthesis processes have to overcome the issue of creating an oxygen and water free environment to favour the alloy formation, and this is not a trivial task.

The Pt alloy nanoparticles presented in this chapter have been synthesised under Ultra-High Vacuum (UHV), conditions in a magnetron sputter gas aggregation source combined with time-of-flight-mass filtering. The method consists in Ar^+ -sputtering of a Pt-alloy target in order to produce an atomic vapor that is condensed into nanoparticles through collisions with cooled Ar and He gases. Both Pt–Y and Pt–Gd nanoparticles were synthesised by sputtering alloy targets of nominal composition of Pt_9X (X=Y, Gd). The great advantage of this

technique is the extremely low level of oxygen contained in the UHV synthesis chamber (10^{-11} mbar) and its presence in the particles can be drastically reduced. The particles are charged and can be filtered through a time-of-flight filter based on their mass-to-charge ratio, producing samples with a narrow size distribution. A filtered beam of particles is then directed into a separated UHV chamber towards the support (glassy carbon for electrochemical measurements, relevant TEM support for electron microscopy measurements) where the deposition occurs at controlled coverage. The beam current is also monitored and provides the amount of material deposited onto the support, useful information for the electrochemical tests. Furthermore, the chamber is equipped with different instruments (XPS, ISS and SEM) for a first characterization.

5.2 Mass-selected Pt-Y alloy nanoparticles

The use of well defined, monodisperse, size selected specimens allows to conduct studies correlating the catalytic activity to the size and shape of the particles. In fact, broad particle size distribution, as well as undesired or inhomogeneous morphology can play an important role on the catalytic properties, making difficult to link morphology properties with the catalytic behaviour of the catalysts.

Monodisperse Pt_xY nanoparticles were synthesised in 4 different sizes in the range of 3-10 nm from the sputtering of a Pt_0Y alloy target.

5.2.1 Morphology

TEM measurements of the different specimens have been performed on the as-prepared nanoparticles in order to verify if the mass selection process was successful. This allows to quickly discriminate the specimens where the mass selection failed [Paper 3] as shown in Figure 5.1. Here an expected monomodal distribution with particle size of 9 nm was clearly missed. The trimodal particle size distribution (PSD) indicates high peaks at 9, 11 and 13 nm, i.e. particles with mass double or triple the intended mass have also been deposited (the procedure for extracting the PSD is described in the Appendix A at the end of this thesis). This problem is a known undesirable effect due to the fact that the mass selection is performed controlling the mass-to-charge ratio of the nanoparticles. Masses that are an integer multiple n of the intended mass can be filtered if their charge is also a multiple according to the same integer n [76]. Although not completely avoidable, this effect has been minimised by tuning the synthesis conditions.

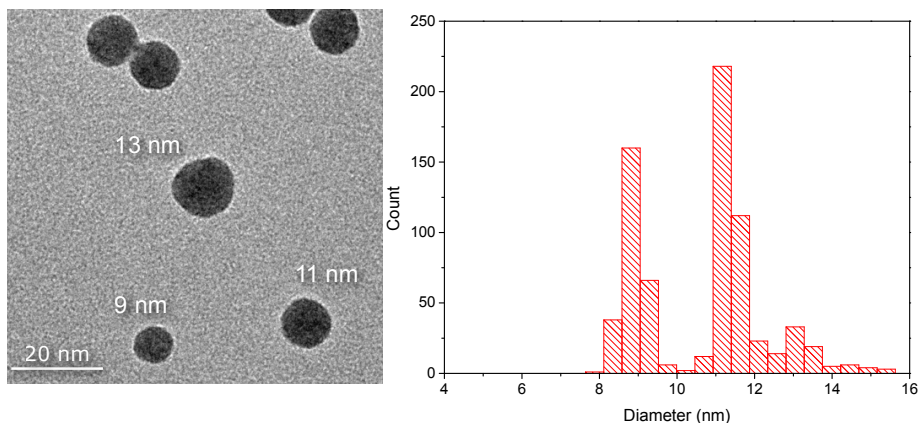


Figure 5.1: Particle size distribution of 9 nm Pt_xY nanoparticles. Undesired double and triple mass particles are present.

Figure 5.2 shows the successful mass filtering of four different samples. The size distributions were extracted from TEM images of the different samples. Sharp, narrow peaks in all the PSDs indicate a good mass filtering of the particles. For the sake of simplicity, the different samples are labelled according to the intended size. Nevertheless, the measured diameter from the PSDs is used on numerical axes when other parameters are plotted in function of the particle size. At higher diameter, especially for bigger particles, small peaks are still visible in the PSDs but they represent a very low amount of particles compared to the desired ones.

Figure 5.3 shows high-resolution TEM micrographs of the 4, 5, 7 and 9 nm Pt_xY nanoparticles. Samples of 4 and 5 nm size show a crystalline structure while the 7 and 9 nm nanoparticles exhibit a random-alloy disordered structure. The peculiar morphology is dictated by the gas-aggregation technique, where small clusters collide to form the nanoparticle. Regardless of the structure, the different particles preserve a spherical morphology and a homogeneous distribution on the carbon film support.

5.2.2 Catalytic activity and stability

Once the particle size distributions confirmed the successful mass selection, the electrochemical catalytic activity and stability were tested on the different samples and the results are shown in Figure 5.4. The activity measurements were performed by inserting the samples into an electrochemical cell in N_2 saturated

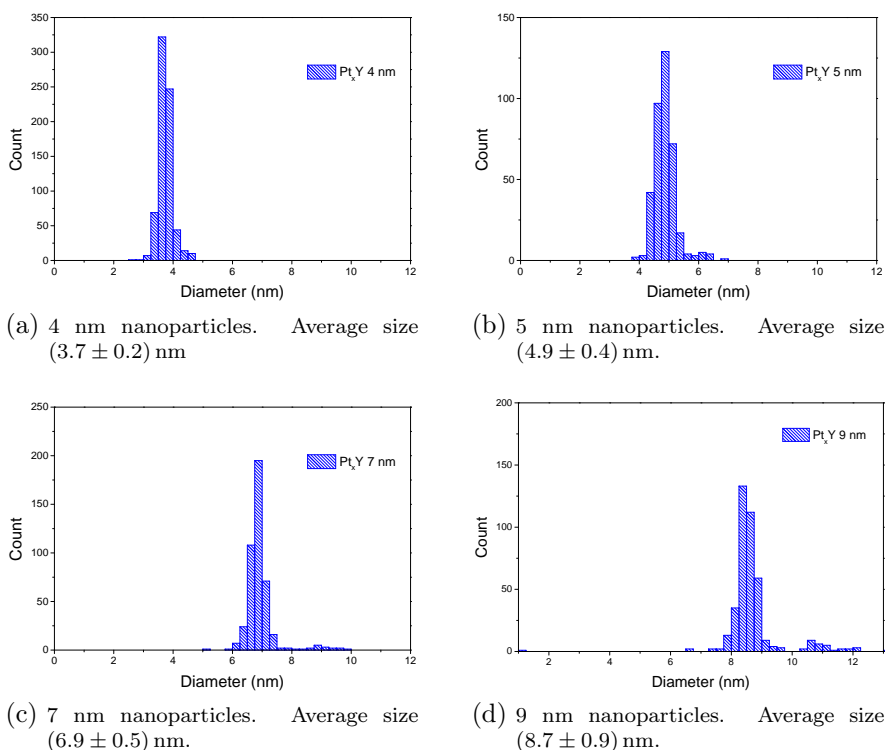


Figure 5.2: Particle Size Distributions of the different specimens obtained from TEM micrographs. The average size and standard deviation for each sample is reported.

0.1 M HClO_4 electrolyte and cycled between 0.05 V to 1 V at a sweep rate of 50 mV/s until a stable cyclic voltammogram was obtained (the details on the electrochemical measurements are available in Paper 2 attached to this thesis). The ORR activity test was then carried out in O_2 saturated 0.1 M HClO_4 electrolyte.

Compared to pure Pt particles of the same size, the Pt_xY nanoparticles show higher ORR activity (red curve in Figure 5.4). The activity increases with the particle size and best performances are exhibited at 9 nm particle diameter, with a mass activity of $3.05 \text{ A mg}_{\text{Pt}}^{-1}$, more than 5 times higher than the best Pt commercial catalyst [77] and more than 3 times higher than the best Pt particles prepared with the same mass selection process [31]. Such high mass activities are overtaken only by recently discovered Pt–Ni nanoparticles [78, 79]. The catalytic stability is verified by subjecting the nanoparticles to an accelerated

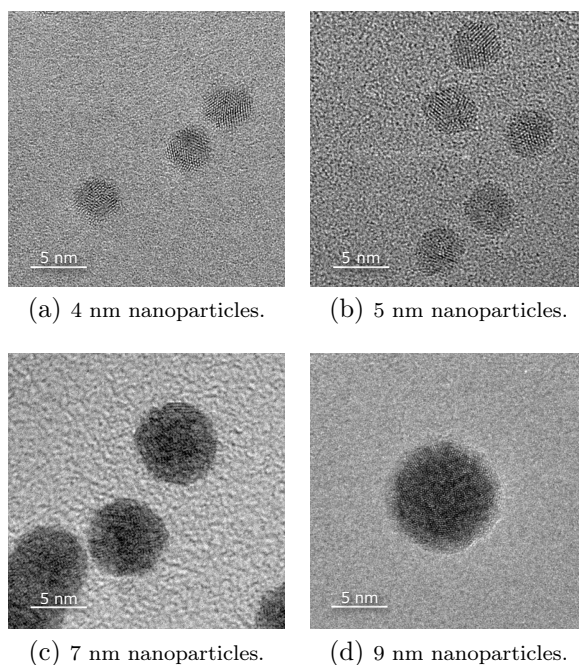


Figure 5.3: Representative high-resolution TEM micrographs of Pt_xY nanoparticles with different sizes.

ageing test by cycling the electrode potential between 0.6 V and 1 V 9000 times. Although activity losses are observed for all particle sizes, the mass activity of the 9 nm particles (blue curve in Figure 5.4) is still almost 4 times higher than for pure Pt as shown in (black curve in Figure 5.4). Complementary ORR tests have indicated that almost all the activity losses occur within the first 600 cycles.

CO stripping measurements have shown that the surface coverage is constant during the potential cycling (details are available in the supporting information of Paper 2). For this reason, the loss in activity must be related to the specific activity of the active sites on not due to a loss of active surface area. The nanoparticles should then experience low mobility and no coalescence or detachment from the carbon support. To verify this, Identical Location (IL) TEM studies have been performed on the 9 nm Pt_xY nanoparticles. Bright-field TEM images of the same sample areas before and after prolonged exposure to ORR conditions have been acquired. Figure 5.5 shows the comparison between as-prepared and after stability test (9000 potential cycles) of the 9 nm nanoparticles. From large view images (5.5a-b) it is already possible to ascer-

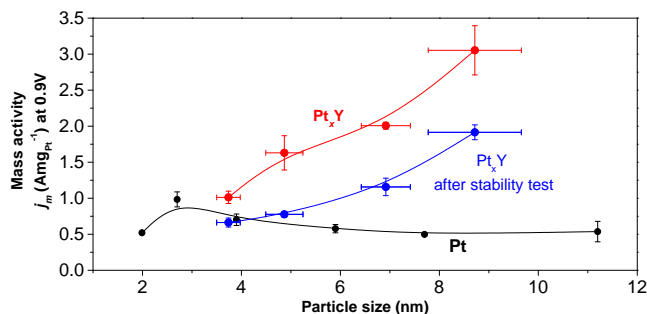


Figure 5.4: ORR mass activity of the Pt_xY nanoparticles. The kinetic current density have been recorded after activity (red) and stability (blue) measurements at 0.9 V, 50 mV s⁻¹, 1600 RPM and room temperature in O₂-saturated 0.1 M HClO₄ electrolyte. The mass activity of Pt nanoparticles prepared and tested in the same way are plotted for comparison [31]. Measurements performed by Patricia Hernandez-Fernandez.

tain that the particles are stable on the carbon film. Stability is then clearly observed in the magnified areas shown in 5.5c-d: when overlapped (5.5-e), the resulting image shows how the particle positions are basically unchanged. Further proof of the nanoparticle stability on the carbon film support is shown in the Appendix A.

Figure 5.6 shows high-resolution TEM micrographs of the 9 nm sample nanoparticles before and after ORR stability test. Both intended mass and double-mass particles are present in the images. The coalescence of the particles in Figure 5.6-b is not related to the electrochemical test but induced by the TEM electron beam, as it was directly observed during image acquisition.

Although the disordered structure is maintained, a change in the nanoparticles surface is visible. Before the electrochemical test the particles appear covered by amorphous material. Since the as-prepared samples have been exposed to air before being measured in the electron microscope, either a carbon or an oxide layer could be covering the nanoparticles. This layer is removed during the electrochemical test, where it is dissolved in the acidic electrolyte. This scenario is suggested by the XPS measurements performed on the 7 nm nanoparticles but supported on glassy carbon (Figure 5.7). The XPS spectra show the change in the chemical state of Y. When measured in UHV right after the deposition, Y is mostly found in its metallic state. Nevertheless, a second chemical state is present and ascribed to the interaction with the carbon support (Figure 5.7-a). Subsequently, after exposure to air, the Y at the surface is oxidised (5.7-b); the oxide is then dissolved in the electrolyte when the ORR test is performed, leaving the remaining Y in its metallic state (5.7-c). Furthermore, the atomic ratio between Pt and Y has been extracted from the XPS data. Figure 5.8

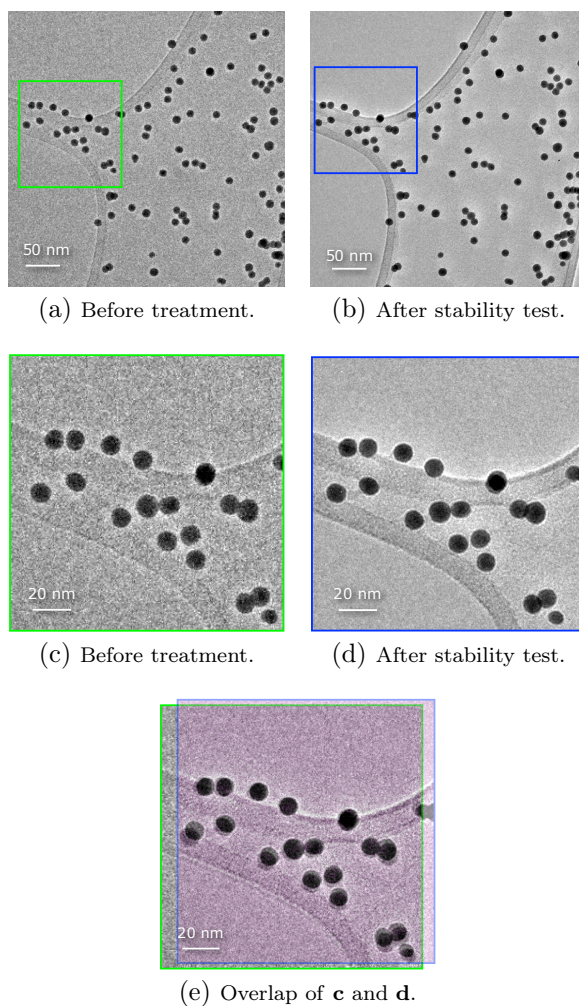


Figure 5.5: Identical location bright-field TEM of 9 nm Pt_xY nanoparticles. Large view and high magnification images of the untreated sample are shown on the left (**a** and **c**). The same areas of the sample after stability test are shown on the right (**b** and **d**). In **e**, the overlap of (**c**) and (**d**) (purple) is shown.

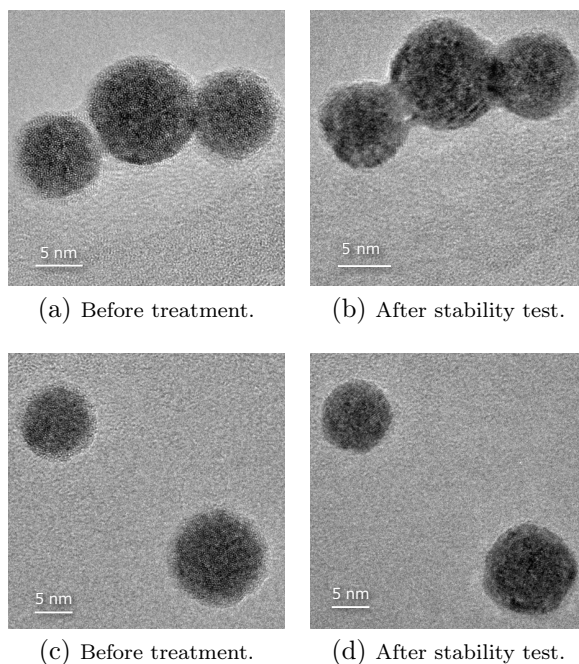


Figure 5.6: High-resolution TEM identical location studies on 9 nm Pt_xY nanoparticles. The untreated sample is shown in (a) and (c). Same particles after the stability test are shown in (b) and (d).

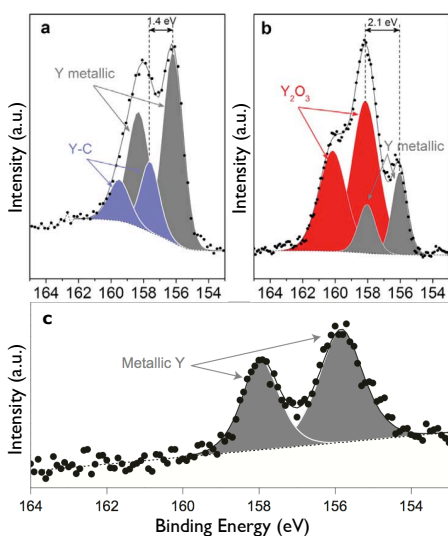


Figure 5.7: **a:** XPS spectrum of the Y-3d core level region of the as-prepared 7 nm Pt_xY sample in vacuum. **b:** Spectrum after exposure to air. **c:** Spectrum after exposure to ORR conditions. Grey colour refers to metallic Y phase. Blue phase in (a) is ascribed to Y-C interaction. The red phase in (b) shows the Y oxide phase dominance. Measurements performed by Federico Masini and Paolo Malacrida.

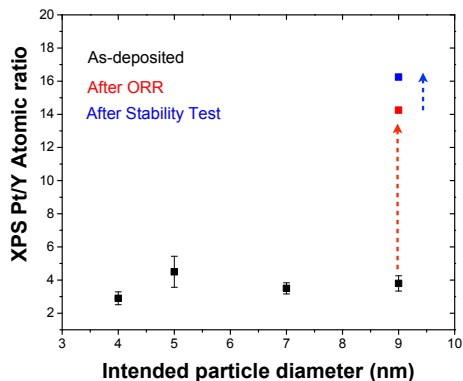


Figure 5.8: Pt to Y atomic ratio in function of the nominal particle size calculated from XPS data. Measurements performed by Federico Masini and Paolo Malacrida.

shows that the Pt/Y atomic ratio is very similar for the different sizes and with a good reproducibility. For the 9 nm sample the Pt/Y atomic ratio has also been calculated after ORR activity and stability test and a significant increase in the Pt content is observed. This is an indication that Y has been removed from the region close to the surface of the nanoparticles, leaving a Y-depleted region behind.

5.2.3 Electron spectroscopy

The electrocatalytic activity and stability tests, together with the XPS surface analysis, suggest that the Pt_xY nanoparticles reach a stable state after a surface depletion of Y. A Pt-rich thick overlayer is formed by segregation and subsequent dissolution of the Y from the surface to the electrolyte, similarly to the dealloying process happening in high surface area polycrystalline electrodes of same composition [80]. For this reason the enhanced activity of the alloy nanoparticles has to be related to the distribution of the different metals in the catalyst volume. To give clear and robust support to the process suggested so far, the analysis of the structure and composition of the nanoparticles with a spatial resolution down to the nanoscale is of fundamental importance. For this reason electron spectroscopy techniques have been employed in the TEM. Specifically, we have used STEM combined with EELS and EDS to map the distribution of Pt and Y at the nanoparticle level.

Figure 5.9 shows the HAAD-STEM micrograph of a 9 nm Pt_xY nanoparticle and the HAADF-intensity profile extracted from the image along the white line.

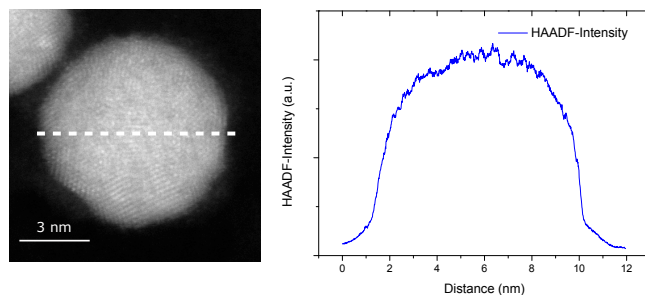


Figure 5.9: HAADF-STEM image and extracted intensity linescan along the purple line.

Table 5.1: Core-loss edges for Pt and Y elements (from EELS Atlas).

Edge	Energy (eV)	Type
Y-L _{2,3}	2080	Sharp delayed edge
Pt-M _{4,5}	2122	Delayed edge

The trend of the signal along the particle indicates an homogeneous random distribution [69] of the Pt and Y since there are no visible variations of contrast due to the difference in atomic number.

EELS spectroscopy

In Table 5.1 the EELS core-loss edges for Pt and Y are listed. Pt and Y have edges in the far region of the EELS spectrum (above 2000 eV). Although the quantification of Pt through the Pt-M_{4,5} edge has been shown in alloy nanoparticles [35, 81–83], the intrinsically low intensity of the EELS signal in this part of the spectrum required long acquisition times for the collection of the Pt_xY nanoparticle spectra.

Figure 5.10-a shows the EELS core-loss spectrum acquired positioning the STEM probe on the 9 nm Pt_xY nanoparticle shown in Figure 5.10-b. Since the double differential cross section for electron inelastic scattering is inversely proportional to the energy of the incident electrons [56], an accelerating voltage of 120 kV was chosen. The delayed Y-L_{2,3} feature is identified in the spectrum with the small peak at ~ 2100 eV while the Pt-M_{4,5} is recognisable as the broad edge in the range 2150-2350 eV, confirming the presence of both elements in the nanopar-

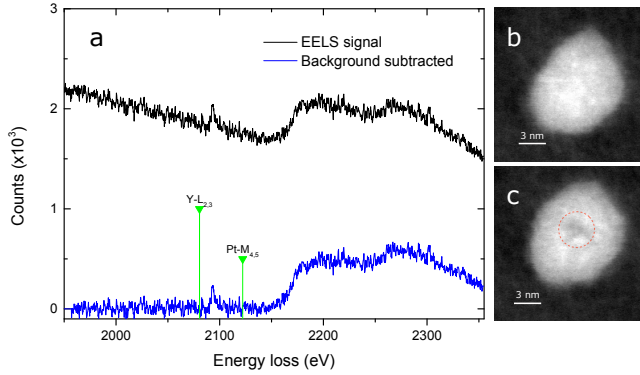


Figure 5.10: **a:** Single-point acquisition EELS spectrum: black line is the spectrometer signal and blue line is the background-subtracted signal (acquisition time of 30 s, accelerating voltage 120 kV, 48 mm camera length, 0.3 eV/ch spectrometer dispersion, 2.5 mm entrance aperture). **b** and **c:** HAADF-STEM image of a 9 nm Pt_xY nanoparticle before and after the acquisition, respectively. Beam damaged region is red circled.

Table 5.2: Low-loss edges for Pt and Y elements (from EELS Atlas).

Edge	Energy (eV)	Type
Y-N _{2,3}	26	Major/broad delayed edge
Pt-O _{2,3}	52	Week delayed edge
C-($\pi + \sigma$)	~ 20	Plasmonic resonance

ticle. Due to the low EELS signal intensity at such high energy-losses, an acquisition time of 30 seconds was needed for collecting the spectrum, causing the nanoparticle to be damaged by the electron probe. The effect is visible in Figure 5.10-c. The low contrast region in the middle of the particle shows where the probe was positioned during the acquisition.

Figure 5.11 shows the beam damage induced by the electron beam when a linescan acquisition was performed. The measurement consisted in a five-points linescan with a dwell time of 20 seconds per point. After the measurement the particle is severely damaged with the mark of the scanning probe clearly visible.

In order to decrease the beam damage by decreasing the acquisition time, the low-loss region of the EELS spectrum has been analysed. Both Y and Pt have edges in the range of 20-60 eV as listed in Table 5.2.

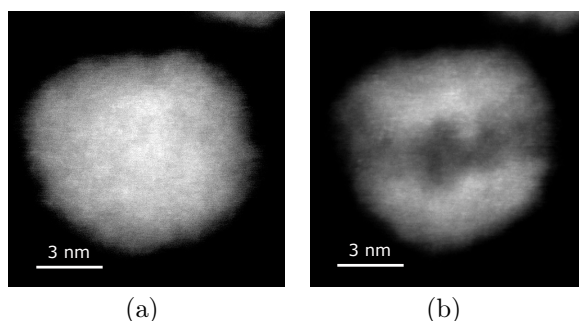


Figure 5.11: **a:** HAADF-STEM image of a 9 nm Pt_xY nanoparticle. **b:** Beam damage evidence after 5-points EELS linescan spectrum acquisition (acquisition time 100 s, accelerating 120 kV, 100 mm camera length, 0.3 eV/ch spectrometer dispersion, 2.5 mm entrance aperture).

The main issue of using the low-loss part of the EELS spectrum arises from the fact that the carbon film supporting the nanoparticles has a plasmonic resonance at ~ 20 eV [84]. this resonance is visible in Figure 5.12 where the spectra have been acquired with the STEM probe is positioned on a supported 9 nm Pt_xY nanoparticle and on the carbon support respectively. Although the spectra can be acquired with very short dwell times (200 ms) and improved signal-to-noise ratio (SNR) compared to the core-loss spectra, the carbon plasmonic feature is dominant over those of the other elements.

In order to minimize the undesirable feature of the carbon, the low-loss EELS spectra have been acquired by positioning the STEM probe onto particles attached at the edge of the carbon support, as shown in Figure 5.13 (inset picture). The spectra acquired in this way present a different shape with respect to the one fully supported on the carbon film. The spectra of these particles have also been compared to the spectrum of a pure 9 nm Pt nanoparticle, synthesised with the same technique, in the same geometrical position, that is, suspended on a carbon edge. The results are shown in Figure 5.13. Pt_xY presents very different low-loss features compared to pure Pt. Nevertheless, this part of the spectrum is challenge to interpret due to the difficulty in separating the pure Y and Pt features. In principle it would be possible to identify Pt-rich zones from Pt_xY zones in the nanoparticles by comparing the shape of the respective spectra in a linescan or spectrum image acquisition. Although feasible, the main problem remains the presence of carbon: due to the longer time needed with the STEM probe on the particle for a linescan or a map acquisition, the analysed area is rapidly contaminated with carbon species that quickly dominates the signal making this method impractical.

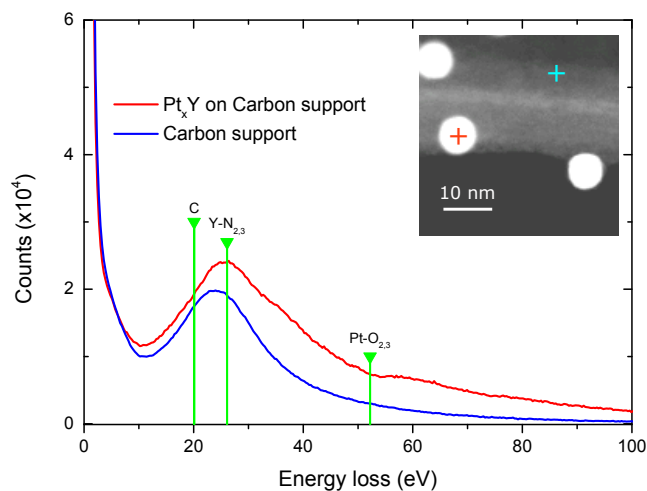


Figure 5.12: STEM-EELS spectra of one supported 9 nm Pt_xY nanoparticle (black line) with the STEM probe positioned on the red cross in the inset picture. The blue line represents the EELS spectrum with the probe positioned on the carbon support indicated by the light blue cross in the inset (acquisition time 0.2 s, high tension 120kV, 0.3 eV/ch spectrometer dispersion).

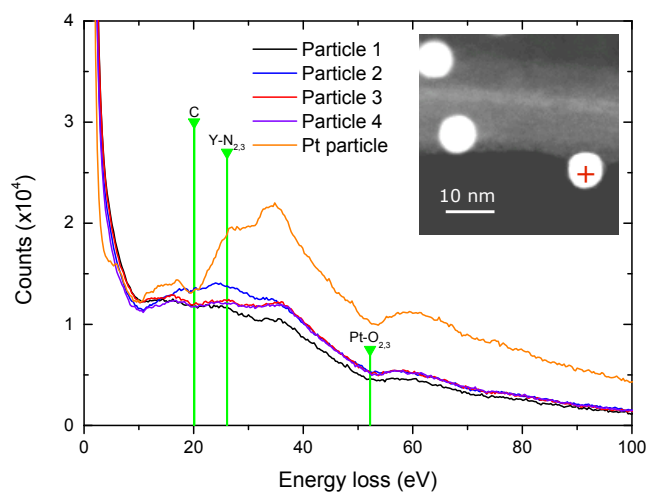


Figure 5.13: Particle 1-4 curves represent the low-loss spectra acquired on suspended 9 nm Pt_xY nanoparticles (red mark in the inset micrograph). The orange line represent the spectrum of a pure Pt nanoparticle synthesized in the same cluster source with same size of the Pt_xY ones (acquisition time 0.2 s, high tension 120kV, 0.3 eV/ch spectrometer dispersion).

EDS spectroscopy

Although STEM-EELS have been useful to confirm the presence of both Pt and Y at the nanoparticle level, for this particular system the electron energy-loss spectroscopy is not practically applicable for two-dimensional compositional imaging. Consequently, energy dispersive X-Ray spectroscopy has been employed in order to obtain the elemental distribution in the Pt_xY nanoparticles [29, 85–87]. Even though the Titan Analytical TEM at DTU Cen possesses EDS capabilities, the acquisition times for chemical mapping at the nanoscale are too long, and over the required time particles would suffer severe damage. Therefore, EDS spectrum images have been acquired in a FEI Osiris microscope. The total EDS solid collection angle of 0.9 sr allows a high sensitivity and efficient collection of the X-Rays emerging from the sample and therefore high count rates with short acquisition times can be achieved. Another important feature of this microscope is related to the software handling the signal coming from the detectors. The advantage of the Bruker Esprit Software is the sequential stacking of consecutive spectrum images of the same region. Combined with drift correction capabilities, short dwell time maps can be acquired and added. In this way the number of counts and the SNR is improved and the sample damage minimized.

Figures 5.14a-d show the HAADF-STEM image of an as-prepared 9 nm Pt_xY nanoparticle with the respective $\text{Y-K}_\alpha = 14.93$ eV, $\text{Pt-L}_\alpha = 9.44$ eV and combined Pt+Y elemental EDS intensity maps. A 7x7 pixels average smoothing filter has been applied via the Bruker Esprit software. (The effect of the average filter on the raw data can be seen in the Appendix A). The EDS maps show, as expected, a homogeneous distribution of the two metals on the entire volume of the particle. This is more evident by looking at the linescan in Figure 5.14-e extracted from the EDS data cube across the particle along the purple line drawn on the HAADF-STEM image. The signal represent the background-subtracted integrated intensity of the Y-K_α and Pt-L_α . For a clearer view, smoothing has been applied to the two signals and the result is shown in Figure 5.14-f. The Pt signal has been smoothed with a 7 points average filter while for the Y signal a Savitzky–Golay filter has been preferred since it is more suited for low SNR images [88]. Both signal profiles increase in intensity from one side of the particle following its shape, to then decrease when reaching the opposite surface.

EDS maps have also been acquired after the ORR activity test. In Figure 5.15 the HAADF-STEM and respective elemental maps of two 9 nm nanoparticles are shown. It is clearly visible that the outermost part of the particle has been depleted of Y, while the innermost part shows the presence of both Y and Pt. In fact, by looking at the EDS intensity linescan profile it is noticeable

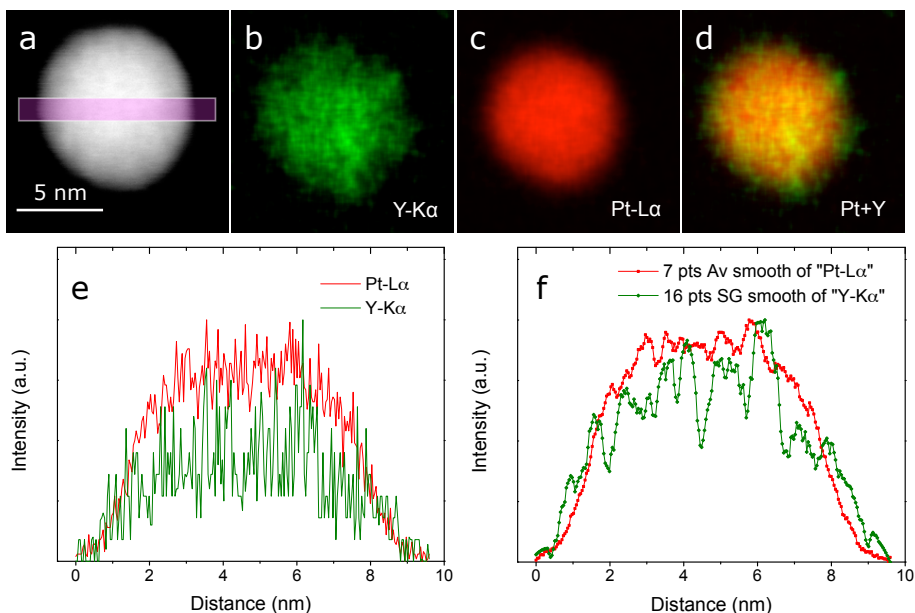


Figure 5.14: **a:** HAADF-STEM image of an as-prepared 9 nm Pt_xY nanoparticle. **b-d:** $\text{Y-K}\alpha$, $\text{Pt-L}\alpha$ and combined Pt+Y EDS elemental maps of **(a)**. Spectrum images acquired with a probe current of 0.50 nA and a dwell time of 100 μs for a total acquisition time of 758 s. A 7x7 pixels average smoothing filter is applied. **e:** EDS intensity line profile extracted from the spectrum image data cube along the purple line drawn in **(a)**. **f:** Smoothed and normalised line profiles shown in **(e)**.

how the Y signal becomes detectable and increases at a position ~ 1 nm away from the particle's surface and after the Pt signal (the estimation of the shell thickness is reported in the Appendix A). This is consistent with the XPS data showing an increased Pt/Y ratio at the surface of the ORR-tested nanoparticles. As expected, the core-shell structure is also formed in the Pt_xY nanoparticles subjected to the electrochemical stability test. Figure 5.16 shows the Pt-rich shell formation on a Pt-Y core. Interestingly, there is no significant increase in the Pt shell thickness due to the prolonged CV cycling of the stability test. As previously mentioned, the electrochemical tests have shown how the activity remains constant after the initial 37% drop over the first ~ 600 potential cycles where the Y is leached out of the surface. The similar shell thickness seen in the EDS maps of Figure 5.16 indicates that the dissolution of Y is prevented after the formation of the Pt-rich shell that stabilise the nanoparticle.

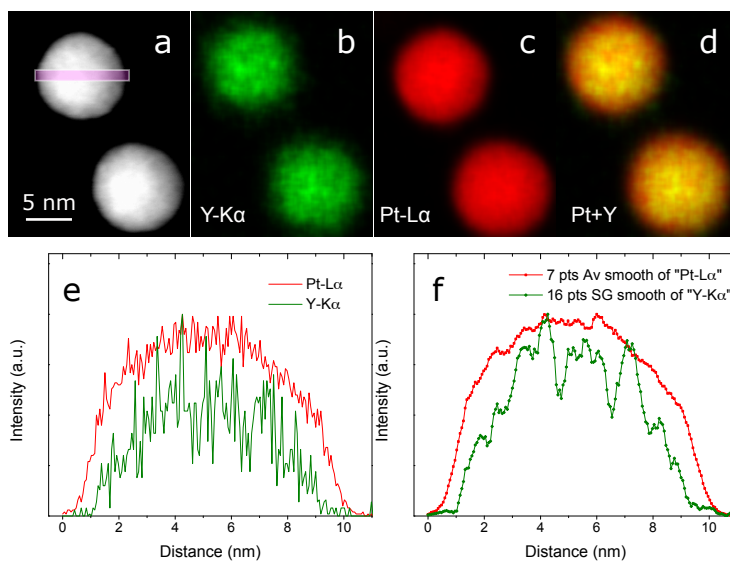


Figure 5.15: **a:** HAADF-STEM image of 9 nm Pt_xY nanoparticles after ORR activity test. **b-d:** Y-K α , Pt-L α and combined Pt+Y EDS elemental maps of **(a)**. Spectrum images acquired with a probe current of 0.90 nA and a dwell time of 300 μ s for a total acquisition time of 725 s. 7x7 pixels average smoothing filter is applied. **e:** EDS intensity line profile extracted from the spectrum image data cube along the purple line drawn in **(a)**. **f:** Smoothed and normalised line profiles shown in **(e)**.

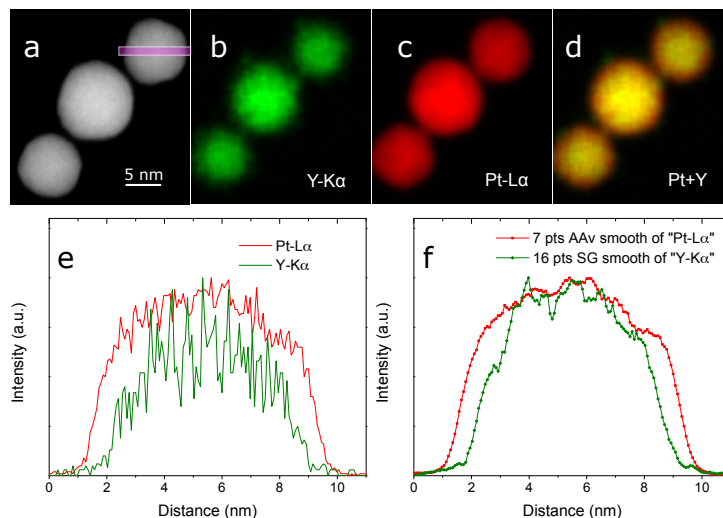


Figure 5.16: textbfa: HAADF-STEM image of 9 nm Pt_xY nanoparticles after stability test. **b-d:** Y-K_α, Pt-L_α and combined Pt+Y EDS elemental maps of **(a)**. Spectrum images acquired with a probe current of 0.48 nA and a dwell time of 100 μs for a total acquisition time of 2402 s. 7x7 pixels average smoothing filter is applied. **e:** EDS intensity line profile extracted from the spectrum image data cube along the purple line drawn in **(a)**. **f:** Smoothed and normalised line profiles shown in **(e)**.

EDS quantification

The EDS intensity line scans extracted from the chemical maps qualitatively show the distribution of the Pt and Y along the particle. The Y-K_α peak at around 15 keV was initially chosen for the spectrum images since it is well isolated and does not overlap with other element peaks. Nonetheless, the signal is quite noisy and any quantification procedure would be meaningless with such low counts. In order to perform more reliable quantitative analysis, the EDS maps have been extracted by using the Y-L_α peak at 1.923 keV. This peak has better SNR and higher intensity compared to the Y-K_α and therefore more suited for the quantification, should the peak be correctly separated from any other overlapping peaks. In fact, both Pt and Au (this last from the TEM grid supporting the samples) have M_α peaks at 2.059 keV and 2.121 keV and many overlapping lines in each family are present, but deconvolution has been used to separate the peaks. Pt and Y abundance have been extracted from the EDS spectra for the core and the shell regions of the nanoparticles as depicted in Figure 5.17. Both areas have been chosen in order to have the same number of pixels and a similar number of X-Ray counts for a comparable quantification.

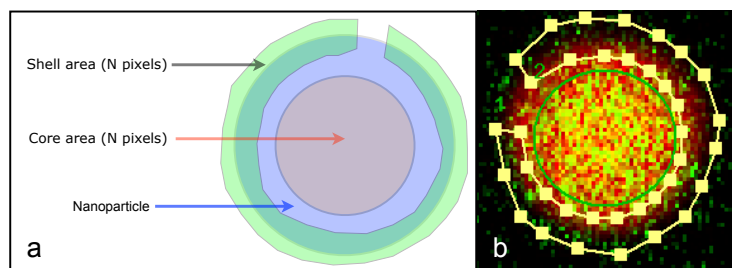


Figure 5.17: **a:** Schematics of the nanoparticle core and shell areas chosen for the EDS quantification. **b:** Printscreen of the Bruker Esprit software with the two areas drawn on a Pt_xY nanoparticle.

Figure 5.18 shows the EDS chemical maps extracted from the Y-L_α and the deconvoluted spectra of the core and shell regions for the 9 nm Pt_xY as-prepared nanoparticle, as well as the samples after ORR activity test and stability test. The maps result similar to the previous ones obtained with the Y-K_α , indicating a correct deconvolution of the Y-L_α from the overlapping peaks. The atomic percentages have been calculated from the EDS spectra with the standardless Cliff-Lorimer method. The full procedure has been performed with the Bruker Esprit software. For each spectrum, the background has been fitted with a polynomial function through a manual background-window selection and successively subtracted. Different corrections such as detector escape peak, peak shift and signal pileup are taken into account automatically by the software. The overlapping peaks have been separated with a series-fit deconvolution where element peaks are fitted with modified-gaussian curves.

All the core and shell spectra in Figure 5.18 show the broad peaks at energies around 2.1 keV and 9.5 keV. The first is deconvoluted with the Y-L_α , Pt-M_α and Au-M_α peaks, while the second is deconvoluted with the Pt-L_α and Au-L_α . Figure 5.19 shows the EDS Pt-Y atomic ratio extracted from the spectra in Figure 5.18. Although affected by important uncertainties, the Pt-Y ratio can give useful information on the spatial distribution of the two elements. The atomic ratio between Pt and Y is expected to be constant for the untreated particles while it should increase for the electrochemically tested ones, since Y is leached out from the surface. In the as-prepared sample, the Pt-Y ratio is surprisingly higher in the core region than in the shell. A reasonable explanation can come from the presence of yttrium oxide covering the particle, as seen (compositionally) in the XPS spectrum and (visually) in the TEM micrographs of the air-exposed samples. After the electrochemical tests the ratio increases as expected.

The trend of the EDS Pt-Y atomic ratio is in agreement with XPS data (Figure

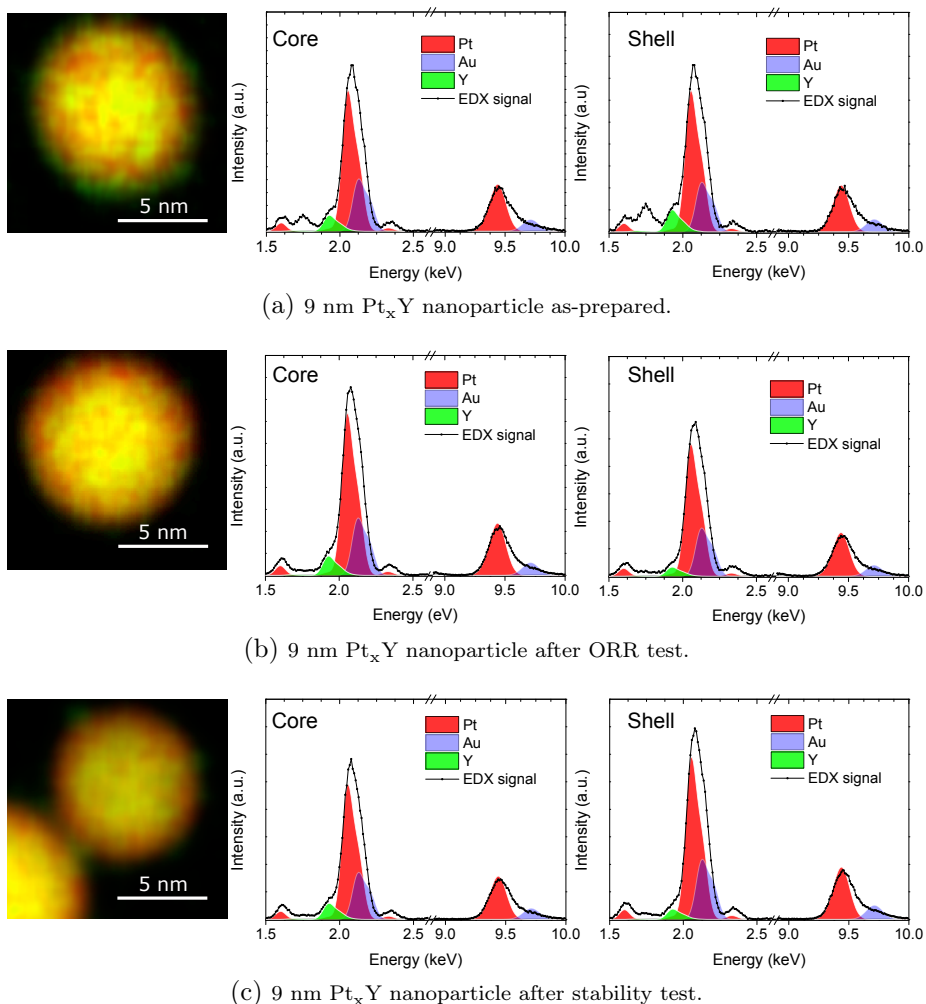


Figure 5.18: EDS elemental maps and spectra of the core and shell regions for the as-prepared sample (a), after ORR electrochemical test (b), after stability test (c). The background-subtracted, deconvoluted Y-L_α peak and the Pt-L_α have been used for the EDS maps. A 5x5 averaging filter has been applied to all the maps.

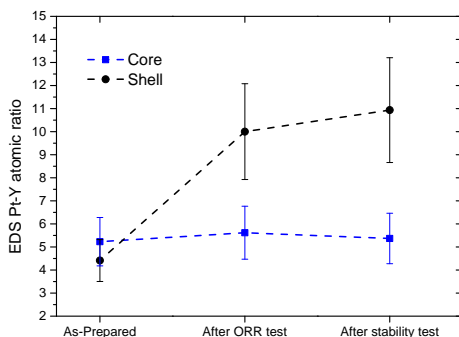


Figure 5.19: EDS Pt/Y atomic ratio from the core and shell regions for the different samples.

5.8), confirming the core-shell structure. Concerning the pure numerical values, the comparison with XPS is more complex. XPS has a very high surface sensitivity, probing circa the first nanometre of the sample surface. In the EDS quantification of the shell region, the selection of the region of interest is the critical part since is performed by manually drawing the perimeter around the core. This inevitably introduces some errors due to the fact that the thickness of the selected shell region will not be perfectly homogeneous all around the particle. Therefore, it is possible that a part of the particle core is also counted. For the core region, it is important to remember that a part of the particle shell is always probed. Since The STEM-EDS map represents a 2-dimensional projection of the 3-dimensional particle volume, the top and bottom part of the shell enclosing the core are also included in the core-region EDS quantification.

The EDS elemental maps, together with the quantification of the spectra in the different regions of the nanoparticles, finally bring a clear evidence of the formation of a core-shell structure with the Pt-rich shell enclosing a Pt-Y alloy core.

5.3 Mass-selected Pt-Gd alloy nanoparticles

Following the scheme adopted for the Pt_xY nanoparticles, the Pt–Gd alloy has been studied in its nanoparticulate form. Different sizes of particles have been synthesized using the same procedure adopted for the Pt_xY ones as explained in the synthesis section. For the microscopy analysis, mass-selected nanoparticles with intended diameters of 3, 5, 8 and 9 nm have been synthesised in the cluster source and soft-landed deposited on Au lacey carbon-coated TEM grids.

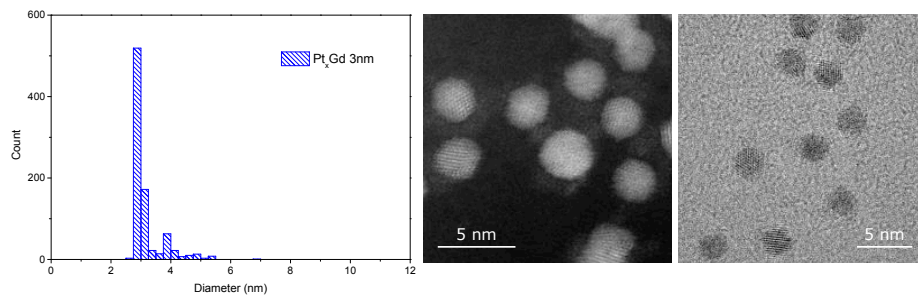
5.3.1 Morphology

In order to study the morphology of the different Pt_xGd nanoparticles, both TEM and STEM imaging have been performed. The particle size distributions have been extracted from HAADF-STEM micrographs and are reported in Figure 5.20 together with representative high-resolution TEM and HAADF-STEM images. Although well monodispersed with sharp peaks in the PSDs at the intended sizes, the samples contain a small fraction of double mass nanoparticles visible as satellite peaks at larger diameters. This undesired effect is particularly visible in the 8 nm sample where the double-mass particles are easily spotted on both the STEM and TEM image. Compared to the other samples, the 9 nm nanoparticles present a less pronounced double-mass feature but a broader peak on the intended size. Similarly to the case of Pt_xY , the bright-field TEM in Figure 5.20 show the presence of an amorphous layer encapsulating the particles.

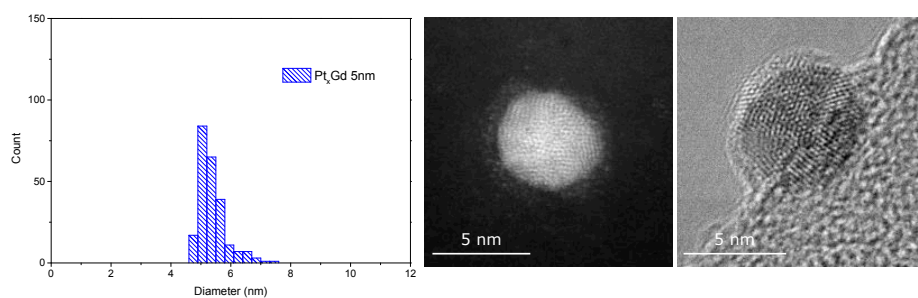
The surface composition of the 9 nm sample has been determined from XPS spectra. Figure 5.21 shows the Gd-4d peak in the XPS spectrum of the 9 nm Pt_xGd nanoparticles during the different steps of the characterization compared to the sputter-cleaned polycrystalline reference, where Gd is in the metallic state. Initially the spectrum was acquired under UHV conditions right after deposition (black curve). The position of the peak is very similar to the polycrystalline reference indicating a Gd metallic state also for the nanoparticles. After exposure to air (green curve) the shift to higher binding energy and the different shape of the peak indicates the surface oxidation of Gd.

5.3.2 Catalytic activity and stability

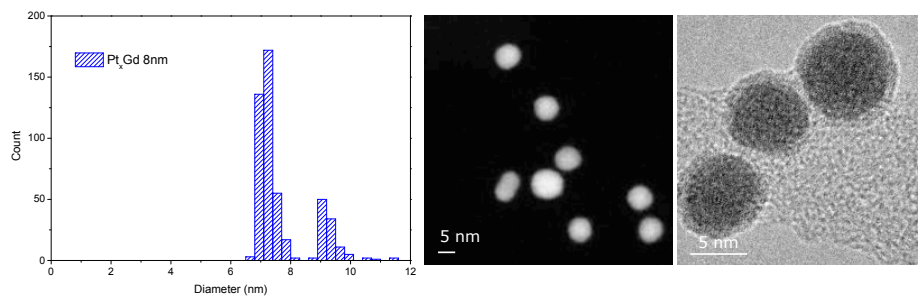
The mass-selected nanoparticles were deposited on glassy carbon supports and electrochemically tested in 0.1 M HClO_4 electrolyte similarly to the Pt_xY alloy nanoparticles. The mass activity as a function of the particle size is shown in



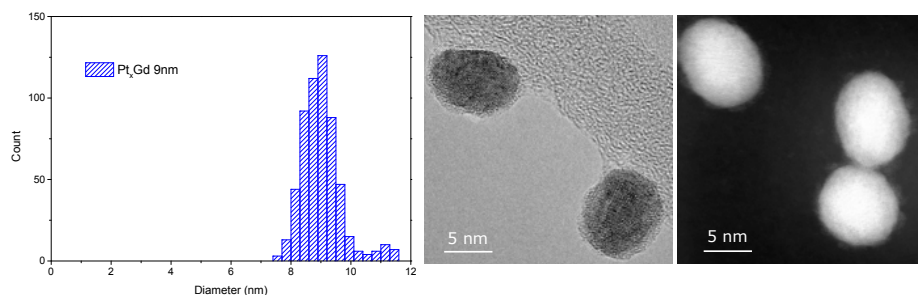
(a) Pt_xGd 3 nm nanoparticles. Average size (3.2 ± 0.5) nm



(b) Pt_xGd 5 nm nanoparticles. Average size (5.4 ± 0.5) nm.



(c) Pt_xGd 8 nm nanoparticles. Average size (7.7 ± 0.9) nm.



(d) Pt_xGd 9 nm nanoparticles. Average size (8.8 ± 0.8) nm.

Figure 5.20: Particle size distribution with representative STEM and TEM images of the different Pt_xGd samples. Average size and standard deviation is also reported.

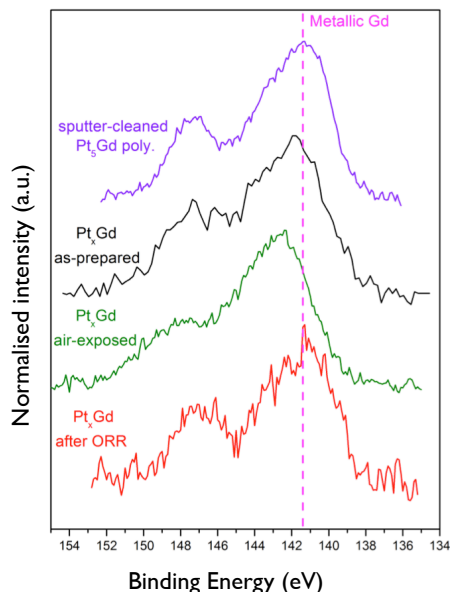


Figure 5.21: XPS spectra of Gd-4d peak for the 9 nm Pt_xGd nanoparticles supported on glassy carbon. Spectra are shown for the as-prepared, air-exposed and after ORR samples. XPS spectrum of sputter-cleaned Pt_5Gd polycrystalline sample is shown for comparison (measurements by Federico Masini and Paolo Malacrida).

Figure 5.22. Both mass-selected Pt and Pt_xY trends are included for comparison. The highest activity is reached by the 8 nm nanoparticles with $3.6 \text{ A mg}_{\text{Pt}}^{-1}$ surpassing even the mass activity of the 9 nm Pt_xY nanoparticles. With this activity peak, the Pt_xGd nanoparticles overtake the newly discovered Pt_xY ones.

After the electrochemical measurements, the Pt_xGd nanoparticles of 5, 8, and 9 nm size were subjected to the activity test with an extended cycling treatment of 10 000 potential cycles. The results are shown in Figure 5.22-b where the initial mass activity of the three samples is compared with the one after 1000 cycles and after 10 000 cycles. Pure Pt and Pt_xY size-selected nanoparticles activities are also reported for comparison. The Pt_xGd nanoparticles show activity losses very similar to the Pt_xY ones. The 8 nm Pt_xGd particles retain 70% of the initial activity after 10 000 cycles, performing slightly better than the 9 nm Pt_xY nanoparticles (63% after 9000 cycles). Consequently, even after an extended treatment, the Pt_xGd nanoparticles perform almost 3 times better than size-selected Pt nanoparticles.

CO-stripping data concluded that the the active surface area of the catalyst

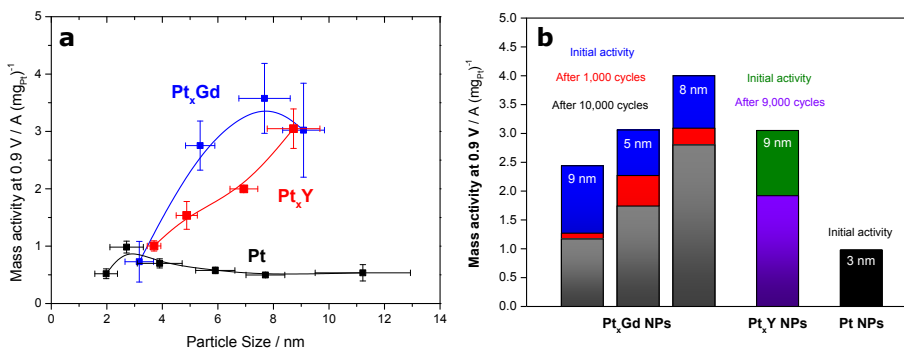
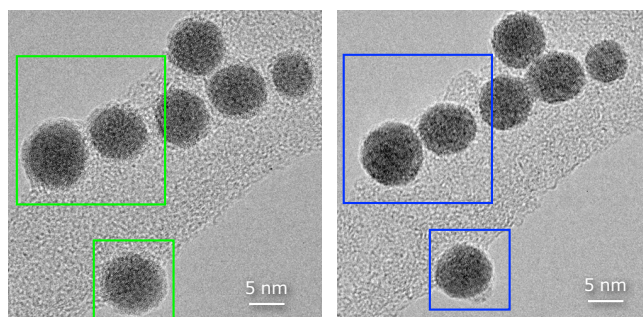


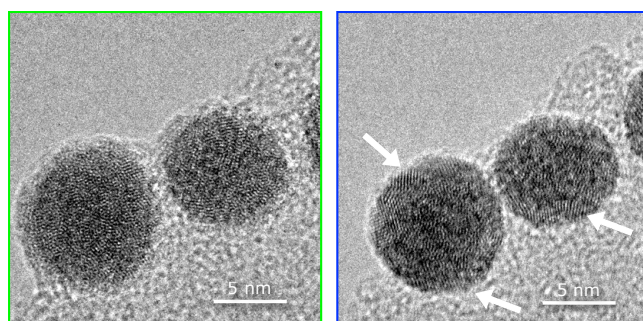
Figure 5.22: **a:** Mass activity trend of Pt_xGd nanoparticles in function of the particle size. **b:** Stability test where the mass activity is measured after 10 000 cycles. Mass-selected Pt_xY [89] and pure Pt [31] nanoparticles are also shown for comparison (Measurements by Amado Velazquez-Palenzuela).

does not change after the stability test (details are available in Paper 4). This means that the particles should be rather stable onto the support without sintering, with the activity losses ascribed to a decrease in specific activity. This conclusion is confirmed by the IL-TEM study of the 8 nm and 9 nm nanoparticles before and after the stability test. Figure 5.23 shows an ensemble of 8 nm Pt_xGd nanoparticles supported on a narrow strip of the carbon film support before and after the stability test. The particles are stable on the support without any sign of agglomeration due to the chemical treatment. The images in Figure 5.23b-c show the particles enclosed in the coloured boxes drawn in Figure 5.23-a. The shell encapsulating the nanoparticles is removed after the exposure to ORR conditions. Similarly to Y in Pt_xY alloy nanoparticles, Gd is expected to segregate from Pt and be leached out from the nanoparticle surface when in contact with the acidic electrolyte. In fact, the XPS Gd-4d peak (red curve in Figure 5.21-a) recovers its metallic features after electrochemical measurements, confirming the dissolution of the oxide in the electrolyte. Furthermore, the outermost region of the nanoparticles seems to undergo a restructuring towards a more crystalline structure rather than the disordered structure visible in the as-prepared samples. Sets of fringes are visible in different parts of the nanoparticles, as indicated by the white arrows.

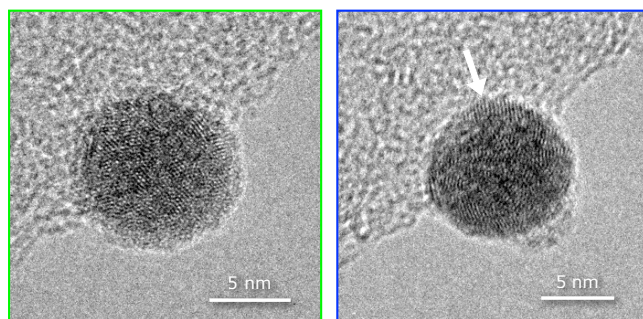
The same effect is clearly observed for the 9 nm sample, as shown in Figure 5.24. The acidic electrolyte is responsible for dissolving the oxide layer covering the particle and leaching the Gd out of the nanoparticle surface. In fact, the Pt/Gd atomic ratio extracted from XPS data increases after the activity test with a size dependency as shown in Figure 5.25.



(a) 8 nm Pt_xGd nanoparticles. Identical location high-resolution images before (left) and after (right) stability test.

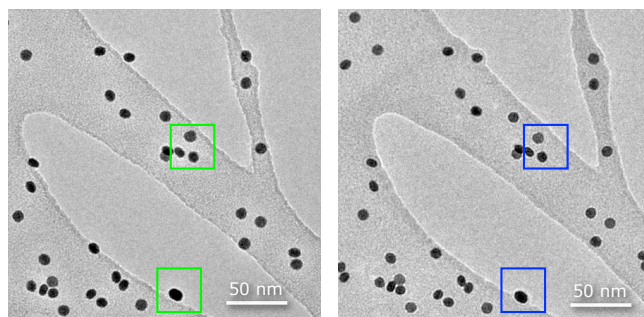


(b) High magnification images of the regions enclosed in the coloured boxes in (a).

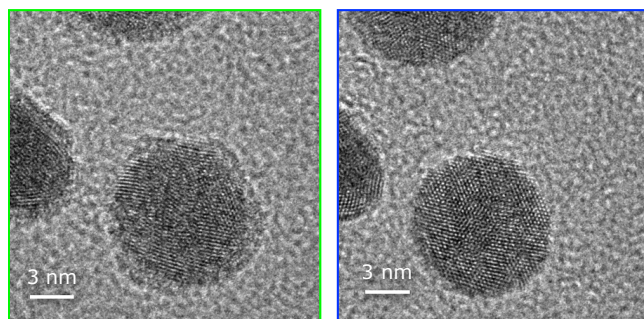


(c) High magnification images of the regions enclosed in the coloured boxes in (a).

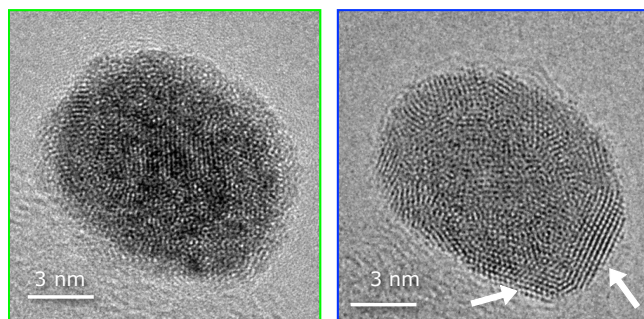
Figure 5.23: Identical Location study on 8 nm Pt_xGd nanoparticles. Lattice fringes appear on the treated particles (white arrows in (b) and (c)).



(a) 9 nm Pt_xGd nanoparticles. Identical location images before (left) and after (right) stability test.



(b) High-resolution images of the regions enclosed in the coloured boxes in (a).



(c) High-resolution images of the regions enclosed in the coloured boxes in (a).

Figure 5.24: Identical Location study on 9 nm Pt_xGd nanoparticles. Lattice fringes appear on the treated particles (white arrows in c).

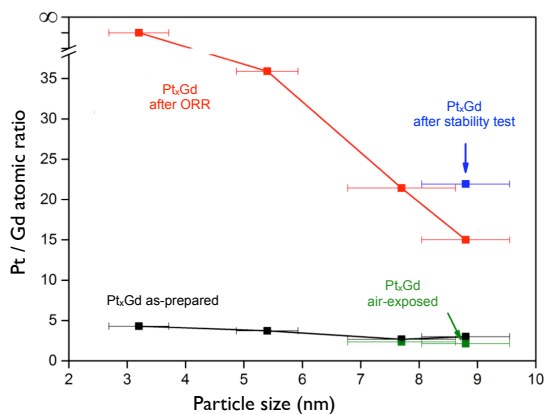


Figure 5.25: XPS Pt/Gd atomic ratio of the as-prepared and after ORR test samples in function of size. For the 9 nm nanoparticles, the Pt/Gd ratio for air-exposed and after stability test samples is also shown (Measurements by Federico Masini and Paolo Malacrida).

For the 9 nm sample, the Pt/Gd ratio increases to almost 15 after the electrochemical activity test. The prolonged cycling of the stability test further dissolves the Gd from the outermost region of the particles leading to an even higher concentration of Pt and therefore to the formation of a core-shell structure.

5.4 Enhanced activity of Pt alloys

STEM-EDS spectrum images have explicitly shown the formation of a Pt-rich shell onto an alloyed Pt-Y core in Pt_xY nanoparticles after the electrochemical tests. This is confirmed by XPS measurements where an increase of the Pt/Y atomic ratio in the near surface region is measured on the same particles with respect to the as-prepared samples. Pt_xGd nanoparticles have shown the same behaviour. The reason is ascribed to the dealloying effect where Y and Gd is dissolved from the surface when in contact with the electrolyte and leached out from the outermost layers. These results are consistent with the measurements performed on extended surface electrodes of Pt_3Y and Pt_5Y showing a 3-4 monolayer thick Pt overlayer [80]. An overlayer of the same thickness was also found after the same measurements on Pt_5Gd extended surfaces [40]. For these large surface electrodes, the ORR enhancement was attributed to compressive strain applied by the bulk alloy to the Pt overlayer, resulting in a weaker bonding of the ORR intermediate species and consequently an enhanced activity.

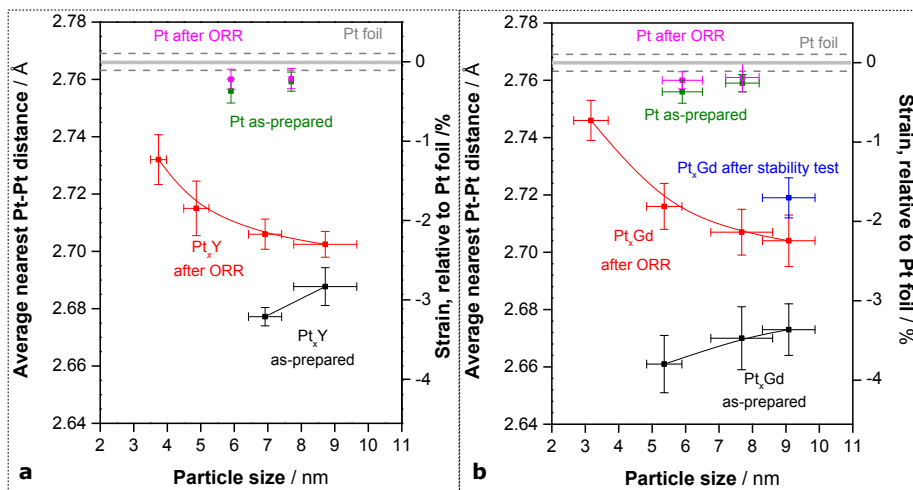


Figure 5.26: Average nearest Pt-Pt distance measured by EXAFS for (a) Pt_xY and (b) Pt_xGd nanoparticles for the different particle sizes. Measurements for as-prepared and after ORR pure Pt particles are also shown for comparison. Grey continuous lines represent the measurements of a Pt foil with dashed lines representing the associated error (figures from Paper 2 and Paper 3 attached to this thesis).

The presence of the rather thick Pt-rich shell in Pt_xY and Pt_xGd nanoparticles excludes the ligand effects as the physical reason for their enhanced activity. Therefore, in light of the extended surfaces results, the high ORR activity is ascribed to strain effects. The strain in the nanoparticles has been quantified by extended X-ray absorption fine structure spectroscopy technique (EXAFS) before and after electrochemical test. The technique allows to measure the average nearest Pt-Pt distance in the nanoparticles and therefore evaluate if the structure is strained with respect to the Pt bulk reference. The results for the Pt_xY and Pt_xGd nanoparticles are shown in Figure 5.26. The details of the measurements can be found in the Paper 2 and 4 attached to this thesis.

Figure 5.26 shows the average nearest Pt-Pt distance of the particles, before and after electrochemical treatment, as a function of the particle size. The values for pure Pt nanoparticles and Pt foil are also shown for comparison. The as-prepared samples exhibit a compressive strain close to 3% due to alloying. After the ORR measurements, a change can be observed. For all the particle sizes, the Pt-Pt distance relaxes towards the pure Pt one with a clear size dependency. Where the core is expected to be very small like in the smallest particles (3 nm Pt_xGd and 4 nm Pt_xY nanoparticles), a higher relaxation towards pure Pt occurs.

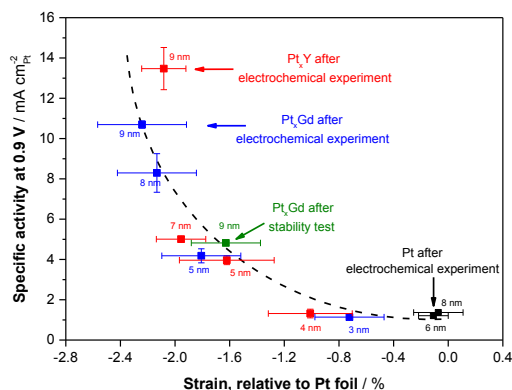


Figure 5.27: Specific activity as a function of the strain (relative to Pt foil) for Pt_xY and Pt_xGd nanoparticles for different sizes. Pure Pt nanoparticles values are shown for comparison (figure from Paper 3 attached to this thesis).

The Pt-Pt distance determined by EXAFS represents the interatomic distance averaged over the entire particle, that is the alloyed core and the Pt-rich shell. For the Pt_xY nanoparticles, the shell thickness estimation by means of STEM-EDS has provided a fundamental parameter for the calculation of the Pt-Pt distance in the solely shell [89]. By considering a particle model formed by an alloyed core and a pure 1 nm thick Pt shell, the average shell strain in the 9 nm particles is calculated to be about -1.6% . This means that the shell is relieved from some of the strain applied by the core, but a significant part is retained. The topmost active layer would probably be even more relaxed since is the farthest layer from the core, but still able to weaken the HO^* binding to the surface and increase the ORR activity.

By correlating the specific activity of the alloyed nanoparticles with the nearest Pt-Pt distance (Figure 5.27), it is clearly demonstrated that the enhancement in the ORR performance is strongly correlated to the strain in the nanoparticles, with Pt_xY and Pt_xGd particles following the same trend, consistently with the observations by Strasser *et al.* for dealloyed Pt–Cu nanoparticles [29].

Figure 5.28 shows the schematics of the expected behaviour of the rare-earth Pt alloyed nanoparticles along the different steps. When prepared in UHV conditions, the nanoparticles are fully alloyed. The non-precious metal at the surface oxidise upon exposure to air. During ORR tests the oxide species are dissolved into the electrolyte due to the strong acidic environment. A core-shell structure is formed with a Pt-rich shell enclosing an alloyed core. Further

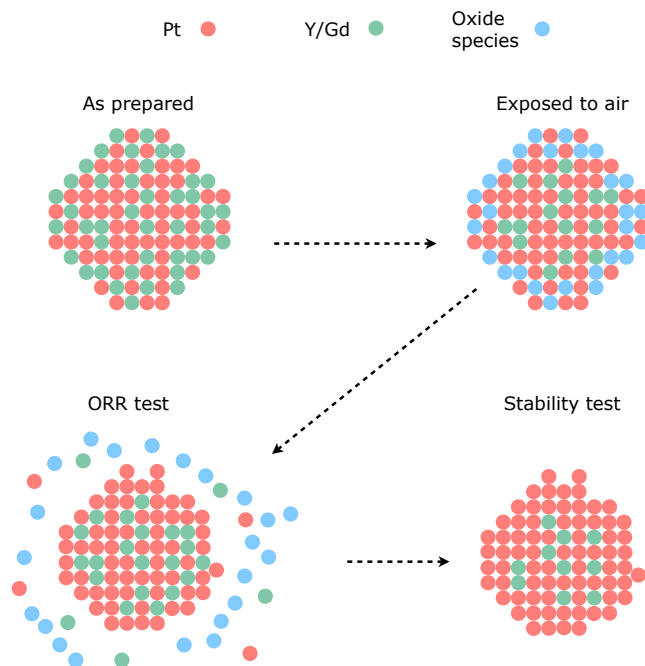


Figure 5.28: Alloy nanoparticle transformation along the different steps of the analysis.

cycling in the stability test leaches out more rare-earth atoms from the shell until a metastable condition is reached, with a thicker Pt shell protecting the alloyed core from further dealloying (as observed by XPS and STEM-EDS) which still keeps the Pt shell negatively strained and thereby the enhanced activity.

CHAPTER 6

Nanoparticle alloy catalysts for H_2O_2 production

This chapter reports the electron microscopy results of mercury-based alloy catalysts recently discovered as highly active catalysts for the electrochemical synthesis of hydrogen peroxide H_2O_2 . Pt–Hg and Pd–Hg structures have been predicted by DFT calculations and successive experimental catalytic activity studies performed on extended polycrystalline surfaces. Finally, they have been synthesised in nanoparticulate form and fully characterised. The DFT calculations have been performed at CAMD at DTU-Physics, the electrochemical tests and XPS analysis have been performed at CINF at DTU-Physics. The electron microscopy has been done at DTU Cen and CIME-EPFL. Part of the data presented here has been published in Papers 5 and 6 attached to this thesis.

6.1 Pt-Hg alloy nanoparticles

To be industrially viable, a catalyst with high surface-area is required. For this reason, Pt–Hg nanoparticles supported on carbon have been synthesized. Pt–Hg catalyst has been prepared by drop casting a Pt/C ink on a glassy carbon electrode. Hg has then been electrodeposited onto the electrode following the recipe of Wu *at al.* [90]. The synthesis details can be found in the Paper 5

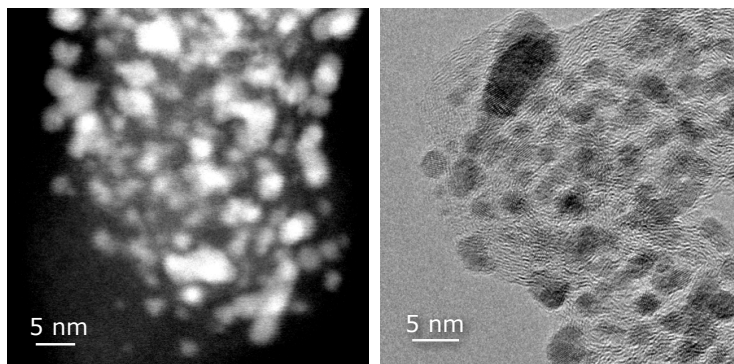


Figure 6.1: Bright-field TEM and HAADF-STEM of Pt-Hg/C nanoparticles.

attached to the thesis. In order to deposit the sample on the TEM grid, 10 ml of isopropanol were drop casted on the glassy carbon with freshly prepared PtHg nanoparticles. The isopropanol was then pipetted back and dropcasted on a lacey-carbon coated Cu TEM grid.

Figure 6.1 shows the bright-field TEM and HAADF-STEM micrographs of Pt-Hg nanoparticles well distributed on the carbon support with sizes spanning from 1 to more than 10 nm. Particles oriented in low-index zone axis have been imaged and representative micrographs are shown in Figure 6.2. From the analysis of the Fast-Fourier Transform (FFT), the resulting structure matches the Pt fcc crystal structure. The (200) and (220) planes are highlighted with white lines. The high resolution TEM images do not give any evidence of Hg alloying with Pt. However, complementary XPS analysis performed on the nanoparticles shows the presence of both elements, as visible in Figure 6.3, confirming the presence of Hg on the surface. The presence of oxidized peaks in the Hg spectrum is ascribed to the exposure of the sample to air during the transfer of the specimen.

XPS still gives a macroscopic analysis of the sample's surface. In order to elucidate the local composition of the nanoparticles, STEM-EDS spectroscopy was employed. Figure 6.4 shows the HAADF-STEM micrograph and the respective EDS spectrum acquired with the electron probe positioned on the red mark of the image. The Hg - L_α and Hg - L_β peaks appear at ~ 10 keV and ~ 12 keV and indicate the presence of both Pt and Hg in the nanoparticle. The Cu peaks are due to the supporting TEM grid.

The EDS technique could not be exploited further with the Pt-Hg system due to different challenges related to the sample. First, the sample suffered heavily from charging under the illumination of the STEM probe. Second, the alloy

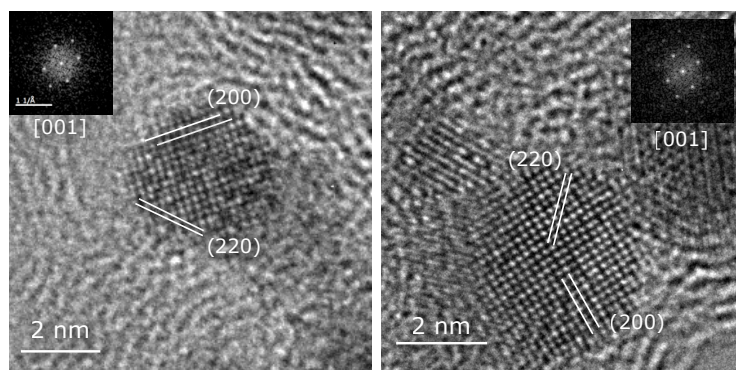


Figure 6.2: High resolution TEM of Pt–Hg nanoparticles along [001] zone axis. The respective FFTs are shown in the insets. White marks highlight the fringes associated with the (200) and (220) family planes of the fcc structure.

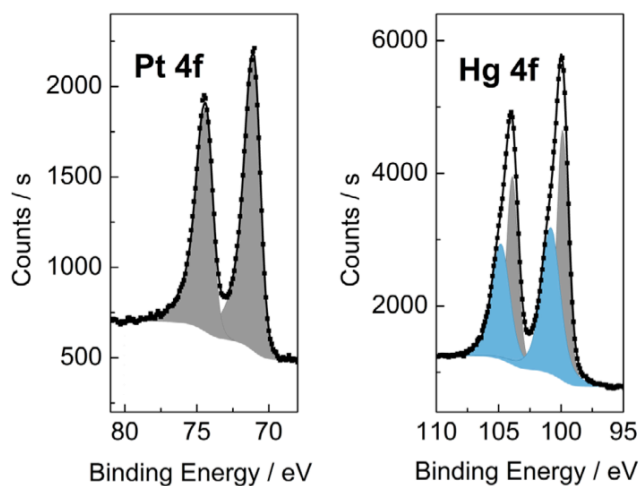


Figure 6.3: XPS Pt-4f and Hg-4f peaks in Pd–Hg/C nanoparticles. The metallic phase is indicated by grey areas and oxide phase with blue ones. Measurements performed by Paolo Malacrida.

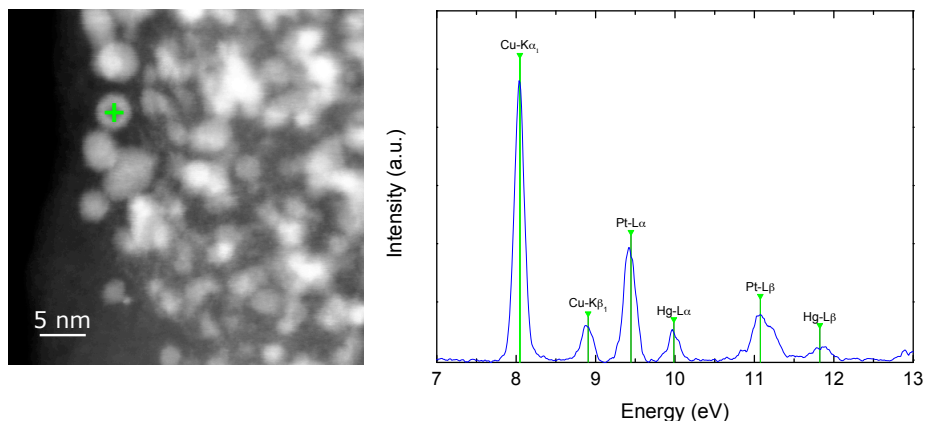


Figure 6.4: STEM-EDS spectrum of a single Pt-Hg particle acquired with the probe positioned on the green mark of the HAADF image. The spectrum has been acquired at 120 kV accelerating voltage with a SiLi EDS detector with an acquisition time of 60 s.

has some instability in high vacuum conditions. This has been experienced both in the electron microscope and, by the colleagues at CINF, in UHV XPS chambers. To show the decrease of Hg content in the sample, two EDS spectra of large areas of the sample have been collected: one has been acquired right after the insertion of the sample in the electron microscope and the other has been acquired approx. 8 hours later with the specimen kept inside the column at all times. As shown in Figure 6.5, the spectra have been acquired on areas of identical size but in different positions in order to exclude possible beam effects. The Hg peaks in the EDS spectrum acquired last show a drop in intensity, suggesting that the mercury is depleted under high vacuum conditions.

The electrochemical tests on the Pt-Hg nanoparticles have indicated superior performances [52]. Compared to the polycrystalline Pt-Hg, the nanoparticles exhibit almost 5 times improvement in terms of specific activity. When compared to carbon-supported Au-Pd or Au [50] nanoparticles, Pt-Hg nanoparticles show more than one order of magnitude improvement in mass activity, with a selectivity toward production of H_2O_2 up to 96%. Furthermore, the catalyst presents high stability: after 8000 potential cycles between 0.05 and 0.8 V in O_2 -saturated electrolyte, no loss in activity has been observed.

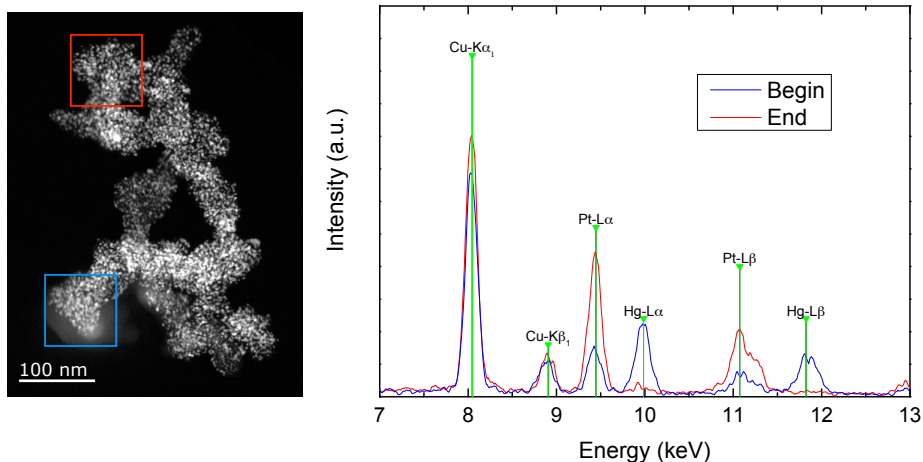


Figure 6.5: STEM-EDS spectra of large areas of Pt–Hg/C acquired at 120 kV accelerating voltage with a SiLi EDS detector and an acquisition time of 60 s.

6.2 Pd-Hg alloy nanoparticles

After the discovery of the Pt–Hg alloy, the methodology has been applied in a systematic way to other metals and alloys in order to explore the possibility of finding an even better catalyst. Hg can also be electrodeposited on Cu, Pd and Ag forming stable alloys under the conditions where the ORR takes place [53]. Similarly to Pt–Hg, an active site configuration with single Pd atoms as active sites surrounded by Hg has been found to be a potentially better catalyst. Figure 6.6 shows the Pd_2Hg_5 surface computed in the DFT calculations, with the reactive Pd atoms (green colour) surrounded by the less reactive Hg (blue).

Electrocatalytic measurements have been initially performed on extended surface polycrystalline electrodes with Pd–Hg showing improved activity over the newly discovered Pt–Hg. Therefore, the Pd-Hg catalysts have been prepared in the more technologically appealing form of nanoparticles. The catalyst has been prepared with the same synthesis procedure of the Pt–Hg/C nanoparticles. An ink of carbon-supported Pd nanoparticles was prepared and drop-casted on a glassy carbon electrode. Subsequently, mercury was electrodeposited onto the electrode. Compared to the highly active Pt–Hg/C nanoparticles, the Pd–Hg/C catalyst presents a 5 times improvement in mass activity at 50 mV, with a 95% selectivity. Furthermore, the catalytic nanoparticles show high electrochemical stability, with negligible losses after 8000 potential cycles between 0.2 and 0.7 V.

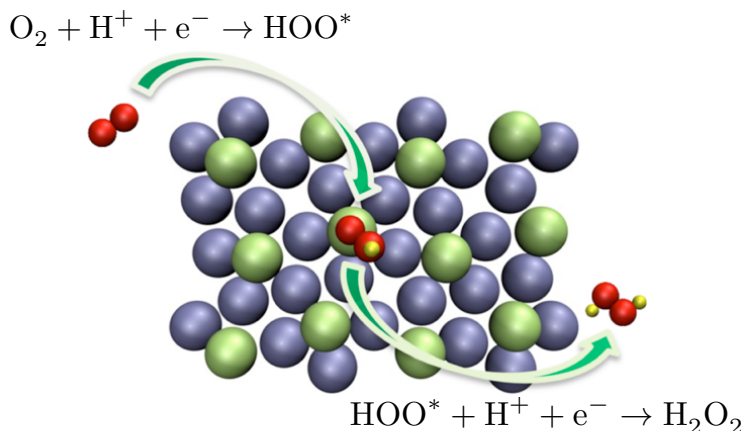


Figure 6.6: Reactions occurring at the Pd-Hg surface. The reaction steps are also illustrated (image adapted from [53]).

Figure 6.7 shows bright-field TEM and HAADF-STEM overviews of the Pd-Hg nanoparticles supported on carbon. The sample contains particles with diameters spanning from few nanometres to more than 10 nanometres. Since Hg has been electrodeposited onto the Pd particles, it is expected that the heavy element is alloyed at least in the outermost part of the particle volume, giving rise to a core-shell structure. This is suggested by the XPS analysis performed on the sample (Figure 6.8). The Pd spectrum indicates the presence of both pure (grey curves) and alloyed (green curves) phases of the metal. For the Hg, the XPS spectrum shows that the metal is in its alloyed form.

Figures 6.9-a show the bright-field TEM and HAADF-STEM images of the same Pd-Hg nanoparticle. A contrast variation along the particle is detected in both images resembling to a core-shell structure. This is more clear in the intensity linescans extracted from the images along the red and blue lines drawn in Figure 6.9-b and shown in 6.9-c. The HAADF-STEM linescan (red line in 6.9-b) shows high intensity in the outer part of the round shaped particle while it decreases on the central part. Due to the atomic-number dependence of the HAADF signal the contrast can be interpreted as a Hg-rich outermost region on a Pd-rich inner part. In fact, the respective linescan from the bright-field TEM image (blue line in 6.9) shows the opposite trend. Heavy-metal enriched parts of the particle appear darker in the image due to mass contrast, while the lighter Pd-rich central part appears brighter, therefore the high intensity of the signal. The oscillations in the TEM linescan signal arise from the phase contrast of the image. For a clearer view, the line profile has been smoothed and the subtended area highlighted.

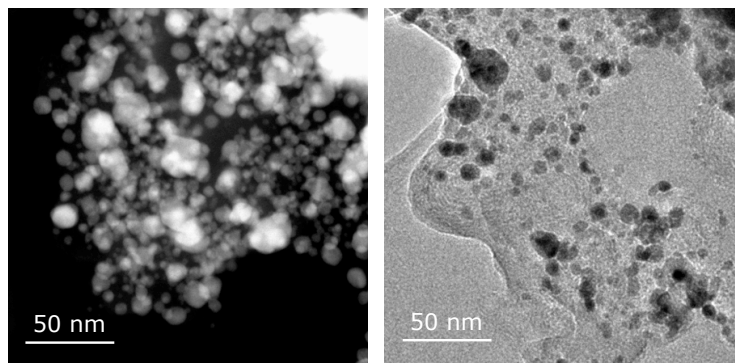


Figure 6.7: Bright-field TEM and HAADF-STEM of Pd-Hg nanoparticles on carbon support.

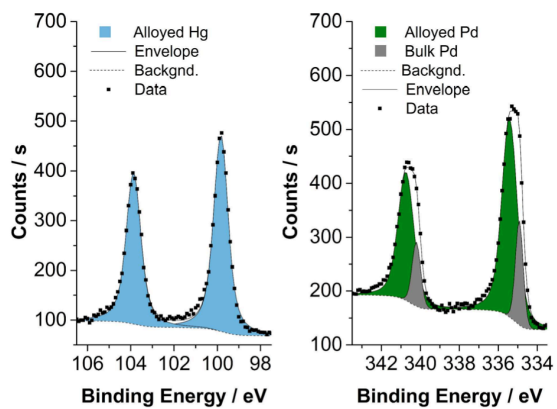


Figure 6.8: XPS Hg-4f and Pd-3d peaks of Pd-Hg/C nanoparticles. The Hg is in the alloyed form, while Pd is present in both alloyed and bulk phase.

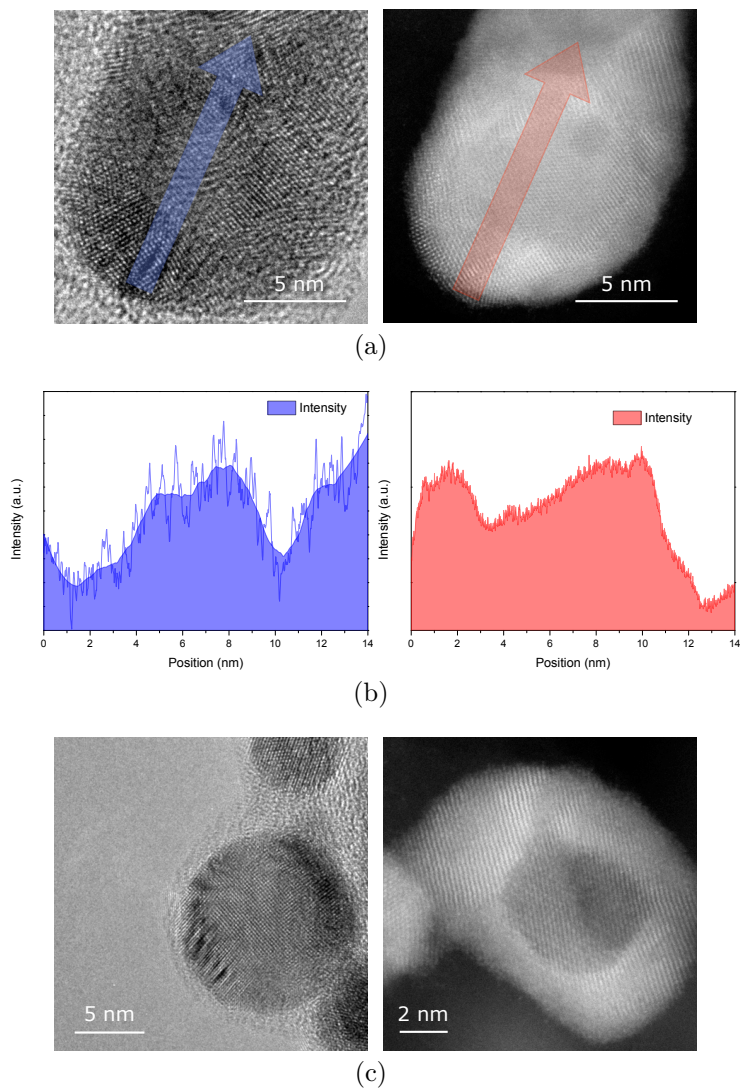


Figure 6.9: **a:** Bright-field TEM and HAADF-STEM images of the same Pd–Hg nanoparticle. **b:** Intensity line scans along the coloured lines drawn over the images in (a). **c:** Bright-field TEM and HAADF-STEM images of two different particles showing a clear core-shell structure.

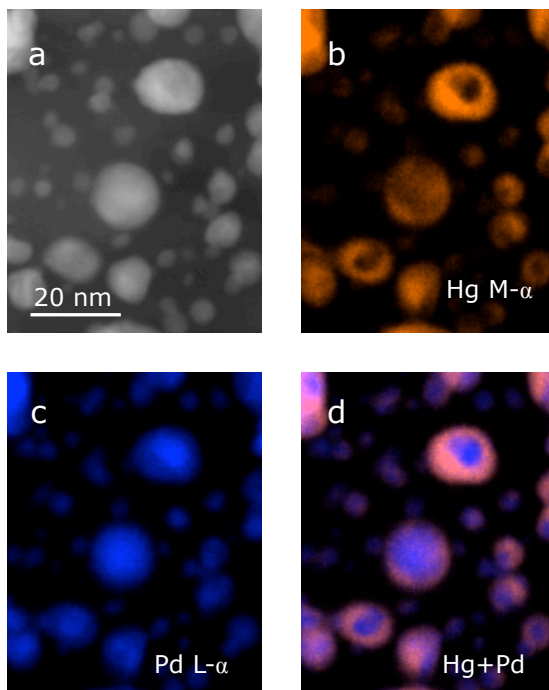


Figure 6.10: a: HAADF-STEM image of the analysed region. b-d: Hg-M $_{\alpha}$, Pd-L $_{\alpha}$ and combined Pd + Hg chemical maps.

6.2.1 Spectroscopy studies and elemental distribution

In order to support the interpretation of the contrast in the TEM and STEM images of the Pd-Hg nanoparticles, X-Ray STEM-EDS spectrum imaging was employed. Figure 6.10 shows the HAADF-STEM image of the analysed region along with Hg, Pd and Hg+Pd elemental maps of the analysed region. The maps clearly indicate the formation of a Hg-rich shell on top of a Pd-rich core. It is noticeable that the thickness of the shell is not uniform around the particles.

This anisotropy is more easily observed in Figure 6.11, where four different linescans have been traced and extracted from the spectrum image data cube. The Hg signal peaks on the shell region but extends differently around the particle, while it drops on the core region. For the Pd signal the trend is opposite. The linescans show both Hg and Pd present in the shell, indicating a possible alloy formation. The different reactivity of the Pd nanoparticle facets could play a role on the ability of the two metal to alloy, hence the anisotropy of the shell thickness.

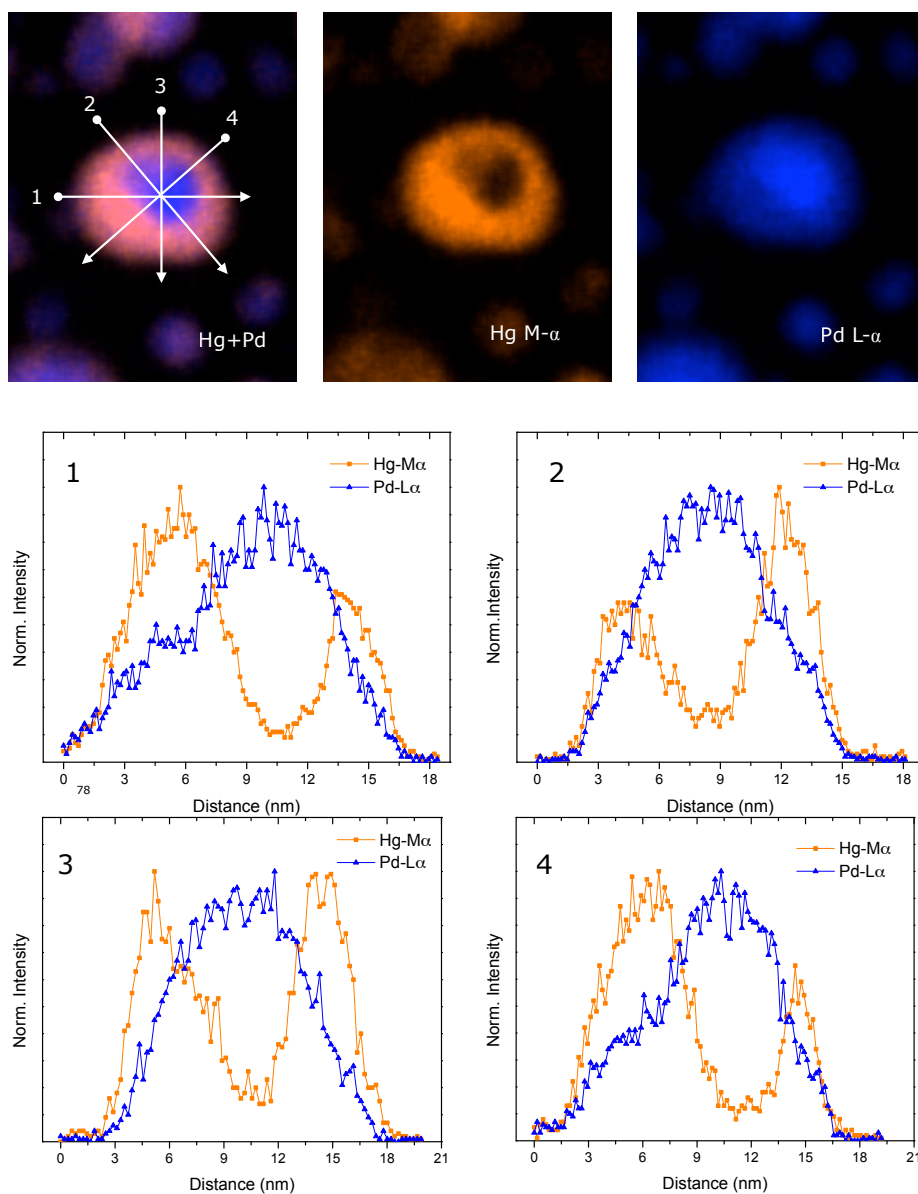


Figure 6.11: On top, magnified view of the elemental maps in figure 6.10b-d. Labelled white arrows corresponds to the linescans 1-4 at the bottom.

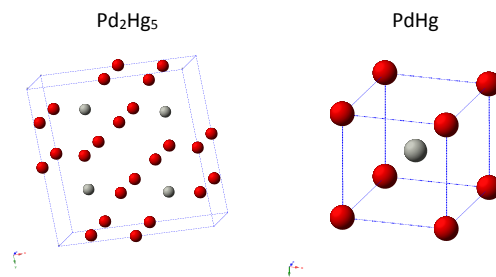


Figure 6.12: Unit cells of possible stable crystal structures for Pd-Hg ordered alloy.

6.2.2 High-resolution STEM

Pd and Hg is known to form two stable alloy crystal structures, Pd_2Hg_5 (the structure used in the DFT calculations) and PdHg [91] with their respective unit cells shown in Figure 6.12. In light of the EDS maps, the TEM and STEM images in Figure 6.9 reveal more information about the structure of the shell. The appearance of fringes on the alloyed regions indicates the formation of an ordered alloy structure of the shell. This has been confirmed by high-resolution HAADF-STEM.

Figure 6.13-a shows a 15 nm diameter particle. The core-shell structure is clearly visible and the magnified region of the shell shows alternating high brightness planes with a lattice distance of 2.9 Å (Figure 6.13c-d). The contrast features exhibited by the particle shell can be explained as planes with high Hg content. In fact the $\{001\}$ planes of Pd_2Hg_5 and $\{010\}$ of PdHg structures (Figure 6.13-b) contain only Hg, with interplanar distances of 3.03 Å and 3.02 Å, respectively. Therefore, the distances between the bright planes measured in the HAADF-STEM images can be associated to both structures.

Different particles show similar features on various part of the shell as reported in Figure 6.14. In this case the alloy extends for a large portion of the particle showing the Hg/Pd alternating planes. From the intensity linescan extracted along the blue line drawn on the image, the distance between Hg planes is measured with a value of 3.81 Å. This lattice distance can only be ascribed to the 3.706 Å $\{001\}$ distance of the PdHg structure.

Well aligned particles have been searched for a more reliable identification of the alloy phase. Figure 6.15-a shows a low index zone-axis oriented Pd-Hg nanoparticle. The core-shell structure is recognisable, with the Pd core oriented along the $[011]$ zone-axis as indicated by its FFT. On the bottom of the image

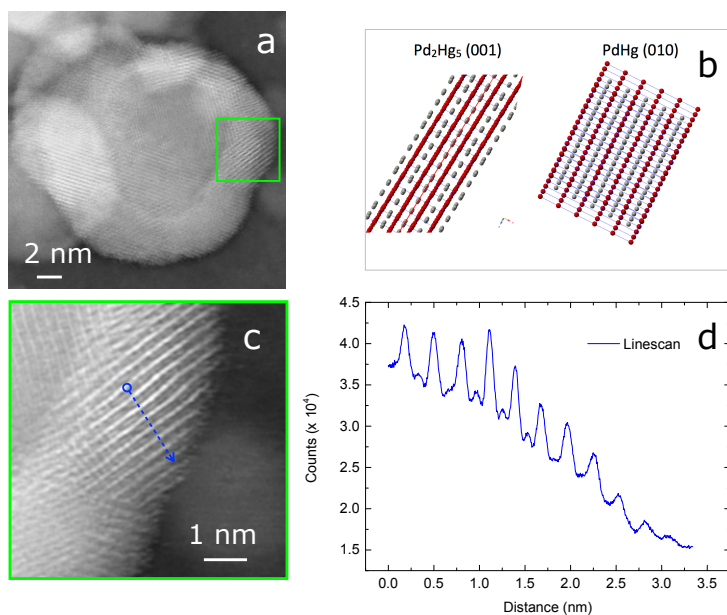


Figure 6.13: **a:** Pd-Hg alloy core-shell nanoparticle. **b:** {001} planes of Pd₂Hg₅ and {010} of PdHg (Hg and Pd atoms are shown in red and grey colours, respectively). **c:** High magnification HAADF-STEM image of the shell region enclosed in the square draw region of (a). **d:** HAADF intensity linescan extracted from (c) along the blue line. Alternating high/low intensity peaks indicates a strong contrast variation interpreted as alternating Hg/Pd planes.

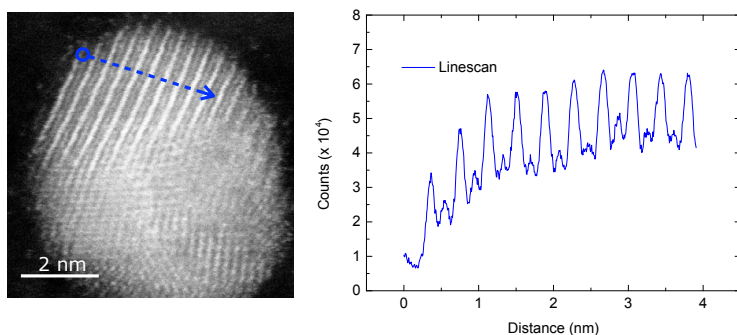


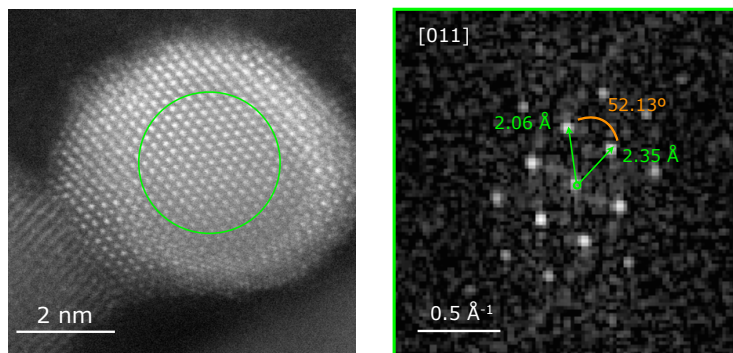
Figure 6.14: HAADF-STEM image of a Pd-Hg nanoparticle and intensity linescan extracted from the image along the blue line. The distance between the bright planes is measured as 3.81 Å.

it is visible how the structure changes from the core to the shell, while in other areas, like on the left and right shell regions of the particle, a sort of decoration effect seems to appear. In these parts the structure seems to be similar to the core, but brighter atom columns are visible. This is also visible by the intensity linescans extracted from the image as shown in Figure 6.15-a and 6.15-b. The linescans are taken along the atomic columns crossing the core and the shell parts, showing high peaks when approaching the shell region. Although contrast enhancement from channeling effects could arise, it is plausible that heavy Hg atoms decorate the surface.

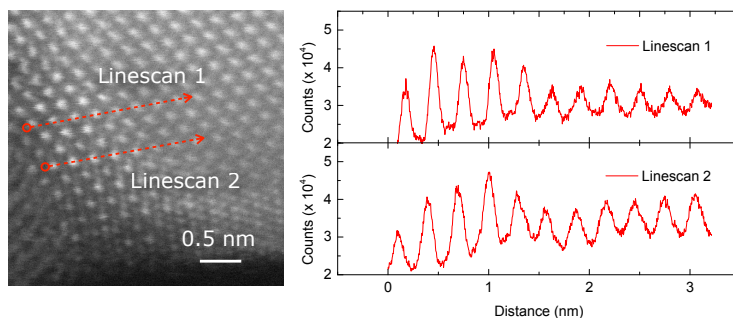
Figure 6.16-a shows another Pd-Hg nanoparticle with a core-shell structure presenting a part of the shell aligned along a low-index zone axis. The atomic columns are well visible and the HAADF intensity linescans, extracted from two orthogonal lines along the atomic columns, clearly reveal the alternating contrast due to alternating abundance of Hg and Pd. Along the vertical direction (red curve, Figure 6.16-b) brighter columns have similar intensity and are assigned to Hg-rich columns. On the other hand, the horizontal linescan (blue curve, Figure 6.16-b) shows two intensity levels associated to the Hg- and Pd-rich columns. By calculating the FFT of the shell region, the crystal structure has been identified. Figure 6.17-a shows the FFT of the shell region: the two measured spots, corresponding to 2.19 \AA and 1.93 \AA , are indexed as the $(1\bar{1}0)$ and $(00\bar{2})$ reflections of the HgPd structure along the $[110]$ zone axis. This is further confirmed by the good matching between the FFT and the simulated diffraction pattern (Figure 6.17-b). Although the structure of the alloy has been identified for few particles, the complexity of the system requires the use of image simulations for a more exhaustive understanding of the alloy. The major challenge for the simulations is the modelling of the particle: specifically, the epitaxial relation between the ordered alloy and the metal core is unknown. Furthermore, from the STEM images the alloying appears facet-dependent, increasing the overall complexity of the particle model.

6.2.3 Summary

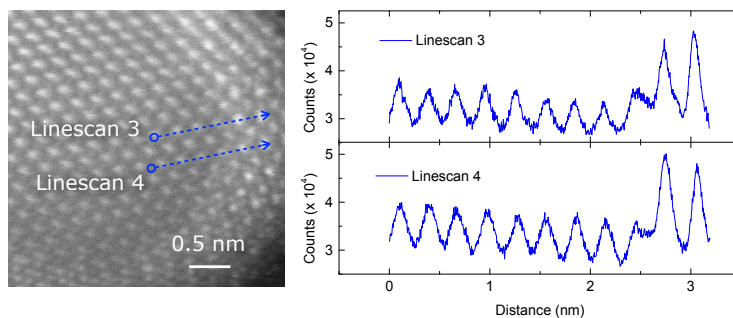
The (S)TEM analysis, together with the STEM-EDS spectroscopy, have indicated the presence of an alloy structure in the outermost region of the Pd–Hg/C nanoparticles. Hg and Pd atoms form an ordered phase as predicted, although not evenly on the whole surface and show a facet-dependency. The alloying on the surface of the particles has an important impact on the electrochemical activity even if the crystal structure of the shell of the analysed particles does not coincide with the structure used in the DFT calculations for the model surface. It is to be noticed that the termination and stoichiometry of the outermost atomic layer of the surface cannot be assessed from the high-resolution STEM



(a) Pd-Hg Core-shell alloy nanoparticle (left). The FFT of the core region is shown on the right. The measured spot distances, 2.06 Å and 2.35 Å, are indexed as (200) and (11 $\bar{1}$) reflections of the metallic Pd structure.



(b) HAADF intensity linescans extracted from the shell region on the left of the particle in (a).



(c) HAADF intensity linescans extracted from the shell region on the right of the particle in (a).

Figure 6.15: Core-shell nanoparticle in low index zone axis.

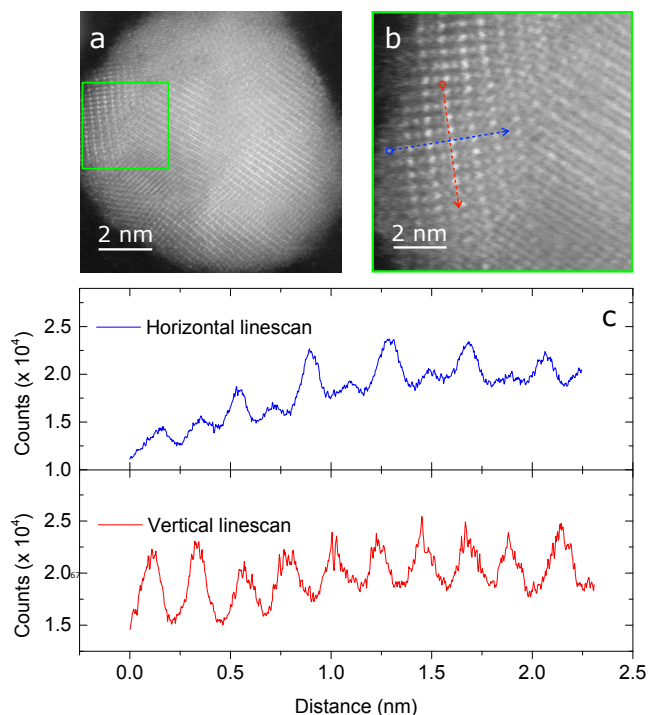


Figure 6.16: **a:** HAADF-STEM images of a core-shell Pd-Hg nanoparticle. **b:** High resolution image of the shell region enclosed in the green square drawn in **(a)**. **c:** HAADF intensity line scans extracted from the shell region along the blue and red lines in **(b)**.

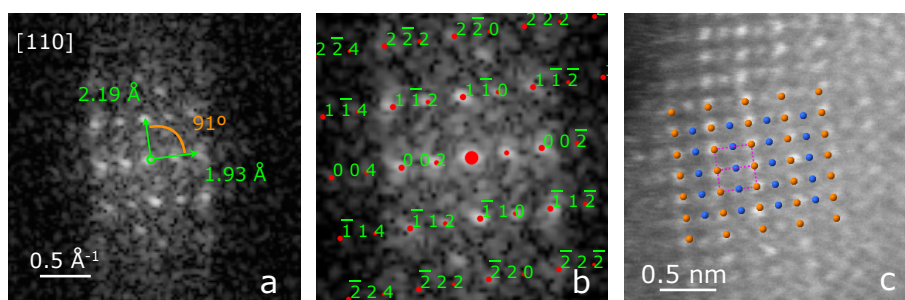


Figure 6.17: **a:** FFT of the region in Figure 6.16-b. **b:** Simulated diffraction pattern of PdHg along $[110]$ zone axis superimposed to the FFT shown in **(a)**. **c:** Region of the shell shown in Figure 6.15-b with superimposed a portion of the PdHg structure along the $[110]$ zone axis. Hg and Pd atoms are represented by orange and blue coloured spheres, respectively.

images and remains therefore still unknown. Furthermore, the analysis cannot be fully representative of the whole sample since it has been limited to particles in the range of 6 nm to 15 nm while the sample consists of a large variety of particle sizes.

Conclusions and Outlook

In this project, transmission electron microscopy, in combination with EELS and X-ray EDS spectroscopy, has been employed in the study of metal nanoparticle catalysts. These techniques have played a fundamental role in the characterisation of the studied materials. Two challenges of designing active and stable catalysts have been addressed in this thesis: 1) understanding the sintering behaviour of mass-selected monomodal Pt cluster catalysts; 2) understanding the morphology, stability and local composition of novel alloy nanoparticle electrocatalysts. These properties are essential in order to explain the outstanding catalytic performances of the new alloys.

Sintering resistance of Pt clusters

In situ INPS measurements indicated that sintering occurs when Pt clusters with a broad particle size distribution and mass-selected clusters with a bimodal distribution are heated at 453 K in Ar for 21 hours. At the same conditions, mass-selected clusters with a monomodal size distribution have shown a resistance towards sintering. The resistance is observed also at higher temperature in the harsher conditions of the water oxidation reaction. To understand this remarkable behaviour, a statistical analysis of the Pt clusters has been performed via *ex situ* scanning transmission electron microscopy. The analysis of

the area distribution histograms of the unselected clusters and bimodal mass-selected clusters have shown that small particles decrease in number while the population of larger particles increases. As the coverage was unchanged after treatment, it was concluded that no particle coalescence occurred. Hence Ostwald ripening is believed to be the dominant sintering mechanism. The sintering resistance of the mass-selected clusters is then assigned to the elimination of the main driving force of the Ostwald ripening, i.e. the difference in chemical potential between clusters of different sizes. This is achieved by creating a narrow monomodal size distribution.

Although the experiments have been performed on model catalytic systems, the findings have a general validity since the reason for the observed sintering resistance is of fundamental nature. Larger nanoparticles are also expected to show resistance towards sintering when synthesised with a monomodal size distribution.

Pt alloy nanoparticles for ORR

Thanks to the gas aggregation technique, combined with time-of-flight mass filtering, mass-selected Pt_xY and Pt_xGd nanoparticles of different size have been synthesised. Transmission electron microscopy and spectroscopy have played an essential role in explaining their high electrochemical ORR activity and stability compared to the current Pt/C catalyst used in PEMFCs. All the particles presented a narrow size distribution, a clear sign of a successful mass selection, and a random-alloy disordered structure. Identical location studies proved that particles are highly stable on carbon support showing no sign of sintering or detachment after ORR catalytic tests and even after prolonged ageing tests. This demonstrates that the loss in the ORR performance cannot be assigned to a decrease of active surface area, but must be related to a drop in the specific activity. STEM-EDS spectrum imaging on the 9 nm Pt_xY nanoparticles has clearly shown the change in the particle elemental distribution before and after catalytic tests. A core-shell structure is formed during the ORR activity test, with an alloyed core and a ~ 1 nm thick Pt-rich shell left behind after yttrium has segregated from the surface and dissolved into the electrolyte. After the stability test, the same structure is maintained with a slight thickening of the Pt-rich shell. This effect is visible in the Pt/Y atomic ratio calculated from the EDS maps. While the core region is characterised by a constant Pt/Y ratio throughout the different steps of the catalytic tests, the ratio on the shell region increases dramatically after the ORR measurements. A small increment is registered after the stability test. The presence of the thick shell excludes ligand effects as a possible explanation for the high activity of the particle. The estimation of the average Pt-Pt distance in the particles by EXAFS, together

with compositional analysis by STEM-EDS, have confirmed strain effects at the surface as the reason for the enhanced activity.

The ultra-high vacuum cluster source has given the opportunity of synthesising Pt and rare-earths metallic alloy samples. Nonetheless, this physical method is not suited for mass production. For this reason, the development of an economically viable process for the chemical synthesis of this class of catalysts is of great interest. Different methods are currently under study.

Alloy nanoparticles for H₂O₂ production

Pt–Hg and Pd–Hg alloy nanoparticles have been predicted by DFT as highly active electrocatalysts for H₂O₂ production. The enhanced activity is expected to be provided by an alloyed surface where reactive atoms (Pt and Pd) are surrounded by more inert Hg atoms. After being synthesised in nanoparticulate form, their catalytic tests have shown outstanding performance. In order to confirm the presence of the alloy on the surface, the particles have been analysed by (S)TEM and X-Ray EDS. In Pt–Hg nanoparticles the presence of both elements on single particles is confirmed by EDS but high-resolution TEM images show particles with a structure only compatible with pure Pt. As also XPS results confirmed the presence of Hg and Pt on the surface, it is believed that the alloy is formed on the surface of the particle. In the Pd–Hg nanoparticles, STEM imaging and EDS spectrum imaging have shown the formation of a core-shell structure. A pure Pd core is enclosed in a non-uniform shell composed of a Pd–Hg alloy. The anisotropy of the shell around the core is ascribed to the different surface energy of the particle facets that influences the formation of the alloy. Atomic-resolution STEM images have shown an ordered alloy structure on the shell. Although this structure does not coincide with the theoretical model, the Hg is stabilised in an intermetallic alloy together with Pd, forming a highly active and stable catalytic surface.

The next step would be to fine-tune the particle shape, size and composition in order to improve even further the mass activity. Moreover, the combination of DFT calculations, synthesis and advanced electron microscopy characterisation will be extended to other reactions.

Summary and final remarks

The interplay between theoretical calculations, synthesis and characterisation has been proven to be an effective and successful strategy for the discovery of novel nanoparticle electrocatalysts with state-of-the-art performance. The work presented in this thesis shows the fundamental role that transmission electron microscopy and spectroscopy techniques have played in the characterisation of the nanoparticles. By combining the structural, morphological and compositional properties given by electron microscopy with the information provided by complementary techniques, the origin of the enhanced catalytic properties of the novel particles has been revealed.

The continuous improvements in the analytical capabilities of TEMs at higher resolutions allow new exciting horizons to be seen in the characterisation of the materials at the atomic scale. Especially for bimetallic nanoparticles, a deeper understanding of their promising catalytic properties will be possible thanks to a more accurate determination of their compositional properties, giving invaluable information towards the design of better catalysts.

Appendix

Particle size distribution procedure

The particle size distributions for the Pt_xY and Pt_xGd nanoparticles have been extracted from TEM and STEM images, respectively, acquired at 300 kV accelerating voltage in the Titan microscopes. The same procedure has been applied for the extraction of all the PSDs. All the micrographs used for one PSD have been acquired at same magnification and same beam conditions as well as the acquisition parameters. The images have analysed with Fiji ImageJ 1.48t software and the results of the analysis have been converted in histograms with OriginPro 9.0 Software. For each set of images of each sample the following steps have been followed:

- Intensity thresholding of the image is performed to separate the particles from the background. After optimising it for the first micrograph, the threshold level is kept constant within the sets of images.
- The detection and the area measurement of the particles is performed with the *Particle analysis* algorithm integrated in ImageJ after tuning the optimal value of circularity and size thresholds of the areas corresponding to the nanoparticles. This allows to discriminate most of the overlapping

particles. Both circularity and size thresholds are kept constant within the sets of images.

- For each micrograph, a contour-drawing image of the particles counted by the algorithm is produced and manually compared with the original micrograph. This allows to spot residual overlapping particles not excluded by the automated procedure as shown in Figure A.1.
- The diameter of each particle is calculated from the value of the measured area assuming a spheroidal shape.

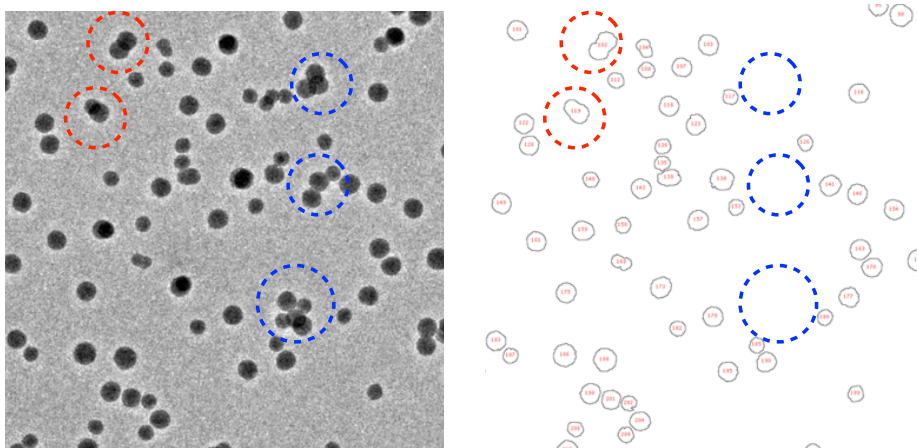


Figure A.1: Bright-field TEM micrograph of Pt_xY nanoparticles (left) and corresponding contour image (right). Blue circles indicate the detected overlap by the automated procedure thanks to circularity and size thresholds. Red circles indicate the overlapping particles not discriminated by the algorithm. In this last case, the counted areas are manually removed from the PSD.

Identical location study - PSD

To show further the stability of the Pt_xY nanoparticles in the ORR environment, two large-view images of the same identical region of a 7 nm particles sample before and after the ORR stability test are reported in Figure A.2, showing how stable the particles are on the carbon support. This is also clear from the PSDs before and after the stability test shown in Figure A.3, where no sign of sintering is observed.

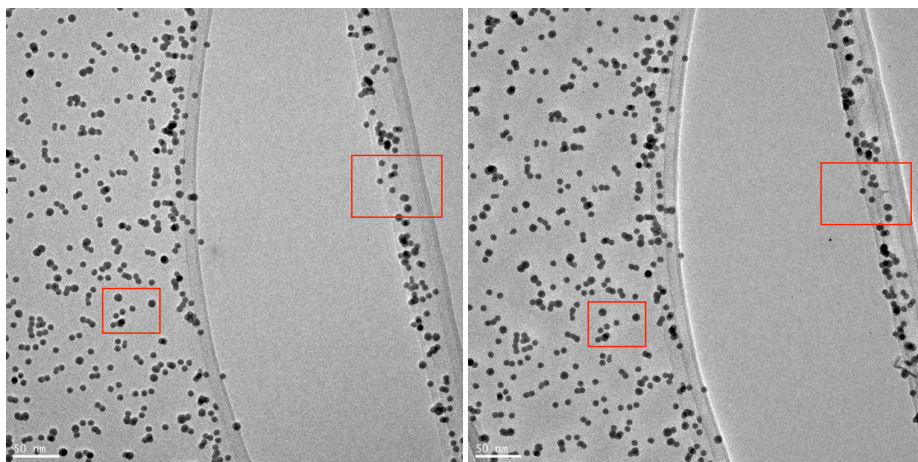


Figure A.2: Identical location TEM of a sample containing 7 nm Pt_xY nanoparticles before (left) and after (right) ORR stability test. The red-highlighted areas show how the particles are stable on their positions.

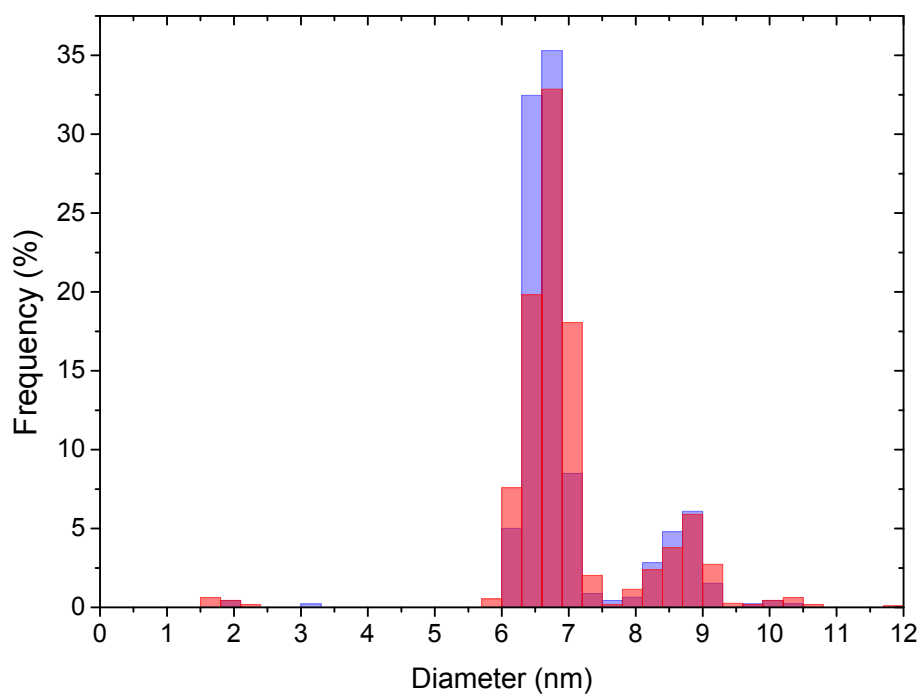


Figure A.3: Particle size distribution frequency histograms of a sample containing 7 nm Pt_xY nanoparticles before (blue) and after (red) ORR stability test. No evidence of sintering is observed.

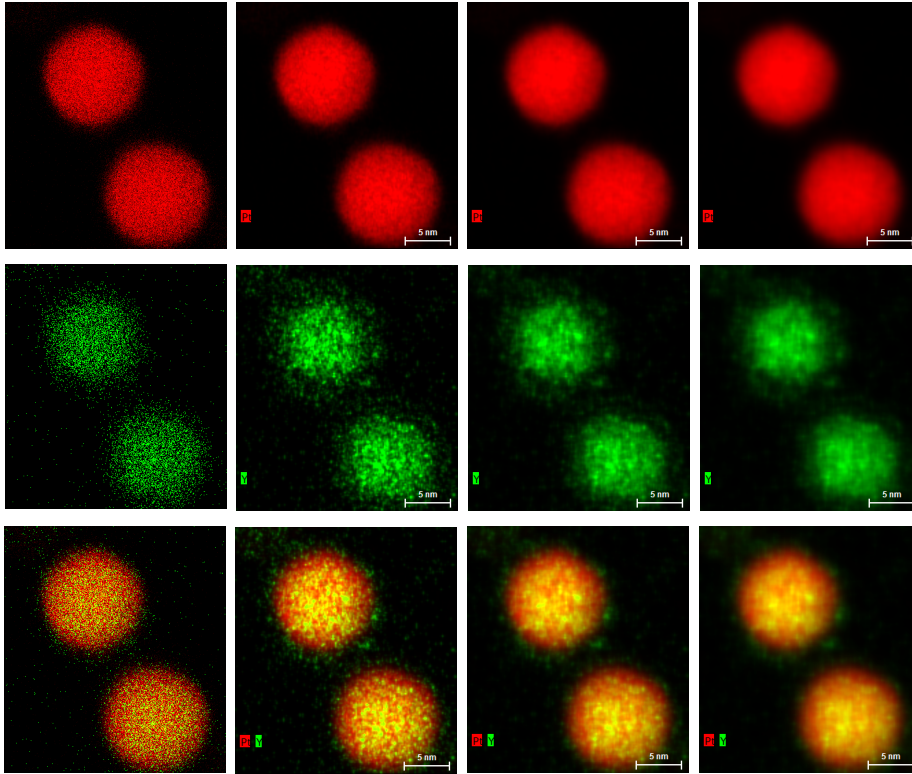


Figure A.4: Effect of the smoothing algorithm applied by the Bruker Esprit software on the maps in Figure 5.15. From left to right, unfiltered data and 3x3, 5x5, 7x7 average filter are shown.

X-ray EDS spectrum imaging

Smoothing algorithm effect

Figure A.4 shows the application of the smoothing filter option available in the Bruker Esprit software employed for the acquisition and analysis of the XEDS maps presented in this thesis. The filter applies an averaging algorithm where each pixel is replaced with the average of itself and a number of neighbouring pixels over a square region around the selected pixel. The available neighbourhood sizes are regions of 3x3, 5x5, 7x7 and 9x9 pixels.

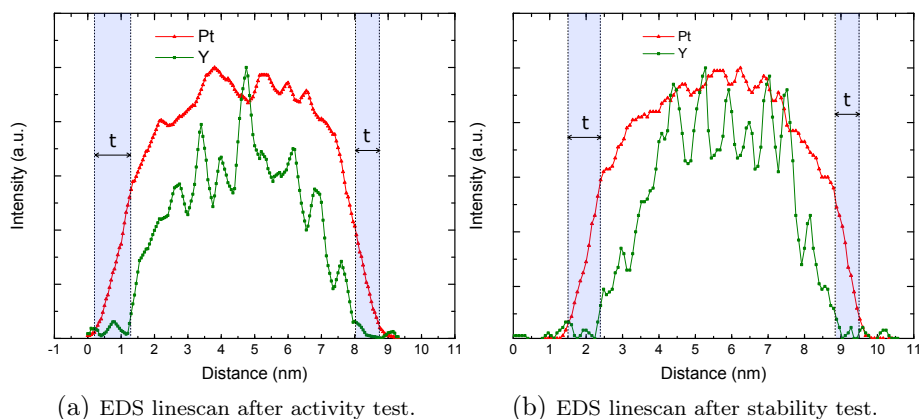


Figure A.5: EDS linescans for the electrochemically tested Pt_xY nanoparticles. t is the estimated Pt-rich shell thickness.

Pt Shell thickness estimation

For the Pt_xY nanoparticles after electrochemical tests, the average thickness of the Pt-rich shell has been estimated from the EDS elemental maps by extracting 10 different linescans across the particles. Representative linescans for the particles after activity and stability tests are shown in Figure A.5. For each sample the shell thickness is estimated by the average of 20 values extracted from the linescans as shown by the blue areas in Figure A.5. The calculated thickness in the activity-tested sample resulted $t = (1.0 \pm 0.3)$ nm, while the thickness in the stability-tested sample resulted $t = (1.2 \pm 0.4)$ nm.

Software

High-resolution TEM and STEM images presented in this thesis have been analysed with the Gatan Digital Micrograph[®] 1.84 software. Lattice parameter measurements have been performed through the analysis of FFTs obtained with the DM-plugin *Diffraction Tools* from the University of Cadiz. The lattice planes and the crystallographic orientation determination of the different nanoparticles, as well as the diffraction pattern simulations, have been performed via the *Eje-Z* web-software [92, 93]. Table A.1 summarises the bulk structures used in the *Eje-Z* software and found in the international crystal structure database (ICSD).

Table A.1: Crystal structures files from the ICSD.

Compound	ICSD database card
Pt	64919
Pd	52251
PtHg ₄	659824
PdHg	40322
Pd ₂ Hg ₅	104334

The Crystal Maker[®] software has been used for the crystal structure and diffraction pattern drawings.

Bibliography

- [1] H. A. Gasteiger and J. Garche, "Fuel Cells," in *Handbook of Heterogeneous Catalysis*, pp. 3031–3121, 2008.
- [2] M. K. Debe, "Electrocatalyst approaches and challenges for automotive fuel cells.," *Nature*, vol. 486, pp. 43–51, June 2012.
- [3] H. A. Gasteiger, S. S. Kocha, B. Sompalli, and F. T. Wagner, "Activity benchmarks and requirements for Pt, Pt-alloy, and non-Pt oxygen reduction catalysts for PEMFCs," *Applied Catalysis B: Environmental*, vol. 56, pp. 9–35, Mar. 2005.
- [4] I. E. L. Stephens, A. S. Bondarenko, U. Grønbjerg, J. Rossmeisl, and I. Chorkendorff, "Understanding the electrocatalysis of oxygen reduction on platinum and its alloys," *Energy & Environmental Science*, vol. 5, no. 5, p. 6744, 2012.
- [5] C. Yang, "An impending platinum crisis and its implications for the future of the automobile," *Energy Policy*, vol. 37, pp. 1805–1808, May 2009.
- [6] F. Jaouen, E. Proietti, M. Lefevre, R. Chenitz, J.-P. Dodelet, G. Wu, H. T. Chung, C. M. Johnston, and P. Zelenay, "Recent advances in non-precious metal catalysis for oxygen-reduction reaction in polymer electrolyte fuel cells," *Energy & Environmental Science*, vol. 4, no. 1, p. 114, 2011.
- [7] A. Topalov, I. Katsounaros, M. Auinger, S. Cherevko, J. C. Meier, S. O. Klemm, and K. J. J. Mayrhofer, "Dissolution of platinum: limits for the deployment of electrochemical energy conversion?," *Angewandte Chemie*, vol. 51, pp. 12613–12615, Dec. 2012.

- [8] Y. Shao-Horn, W. C. Sheng, S. Chen, P. J. Ferreira, E. F. Holby, and D. Morgan, "Instability of Supported Platinum Nanoparticles in Low-Temperature Fuel Cells," *Topics in Catalysis*, vol. 46, pp. 285–305, Nov. 2007.
- [9] L. Dubau, L. Castanheira, F. Maillard, M. Chatenet, O. Lottin, G. Maranzana, J. Dillet, A. Lamibrac, J.-C. Perrin, E. Moukheiber, A. ElKaddouri, G. De Moor, C. Bas, L. Flandin, and N. Caqué, "A review of PEM fuel cell durability: materials degradation, local heterogeneities of aging and possible mitigation strategies," *WIREs Energy and Environment*, vol. 3, Mar. 2014.
- [10] T. W. Hansen, *Sintering and Particle Dynamics in Supported Metal Catalysts*. Phd thesis, 2006.
- [11] A. K. Datye, Q. Xu, K. C. Kharas, and J. M. McCarty, "Particle size distributions in heterogeneous catalysts: What do they tell us about the sintering mechanism?," *Catalysis Today*, vol. 111, pp. 59–67, Jan. 2006.
- [12] T. W. Hansen and J. B. Wagner, "Catalysts under Controlled Atmospheres in the Transmission Electron Microscope," *ACS Catalysis*, vol. 4, pp. 1673–1685, June 2014.
- [13] S. Simonsen, I. Chorkendorff, S. Dahl, M. Skoglundh, J. Sehested, and S. Helveg, "Direct observations of oxygen-induced platinum nanoparticle ripening studied by in situ TEM," *Journal of the American Chemical Society*, vol. 132, pp. 7968–7975, June 2010.
- [14] A. D. Benavidez, L. Kovarik, A. Genc, N. Agrawal, E. M. Larsson, T. W. Hansen, A. M. Karim, and A. K. Datye, "Environmental Transmission Electron Microscopy Study of the Origins of Anomalous Particle Size Distributions in Supported Metal Catalysts," *ACS Catalysis*, vol. 2, pp. 2349–2356, Nov. 2012.
- [15] T. W. Hansen, A. T. Delariva, S. R. Challa, and A. K. Datye, "Sintering of catalytic nanoparticles: particle migration or Ostwald ripening?," *Accounts of chemical research*, vol. 46, pp. 1720–1730, Aug. 2013.
- [16] P. J. Ferreira, G. J. la O, Y. Shao-Horn, D. Morgan, R. Makharia, S. Kocha, and H. A. Gasteiger, "Instability of Pt-C Electrocatalysts in Proton Exchange Membrane Fuel Cells," *Journal of The Electrochemical Society*, vol. 152, no. 11, pp. A2256–A2271, 2005.
- [17] M. A. Asoro, D. Kovar, Y. Shao-Horn, L. F. Allard, and P. J. Ferreira, "Coalescence and sintering of Pt nanoparticles: in situ observation by aberration-corrected HAADF STEM.," *Nanotechnology*, vol. 21, Jan. 2010.

- [18] A. V. Virkar and Y. Zhou, "Mechanism of Catalyst Degradation in Proton Exchange Membrane Fuel Cells," *Journal of The Electrochemical Society*, vol. 154, no. 6, p. B540, 2007.
- [19] P. Parthasarathy and A. V. Virkar, "Electrochemical Ostwald ripening of Pt and Ag catalysts supported on carbon," *Journal of Power Sources*, vol. 234, pp. 82–90, July 2013.
- [20] S. Chen, H. A. Gasteiger, K. Hayakawa, T. Tada, and Y. Shao-Horn, "Platinum-Alloy Cathode Catalyst Degradation in Proton Exchange Membrane Fuel Cells: Nanometer-Scale Compositional and Morphological Changes," *Journal of The Electrochemical Society*, vol. 157, no. 1, p. A82, 2010.
- [21] K. Yu, D. J. Groom, X. Wang, Z. Yang, M. Gummalla, S. C. Ball, D. Myers, and P. J. Ferreira, "Degradation Mechanisms of Platinum Nanoparticle Catalysts in Proton Exchange Membrane Fuel Cells: The Role of Particle Size," *Chemistry of Materials*, vol. 20, pp. 482–483, Aug. 2014.
- [22] J. K. Nørskov and J. Rossmeisl, "Origin of the overpotential for oxygen reduction at a fuel-cell cathode," *Journal of physical chemistry B*, no. 108, pp. 17886–17892, 2004.
- [23] V. Viswanathan, H. A. Hansen, J. Rossmeisl, and J. K. Nørskov, "Unifying the 2e⁻ and 4e⁻ Reduction of Oxygen on Metal Surfaces," *The Journal of Physical Chemistry Letters*, vol. 3, pp. 2948–2951, Oct. 2012.
- [24] I. E. L. Stephens, A. S. Bondarenko, F. J. Perez-Alonso, F. Calle-Vallejo, L. Bech, T. P. Johansson, A. K. Jepsen, R. Frydendal, B. P. Knudsen, J. Rossmeisl, and I. Chorkendorff, "Tuning the activity of Pt(111) for oxygen electroreduction by subsurface alloying," *Journal of the American Chemical Society*, vol. 133, pp. 5485–91, Apr. 2011.
- [25] V. Tripković, E. Skúlason, S. Siahrostami, J. K. Nørskov, and J. Rossmeisl, "The oxygen reduction reaction mechanism on Pt(111) from density functional theory calculations," *Electrochimica Acta*, vol. 55, pp. 7975–7981, Nov. 2010.
- [26] V. R. Stamenkovic, B. S. Mun, K. J. J. Mayrhofer, P. N. Ross, and N. M. Markovic, "Effect of surface composition on electronic structure, stability, and electrocatalytic properties of Pt-transition metal alloys: Pt-skin versus Pt-skeleton surfaces," *Journal of the American Chemical Society*, vol. 128, pp. 8813–9, July 2006.
- [27] S. Chen, W. Sheng, N. Yabuuchi, P. J. Ferreira, L. F. Allard, and Y. Shao-Horn, "Origin of Oxygen Reduction Reaction Activity on "Pt₃Co" Nanoparticles: Atomically Resolved Chemical Compositions and Structures," *The Journal of Physical Chemistry C*, vol. 113, pp. 1109–1125, Jan. 2009.

- [28] J. Kitchin, J. K. Nørskov, M. Barteau, and J. Chen, "Role of Strain and Ligand Effects in the Modification of the Electronic and Chemical Properties of Bimetallic Surfaces," *Physical Review Letters*, vol. 93, p. 156801, Oct. 2004.
- [29] P. Strasser, S. Koh, T. Anniyev, J. Greeley, K. L. More, C. Yu, Z. Liu, S. Kaya, D. Nordlund, H. Ogasawara, M. F. Toney, and A. Nilsson, "Lattice-strain control of the activity in dealloyed core-shell fuel cell catalysts," *Nature chemistry*, vol. 2, pp. 454–60, June 2010.
- [30] S. Mostafa, F. Behafarid, J. R. Croy, L. K. Ono, L. Li, J. C. Yang, A. I. Frenkel, and B. R. Cuenya, "Shape-dependent catalytic properties of Pt nanoparticles," *Journal of the American Chemical Society*, vol. 132, pp. 15714–9, Nov. 2010.
- [31] F. J. Perez-Alonso, D. N. McCarthy, A. Nierhoff, P. Hernandez-Fernandez, C. E. Streb, I. E. L. Stephens, J. H. Nielsen, and I. Chorkendorff, "The Effect of Size on the Oxygen Electroreduction Activity of Mass-Selected Platinum Nanoparticles," *Angewandte Chemie*, vol. 51, pp. 4641–4643, Mar. 2012.
- [32] U. Paulus, A. Wokaun, G. Scherer, T. Schmidt, V. R. Stamenkovic, N. M. Markovic, and P. Ross, "Oxygen reduction on high surface area Pt-based alloy catalysts in comparison to well defined smooth bulk alloy electrodes," *Electrochimica Acta*, vol. 47, pp. 3787–3798, Aug. 2002.
- [33] M. Oezaslan and P. Strasser, "Activity of dealloyed PtCo₃ and PtCu₃ nanoparticle electrocatalyst for oxygen reduction reaction in polymer electrolyte membrane fuel cell," *Journal of Power Sources*, vol. 196, pp. 5240–5249, June 2011.
- [34] M. Oezaslan, F. Hasche, and P. Strasser, "Oxygen Electroreduction on PtCo₃, PtCo and Pt₃Co Alloy Nanoparticles for Alkaline and Acidic PEM Fuel Cells," *Journal of The Electrochemical Society*, vol. 159, no. 4, p. B394, 2012.
- [35] M. Heggen, M. Oezaslan, L. Houben, and P. Strasser, "Formation and Analysis of Core Shell Fine Structures in Pt Bimetallic Nanoparticle Fuel Cell Electrocatalysts," *The Journal of Physical Chemistry C*, vol. 116, pp. 19073–19083, Sept. 2012.
- [36] M. Oezaslan, F. Hasche, and P. Strasser, "Pt-Based Core-Shell Catalyst Architectures for Oxygen Fuel Cell Electrodes," *The Journal of Physical Chemistry Letters*, vol. 4, pp. 3273–3291, Oct. 2013.
- [37] K. Neyerlin, R. Srivastava, C. Yu, and P. Strasser, "Electrochemical activity and stability of dealloyed Pt–Cu and Pt–Cu–Co electrocatalysts for the

- oxygen reduction reaction (ORR)," *Journal of Power Sources*, vol. 186, pp. 261–267, Jan. 2009.
- [38] J. Greeley, I. E. L. Stephens, A. S. Bondarenko, T. P. Johansson, H. A. Hansen, T. F. Jaramillo, J. Rossmeisl, I. Chorkendorff, and J. K. Nørskov, "Alloys of platinum and early transition metals as oxygen reduction electrocatalysts," *Nature chemistry*, vol. 1, pp. 552–6, Oct. 2009.
- [39] P. Malacrida, M. Escudero-Escribano, A. Verdaguier-Casadevall, I. E. L. Stephens, and I. Chorkendorff, "Enhanced activity and stability of Pt–La and Pt–Ce alloys for oxygen electroreduction: the elucidation of the active surface phase," *Journal of Materials Chemistry A*, vol. 2, no. 12, p. 4234, 2014.
- [40] M. Escudero-Escribano, A. Verdaguier-Casadevall, P. Malacrida, U. Grønberg, B. P. Knudsen, A. K. Jepsen, J. Rossmeisl, I. E. L. Stephens, and I. Chorkendorff, "Pt5Gd as a highly active and stable catalyst for oxygen electroreduction," *Journal of the American Chemical Society*, vol. 134, pp. 16476–9, Oct. 2012.
- [41] R. Behm and Z. Jusys, "The potential of model studies for the understanding of catalyst poisoning and temperature effects in polymer electrolyte fuel cell reactions," *Journal of Power Sources*, vol. 154, pp. 327–342, Mar. 2006.
- [42] J. M. Campos-Martin, G. Blanco-Brieva, and J. L. G. Fierro, "Hydrogen peroxide synthesis: an outlook beyond the anthraquinone process," *Angewandte Chemie*, vol. 45, pp. 6962–84, Oct. 2006.
- [43] IHS-Chemical, "Hydrogen Peroxide," *IHS chemical*, 2009.
- [44] G. I. Analysts, "Hydrogen Peroxide - A global strategic business report," *Global Industry Analysts*, 2012.
- [45] R. Hage and A. Lienke, "Applications of Transition-Metal Catalysts to Textile and Wood-Pulp Bleaching," *Angewandte Chemie*, vol. 45, pp. 206–222, Jan. 2006.
- [46] J. A. Lopez-Sanchez, N. Dimitratos, P. Miedziak, E. Ntainjua, J. K. Edwards, D. Morgan, A. F. Carley, R. Tiruvalam, C. J. Kiely, and G. J. Hutchings, "Au-Pd supported nanocrystals prepared by a sol immobilisation technique as catalysts for selective chemical synthesis," *PCCP*, vol. 10, pp. 1921–30, Apr. 2008.
- [47] J. K. Edwards, B. Solsona, E. Ntainjua, A. F. Carley, A. A. Herzing, C. J. Kiely, and G. J. Hutchings, "Switching off hydrogen peroxide hydrogenation in the direct synthesis process," *Science*, vol. 323, no. February, pp. 1037–1041, 2009.

- [48] I. Yamanaka, T. Hashimoto, R. Ichihashi, and K. Otsuka, "Direct synthesis of H₂O₂ acid solutions on carbon cathode prepared from activated carbon and vapor-growing-carbon-fiber by a H₂/O₂ fuel cell," *Electrochimica Acta*, vol. 53, pp. 4824–4832, May 2008.
- [49] R. Tiruvalam, J. C. Pritchard, N. Dimitratos, J. A. Lopez-Sanchez, J. K. Edwards, A. F. Carley, G. J. Hutchings, and C. J. Kiely, "Aberration corrected analytical electron microscopy studies of sol-immobilized Au + Pd, Au{Pd} and Pd{Au} catalysts used for benzyl alcohol oxidation and hydrogen peroxide production," *Faraday Discussions*, vol. 152, p. 63, 2011.
- [50] J. S. Jirkovsky, I. Panas, E. Ahlberg, M. Halasa, S. Romani, and D. J. Schiffrin, "Single atom hot-spots at Au-Pd nanoalloys for electrocatalytic H₂O₂ production.," *Journal of the American Chemical Society*, vol. 133, pp. 19432–41, Dec. 2011.
- [51] F. L. Deepak, G. Casillas-Garcia, R. Esparza, H. Barron, and M. Jose-Yacamán, "New Insights into the structure of Pd-Au nanoparticles as revealed by aberration-corrected STEM.," *Journal of crystal growth*, vol. 325, pp. 60–67, June 2011.
- [52] S. Siahrostami, A. Verdaguer-Casadevall, M. Karamad, D. Deiana, P. Malacrida, B. Wickman, M. Escudero-Escribano, E. A. Paoli, R. Frydendal, T. W. Hansen, I. Chorkendorff, I. E. L. Stephens, and J. Rossmeisl, "Enabling direct H₂O₂ production through rational electrocatalyst design.," *Nature materials*, vol. 12, pp. 1137–43, Dec. 2013.
- [53] A. Verdaguer-Casadevall, D. Deiana, M. Karamad, S. Siahrostami, P. Malacrida, T. W. Hansen, J. Rossmeisl, I. Chorkendorff, and I. E. L. Stephens, "Trends in the electrochemical synthesis of H₂O₂: enhancing activity and selectivity by electrocatalytic site engineering.," *Nano letters*, vol. 14, pp. 1603–1608, Feb. 2014.
- [54] I. Chorkendorff and J. W. Niemantsverdriet, *Concepts of modern catalysis and kinetics*. John Wiley and Sons Ltd, 2003.
- [55] S. J. Pennycook and P. D. Nellist, *Scanning transmission electron microscopy : imaging and analysis*. Springer, 2011.
- [56] R. Egerton, *Electron energy-loss spectroscopy in the electron microscope*. Springer, 2011.
- [57] D. B. Williams and B. C. Carter, *Transmission Electron Microscopy*. Boston, MA: Springer US, 2009.
- [58] N. J. Zaluzec, "Analytical Formulae for Calculation of X-Ray Detector Solid Angles in the Scanning and Scanning/Transmission Analytical Electron

- Microscope.," *Microscopy and Microanalysis*, vol. 20, pp. 1318–1326, May 2014.
- [59] M. Watanabe, D. Ackland, A. Burrows, C. J. Kiely, D. B. Williams, O. L. Krivanek, N. Dellby, M. Murfitt, and Z. Szilagy, "Improvements in the X-Ray Analytical Capabilities of a Scanning Transmission Electron Microscope by Spherical-Aberration Correction," *Microscopy and Microanalysis*, vol. 12, p. 515, Oct. 2006.
- [60] N. J. Zaluzec, "Innovative Instrumentation for Analysis of Nanoparticles: The π Steradian Detector," *Microscopy Today*, vol. 17, p. 56, June 2009.
- [61] P. Kotula, J. Michael, and M. Rohde, "Results from Two Four-Channel Si-drift Detectors on an SEM: Conventional and Annular Geometries," *Microscopy and Microanalysis*, vol. 14, pp. 116–117, Aug. 2008.
- [62] H. S. V. Harrach, P. Dona, B. Freitag, H. Soltau, A. Niculae, and M. Rohde, "An integrated Silicon Drift Detector System for FEI Schottky Field," *Microscopy and Microanalysis*, vol. 15, no. Suppl 2, pp. 8–9, 2009.
- [63] J. I. Goldstein, *Scanning electron microscopy and X-ray microanalysis*. Springer, 2007.
- [64] G. Cliff and G. W. Lorimer, "The quantitative analysis of thin specimens," *Journal of Microscopy*, vol. 103, pp. 203–207, Mar. 1975.
- [65] S. Kunz, K. Hartl, M. Nesselberger, F. F. Schweinberger, G. Kwon, M. Hanzlik, K. J. J. Mayrhofer, U. Heiz, and M. Arenz, "Size-selected clusters as heterogeneous model catalysts under applied reaction conditions.," *Physical chemistry chemical physics : PCCP*, vol. 12, pp. 10288–91, Sept. 2010.
- [66] F. F. Schweinberger, *Catalysis with supported size-selected Pt clusters*. New York: Springer International Publishing, 2014.
- [67] C. Langhammer, E. M. Larsson, B. Kasemo, and I. Zorić, "Indirect nanoplasmonic sensing: Ultrasensitive experimental platform for nanomaterials science and optical nanocalorimetry," *Nano Letters*, vol. 10, pp. 3529–3538, 2010.
- [68] N. Young, Z. Li, Y. Chen, S. Palomba, M. Di Vece, and R. Palmer, "Weighing Supported Nanoparticles: Size-Selected Clusters as Mass Standards in Nanometrology," *Physical Review Letters*, vol. 101, p. 246103, Dec. 2008.
- [69] R. Palmer, *Metal nanoparticles and nanoalloys*. Elsevier, 2012.
- [70] E. M. Larsson, C. Langhammer, I. Zorić, and B. Kasemo, "Nanoplasmonic probes of catalytic reactions.," *Science*, vol. 326, pp. 1091–1094, 2009.

- [71] E. M. Larsson, J. Millet, S. Gustafsson, M. Skoglundh, V. P. Zhdanov, and C. Langhammer, "Real Time Indirect Nanoplasmonic in Situ Spectroscopy of Catalyst Nanoparticle Sintering," *ACS Catalysis*, vol. 2, pp. 238–245, Feb. 2012.
- [72] J. Moulijn, A. van Diepen, and F. Kapteijn, "Catalyst deactivation: is it predictable? What to do?," *Applied Catalysis A*, vol. 212, pp. 3–16, Apr. 2001.
- [73] Z. L. Wang, J. M. Petroski, T. C. Green, and M. A. El-Sayed, "Shape Transformation and Surface Melting of Cubic and Tetrahedral Platinum Nanocrystals," *The Journal of Physical Chemistry B*, vol. 102, pp. 6145–6151, Aug. 1998.
- [74] G. Guisbiers, G. Abudukelimu, and D. Hourlier, "Size-dependent catalytic and melting properties of platinum-palladium nanoparticles.," *Nanoscale research letters*, vol. 6, p. 396, Jan. 2011.
- [75] S. Abbet, K. Judai, L. Klinger, and U. Heiz, "Synthesis of monodispersed model catalysts using softlanding cluster deposition," *Pure and Applied Chemistry*, vol. 74, pp. 1527–1535, Jan. 2002.
- [76] F. Masini, P. Hernandez-Fernandez, D. Deiana, C. E. Strebler, D. N. McCarthy, A. Bodin, P. Malacrida, I. E. L. Stephens, and I. Chorkendorff, "Exploring the phase space of time of flight mass selected PtxY nanoparticles.," *PCCP*, July 2014.
- [77] M. Nesselberger, M. Roefzaad, R. F. Hamou, P. U. Biedermann, F. F. Schweinberger, S. Kunz, K. Schloegl, G. K. H. Wiberg, S. Ashton, U. Heiz, K. J. J. Mayrhofer, and M. Arenz, "The effect of particle proximity on the oxygen reduction rate of size-selected platinum clusters.," *Nature materials*, vol. 12, pp. 919–24, Oct. 2013.
- [78] S. I. Choi, S. Xie, M. Shao, J. H. Odell, N. Lu, H. C. Peng, L. Protsailo, S. Guerrero, J. Park, X. Xia, J. Wang, M. J. Kim, and Y. Xia, "Synthesis and characterization of 9 nm Pt-Ni octahedra with a record high activity of 3.3 A/mgPt for the oxygen reduction reaction," *Nano Letters*, vol. 13, pp. 3420–3425, 2013.
- [79] C. Chen, Y. Kang, Z. Huo, Z. Zhu, W. Huang, H. L. Xin, J. D. Snyder, D. Li, J. a. Herron, M. Mavrikakis, M. Chi, K. L. More, Y. Li, N. M. Markovic, G. a. Somorjai, P. Yang, and V. R. Stamenkovic, "Highly crystalline multimetallic nanoframes with three-dimensional electrocatalytic surfaces.," *Science*, vol. 343, pp. 1339–43, 2014.

- [80] I. E. L. Stephens, A. S. Bondarenko, L. Bech, and I. Chorkendorff, "Oxygen Electroreduction Activity and X-Ray Photoelectron Spectroscopy of Platinum and Early Transition Metal Alloys," *ChemCatChem*, vol. 4, pp. 341–349, Mar. 2012.
- [81] M. Oezaslan, M. Heggen, and P. Strasser, "Size-dependent morphology of dealloyed bimetallic catalysts: linking the nano to the macro scale.," *Journal of the American Chemical Society*, vol. 134, pp. 514–24, Jan. 2012.
- [82] D. Wang, H. L. Xin, R. Hovden, H. Wang, Y. Yu, D. A. Muller, F. J. Disalvo, and H. D. Abruna, "Structurally ordered intermetallic platinum-cobalt core-shell nanoparticles with enhanced activity and stability as oxygen reduction electrocatalysts.," *Nature materials*, vol. 11, pp. 1–7, Oct. 2012.
- [83] D. Wang, Y. Yu, H. L. Xin, R. Hovden, P. Ercius, J. a. Mundy, H. Chen, J. H. Richard, D. A. Muller, F. J. Disalvo, and H. D. Abruna, "Tuning Oxygen Reduction Reaction Activity via Controllable Dealloying: A Model Study of Ordered Cu(3)Pt/C Intermetallic Nanocatalysts.," *Nano letters*, Sept. 2012.
- [84] F. Wang, R. Egerton, and M. Malac, "Fourier-ratio deconvolution techniques for electron energy-loss spectroscopy (EELS).," *Ultramicroscopy*, vol. 109, pp. 1245–9, Sept. 2009.
- [85] J. Suntivich, Z. Xu, C. E. Carlton, J. Kim, B. Han, S. W. Lee, N. Bonnet, N. Marzari, L. F. Allard, H. A. Gasteiger, K. Hamad-Schifferli, and Y. Shao-Horn, "Surface Composition Tuning of Au-Pt Bimetallic Nanoparticles for Enhanced Carbon Monoxide and Methanol Electro-oxidation.," *Journal of the American Chemical Society*, vol. 135, pp. 7985–91, May 2013.
- [86] A. A. Herzing, M. Watanabe, J. K. Edwards, M. Conte, Z.-R. Tang, G. J. Hutchings, and C. J. Kiely, "Energy dispersive X-ray spectroscopy of bimetallic nanoparticles in an aberration corrected scanning transmission electron microscope," *Faraday Discussions*, vol. 138, p. 337, 2008.
- [87] G. J. Hutchings and C. J. Kiely, "Strategies for the Synthesis of Supported Gold Palladium Nanoparticles with Controlled Morphology and Composition," *Accounts of chemical research*, vol. 46, pp. 1759–1772, Apr. 2013.
- [88] J. C. Russ, *The image processing handbook*. CRC/Taylor and Francis, 2007.
- [89] P. Hernandez-Fernandez, F. Masini, D. N. McCarthy, C. E. Strebler, D. Friebel, D. Deiana, P. Malacrida, A. Nierhoff, A. Bodin, A. M. Wise, J. H. Nielsen, T. W. Hansen, A. Nilsson, I. E. L. Stephens, and I. Chorkendorff, "Mass-selected nanoparticles of Pt_xY as model catalysts for oxygen electroreduction," *Nature Chemistry*, vol. 6, pp. 732–738, July 2014.

-
- [90] H. L. Wu, S. Yau, and M. S. Zei, "Crystalline alloys produced by mercury electrodeposition on Pt(111) electrode at room temperature," *Electrochimica Acta*, vol. 53, pp. 5961–5967, Aug. 2008.
- [91] B. C. Gumlnski, "The Hg-Pd (Mercury-Palladium) system," *Journal of Phase Equilibria*, vol. 11, no. 1, pp. 22–26, 1990.
- [92] J. Perez-Omil, *PhD thesis*. PhD thesis, University of Cadiz, Spain, 1994.
- [93] S. Bernal, F. Botana, J. Calvino, C. Lopez-Cartes, J. Perez-Omil, and J. Rodriguez-Izquierdo, "The interpretation of HREM images of supported metal catalysts using image simulation: profile view images," *Ultramicroscopy*, vol. 72, pp. 135–164, 1998.

Included papers

High Sintering Resistance of Size-Selected Platinum Cluster Catalysts by Suppressed Ostwald Ripening

Kristina Wettergren,^{†,‡} Florian F. Schweinberger,^{‡,‡} Davide Deiana,[§] Claron J. Ridge,[‡] Andrew S. Crampton,[‡] Marian D. Rötzer,[‡] Thomas W. Hansen,[§] Vladimir P. Zhdanov,^{†,||} Ueli Heiz,^{*,‡} and Christoph Langhammer^{*,†}

[†]Department of Applied Physics, Chalmers University of Technology, 41296 Göteborg, Sweden

[‡]Chair of Physical Chemistry, Catalysis Research Center and Chemistry Department, Technische Universität München, 85748 Garching, Germany

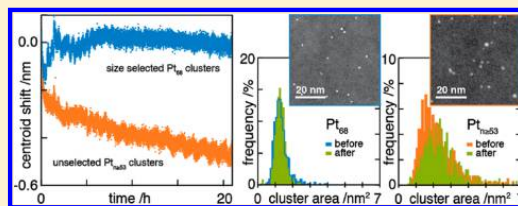
[§]Center for Electron Nanoscopy, Technical University of Denmark, 2800 Kongens Lyngby, Denmark

^{||}Boriskov Institute of Catalysis, Russian Academy of Sciences, Novosibirsk 630090, Russia

Supporting Information

ABSTRACT: Employing rationally designed model systems with precise atom-by-atom particle size control, we demonstrate by means of combining noninvasive in situ indirect nanoplasmonic sensing and ex situ scanning transmission electron microscopy that monomodal size-selected platinum cluster catalysts on different supports exhibit remarkable intrinsic sintering resistance even under reaction conditions. The observed stability is related to suppression of Ostwald ripening by elimination of its main driving force via size-selection. This study thus constitutes a general blueprint for the rational design of sintering resistant catalyst systems and for efficient experimental strategies to determine sintering mechanisms. Moreover, this is the first systematic experimental investigation of sintering processes in nanoparticle systems with an initially perfectly monomodal size distribution under ambient conditions.

KEYWORDS: Size-selected clusters, indirect nanoplasmonic sensing, sintering resistance, Ostwald ripening, platinum



Metal nanoparticles and clusters are characterized by size-dependent properties, high surface area to volume ratio, and a large number of low coordination sites. This makes them highly desirable as active components in catalytic reactions and other applications.^{1–4} However, the high number of low coordination sites also significantly destabilizes such particles and makes them prone to sintering. The resulting loss of active surface area and activity is a major problem causing substantial unwanted catalyst regeneration cost.⁵ Combined with dwindling supplies of precious metals and increasing demand, this makes finding strategies for the rational design of sintering resistant catalyst systems increasingly urgent. Corresponding state-of-the-art experimental studies^{6–10} aiming at determining the underlying sintering mechanism, which is key to the rational design of more sintering resistant catalyst systems, have been limited to (with few exceptions^{11,12}) catalysts characterized by a relatively wide distribution of particle sizes as the starting point.

In the field there is agreement that sintering of supported metal nanoparticles can occur via two principal mechanisms: (i) particle migration and coalescence and (ii) Ostwald ripening.^{6,11,13–17} Sintering via particle migration involves Brownian motion of particles on the surface, facilitated by relatively weak particle–support interactions and consequent coalescence when two particles end up in close proximity. Ostwald ripening

is mechanistically described as larger particles growing at the expense of smaller ones due to the size-dependent difference in surface energy.^{16,17} In the latter case, mass transport between shrinking and growing particles is governed by detachment of species (typically atoms or complexes with reactants^{16,17}) from small particles with high chemical potential, diffusion on the support (or in the gas phase), and finally followed by attachment to larger particles with lower chemical potential. Thus, in principle, these steps can be suppressed by using particles with identical size that have a reasonably strong interaction with their support (i.e., diffusion barrier) at the considered temperature.

Herein, this prediction is experimentally investigated, and its implications for the rational design of sintering resistant catalysts are rigorously verified. Thus, this is the first demonstration of a generic design strategy for sintering resistant catalysts and other nanoparticle-based materials systems such as colloidal nanoparticles, materials synthesized by precipitation methods and all nanomaterials under thermal stress, which is directly derived from the fundamental understanding of the sintering mechanism. Consequently, the

Received: July 15, 2014

Revised: August 31, 2014



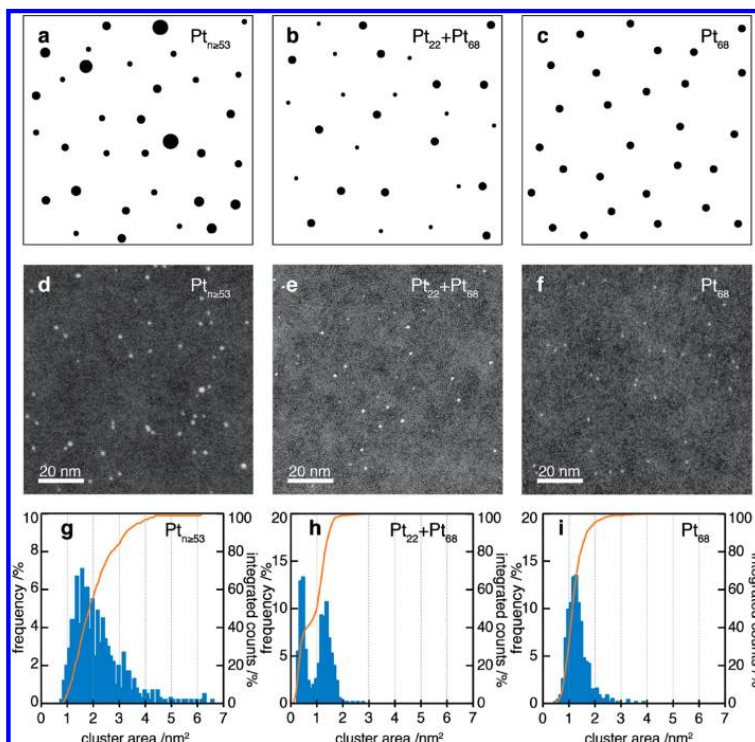


Figure 1. Size-selected Pt cluster model systems for sintering experiments. Top: Schematic representation of unselected $\text{Pt}_{n \geq 53}$ clusters with 53 or more atoms (A); size-selected $\text{Pt}_{22} + \text{Pt}_{68}$ clusters with symmetric bimodal particle size distribution (PSD) (B); and size-selected Pt_{68} clusters with monomodal PSD (C). Middle: Excerpts ($100 \times 100 \text{ nm}^2$) of HAADF-STEM images with soft-landed Pt clusters on Si_3N_4 supports prior to sintering (D–F). Bottom: Corresponding PSDs (at least 500 particles) of the projected cluster areas normalized to relative frequencies. $\text{Pt}_{n \geq 53}$ shows a typical broad PSD of unselected clusters (G). For $\text{Pt}_{22} + \text{Pt}_{68}$ two peaks (H) and for Pt_{68} one distinct peak (I) corresponding to the distinct respective sizes are seen. The deviations from perfect δ -function PSDs in panels H and I are related to different clusters isomers, as well as thresholding effects in STEM image analysis. The orange lines show the integrated frequency.

successful concept implementation shown here also constitutes the first direct verification of the Ostwald ripening mechanism under nonidealized conditions.

To construct model systems with direct relevance for heterogeneous catalysis for our experiments, we deposit soft-landed Pt clusters on flat amorphous Si_3N_4 with native oxide and sputter-deposited amorphous SiO_2 surfaces by using a field-controlled supersonic cluster source with atom-by-atom size control.¹⁸ This approach allows us to overcome the problem of wide size distributions as the starting point of a sintering experiment. We either (i) eliminate it by applying size-selection with accuracy down to a single atom (monomodal Pt_{68} clusters); (ii) deliberately create it by depositing a controlled bimodal distribution of size-selected clusters with two distinct sizes (bimodal $\text{Pt}_{22} + \text{Pt}_{68}$ clusters at 50% relative amounts); or (iii) produce a distribution of sizes by turning off the size-selection during deposition (polydisperse $\text{Pt}_{n \geq 53}$), as summarized in Figure 1. Importantly, we note that the implications of our findings made by employing size-selected clusters in the $n < 100$ atoms regime are not limited to that size range. In contrast, they are generic and directly applicable to larger (and more relevant for today's applications) particle sizes since they are derived directly from the physics of the sintering mechanism.

We use real-time indirect nanoplasmonic sensing (INPS)^{19–21} to monitor the sintering kinetics of our three model systems in situ, and ex situ scanning transmission electron microscopy (STEM) imaging before and after the respective treatment. INPS is a new in situ experimental technique, which, owing to its robustness in combination with a relatively simple setup, allows efficient screening of sintering processes with high temporal resolution at atmospheric (or higher pressures). In combination with ex situ STEM, our experimental approach thus constitutes a powerful platform for the study of sintering processes, where INPS can be used to identify the relevant sintering conditions and to obtain real-time kinetics in situ, and where the more advanced TEM analysis can be optimized to the most important samples and conditions. For the INPS measurements, “chips” comprising plasmonic gold nanodisks fabricated on a glass substrate^{19,22} and covered by a thin layer of dielectric material (10 nm Si_3N_4) mimicking the support of a real catalyst were used as sensors. The Pt clusters were deposited on these “chips” (Figure 2A). Upon illumination with low power polychromatic light the localized surface plasmon resonance (LSPR) in the Au disks is excited and acts as nanoscopic local probe of the Pt clusters on the Si_3N_4 layer via enhanced optical near fields. The change in LSPR wavelength of the Au disk sensors is proportional to the

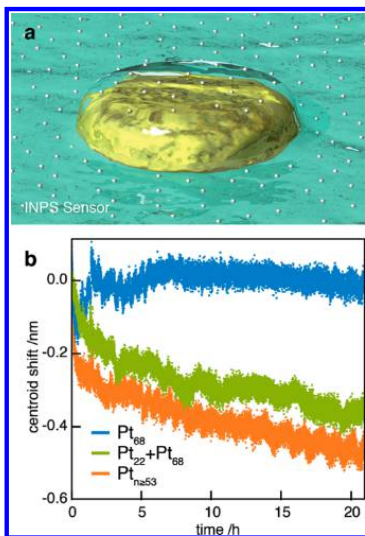


Figure 2. (A) Schematic illustration of an indirect nanoplasmonic sensor. The Pt clusters are probed in situ by the optical fields created by plasmon resonance in the Au nanoantenna. (B) INPS centroid shift (the center of mass of the top part of the LSPR “peak”, see Supporting Information for details) vs time in Ar at 453 K for unselected $Pt_{n>53}$, size-selected bimodal $Pt_{22} + Pt_{68}$, and size-selected monomodal Pt_{68} clusters. A negative centroid shift signifies sintering.²¹ Inserting the cold samples into the hot reactor is the reason for the observed initially instabilities in INPS signal since temperature equilibration with the holder and desorption of, e.g., water, is registered by the sensor.

adjacent catalyst particle density and particle size on the dielectric layer.²¹ This readout is completely noninvasive, eliminating the risk for artifacts like, e.g., electron beam induced sintering of the clusters. Figure 2B shows the obtained real time in situ sintering kinetics in Ar at atmospheric pressure at 453 K after subtraction of a corresponding blank INPS chip reference measurement (Figure S2, Supporting Information) for the three different Pt cluster arrangements in Figure 1. These conditions are quite harsh for clusters in the $n < 100$ atoms size range since, e.g., the Hüttig temperature (where surface diffusion becomes important) for bulk Pt is of the order of 600 K and is expected to be much lower for clusters due to the size dependence of the melting temperature.²³

The INPS centroid shift signal is relatively stable during the entire experiment for the size-selected Pt_{68} clusters, whereas a distinct time-dependent negative centroid shift (indicating sintering²¹) is observed for both the unselected polydisperse $Pt_{n>53}$ and the size-selected bimodal $Pt_{22} + Pt_{68}$ clusters (Figure 2B). Thus, the in situ INPS measurements clearly show that the size-selected Pt_{68} clusters do not sinter at the applied conditions, in contrast to both the unselected $Pt_{n>53}$ sample and the size-selected $Pt_{22} + Pt_{68}$ sample with bimodal particle size distribution (PSD).

To corroborate these results, we performed ex situ STEM image analysis. We used cluster samples identical to those on the INPS chips but deposited on Si_3N_4 TEM windows²⁴ and treated them simultaneously. The corresponding PSDs together with representative difference histograms to highlight changes in the PSD are shown in Figure 3. They confirm that size-selected Pt_{68} clusters do not sinter significantly under the

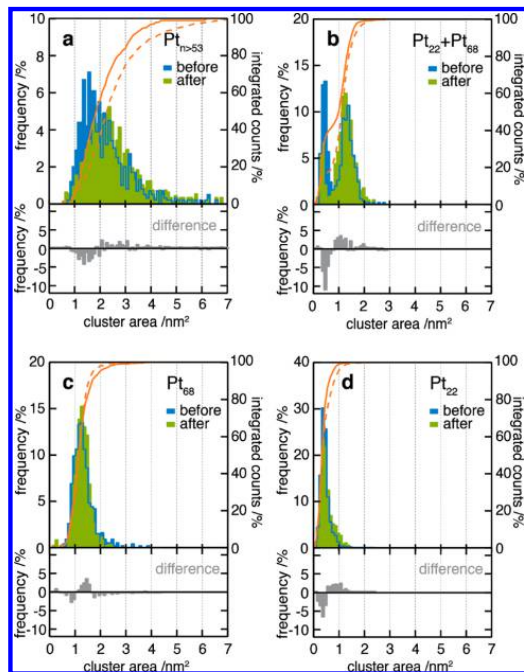


Figure 3. Analysis of STEM micrographs before and after 21 h in Ar at 453 K. Area histograms (minimum 500 clusters) normalized to relative frequencies and corresponding integrated counts (orange line before; orange dashed line after) are shown together with a difference histogram to highlight changes in the PSD. Data for (A) unselected $Pt_{n>53}$, (B) bimodal size-selected $Pt_{68} + Pt_{22}$, (C) monomodal size-selected Pt_{68} , and (D) monomodal size-selected Pt_{22} are shown. Significant changes can be observed after treatment for the unselected (A) and bimodal (B) samples, whereas the monomodal size selected Pt_{68} (C) and Pt_{22} (D) clusters are more-or-less intact.

applied conditions (no change in cluster area), whereas the unselected $Pt_{n>53}$ and size-selected bimodal $Pt_{22} + Pt_{68}$ clusters exhibit the features inherent to significant sintering.

These results demonstrate a surprisingly high sintering resistance of the size-selected Pt_{68} clusters. Moreover, they also allow us to identify (i) the sintering mechanism for the two samples exhibiting sintering ($Pt_{n>53}$ and $Pt_{22} + Pt_{68}$), and (ii) the reason for the observed sintering resistance of size-selected Pt_{68} . Apparently, size-selection alone is not enough to prevent sintering if several particle sizes are present since both the bimodal combination of size-selected clusters ($Pt_{22} + Pt_{68}$) and the clusters with a broad and continuous PSD ($Pt_{n>53}$) display distinct sintering kinetics. This is perfectly in line with the Ostwald ripening mechanism where the different chemical potential of particles with different size provides the driving force for sintering. This driving force can be eliminated only if a single size of particles is present, that is, if the particles exhibit a truly monomodal PSD. This conclusion is further backed by a detailed look at the PSDs for the bimodal $Pt_{22} + Pt_{68}$ sample (Figure 3B). The number of Pt_{22} clusters decreases significantly, and their mean area is shrinking, whereas the fraction of larger clusters around Pt_{68} increases, as expected for Ostwald ripening. We also note that the observed slight apparent increase in the number of particles with a size in

between the initial two sizes can be ascribed to shape changes of different cluster isomers (formed during deposition under the applied soft landing conditions) toward more spherical particles during the heat treatment. This effect can, in some cases, actually lead to a smaller projected area despite increasing size (volume). Moreover, as summarized in Table S1 in the Supporting Information, the particle number density remains basically constant before and after our treatment for all samples. This further supports our hypothesis of Ostwald ripening being the dominant sintering mechanism to be considered here since Ostwald ripening at an early stage is characterized by a change in the PSD with maintained number density of particles, while particle migration always gives rise to a decrease in the particle number density.

To rule out particle migration of Pt₂₂ as the reason for the observed sintering of the bimodal Pt₂₂ + Pt₆₈ sample, an additional sample consisting of only size-selected Pt₂₂ clusters was analyzed (Figure 3D), confirming that even the much smaller Pt₂₂ clusters exhibit a surprising sintering resistance (a small amount of sintering is apparent from the difference histogram, however, much smaller than seen in the bimodal Pt₂₂ + Pt₆₈ sample). Remarkably, this is the case even though the surface number density is five times higher for the Pt₂₂ compared to the other three systems (Figure S3 and Table S1, Supporting Information), indicating that particle surface density is not very important, in particular as it remains constant. As a general remark we also want to stress at this point that image analysis of Pt₂₂ clusters truly is at the limit of what is feasible in a reliable way on the used TEM surfaces. Therefore, slight variations between data sets (i.e., before and after treatment) in terms of, e.g., threshold/brightness, cannot be completely excluded and may be partly responsible for the observed apparent small amount of sintering of the Pt₂₂. Thus, in summary our analysis still clearly shows that size-selected clusters, even deep within the nonscalable size regime where the physical properties depend on the exact number of atoms in the cluster, do not sinter (or only surprisingly little) under the applied conditions, unless they are paired with a second population of particles with different size to provide the driving force for Ostwald ripening.

This driving force is the excess surface energy of nanoparticles and clusters. For spherical particles, it can be expressed as $E = 4\pi R^2\gamma$, where R is the particle radius, and γ is the surface energy per unit area. In combination with the expression for the number of atoms in a particle, $n = (4\pi/3)R^3/\nu$ (R is a particle radius, and ν is the atomic volume in the bulk), this expression predicts that the corresponding change of free energy during attachment or detachment of a (metal) atom to or from a particle is $\Delta E(R) = 2\gamma\nu/R$ or $\Delta E(n) = A/n^{1/3}$, respectively, where $A = 2(4\pi/3)^{1/3}\gamma\nu^{2/3}$. On average, this Gibbs–Thomson phenomenology has been confirmed for Pt group metal clusters by recent DFT calculations.^{25,26} Historically, it has been used to describe Ostwald ripening of supported metal nanoparticles with 2D diffusion, attachment, and detachment of monomers.^{13,14} The details depend on whether the attachment is diffusion- or kinetically controlled. In our context, the key general predictions are the same in both cases. In the kinetically controlled regime, for example, one has²⁷

$$\frac{dR}{dt} = \frac{K}{R} \exp\left(-\frac{E_{\text{tot}}}{k_{\text{B}}T}\right) \left[\exp\left(\frac{\Delta E(R_{*})}{k_{\text{B}}T}\right) - \exp\left(\frac{\Delta E(R)}{k_{\text{B}}T}\right) \right] \quad (1)$$

where E_{tot} is the metal bulk sublimation enthalpy minus the adsorption energy of a monomer on the support plus the attachment activation energy of a monomer on the support, R_{*} is the critical radius ($1/R_{*}$ is close to the average of $1/R$), and K is a constant. According to this equation, the particles with $R < R_{*}$ shrink, while those with $R > R_{*}$ grow. Thus, if all particle sizes are equal, i.e., $R = R_{*}$ (or $n = n_{*}$), the sintering rate dR/dt , defined by eq 1, is equal to zero. Notably, this conclusion is also valid if the size-dependence of the excess free energy is significantly stronger or weaker (e.g., due to the existence of closed-shell clusters) than predicted by the Gibbs–Thomson model.²⁷ Mechanistically, this implies that on size-selected monomodal nanoparticles, the rates at which monomers detach from and attach to a particle are the same, and effectively, no sintering is taking place. In practice, this means that the sintering kinetics is now controlled by fluctuations of n around n_{*} . This slow regime of sintering can be maintained (as confirmed by our complementary Monte Carlo simulations mentioned in the Supporting Information) as long as the size (or n) distribution is narrow. The corresponding time scale may be much longer than when the initial PSD is not perfectly monomodal, in agreement with our experimental observations.

To further challenge the observed sintering resistance of monomodal size-selected clusters, we exposed a Pt₆₈ sample on SiO₂ support with a four times higher cluster surface coverage (see Table S1, Supporting Information) to the exothermic ($\Delta H = -250$ kJ/mol) Pt-catalyzed hydrogen oxidation reaction. The used SiO₂ surfaces were sputter deposited onto the TEM membrane and have an amorphous structure. Moreover, they are known to be significantly more defective than both the PE-CVD Si₃N₄ film used on the INPS chips and the Si₃N₄ TEM window membrane. Thus, using these sputtered SiO₂ supports constitutes a means to alter the surface structure in a first simple attempt to explore the importance of the oxide support for the observed sintering resistance. Five ramps (6 K/min, $T_{\text{end}} = 533$ K) were run on the sample, each of which was followed by cooling to room temperature in the reactant mixture (reactant flow rate of 1000 mL/min, corresponding to 3.4 cm/s plug flow velocity) and total reactant concentration of 4% at atmospheric pressure. Since cooling is very slow in our system, the samples have been above the sintering temperature used for the Ar experiments for ca. 5 h in total. Even though this is shorter than the 20 h in the Ar experiments, looking at the INPS curves in Figure 2 shows that after 5 h ca. 70% of the total recorded sintering has been completed for the samples that actually sinter. This indicates that, if significant sintering would take place on the size-selected samples during the hydrogen oxidation reaction, we should have been able to resolve it in our analysis, despite the shorter exposure to high temperature. Moreover, the 533 K does not include the large exothermicity of the hydrogen oxidation reaction ($\Delta H = -250$ kJ/mol) but refers to the nominal gas temperature upstream of the sample only. This means that the actual cluster temperature during reaction locally might have been significantly higher than 533 K and sustained for additional time than the nominal ca. 5 h (in principle until the reaction is no longer self-sustaining via the dissipated reaction heat).

The reactant ratio was $[H_2]/([H_2] + [O_2]) = 0.45$, which, as we have shown before,²⁰ operates the catalyst close to the maximal reaction rate and under oxidizing conditions at the surface. Since oxygen/hydrogen mixtures promote sintering of Pt catalysts,¹⁷ this is a harsher treatment than the previous

experiments in argon. The resulting STEM analysis is shown in Figure 4. In addition to the Pt_{68} peak, there is a small peak at

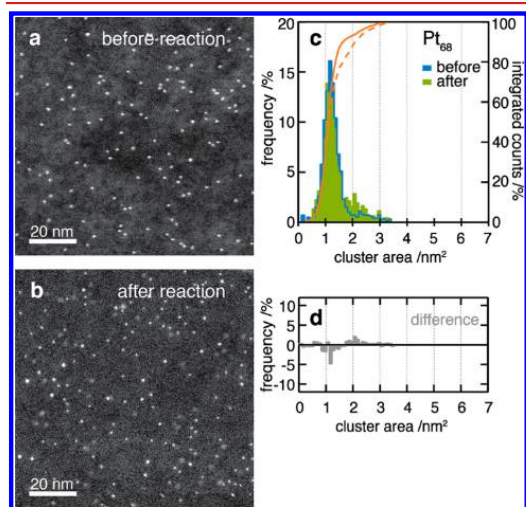


Figure 4. Effect of the hydrogen oxidation reaction on monomodal size-selected Pt_{68} clusters on SiO_2 support. Representative STEM images before (A) and after (B) reaction. Corresponding area histograms of the Pt_{68} samples before and after (C) treatment including integrated counts (orange line before; orange dashed line after). An additional peak (seen here more clearly due to an about four times higher coverage) with low abundance at roughly double the area corresponds to doubly sized clusters with the mass of a dimer. (D) Difference histogram for before and after treatment to highlight changes in the PSD.

roughly double the area corresponding to doubly sized clusters that are formed during cluster deposition²⁸ and is seen more clearly here due to the four times higher coverage compared to the samples used for sintering in Ar only. We note that apparent dimer sizes smaller than the expected double size corresponding to Pt_{136} are caused by isomers with different shapes and thus different projected areas. Comparing the histograms reveals a slight increase of larger sized clusters and a slight decrease of the main Pt_{68} peak after treatment. This fits with our previous analysis for the bimodal $Pt_{68} + Pt_{22}$ sample, i.e., that the availability of a small number of doubly sized clusters provides a small driving force for sintering. The effect is, however, very small due to their low abundance. Thus, despite both higher Pt cluster loading (increased proximity of the clusters) and harsher reaction conditions, only very little sintering is observed. It could probably be completely eliminated at the time scale under consideration by avoiding the deposition of double sized clusters.

In conclusion, we have demonstrated an impressive sintering resistance of monomodal size-selected Pt clusters on Si_3N_4 and SiO_2 supports during exposure to high temperature at atmospheric pressure in Ar, as well as in the sintering-promoting hydrogen oxidation reaction. As the reason we identify the efficient suppression of Ostwald ripening by elimination of its main driving force through size selection of the catalyst particles. This becomes possible due to the unique design of the used model systems featuring ultimate atomic control of particle size. Our study is thus the first

demonstration of a design strategy for sintering resistant supported nanoparticle systems, which is entirely based on the physics behind the sintering mechanism. It also suggests that the observed sintering resistance effect is present in larger nanoparticle systems since the reason for the observed sintering resistance is of fundamental nature and thus generic. This makes our findings highly relevant for real applications in today's catalyst systems where metal nanoparticles in the few nm size range (rather than the $n < 100$ atom clusters considered here) are employed. We also anticipate that the sintering resistance will prevail to higher temperatures for larger nanoparticles since they generally feature both lower surface energies and higher melting and thus Hüttig/Tammann temperatures. Finally, the found sintering resistance of size-selected clusters in the nonscalable size regime also clearly illustrates that such structures indeed may constitute a unique tool for atom-by-atom engineering of catalytic properties in real applications in the future.

Methods. INPS and TEM Sample Surface Preparation.

The INPS samples consisted of borofloat glass pieces ($15 \times 15 \text{ mm}^2$) patterned with quasi-random arrays of gold nanodisks (diameter = 80 nm; height = 20 nm) using hole-mask colloidal lithography.²² After fabrication, the gold nanoparticles were heat treated for 3 h in air at 888 K to make them thermally stable through recrystallization. After the heat treatment, 10 nm of Si_3N_4 was plasma-enhanced chemically vapor deposited (PE-CVD, STS) onto the gold nanoparticles. The PE-CVD deposition process yields an amorphous Si_3N_4 film, as verified by TEM electron diffraction. The PE-CVD growth process was followed by a second heat treatment of the complete INPS sensor at 888 K in air for 36 h to stabilize the Si_3N_4 layer and produce a native surface oxide. This layer was grown in an attempt to generate the best possible compatibility in terms of surface chemistry between the TEM samples and the INPS ones. The used TEM windows were fabricated according to the recipe introduced by Grant et al.²⁴ and feature an oxidized Si_3N_4 surface (the membrane itself).

To introduce a second type of surface for the hydrogen oxidation experiments, we deposited an additional RF-sputtered (FHR MS150 sputter system) 10 nm thick SiO_2 layer onto the TEM windows prior to cluster deposition. As verified by electron diffraction, the sputtered 10 nm SiO_2 layer is amorphous. Moreover, it is known to be significantly more defective than both the PE-CVD Si_3N_4 film used on the INPS chips and the Si_3N_4 TEM window membrane.

Pt Cluster Deposition. The clusters were deposited on the INPS samples and TEM windows described above using a high frequency laser ablation cluster source and a transfer chamber, described in detail elsewhere.^{18,29} Briefly, the beam of a diode pumped Nd:YAG laser (InnoLas, Germany; DPSS Spitlite, 100 Hz, 70 mJ at 532 nm) was focused onto a rotating (1 Hz) metal target (99.99% Pt, Goodfellow, USA). Cooling of the resulting plasma was achieved by a delayed helium (He 6.0, Westfalen, Germany) gas pulse and afterwards an adiabatic expansion of the helium platinum vapor through a nozzle into the vacuum.

Ion lenses and an octupole subsequently guided the cluster beam along the axis of the differentially pumped vacuum chamber until the positively charged clusters were separated from the neutral ones in a quadrupole bender. The deflector was operated in such a way that the cationic clusters were focused into a QMS (ABB Extrel Merlin, U.S.A.) with a mass limit of 16 000 amu where mass selection down to a single cluster size is achieved. The QMS was operated and optimized

for highest transmission while still ensuring size selection down to a single mass. Using only the radiofrequency (RF only mode) of the QMS, it was operated as a high-pass mass filter, and consequently, unselected clusters with a tunable minimum size (in the presented study 53 atoms, short $Pt_{n \geq 53}$) were generated. After size selection the beam passed through an aperture of 9 mm and was focused onto the substrates (INPS chip or TEM window). The clusters were deposited under soft-landing conditions on the support, i.e., at deposition energies lower than 2 eV per cluster. Because of the nonconductive nature of the used samples (both INPS samples and TEM windows) neutralization of the positive charges on the support was achieved by means of an electron shower.³⁰ For this purpose a Ta-filament, typically operated at 4 A and 10 V, resulting in a constant electron flux of around 250 pA, provided electrons and was tuned in such a way that it overcompensated the arriving charges. Recording the discharge current on the support (coverage reported in the unit charges per area: e/nm^2), when turning off the electron shower for a short interval of time during deposition, the coverage of the deposited clusters was estimated. Having very stable cluster current over the course of the deposition period allowed for comparable coverage on the different samples, see statistics of the STEM micrographs shown in the Supporting Information.

Sintering and Hydrogen Oxidation Experiments. At the start of each sintering experiment the reactor was preheated to the sintering temperature (453 K), and then the INPS sample and the corresponding TEM window were inserted into the hot reactor in order to be able to trace potential fast initial sintering directly (not blurred by a heating ramp). The procedure of inserting the (cold) samples into the hot reactor is the reason for the observed initially slightly unstable INPS signal in all three sintering experiments (Figure 2) since both the necessary temperature equilibration of the sample and most importantly the sample holder (see Figure S1, Supporting Information, for the specifics of the setup) with the reactor and desorption of water from the sample surface are registered by the sensor during the initial stage of the experiment. The Ar flow rate (Ar 6.0, 99.9999% purity, AGA, Sweden) during sintering was 200 mL/min. To obtain the INPS centroid shift induced by the cluster sintering and to correct for instabilities/fluctuations/temperature equilibration effects of the measurement setup, a measurement obtained from a blank INPS sensor was subtracted from the cluster measurements. The corresponding raw data used in this way to obtain the sintering kinetics shown in Figure 2 are presented in Figure S2 in the Supporting Information.

For the hydrogen oxidation experiments, the gas flow rate was 1000 mL/min and the total reactant concentration was 4%, at a reactant ratio of $[H_2]/([H_2] + [O_2]) = 0.45$. The experiments consisted of running a total of five temperature ramps (6 K/min) in the gas mixture up to 533 K, and then cooling back to room temperature in the reactant mixture.

Local Structural Characterization (STEM) and Image Analysis. Scanning transmission electron microscopy measurements were performed at DTU Cen in a FEI Titan Analytical 80–300 equipped with a CEOS Cescor probe spherical aberration corrector and operated at 300 kV accelerating voltage. Within each specimen, the analysis was carried out with the same microscope condition and constant acquisition dwell time and HAADF detector settings.

The analysis of the TEM micrographs was performed using an algorithm of in-house design based on the IGOR Pro 6.22

Particle Analysis Tool (Wavemetrics, USA).³⁰ The shown statistics for the (projected) cluster area, i.e., area distribution functions (ADF) are the results of the analysis of multiple images (at least three) and are based on the analysis of at least 500 particles per sample type (counting each size as well as before and after separately). Representative STEM micrographs for all samples before and after treatment (in Ar at 453 K for 21 h) are shown in Figure S3, Supporting Information. In Figure S4, Supporting Information, the histograms of the size-selected Pt_{22} before and after sintering treatment are shown for easy comparison.

■ ASSOCIATED CONTENT

Supporting Information

INPS and TEM window sample preparation, INPS measurement setup, kinetic Monte Carlo simulations of cluster ripening, and additional STEM material. This material is available free of charge via the Internet at <http://pubs.acs.org>.

■ AUTHOR INFORMATION

Corresponding Authors

*(U.H.) E-mail: ulrich.heiz@mytum.de.

*(C.L.) E-mail: clangham@chalmers.se.

Author Contributions

[†](K.W. and F.F.S.) These authors contributed equally to this work. The manuscript was written through contributions of all authors. All authors have given approval to the final version of the manuscript

Notes

The authors declare no competing financial interest.

■ ACKNOWLEDGMENTS

We acknowledge the Swedish Research Council Project 2010-4041 (C.L., K.W.), the Swedish Foundation for Strategic Research Framework Program RMA11-0037 (C.L.) and the Chalmers Area of Advance for Nanoscience and Nanotechnology (C.L.), as well as by the DFG through the Nanosystems Initiative Munich (NIM) (F.F.S., C.J.R., A.S.C. and U.H.), an ERC Advanced Grant (ERC-2009-AdG 246645-ASC3) (A.S.C., M.D.S. and U.H.) and DFG (Project He 3454/9-2) (F.F.S. and U.H.).

■ REFERENCES

- (1) Dahl, S.; Logadottir, A.; Egeberg, R. C.; Larsen, J. H.; Chorkendorff, I.; Törnqvist, E.; Norskov, J. K. *Phys. Rev. Lett.* **1999**, *83*, 1814–1817.
- (2) Behrens, M.; Studt, F.; Kasatkin, I.; Kühl, S.; Hävecker, M.; Abild-Pedersen, F.; Zander, S.; Girgsdies, F.; Kurr, P.; Knief, B.-L.; Tovar, M.; Fischer, R. W.; Norskov, J. K.; Schlögl, R. *Science* **2012**, *336*, 893–897.
- (3) Roduner, E. *Chem. Soc. Rev.* **2006**, *35*, 583–592.
- (4) Zhu, W.; Michalsky, R.; Metin, Ö.; Lv, H.; Guo, S.; Wright, C. J.; Sun, X.; Peterson, A. A.; Sun, S. J. *Am. Chem. Soc.* **2013**, *135*, 16833–16836.
- (5) Bartholomew, C. H.; Farrauto, R. J. *Fundamentals of Industrial Catalytic Processes*, 2nd ed.; John Wiley & Sons: New York, 2005.
- (6) Hansen, T. W.; DeLaRiva, A. T.; Challa, S. R.; Datye, A. K. *Acc. Chem. Res.* **2013**, *46*, 1720–1730.
- (7) Benavidez, A. D.; Kovarik, L.; Genc, A.; Agrawal, N.; Larsson, E. M.; Hansen, T. W.; Karim, A. M.; Datye, A. K. *ACS Catal.* **2012**, *2*, 2349–2356.
- (8) Simonsen, S. B.; Chorkendorff, I.; Dahl, S.; Skoglundh, M.; Sehested, J.; Helveg, S. *J. Am. Chem. Soc.* **2010**, *132*, 7968–7975.

- (9) Morgenstern, K.; Rosenfeld, G.; Comsa, G. *Surf. Sci.* **1999**, *441*, 289–300.
- (10) Clausen, B. S.; Grabaek, L.; Topsøe, H.; Hansen, L. B.; Stoltze, P.; Norskov, J. K.; Nielsen, O. H. *J. Catal.* **1993**, *141*, 368–379.
- (11) Fukamori, Y.; König, M.; Yoon, B.; Wang, B.; Esch, F.; Heiz, U.; Landman, U. *ChemCatChem* **2013**, *5*, 3330–3341.
- (12) Popescu, R.; Schneider, R.; Gerthsen, D.; Böttcher, A.; Löffler, D.; Weis, P.; Kappes, M. M. *Surf. Sci.* **2009**, *603*, 3119–3125.
- (13) Wynblatt, P.; Gjostein, N. A. *Acta Metall.* **1976**, *24*, 1165–1174.
- (14) Wynblatt, P.; Gjostein, N. A. *Prog. Solid State Chem.* **1975**, *9*, 21–58.
- (15) Kolmakov, A.; Goodman, D. W. *Chem. Rec.* **2002**, *2*, 446–457.
- (16) Parker, S. C.; Campbell, C. T. *Phys. Rev. B* **2007**, *75*, 035430.
- (17) Ouyang, R.; Liu, J.-X.; Li, W.-X. *J. Am. Chem. Soc.* **2013**, *135*, 1760–1771.
- (18) Heiz, U.; Vanolli, F.; Trento, L.; Schneider, W.-D. *Rev. Sci. Instrum.* **1997**, *68*, 1986–1994.
- (19) Langhammer, C.; Larsson, E. M.; Kasemo, B.; Zorić, I. *Nano Lett.* **2010**, *10*, 3529–3538.
- (20) Larsson, E. M.; Langhammer, C.; Zorić, I.; Kasemo, B. *Science* **2009**, *326*, 1091–1094.
- (21) Larsson, E. M.; Millet, J.; Gustafsson, S.; Skoglundh, M.; Zhdanov, V. P.; Langhammer, C. *ACS Catal.* **2012**, *2*, 238–245.
- (22) Fredriksson, H.; Alaverdyan, Y.; Dmitriev, A.; Langhammer, C.; Sutherland, D. S.; Zaech, M.; Kasemo, B. *Adv. Mater.* **2007**, *19*, 4297–4302.
- (23) Moulijn, J. A.; van Diepen, A. E.; Kapteijn, F. *Appl. Catal. A: Gen.* **2001**, *212*, 3–16.
- (24) Grant, A. W.; Hu, Q.-H.; Kasemo, B. *Nanotechnology* **2004**, *15* (9), 1175.
- (25) Kozlov, S. M.; Aleksandrov, H. A.; Goniakowski, J.; Neyman, K. M. *J. Chem. Phys.* **2013**, *139*, 084701.
- (26) Yudanov, I. V.; Metzner, M.; Genest, A.; Rosch, N. *J. Phys. Chem. C* **2008**, *112*, 20269–20275.
- (27) Campbell, C. T.; Parker, S. C.; Starr, D. E. *Science* **2002**, *298*, 811–814.
- (28) Abbet, S.; Judai, K.; Klinger, L.; Heiz, U. *Pure Appl. Chem.* **2002**, *74*, 1527–1535.
- (29) Kunz, S.; Hartl, K.; Nesselberger, M.; Schweinberger, F. F.; Kwon, G.; Hanzlik, M.; Mayrhofer, K. J. J.; Heiz, U.; Arenz, M. *Phys. Chem. Chem. Phys.* **2010**, *12*, 10288–10291.
- (30) Schweinberger, F. F. *Catalysis with Supported Size-Selected Pt Clusters*; Springer International Publishing: New York, 2014.

Mass-selected nanoparticles of Pt_xY as model catalysts for oxygen electroreduction

Patricia Hernandez-Fernandez¹, Federico Masini¹, David N. McCarthy¹, Christian E. Strebelt¹, Daniel Friebe², Davide Deiana³, Paolo Malacrida¹, Anders Nierhoff¹, Anders Bodin¹, Anna M. Wise², Jane H. Nielsen¹, Thomas W. Hansen³, Anders Nilsson², Ifan E. L. Stephens^{1*} and Ib Chorkendorff^{1*}

Low-temperature fuel cells are limited by the oxygen reduction reaction, and their widespread implementation in automotive vehicles is hindered by the cost of platinum, currently the best-known catalyst for reducing oxygen in terms of both activity and stability. One solution is to decrease the amount of platinum required, for example by alloying, but without detrimentally affecting its properties. The alloy Pt_xY is known to be active and stable, but its synthesis in nanoparticulate form has proved challenging, which limits its further study. Herein we demonstrate the synthesis, characterization and catalyst testing of model Pt_xY nanoparticles prepared through the gas-aggregation technique. The catalysts reported here are highly active, with a mass activity of up to 3.05 A mg_{Pt}⁻¹ at 0.9 V versus a reversible hydrogen electrode. Using a variety of characterization techniques, we show that the enhanced activity of Pt_xY over elemental platinum results exclusively from a compressive strain exerted on the platinum surface atoms by the alloy core.

Polymer electrolyte membrane fuel cells (PEMFCs) hold the potential to provide a zero-emission power source for future automotive applications. However, their widespread commercialization is hindered by the high loadings of Pt required to catalyse the oxygen reduction reaction (ORR) at the cathode^{1–4}. An order of magnitude increase in ORR mass activity (that is, current density per unit mass Pt) over state-of-the-art commercial pure Pt catalysts would bring the precious-metal loading in fuel cells to a similar level to that used for emission control in internal combustion engines^{3,5}. Some alloys of PtX (X = Co, Ni, Cu) show higher ORR activity in comparison to pure Pt (refs 1–4), but typically their long-term performance is compromised by their poor stability against dealloying^{6,7}. In recent years, progress has been made towards the stabilization of Pt-based catalysts^{8–12}. Even so, further improvements could be engendered by developing new Pt-based alloy catalysts that are active but inherently less prone to dealloying.

In collaboration with Nørskov, Rossmeisl and co-workers, we discovered a new catalyst that could bring us one step closer to this goal¹³. Pt₃Y exhibited the highest ORR activity ever measured on an extended polycrystalline surface, to the best of our knowledge only surpassed by single-crystal Pt₃Ni(111) (ref. 14). Subsequent studies from our laboratory show that extended surfaces of polycrystalline Pt₃Y, Pt₃Gd and Pt₃La also exhibited high ORR activity^{3,15,16}. The uniquely negative heat of formation of Pt–rare-earth alloys should provide them with greater kinetic stability than the more commonly tested alloys of Pt and late transition metals (LTMs)^{13,16,17}. This notion is supported by our own stability tests on extended surfaces¹⁶, as well as by those of Lim and co-workers on sputtered thin films^{18,19}.

To understand the effect of alloying on the ORR activity of Pt, we invoke the theoretical model developed by Nørskov, Rossmeisl and co-workers^{13,27}. The potential losses, or overpotential, for the ORR on pure Pt catalysts originate from the final step in the reaction,

the electroreduction of HO* to H₂O (where HO* is an adsorbed hydroxyl intermediate²⁰). Typically, Pt alloy ORR catalysts are encased by an overlayer of pure Pt; the less-noble metal will dissolve from the surface^{9,15,21–26}. Alloying Pt decreases the overpotential for the electroreduction of HO* to H₂O by weakening the binding to HO* (refs 13,14,24). The optimal catalyst should have an HO* binding that is ~0.1 eV weaker than that of Pt(111) (refs 3,27). Density functional theory (DFT) calculations originally suggested that the activity of Pt₃Y should be contingent on a substantial concentration of Y in the second surface layer¹³, that is from ligand effects^{24,28,29}. Nonetheless, subsequent experiments showed that the active phases of polycrystalline Pt₃Y and Pt₂Y are encased by an overlayer of pure Pt that is 3–4 monolayers thick¹⁵. The considerable thickness of these overlayers excludes the possibility that the enhanced ORR activity of Pt_xY is caused by ligand effects. Consequently, the underlying mechanism for the enhanced activity of Pt_xY alloys is still unclear.

One hypothesis that we proposed to test was that the activity results from strain effects³⁰, which can be exerted over at least ten atomic layers²⁵. For many Pt alloys, a compressive surface strain is the most probable cause of the enhanced ORR activity, as demonstrated for dealloyed PtCu_x (ref. 25). Given that Y has a larger covalent radius than Pt (ref. 31), one would intuitively expect a Pt overlayer on a Pt–Y alloy core to impose tensile strain on the Pt surface atoms. Even so, this notion is inconsistent with the ORR activity data, as a tensile strain would strengthen²⁵ rather than weaken the binding of Pt to HO*, which should lead to a higher overpotential for the ORR.

Thus far, the ORR activity of Pt_xY has only been demonstrated on extended polycrystalline surfaces and thin films^{13,15,18,19}. For Pt_xY to make an impact on PEMFCs, the catalyst needs to be synthesized in the nanoparticulate form. In the case of Pt_xY and other alloys of Pt and rare earths, such a task is not trivial, given the high affinity of rare-earth elements for oxygen³². There are

¹Center for Individual Nanoparticle Functionality, Department of Physics, Technical University of Denmark, Kgs Lyngby DK-2800, Denmark, ²SLAC National Accelerator Laboratory, 2575 Sand Hill Road, MS31, Menlo Park CA 94025, USA, ³Center for Electron Nanoscopy, Technical University of Denmark, Kgs Lyngby DK-2800, Denmark. *e-mail: ifan@fysik.dtu.dk; ibchork@fysik.dtu.dk

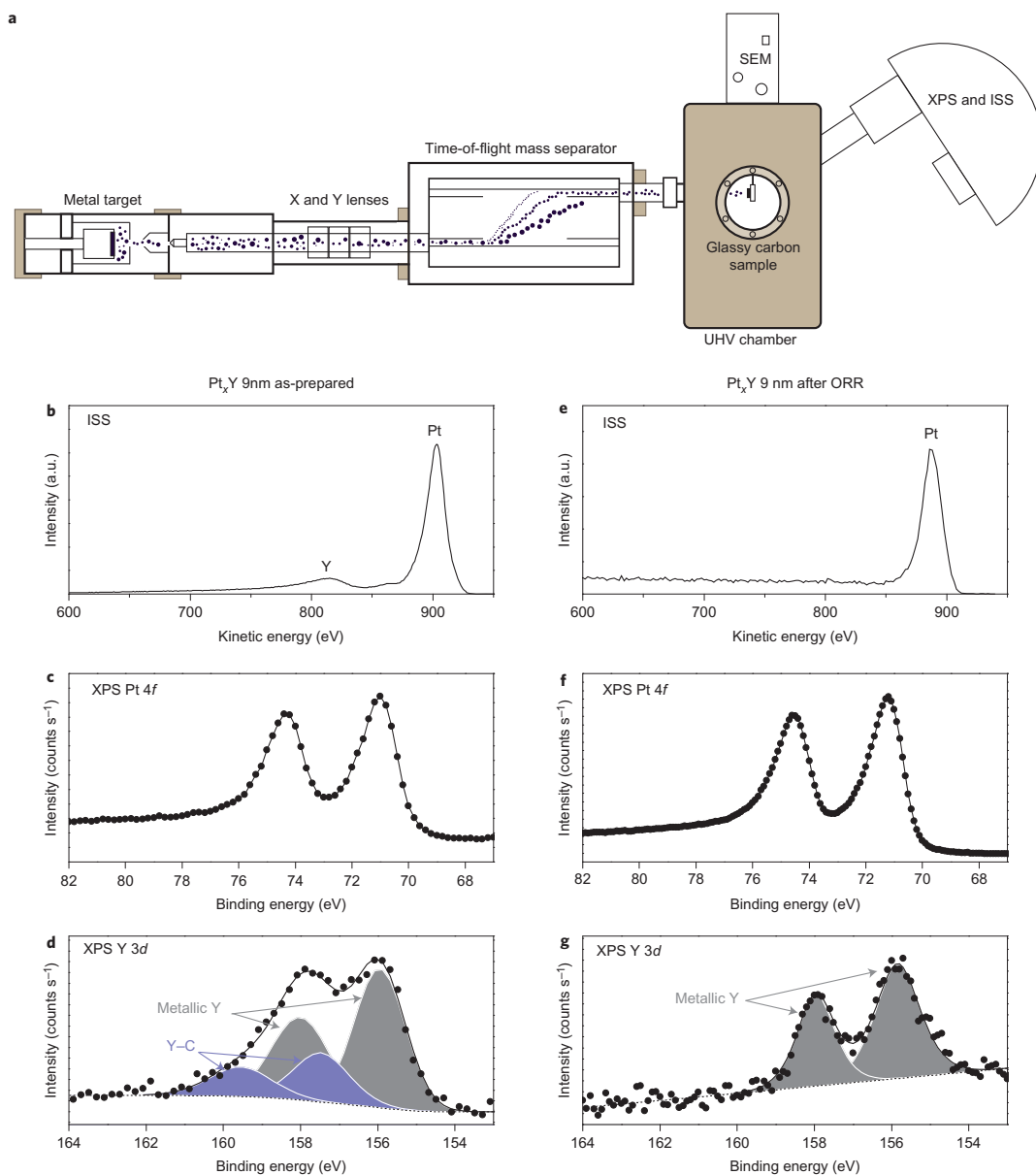


Figure 1 | Surface characterization of the Pt_xY nanoparticles before and after ORR activity measurements. **a**, Schematic representation of the cluster source. **b–d**, Representative surface characterization data for the as-prepared Pt_xY 9 nm particles. **e–g**, Equivalent data for the Pt_xY 9 nm particles following exposure to the ORR conditions. **b, e**, ISS spectra. **c, f**, Detailed XPS survey of Pt 4f core-level region spectra. **d, g**, Detailed XPS survey of Y 3d core-level region spectra. Based on the XPS data, the Pt:Y ratio in the near-surface region of the as-prepared particles is four, whereas it is 14.3 for the particles after the ORR. a.u., arbitrary units; SEM, scanning electron microscope; UHV, ultrahigh vacuum.

reports in the literature in which researchers have attempted to produce nanoparticles of this or similar catalysts^{33,34}. Nevertheless, there is no firm evidence that metallic Pt_xY can be synthesized in the nanoparticulate form and that it shows superior catalytic performance in the ORR. In contrast, alloys of Pt and LTMs, such as Ni, Co, Cu, Pd and Fe, are less challenging to synthesize; the solute

metal element will typically have a much lower negative reduction potential than rare earths such as Y, Gd or La (ref. 32). However, alloys or core-shell structures of Pt and LTMs have been investigated for more than 25 years^{35,36}. Despite recent advances in the ORR on Pt-LTM alloys^{8–12,37,38}, we envision that the relatively uncharted territory offered by alloys of Pt and rare earths should provide much

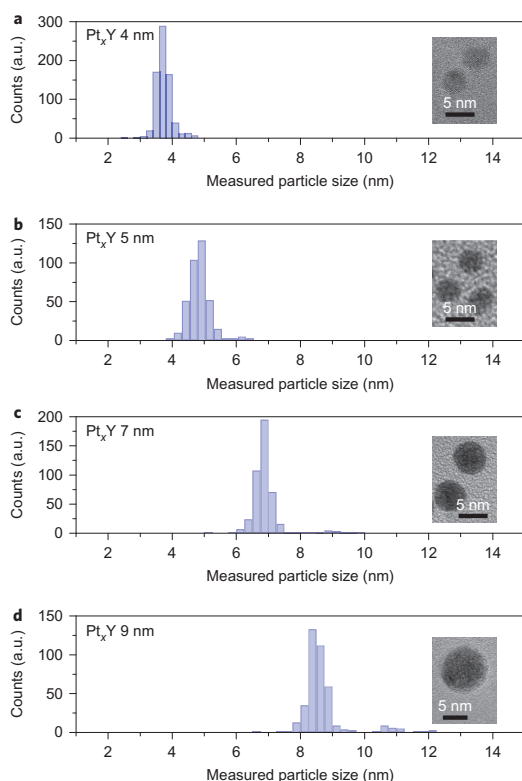


Figure 2 | Particle-size distributions and representative TEM micrographs for the Pt_xY catalysts. **a**, 4 nm. **b**, 5 nm. **c**, 7 nm. **d**, 9 nm.

room for improvement, should it be possible to synthesize nanoparticles of the catalyst (ultimately on a large scale).

Thus, to further the development of Pt_xY as a catalyst for the ORR, two critical questions should be addressed. What is the origin of the enhanced catalytic activity and can the high activity of extended surfaces be achieved with nanoparticles? Herein we address these challenges by preparing model size-selected nanoparticles of Pt_xY by gas aggregation. Furthermore, we characterize the structure and composition of the nanoparticles before and after ORR conditions using X-ray photoelectron spectroscopy (XPS), ion scattering spectroscopy (ISS), transmission electron microscopy (TEM) and X-ray absorption spectroscopy (XAS) measurements.

Results and discussion

The mass-selected Pt_xY particles were prepared through the gas aggregation of a Pt_3Y target and time-of-flight separation, as shown in Fig. 1a. Subsequently, the charged nanoparticles were deposited directly onto a planar glassy carbon substrate under ultra-high vacuum (UHV) conditions. By resorting to a physical method, we can elucidate fundamental relationships between reactivity and particle size, shape and morphology^{39–43}, without the inherent artefacts introduced by wet chemical synthesis from the precursors or surfactants^{44–46}. Moreover, this process allows for the production of well-defined nanoparticles of materials that are otherwise challenging to synthesize by conventional chemical methods.

The results of the characterization are summarized in Figs 1b–g and 2. We first attempted to produce the catalysts from a Pt_3Y

(rather than a Pt_3Y) target. However, this resulted in the formation of nanoparticles with a very high Y content, and the particles corroded excessively, analogous to our earlier results on extended surfaces of PtY and Pt_2Y (ref. 15).

The surface composition of the as-prepared catalysts was characterized by ISS and XPS, as shown in Fig. 1b–e. Figure 1c,d show the XPS spectra of the Pt 4f and Y 3d, respectively, core-level regions acquired after deposition. The Pt:Y ratios of the as-prepared samples are all about four, as shown in Supplementary Fig. 1. The XPS spectrum of the Y 3d core-level region for the as-prepared nanoparticles could not be fitted by a single set of peaks, which suggests that Y is in more than one chemical state. The position of the most-intense peak of low binding energy is consistent with metallic Y. However, the shift between the metallic Y species and the second, less-intense Y species is inconsistent with the notion that this latter species is Y_2O_3 (ref. 47; see the air-exposed samples in Supplementary Fig. 3). The unidentified species may be formed from the reaction of Y with the carbon substrate, although the presence of Y hydrate or Y hydroxide cannot be excluded. The presence of both Pt and Y in the ISS spectrum shown in Fig. 1b confirms that the surface layer is composed of both elements.

The particle-size distribution (PSD) histograms of the different particles, determined using TEM, are plotted in Fig. 2. In the text and figure captions we refer to the particle according to the intended

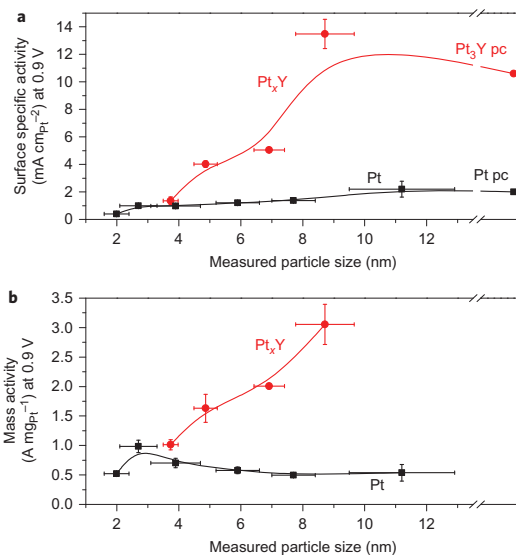


Figure 3 | Catalyst activity of Pt_xY in nanoparticles in comparison to Pt. **a**, **b**, Surface specific activity (**a**) and mass activity (**b**) of Pt_xY (red). All data are taken at 0.9 V, recorded at 50 $mV s^{-1}$, 1,600 revolutions per minute and $23 \pm 1^\circ C$ in O_2 -saturated 0.1 M $HClO_4$, taken from the anodic cycle and corrected for mass-transport limitations. For comparison, the previously published mass and specific activities of pure Pt nanoparticles, prepared in the same way, and an extended surface of polycrystalline Pt (Pt pc) are also plotted (black)⁴⁰. The Supplementary Information gives details of the quantification of mass and surface area⁴⁰. The Pt_3Y pc data represent a sputter-cleaned extended surface of polycrystalline Pt_3Y tested under the same conditions¹⁶. Each data point corresponds to the mean value from at least three independent activity tests; the error bars show the standard deviation in the electrochemical measurements and the PSD. The lines serve as a guide for the eye.

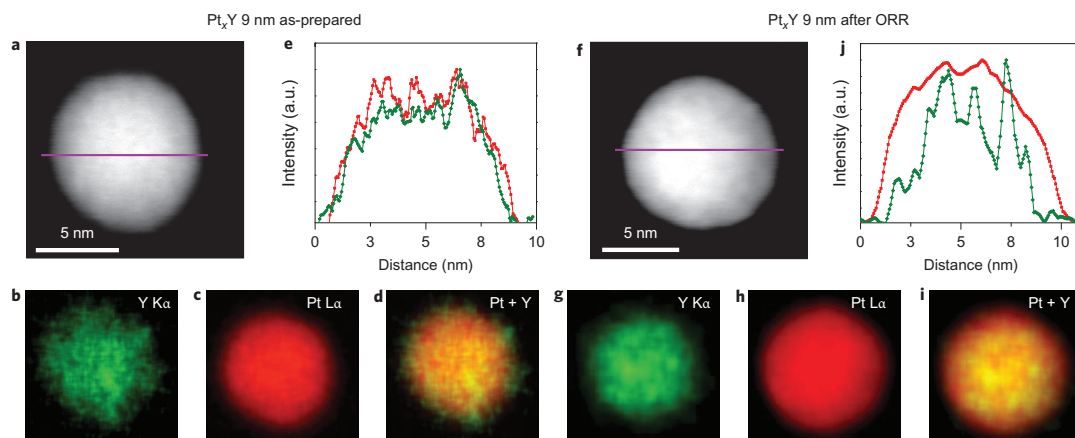


Figure 4 | High-angle annular dark-field (HAADF)-STEM images and EDS elemental maps for Pt_xY_9 nm. Images for the as-prepared sample (**a–e**) and for the catalyst after ORR conditions (**f–j**). **a, f**, HAADF-STEM images. **b, g**, EDS elemental maps of $\text{Y K}\alpha$. **c, h**, EDS elemental maps of $\text{Pt L}\alpha$. **d, i**, Combined elemental maps of $\text{Pt} + \text{Y}$. **e, j**, EDS intensity line profiles extracted from the spectrum image data cube along the purple lines drawn on **a** and **f**. We estimated the Pt-shell thickness of the nanoparticles by extracting ten line profiles across each particle of **f** and obtained a value of 1.0 ± 0.3 nm.

size, rather than the measured size. However, when plotting data on numerical axes we use the measured size from the mean value in the PSDs. The sharp narrow peaks on the PSDs clearly demonstrate the high quality of the mass selection. The presence of satellite peaks at higher diameters results from the formation of doubly charged nanoparticles (that is, with a mass twice the intended mass). This artefact was minimized by optimizing the synthesis conditions. The particles preserve their spherical shape, independent of diameter. Close inspection of the TEM images suggests that the nanoparticles mostly consist of several crystallites (Supplementary Fig. 10).

Once deposited and characterized, the alloy catalyst-loaded electrode was transferred from the vacuum chamber to the arbour of a rotating ring disc electrode assembly, in which the ORR activity was evaluated in a liquid half-cell containing 0.1 M HClO_4 . The electrochemical surface area was measured by CO stripping (see Supplementary Fig. 4). The activity of the alloy catalysts, expressed as a kinetic current density at 0.9 V, is summarized in Fig. 3a in terms of specific activity (that is, mA cm^{-2} microscopic surface area) and in Fig. 3b in terms of mass activity (that is, $\text{A mg}_{\text{Pt}}^{-1}$). For the purpose of comparison, the plots also include the activity of extended surfaces of sputter-cleaned polycrystalline Pt_3Y , as well as our previously reported data for pure Pt surfaces^{13,15,16,40}. Each of the Pt_xY catalysts exhibits a marked enhancement in specific activity over pure Pt of the same size, with the exception of the smallest nanoparticles (4 nm). Similar to that of pure Pt, the specific activity of Pt_xY increases with particle size, with the activities of the larger nanoparticles converging towards those of extended polycrystalline surfaces. Most notably, the mass activity of Pt_xY is not only significantly higher than that of pure Pt, but within the range of particle sizes studied here it increases monotonically with particle size. This trend is of great advantage—larger particles are inherently more stable against dissolution, sintering and Ostwald ripening^{3,48}. In contrast, pure Pt exhibits a peak in mass activity at ~ 3 nm, a sub-optimal particle size in terms of stability. The highest mass activity is found at 9 nm diameter, $3.05 \text{ A mg}_{\text{Pt}}^{-1}$ at 0.9 V. This is close to the highest activity reported in the literature ($3.3 \text{ A mg}_{\text{Pt}}^{-1}$ for Pt_xNi nanoparticles⁴⁹), over 5.5 times higher than the most-active commercial pure Pt catalyst ($0.55 \text{ A mg}_{\text{Pt}}^{-1}$)⁵⁰ and three times higher than the peak mass activity for Pt nanoparticles measured in the same manner⁴⁰.

On extended cycling 9,000 times between 0.6 V and 1 V, the catalyst retained 63% of its initial activity, as shown in Supplementary Fig. 6. Supplementary Fig. 7 highlights that most of the activity losses occur during the first 600 cycles. The surface coverage of Pt, measured on the basis of CO stripping, is constant with time. This suggests that the losses in activity result from a decrease in specific activity rather than the loss of surface area. Consequently, following some initial performance losses, it seems that the catalyst reaches a metastable state that is kinetically hindered from degrading further. Moreover, the specific activity, even after cycling, is still about 2–4 times higher than that of pure Pt nanoparticles of the same size, as shown in Supplementary Fig. 6. The activity and stability of the Pt_xY nanoparticles compare closely to those of the aforementioned Pt_xNi nanoparticles, which exhibited a record high activity⁴⁹. The Pt_xY nanoparticles retained 63% of their activity after 9,000 cycles and the Pt_xNi retained 60% after 5,000 cycles between 0.65 V and 1 V. Nonetheless, a quantitative comparison of the catalyst stability we report here with those of other Pt alloys is challenging. Ideally, the stability of the Pt_xY nanoparticles should be assessed in comparison with other Pt-alloy catalysts prepared and tested under identical conditions.

To understand the cause of the high activity of our nanoparticulate alloy catalysts, we performed a series of *ex situ* examinations of the active phase. We used scanning transmission electron microscopy energy-dispersive X-ray spectroscopy (STEM-EDS) to map the distribution of Pt and Y. The STEM images and the corresponding EDS elemental maps of Pt_xY_9 nm particles before electrochemical treatment and after ORR activity measurements are shown in Fig. 4. The Pt and Y EDS maps and line profiles of the as-prepared particles show a homogeneous distribution of the two elements over the entire particle (Fig. 4b–d). However, the EDS maps in Fig. 4g–i reveal that a Pt-rich shell is formed around the Pt–Y core of the sample that was exposed to the ORR conditions because of dissolution of Y. This overlayer can be seen clearly on the EDS line profile in Fig. 4j. On the basis of the line profile data, we estimate that the Pt shell is ~ 1 nm thick. These microscopic data are confirmed macroscopically by the ISS and XPS spectra shown in Fig. 1b–g. The Pt:Y XPS ratio is four on the as-prepared samples of 9 nm particles, whereas it is 14.3 after the ORR. Moreover, only a single set of Y peaks appears in Fig. 1g, which represents a metallic

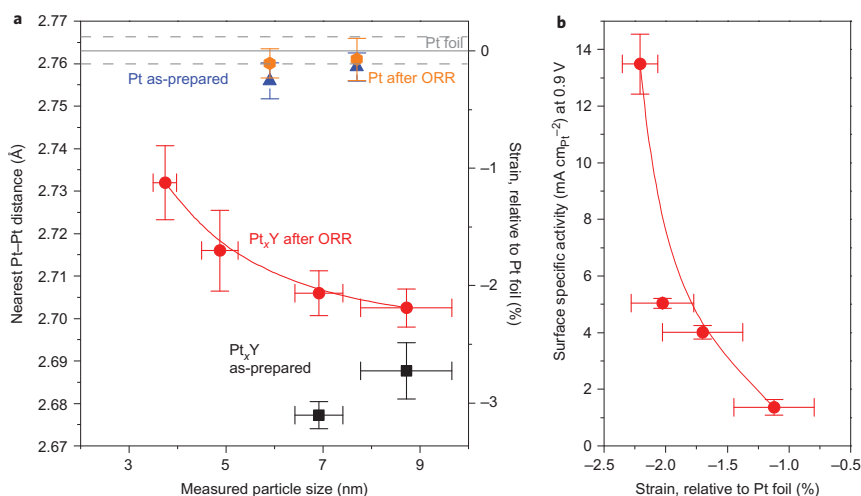


Figure 5 | XAS analysis. **a**, Average nearest-neighbour Pt-Pt distance measured by EXAFS as a function of the particle size for both as-prepared (black) and after ORR (red) recorded on Pt_xY. For the purpose of comparison, EXAFS measurements were also performed on as-prepared (blue) and electrochemically tested (red) Pt nanoparticles. Measurements were performed on a Pt foil (continuous grey horizontal line; the dashed grey horizontal lines show the error from the fitting software) as a reference. The left y axis shows the nearest neighbour Pt-Pt distance; the right axis represents the % strain in the Pt-Pt distance, relative to that of the bulk Pt-foil. The y-axis represents the % strain in the Pt-Pt distance relative to that in the Pt foil. **b**, Surface specific activity, extracted from Fig. 3, as a function of the average compressive strain in the Pt_xY particles relative to bulk Pt, based on the data shown in **a**. The error bars are produced by the fitting software (full details can be found in Supplementary Table 2). The continuous curved lines serve as a guide for the eye.

phase. The presence of the Pt peak and absence of the Y peak on the ISS spectrum in Fig. 1e confirms that there is no Y at the surface of the catalyst. Further evidence for the formation of a core-shell structure is described in Supplementary Fig. 2.

The TEM measurements at identical locations in Supplementary Fig. 8 show that there is no significant change in catalyst morphology or size distribution before and after the reaction conditions. Supplementary Fig. 9 shows the STEM-EDS mapping of the 9 nm nanoparticles after 9,000 cycles, and further confirms the Pt overlayer formation. To summarize our STEM, XPS and ISS data thus far, exposure to ORR conditions results in a significant increase of the Pt:Y ratio in the near-surface region because of Y dissolution. This is consistent with our earlier measurements on extended surfaces of Pt₃Y and Pt₅Y, which have a 3–4 monolayer thick overlayer¹⁵. On this basis, we can conclude that enhanced activity of the Pt_xY nanoparticles cannot be traced back to ligand effects, which led us to investigate strain effects.

To quantify the strain in the Pt_xY catalysts, we employed extended X-ray absorption fine structure measurements (EXAFS), before and after the ORR experiments, in comparison with a bulk Pt foil and pure Pt nanoparticles. The main output of the EXAFS experiments is summarized in Fig. 5a, in which the average nearest-neighbour Pt-Pt distance of the different Pt_xY and Pt nanoparticles is plotted as a function of the particle size (for details, see Supplementary Fig. 11). All of the pure Pt samples exhibited the same Pt-Pt distance, before and after electrochemical testing, independent of the particle size. To the contrary, the Pt_xY catalysts not only exhibited a lower Pt-Pt distance relative to pure Pt, but also maintained this compressive strain after the electrochemical testing. The lowest Pt-Pt distance was displayed by the as-prepared Pt_xY samples, with up to a 3% decrease in Pt-Pt distance (that is, a compressive strain versus pure Pt). After ORR testing, the compression of the Pt_xY structure diminished and is clearly dependent on the particle size, varying from a strain of -1.0% for the 4 nm Pt_xY particles to -2.1% for the 9 nm Pt_xY particles. Our results show

conclusively that alloying Pt with Y brings about an overall compression of the Pt-Pt distance in Pt_xY, which is dependent on particle size. Exposure to ORR conditions removes the Y from the first atomic layers. In the absence of Y in the near-surface region, there is a driving force for the interatomic distance in the Pt overlayers to expand towards that of pure Pt. Assuming that the Pt-Pt distance determined with EXAFS represents the average over the Pt_xY core and Pt shell, and that a ~1 nm thick overlayer is formed, consistent with the TEM measurements, we can estimate the compression of the overlayer. The results of this analysis are shown in Supplementary Fig. 12. This suggests that, for all particle sizes, the overlayer is slightly less strained than the core; for example, in the case of the 9 nm particles the average overlayer strain would be about -1.6%. The interatomic distance for the catalytically active atoms, that is the surface atoms, would be relaxed further towards that of pure Pt than the distance in the deeper layers within the overlayer. Nonetheless, experiments on Pt/Cu(111) and Cu₃Pt(111) single crystals suggest that there would still be some degree of compressive strain within the outermost surface layer, despite the relaxation^{23,25}.

It is somewhat counterintuitive that alloying Pt with Y reduces the Pt-Pt distance in the alloy, given that Y is larger than Pt (ref. 31). However, in bulk Pt₅Y the nearest neighbour Pt-Pt distance is 2.65 Å, which is compressed by 4% relative to pure Pt (ref. 15). Pt₅La and Pt₅Gd have bulk structures similar to that of Pt₅Y, albeit with different stacking^{3,16}. The bulk structure of these compounds consists of alternating rows of pure Pt and Pt with rare-earth atoms. According to earlier DFT calculations, a Pt overlayer that covers an extended surface of Pt₅La would resemble a compressed closely packed Pt layer (Supplementary Fig. 13)³. Essentially, the larger rare-earth atoms deform the closely packed structure of Pt, which allows a larger number of Pt atoms to fit onto the Pt overlayer than onto bulk Pt.

In Fig. 5b we demonstrate that the activity of Pt_xY catalysts is strongly correlated to the average Pt-Pt distance in the particles,

similar to dealloyed PtCu_x (ref. 25). An increase in compression brings about an increased ORR activity, relative to Pt, via slightly weakened HO* binding to the surface. However, Pt_xY nanoparticles should be inherently more stable than PtCu_x and other Pt-LTM alloys against continued dealloying under reaction conditions^{3,13,16,49}. Dealloying via diffusion of Y through the bulk and the Pt overlayer will be hindered by the strong interaction between Y and Pt (ref. 13). The moderate stability we report here could be improved even further through optimization of the catalyst composition and suitable annealing¹². This will be the subject of future studies.

In conclusion, the mass activity of the catalyst, 3.05 A mg_{Pt}⁻¹ at 0.9 V, is as high (within the range of experimental error) as the best reported in the literature. By using mass-selected nanoparticles, not only do we provide a proof-of-concept that nanoparticles of Pt-Y alloys are highly active, but we also shed scientific insight into the underlying mechanism of their enhanced activity. It turns out that their superior performance arises from a compressive strain exerted by the catalyst core onto the surface. Our work provides a strong impetus for the implementation of Pt_xY in fuel cells. Nevertheless, the methods used here do not allow for mass production. The next step is to develop the chemical synthesis of this catalyst in bulk quantities in which the Y content may also be optimized.

Received 3 January 2014; accepted 10 June 2014;
published online 13 July 2014

References

- Gasteiger, H. A., Kocha, S. S., Sompalli, B. & Wagner, F. T. Activity benchmarks and requirements for Pt, Pt-alloy, and non-Pt oxygen reduction catalysts for PEMFCs. *Appl. Catal. B* **56**, 9–35 (2005).
- Gasteiger, H. A. & Markovic, N. M. Just a dream – or future reality? *Science* **324**, 48–49 (2009).
- Stephens, I. E. L., Bondarenko, A. S., Grönberg, U., Rossmeisl, J. & Chorkendorff, I. Understanding the oxygen reduction reaction on platinum and its alloys. *Energy Environ. Sci.* **5**, 6744–6762 (2012).
- Debe, M. K. Electrocatalyst approaches and challenges for automotive fuel cells. *Nature* **486**, 43–51 (2012).
- Wagner, F. T., Lakshmanan, B. & Mathias, M. F. Electrochemistry and the future of the automobile. *J. Phys. Chem. Lett.* **1**, 2204–2219 (2010).
- Chen, S., Gasteiger, H. A., Hayakawa, K., Tada, T. & Shao-Horn, Y. Platinum-alloy cathode catalyst degradation in proton exchange membrane fuel cells: nanometer-scale compositional and morphological changes. *J. Electrochem. Soc.* **157**, A82–A97 (2010).
- Maillard, F. *et al.* Durability of Pt₃Co/C nanoparticles in a proton-exchange membrane fuel cell: direct evidence of bulk Co segregation to the surface. *Electrochem. Commun.* **12**, 1161–1164 (2010).
- Cui, C. H., Gan, L., Heggen, M., Rudi, S. & Strasser, P. Compositional segregation in shaped Pt alloy nanoparticles and their structural behaviour during electrocatalysis. *Nature Mater.* **12**, 765–771 (2013).
- Wang, D. L. *et al.* Structurally ordered intermetallic platinum–cobalt core–shell nanoparticles with enhanced activity and stability as oxygen reduction electrocatalysts. *Nature Mater.* **12**, 81–87 (2013).
- Liu, W. *et al.* Bimetallic aerogels: high-performance electrocatalysts for the oxygen reduction reaction. *Angew. Chem. Int. Ed.* **52**, 9849–9852 (2013).
- Sasaki, K. *et al.* Highly stable Pt monolayer on PdAu nanoparticle electrocatalysts for the oxygen reduction reaction. *Nature Commun.* **3**, 1115 (2012).
- Wang, C. *et al.* Design and synthesis of bimetallic electrocatalyst with multilayered Pt-skin surfaces. *J. Am. Chem. Soc.* **133**, 14396–14403 (2011).
- Greeley, J. *et al.* Alloys of platinum and early transition metals as oxygen reduction electrocatalysts. *Nature Chem.* **1**, 552–556 (2009).
- Stamenkovic, V. R. *et al.* Improved oxygen reduction activity on Pt₃Ni(111) via increased surface site availability. *Science* **315**, 493–497 (2007).
- Stephens, I. E. L., Bondarenko, A. S., Bech, L. & Chorkendorff, I. Oxygen electroreduction activity and X-ray photoelectron spectroscopy of alloys of platinum and early transition metals. *ChemCatChem* **4**, 341–349 (2012).
- Escudero-Escribano, M. *et al.* Pt₅Gd as a highly active and stable catalyst for oxygen electroreduction. *J. Am. Chem. Soc.* **134**, 16476–16479 (2012).
- Johannesson, G. H. *et al.* Combined electronic structure and evolutionary search approach to materials design. *Phys. Rev. Lett.* **88**, 255506 (2002).
- Jong Yoo, S. *et al.* Enhanced stability and activity of Pt–Y alloy catalysts for electrocatalytic oxygen reduction. *Chem. Commun.* **47**, 11414–11416 (2011).
- Hwang, S. J. *et al.* Role of electronic perturbation in stability and activity of Pt-based alloy nanocatalysts for oxygen reduction. *J. Am. Chem. Soc.* **134**, 19508–19511 (2012).
- Sanchez-Casalogue, H. *et al.* Direct observation of the oxygenated species during oxygen reduction on a platinum fuel cell cathode. *Nature Commun.* **4**, 2817 (2013).
- Toda, T., Igarashi, H., Uchida, H. & Watanabe, M. Enhancement of the electroreduction of oxygen on Pt alloys with Fe, Ni, and Co. *J. Electrochem. Soc.* **146**, 3750–3756 (1999).
- Stamenkovic, V. R., Mun, B. S., Mayrhofer, K. J. J., Ross, P. N. & Markovic, N. M. Effect of surface composition on electronic structure, stability, and electrocatalytic properties of Pt–transition metal alloys: Pt-skin versus Pt-skeleton surfaces. *J. Am. Chem. Soc.* **128**, 8813–8819 (2006).
- Yang, R. Z., Strasser, P. & Toney, M. F. Dealloying of Cu₃Pt (111) studied by surface X-ray scattering. *J. Phys. Chem. C* **115**, 9074–9080 (2011).
- Stephens, I. E. L. *et al.* Tuning the activity of Pt(111) for oxygen electroreduction by subsurface alloying. *J. Am. Chem. Soc.* **133**, 5485–5491 (2011).
- Strasser, P. *et al.* Lattice-strain control of the activity in dealloyed core–shell fuel cell catalysts. *Nature Chem.* **2**, 454–460 (2010).
- Johansson, T. *et al.* Pt skin versus Pt skeleton structures of Pt₃Sc as electrocatalysts for oxygen reduction. *Top. Catal.* **57**, 245–254 (2014).
- Norskov, J. K. *et al.* Origin of the overpotential for oxygen reduction at a fuel-cell cathode. *J. Phys. Chem. B* **108**, 17886–17892 (2004).
- Kitchin, J. R., Norskov, J. K., Barteau, M. A. & Chen, J. G. Role of strain and ligand effects in the modification of the electronic and chemical properties of bimetallic surfaces. *Phys. Rev. Lett.* **93**, 156801 (2004).
- Calle-Vallejo, F., Martinez, J. I., Garcia-Lastra, J. M., Rossmeisl, J. & Koper, M. T. M. Physical and chemical nature of the scaling relations between adsorption energies of atoms on metal surfaces. *Phys. Rev. Lett.* **108**, 116103 (2012).
- Mavrikakis, M., Hammer, B. & Norskov, J. K. Effect of strain on the reactivity of metal surfaces. *Phys. Rev. Lett.* **81**, 2819–2822 (1998).
- Cordero, B. *et al.* Covalent radii revisited. *Dalton Trans.* 2832–2838 (2008).
- Pourbaix, M. *Atlas of Electrochemical Equilibria in Aqueous Solutions* 2nd edn (National Association of Corrosion Engineers, 1974).
- Nishanth, K. G., Sridhar, P. & Pitchumani, S. Enhanced oxygen reduction reaction activity through spillover effect by Pt–Y(OH)₂/C catalyst in direct methanol fuel cells. *Electrochem. Commun.* **13**, 1465–1468 (2011).
- Jeon, M. K. & McGinn, P. J. Carbon supported Pt–Y electrocatalysts for the oxygen reduction reaction. *J. Power Sources* **196**, 1127–1131 (2011).
- Luczak, F. J. & Landsman, D. A. Fuel cell cathode catalyst alloy-comprising noble metal, cobalt and a transition metal. US patent 4677092-A (1987).
- Mukerjee, S. & Srinivasan, S. Enhanced electrocatalysis of oxygen reduction on platinum alloys in proton-exchange membrane fuel-cells. *J. Electroanal. Chem.* **357**, 201–224 (1993).
- van der Vliet, D. F. *et al.* Mesostuctured thin films as electrocatalysts with tunable composition and surface morphology. *Nature Mater.* **11**, 1051–1058 (2012).
- Snyder, J., Fujita, T., Chen, M. W. & Erlebacher, J. Oxygen reduction in nanoporous metal–ionic liquid composite electrocatalysts. *Nature Mater.* **9**, 904–907 (2010).
- Nesselberger, M. *et al.* The effect of particle proximity on the oxygen reduction rate of size-selected platinum clusters. *Nature Mater.* **12**, 919–924 (2013).
- Perez-Alonso, F. J. *et al.* The effect of size on the oxygen electroreduction activity of mass-selected platinum nanoparticles. *Angew. Chem. Int. Ed.* **51**, 4641–4643 (2012).
- Li, Z. Y. *et al.* Structures and optical properties of 4–5 nm bimetallic AgAu nanoparticles. *Faraday Discuss.* **138**, 363–373 (2008).
- Yin, F., Wang, Z. W. & Palmer, R. E. Controlled formation of mass-selected Cu–Au core–shell cluster beams. *J. Am. Chem. Soc.* **133**, 10325–10327 (2011).
- Von Issendorff, B. & Palmer, R. E. A new high transmission infinite range mass selector for cluster and nanoparticle beams. *Rev. Sci. Instrum.* **70**, 4497–4501 (1999).
- Li, D. G. *et al.* Surfactant removal for colloidal nanoparticles from solution synthesis: the effect on catalytic performance. *ACS Catal.* **2**, 1358–1362 (2012).
- Solla-Gullon, J., Montiel, V., Aldaz, A. & Clavilier, J. Electrochemical characterisation of platinum nanoparticles prepared by microemulsion: how to clean them without loss of crystalline surface structure. *J. Electroanal. Chem.* **491**, 69–77 (2000).
- Cuenya, B. R., Baeck, S. H., Jaramillo, T. F. & McFarland, E. W. Size- and support-dependent electronic and catalytic properties of Au⁰/Au³⁺ nanoparticles synthesized from block copolymer micelles. *J. Am. Chem. Soc.* **125**, 12928–12934 (2003).
- Reichl, R. & Gaukler, K. H. An investigation of air-grown yttrium oxide and experimental determination of the sputtering yield and the inelastic mean free path. *Appl. Surf. Sci.* **26**, 196–210 (1986).
- Shao-Horn, Y. *et al.* Instability of supported platinum nanoparticles in low-temperature fuel cells. *Top. Catal.* **46**, 285–305 (2007).

49. Choi, S. I. *et al.* Synthesis and characterization of 9 nm Pt–Ni octahedra with a record high activity of 3.3 A/mg_{Pt} for the oxygen reduction reaction. *Nano Lett.* **13**, 3420–3425 (2013).
50. Nesselberger, M. *et al.* The particle size effect on the oxygen reduction activity of Pt catalysts: influence of electrolyte and relation to single crystal models. *J. Am. Chem. Soc.* **133**, 17428–17433 (2011).

Acknowledgements

The authors gratefully acknowledge financial support from the Danish Ministry of Science's UNIK initiative, Catalysis for Sustainable Energy, The Center for Individual Nanoparticle Functionality is supported by the Danish National Research Foundation (DNRF54). The A.P. Møller and Chastine Mc-Kinney Møller Foundation is gratefully acknowledged for its contribution towards the establishment of the Centre for Electron Nanoscopy in the Technical University of Denmark. The Interdisciplinary Centre for Electron Microscopy at École Polytechnique Fédérale de Lausanne is gratefully acknowledged for the use of the FEI Tecnai Osiris TEM. Support for this work was received from the Danish Council for Strategic Research's project NACORR (12-133817) and MEDLYS (10-093906). I.E.L.S. was supported by the ForskEL programme's project CATBOOSTER (2001-1-10669). D.N.M. is the recipient of a HC Ørsted postdoctoral fellowship. Part of this work is supported by Basic Energy Sciences, US Department of through the SUNCAT Center for Interface Science and Catalysis. This research was partly carried out at the Stanford Synchrotron Radiation

Lightsources, a National User Facility operated by Stanford University on behalf of the Basic Energy Sciences, US Department of Energy. We thank J. Bargar, A. Mehta, R. Davis, M. Latimer and E. J. Nelson for support with the EXAFS instrumentation and for helpful discussions.

Author contributions

I.C. and I.E.L.S. conceived the experiments. P.H-F. performed the electrochemical experiments. F.M., D.N.M., C.E.S., P.M. and A.N. performed the UHV experiments. D.F., A.B. and A.M.W. performed the XAS measurements. D.D. performed the microscopy. P.H-F. designed the figures. P.H-F. and I.E.L.S. wrote the first draft of the paper. All authors discussed the results and commented on the manuscript.

Additional information

Supplementary information is available in the [online version](#) of the paper. Reprints and permissions information is available online at www.nature.com/reprints. Correspondence and requests for materials should be addressed to I.E.L.S. and I.C.

Competing financial interests

I.C. and I.E.L.S. have a patent on the catalyst material Pt₃Y, PCT/DK2010/050193. The other authors declare no competing financial interests.



Cite this: DOI: 10.1039/c4cp02144d

Exploring the phase space of time of flight mass selected Pt_xY nanoparticles

Federico Masini,^a Patricia Hernández-Fernández,^{†a} Davide Deiana,^b Christian Ejersbo Strebel,^c David Norman McCarthy,^c Anders Bodin,^a Paolo Malacrida,^a Ifan Stephens^a and Ib Chorkendorff^{**a}

Mass-selected nanoparticles can be conveniently produced using magnetron sputtering and aggregation techniques. However, numerous pitfalls can compromise the quality of the samples, e.g. double or triple mass production, dendritic structure formation or unpredicted particle composition. We stress the importance of transmission electron microscopy (TEM), X-ray photoelectron spectroscopy (XPS) and ion scattering spectroscopy (ISS) for verifying the morphology, size distribution and chemical composition of the nanoparticles. Furthermore, we correlate the morphology and the composition of the Pt_xY nanoparticles with their catalytic properties for the oxygen reduction reaction. Finally, we propose a completely general diagnostic method, which allows us to minimize the occurrence of undesired masses.

Received 16th May 2014,
Accepted 8th July 2014

DOI: 10.1039/c4cp02144d

www.rsc.org/pccp

Introduction

Heterogeneous catalysis of nanoparticles has been the subject of numerous investigations in recent years.^{1–15}

Industrial catalysts are almost always in the nanoparticulate form due to their high surface area to volume ratio. Traditionally, the fundamental properties of catalysts were investigated on extended surfaces, e.g. single crystals. However, in recent years, an increasing number of model studies have been devoted to the direct investigation of nanoparticles. In some cases it turns out that the surface chemistry of nanoparticles is quite distinct from that of extended surfaces.

Size dependent effects have been observed in numerous catalytic systems such as those for Co nanoparticles in the Fischer–Tropsch reaction, where activity drops at particle sizes greater than 6–8 nm.¹⁶ Furthermore, Au nanoparticles showed a remarkably high activity for CO oxidation below 5 nm particle diameter, reaching a maximum in activity at 2–3 nm size.¹⁷ Ruthenium has interesting catalytic properties for CO oxidation if prepared in the form of nanoparticles of diameter between 2 nm and 6 nm.¹⁸

The reason for size dependence is still not entirely clear and has been debated for a long time. However, there are cases in which a combination of theoretical and experimental work has

elucidated the role of different types of sites in the catalytic activity, whose abundance is related to particle size and structure.

On the Ru(0001) surface, the so called B₅ step sites were found to yield a much higher contribution to N₂ dissociation (about nine orders of magnitude) than the facets.¹⁹ Recently, the same sites (B₅) were shown to have analogous properties in Ru nanoparticles,¹⁰ and the concentration of these sites has been correlated with particle size.

The relevance of surface steps and defects for catalytic purposes has been elucidated by the work of Vendelbo *et al.*,^{20,21} who investigated the reactivity of the Ru(0154) surface (Ru(0001) with 4% steps) for methanation. Not only the steps proved to be of paramount importance for successful methane formation, but defects induced by sputtering readily improved the catalytic activity. Importantly, sulfur poisoning of the step sites reduced the catalytic activity, providing further evidence that all the catalytic properties are concentrated in the few defect sites.

A particularly illustrative example of where single crystal surfaces do not model the catalytic properties of nanoparticles can be found in the case of oxygen electroreduction. This reaction limits the efficiency of low temperature fuel cells, and prohibitively high loadings of Pt-based nanoparticles are required to catalyse the reaction. Most, albeit not all, theoretical and experimental studies seem to suggest that the surface specific activity for oxygen reduction should decrease with a decrease in particle size.^{12,22–28} However, this notion is in conflict with the experimental observation that extended single crystal stepped Pt surfaces sometimes exhibit higher oxygen reduction activity than unstepped surfaces.^{29–31}

One strategy to improve the activity of Pt is to alloy it with other metals. Most research has been devoted to the study of

^a Center for Individual Particle Functionality (CINF), Department of Physics, DTU, DK-2800 Kgs. Lyngby, Denmark. E-mail: ibchork@fysik.dtu.dk

^b Center for Electron Nanoscopy (CEN), Department of Physics, DTU, DK-2800 Kgs. Lyngby, Denmark

^c Haldor Topsøe A/S, Nymollevvej 55, DK-2800 Kgs Lyngby, Denmark

[†] Present address: Danish Technological Institute (DTI), Gregersensvej 1, DK-2630 Taastrup, Denmark.

alloys of Pt and late transition metals such as Ni, Co, Cu and Fe.^{32–38} However, in the harsh acidic and oxidising environment of a fuel cell, these alloys degrade by dealloying.^{39–41} In our laboratory we have taken a different approach, namely to study alloys of Pt and rare earths such as Y, Gd, Ce and La.^{33,42–48} These alloys have a particularly negative heat of formation, which should provide them with long term-kinetic stability against dealloying at the cathode of a fuel cell. Extended surfaces of Pt₃Y and Pt₅Gd show particularly high activity for oxygen reduction.^{42,43,47} On the other hand, upon exposure to reaction conditions, alloys such as Pt₂Y or PtY corroded extensively, due to Y dissolution; this suggests that an excessive amount of Y is detrimental to catalyst stability.⁴⁴ Most recently, we demonstrated that Pt_xY is also highly active for the oxygen reduction reaction in nanoparticulate form. The activity increases monotonically with particle size; we attributed this to an increased degree of compressive strain exerted by the alloy core onto the pure Pt shell.⁴⁸

Importantly, size effects are not the only significant characteristics of nanoparticles. Improvements can be made to catalysts by forming non-equilibrium morphologies.^{14,38,49–53} Very recent results by Chen *et al.*¹³ have shown unprecedented capabilities of Pt_xNi “nanoframes” to catalyze oxygen reduction.

It is of utmost importance to conduct studies on monodisperse, size selected nanoparticles, to be able to correlate size, shape and surface structure with the catalytic activity of the nanoparticles. Common problems which could arise are (i) too large particle size distribution, (ii) contaminations, (iii) polydispersity, (iv) undesired morphology *e.g.* dendritic shapes and (v) inadequate particle composition.

To circumvent the first and the second issues, we produce nanoparticles using a cluster source,⁵⁴ interfaced with a von Issendorff (lateral time-of-flight) mass selector.⁵⁵ The source produces particles with narrow size distribution by Ar⁺ plasma sputtering followed by gas phase aggregation under ultra-clean conditions. Nonetheless, it is still necessary to avoid the last three problems to be able to study the catalytic properties of the deposited nanoparticles. To do so, greater attention must be paid to undesired higher mass production. Additionally, particular attention must be paid to the particle morphology and chemical composition.

These issues stress the necessity of checking the quality of the deposited samples, *e.g.* via transmission electron microscopy (TEM), X-ray photoelectron spectroscopy (XPS) and ion scattering spectroscopy (ISS).

In this paper, we show how different Pt_xY chemical composition affects the particle activity for ORR.

Furthermore, we discuss the conditions under which dendritic Pt_xY nanostructures are produced; we show that their electrochemical activity for ORR varies as a function of the morphology of the Pt_xY nanostructure.

Finally, we qualitatively correlate the quality of the deposited nanoparticle sample with the evolution in time of the deposition current *versus* mass curves, measured using a time of flight analyzer (TOF). We present a method to minimize the problem of multiple masses production, thereby greatly reducing the

risk of compromising an experimental sample. Although the study is conducted on Pt_xY particles, the method is completely general.

Experimental

The Pt_xY nanoparticles were prepared using a magnetron sputter gas aggregation source (Birmingham Instruments Inc.), combined with a von Issendorff time-of-flight mass filter, and deposited onto Lacey Carbon-coated Au or Si₃N₄ (for the Ru reference) TEM grids mounted in a multichamber ultrahigh vacuum (UHV) system (Omicron, Multiscan Lab) with a base pressure in the low 10^{−10} mbar region. The gas aggregation technique involves Ar⁺ sputtering of a target (in this study Ru and Pt 9 : 1 Y, Pt 3 : 1 Y alloy targets from Kurt J. Lesker Inc.), to produce an atomic vapor that is condensed into nanoparticles through collisions with cooled Ar and He gas. The gas aggregation method is particularly useful in the context of formation of metallic nanoparticles from materials such as yttrium that have high affinities for oxygen, as it is an ultrahigh vacuum compatible method where oxygen is present at extremely low levels. The second chief advantage arises from the fact that a high fraction of the nanoparticles produced *via* Ar⁺ sputtering are ionized,⁵⁴ thus the particles can be filtered based on their mass-to-charge ratio, which in turn allows the deposition of particles with narrow size distributions. In our experiments the Pt–Y and the Ru nanoparticles are filtered using a time-of-flight mass filter.⁵⁵

Nanoparticle size distributions were obtained from TEM and high angle annular dark field (HAADF) STEM micrographs were acquired using a probe C_s-corrected FEI Titan Analytical 80–300 electron microscope operated at 300 kV accelerating voltage.

The electrochemical experiments were performed using a Bio-Logic Instruments' VMP2 potentiostat, controlled by a computer. The rotating ring disk electrode (RRDE) assemblies and the glassy carbon substrates were provided by Pine Instruments Corporation. All glassware was cleaned in 96% H₂SO₄ (Merck, Emsure) and 30% H₂O₂ (Analar, Normpur) (3 : 1 v/v). Those were subsequently rinsed several times in hot Millipore water (85 °C, > 18.2 MΩ cm^{−1}, TOC < 5 ppb). A standard three-compartment glass cell was used for all the experiments, equipped with an external jacket attached to a water bath with temperature control. The electrolyte, 0.1 M HClO₄ (Merck, Suprapur), was prepared using Millipore water. The counter electrode was a platinum wire and the reference was the Hg/Hg₂SO₄ electrode separated from the working electrode compartment using a ceramic frit. The measurements were conducted at 23 ± 1 °C. All potentials in the manuscript are quoted with respect to the RHE and corrected for Ohmic losses. The catalyst prepared under UHV conditions was inserted into the arbor of a RRDE and was immersed into the electrochemical cell under potential control at 0.05 V in a N₂ saturated 0.1 M HClO₄ electrolyte. The potential was then constantly cycled between 0.05 V and 1.0 V until a stable cyclic voltammogram was recorded. The ORR

activity was measured by cycling the potential between 0 V and 1 V at 50 mV s⁻¹ and 1600 rpm, after saturating the solution in O₂ (N55, AGA), whereas the stability tests were carried out by cycling the potential between 0.6 V and 1 V at 100 mV s⁻¹ and 0 rpm for 9000 potential cycles. The ORR specific activity, mA cm_{Pt}⁻², was calculated from the anodic sweep of the polarization curve. To that purpose, the kinetic current density, j_k , for the ORR was calculated by using the following equation: $1/j = 1/j_k + 1/j_d$, where j is the measured current density and j_d is the diffusion limiting current density. The active surface area of each Pt_xY sample, cm_{Pt}², was measured by CO stripping analyses, which were carried out in a CO-free Ar electrolyte at 50 mV s⁻¹ after CO adsorption. The active surface area was estimated using the area under the CO-stripping peak assuming a charge of 420 μC cm_{Pt}⁻².⁵⁶

Low-energy ion scattering spectroscopy (ISS) was performed after deposition of the nanoparticles. A pressure of 5 × 10⁻⁸ mbar of He was used for the analysis and a primary energy of 1000 eV was used.

XPS measurements of the samples after electrochemical testing were taken on a Theta Probe instrument (Thermo Scientific). This instrument is equipped with a monochromatized Al Kα (1486.7 eV) source, and XPS spectra were obtained with a pass energy of 100 eV. The analyzer has an acceptance angle of 60°, between 20° and 80° to the surface normal. An X-ray beam size of 400 μm was used for all measurements. The atomic concentrations were quantified by integration of the Pt 4f, Y 3d peaks after background removal. A Shirley-type background was chosen for this purpose. The intensities were corrected for the transmission function of the analyzer, relative sensitivity factors and the electron mean free path. The relative sensitivity factors of Pt and Y were experimentally determined, as described earlier,⁵⁷ from the Pt 4f and Y 3d spectra acquired after sputter-cleaning on a Pt(111) single crystal and Y foil, respectively.

Results

As mentioned in the Introduction, the electrochemical stability of polycrystalline Pt₂Y and PtY was rather poor. Therefore, it was decided to decrease the yttrium content of the polycrystalline samples. Further electrocatalytic tests on the polycrystalline Pt₃Y showed that this alloy is a stable catalyst for ORR.

Pt_xY nanoparticles were obtained by sputtering targets with decreasing yttrium content *i.e.* Pt₃Y and Pt₉Y targets.

The nanoparticles produced by sputtering the Pt₃Y target were tested for ORR under the same conditions used for the nanoparticles obtained using the Pt₉Y target. The ORR kinetic current densities at 0.9 V as a function of the particle size for the samples prepared with the Pt₃Y target and the Pt₉Y target are displayed in Fig. 1. The nanoparticles prepared from the Pt₉Y target display a higher activity than the ones produced using the Pt₃Y target. For instance, for the 5 nm case, the specific activity varies from 4.02 mA cm_{Pt}⁻² to 2.25 mA cm_{Pt}⁻². This great difference in activity is due to the difference in

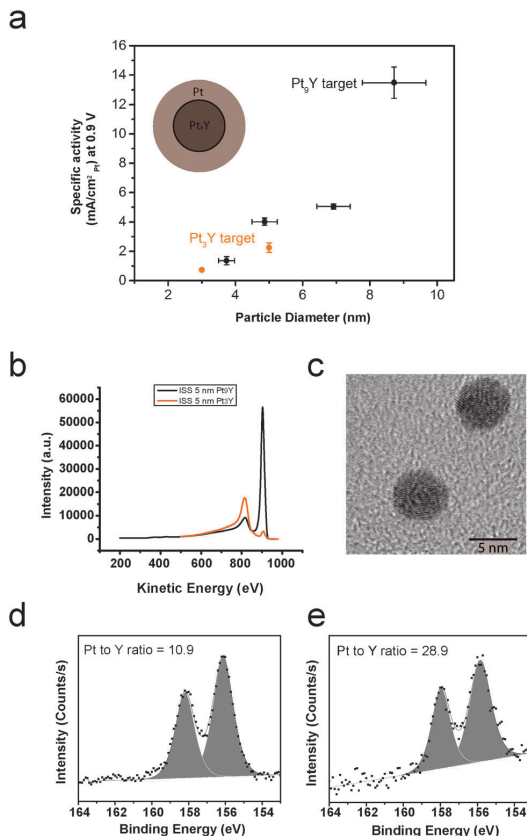


Fig. 1 (a) Specific activity at 0.9 V versus particle size for Pt_xY nanoparticles generated by sputtering two targets, Pt₃Y (black) and Pt₉Y (orange). The cartoon nanoparticle shows the formation of an overlayer of platinum on a Pt_xY core, as a consequence of Y leach-out during ORR. The electrochemical measurements were recorded at 50 mV s⁻¹, 1600 rpm and 23 ± 1 °C in O₂-saturated 0.1 M HClO₄ electrolyte. The current densities have been corrected for mass transport limitations. Each data point is the result of at least three independent measurements. The error bars show the standard deviation. (b) ISS spectra on 5 nm as-deposited particles produced from Pt₃Y target (orange) and Pt₉Y (black). The peak at ~920 eV is attributed to Pt, whereas the peak at ~800 eV is attributed to Y. (c) Representative TEM image of the nanoparticles obtained by sputtering the Pt₃Y target. XPS spectra of the Y3d core level region for 10 nm NPs after ORR (the peaks are attributed to metallic yttrium), obtained from (d) Pt₃Y target and (e) Pt₉Y target. The Pt/Y ratio is reported for each spectrum.

nanoparticle surface composition (Pt/Y ratio), as demonstrated in Fig. 1b, where the ion scattering spectroscopy (ISS), taken on the as deposited particles, are shown for both samples. The ISS spectrum of the Pt₉Y target has an atomic Pt/Y ratio of 2.5, substantially higher than 0.11 for the Pt₃Y target. TEM (Fig. 1d) shows that the particles obtained from the Pt₃Y target are spherical as for the nanoparticles (NPs) obtained sputtering the Pt₉Y target (shown in Fig. 3). This is not surprising: the sputtering conditions for the Pt₃Y target were similar to the sputtering conditions for the Pt₉Y target, and the two targets have similar densities.

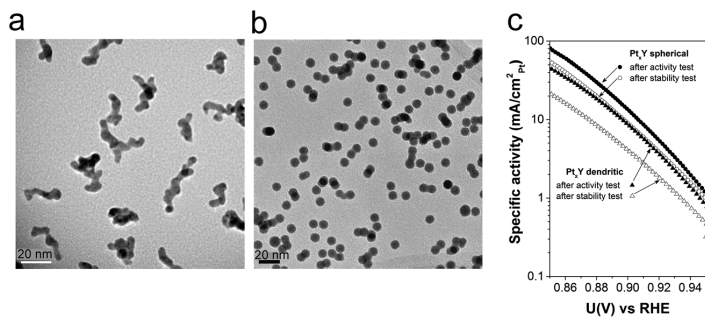


Fig. 2 Representative TEM images of dendritic (a) and spherical (b) nanoparticles obtained by sputtering a Pt_xY target at high and low rates, respectively. (c) ORR Tafel plots for the Pt_xY dendritic and spherical nanoparticles after activity test (black triangles and circles, respectively). The Tafel plots after 9000 potential cycles are also shown (white triangles and circles, respectively). The electrochemical measurements were recorded at 50 mV s⁻¹, 1600 rpm and 23 ± 1 °C in O₂-saturated 0.1 M HClO₄ electrolyte. The current densities have been corrected for mass transport limitations.

Fig. 1d and e show the XPS spectra of the Y3d core level region after ORR for 10 nm nanoparticles. The nanoparticles were fabricated from Pt₃Y and Pt₉Y targets, respectively. The Pt/Y ratios, displayed in the corresponding spectra, are 10.9 and 28.9, respectively.

The chemical composition of the sample is not the only issue which deserves attention when preparing a sample. Morphology also matters.

Fig. 2 displays representative TEM images of two 9 nm Pt_xY nanoparticulate samples displaying different morphologies. In one image, Fig. 2a, the particles have dendritic morphology, whereas in the other image, Fig. 2b, the particles are spherical. The conditions under which the particles were prepared were very different. In the case of the dendritic particles, 70 W and a flow of Ar of 120 ml min⁻¹ and He of 20 ml min⁻¹ were used. The selected particles were positively charged. In the case of the spherical particles, 9 W and an Ar flow of 30 ml min⁻¹ were used. The particles were negatively charged.

The specific activity after ORR and stability studies as a function of the applied potential for both dendritic and spherical Pt_xY particles are shown in Fig. 2c. The two morphologies present dramatically different activities and corrosion resistance. The initial ORR specific activity at 0.9 V is ca. 13.5 mA cm_{Pt}⁻² for the spherical nanoparticles, while for the dendritic ones it decreases to 8.7 mA cm_{Pt}⁻². Not only is the activity, but also the stability influenced by the shape of the particles. Spherical particles only lose around 35 ± 5% of their activity after 9000 potential cycles. Dendritic particles lose around 60 ± 10% of their initial activity.

The first requirement for correct size-selection is the mono-dispersion of the nanoparticles. Using magnetron sputtering techniques, one typically scans a large range of masses to determine the distribution of masses that exit the sputtering chamber. Fig. 3 shows the particle size distribution (PSD) and a TEM image of a Pt_xY sample, where the peak intensity was intended to be 9 nm. It appears obvious that the deposition of monodispersed nanoparticles failed, since the PSD is trimodal and peaked at 8.75 nm, 11.2 nm and 13 nm.

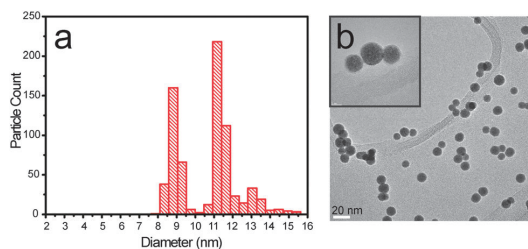


Fig. 3 (a) Particle size distribution for a 9 nm Pt_xY deposition and (b) bright field TEM image. In the inset (top left corner) three particles are magnified to show the presence of undesired double and triple mass particles.

Fig. 4a shows two deposition curves for Pt_xY 7 nm. In this case, a shift in the deposition curve minima was detected (from 2 million amu to 1.6 million amu) and some change in the shape of the deposition curves is noticeable.

A deposition curve is a mass distribution which is recorded before and after the deposition; before the deposition we select a target mass, *M*, which is kept fixed throughout the deposition.

As the deposition is completed, the features of the profile appear less smeared out, compared to the starting deposition curve. Nonetheless, the qualitative aspect of the curve is preserved. Furthermore, after deposition, an increase in the *M*/*2M* ratio was observed; the *M*/*2M* ratio shifts from 0.76 to 4.75.

A fraction of undesired particles, ca. 20%, is observed in both the particle size distribution and TEM micrograph displayed in Fig. 2c for the Pt_xY 7 nm sample. The intended size was ~7 nm.

As a reference for an ideal deposition we show, in Fig. 4d, two current *versus* mass curves for the Ru nanoparticle. In red, the current *versus* mass curve taken before the deposition is shown, and in blue the current *versus* mass curve collected after the deposition is shown. The curves do not vary significantly. The starting value of the *M*/*2M* ratio is 24, where *M* is the selected mass, and the *M*/*2M* ratio slightly increases throughout the deposition. The corresponding PSD and TEM shown in

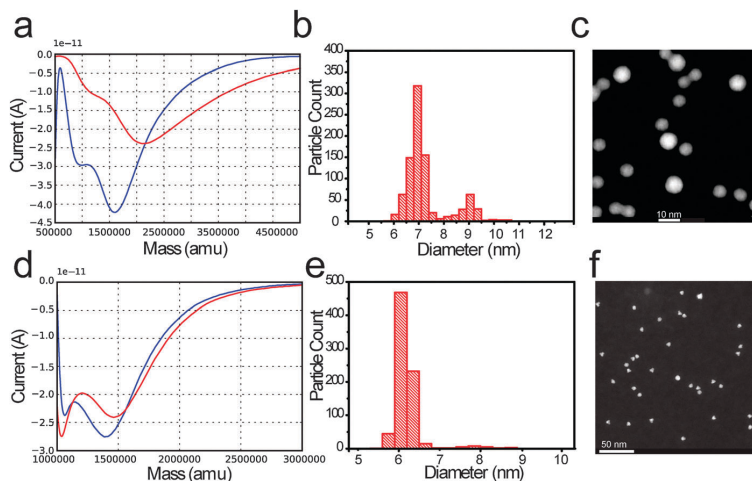


Fig. 4 (a) Current versus mass curve (measured with TOF mass selector) before (red curve) and after (blue curve) Pt_xY NPs deposition. (b) Corresponding particle size distribution and (c) representative dark field STEM image relative to the deposited sample. The intended size was 7 nm. As an ideal deposition reference: (d) current versus mass curve (measured with TOF mass selector) before (red curve) and after (blue curve) Ru NPs deposition. (e) Corresponding particle size distribution and (f) representative dark field STEM image relative to the deposited sample. The intended size was 7 nm.

Fig. 4e and f indicate a very little amount of undesired mass (about 4%) at ~ 7.8 nm.

Discussion

In the first part of the “Results” section, we presented a case which highlights the dependence of the nanoparticle composition on the composition of the sputtering target. The ISS spectra confirm that, at least on the surface, the nanoparticles produced from the Pt₃Y are richer in Y than the ones prepared from the Pt₅Y target. Furthermore, under the assumption that the composition of the Pt_xY alloy is uniform throughout the particle,⁴⁸ XPS after ORR show that the NPs produced from the Pt₃Y target are richer in Y than the NPs produced from the Pt₅Y. This is similar to what was observed by Gan *et al.* in an earlier study on Pt_xNi nanoparticles.⁵⁸

As we proposed recently,⁴⁸ the presence of Y in the Pt lattice induces a compressive surface strain in the Pt overlayer of the NP (Fig. 1a), destabilising OH intermediates of the ORR. However, a Pt/Y ratio different from the optimum one might change the amount of the binding energy shift, resulting in a less efficient catalyst.

Besides particle chemical composition, other parameters must be kept under control. In Fig. 2 we displayed two entirely different morphologies of Pt_xY nanoparticles obtained by sputtering a Pt₅Y target. The conditions of operation were totally different, though. To produce dendritic nanoparticles both the Ar flux and the power employed were around five times to one order of magnitude higher than those required to produce spherical nanoparticles. This provided a much higher rate of sputtering for the dendritic case than for the spherical case, which resulted in a higher rate of aggregation, as discussed by Alayan *et al.*⁵⁹

Importantly, these high sputtering rate conditions are imposed by the choice of positive particle deposition for the dendritic case. Negative particle deposition requires substantially lower sputtering rate, and therefore results in spherical particle production, rather than dendrite formation.

Different morphologies showed different reactivity in the electro-reduction of oxygen and also different corrosion resistance, with the spherical particles losing about a half in activity compared to the dendritic particles. Tentatively, the reduced corrosion resistance for the dendritic nanoparticles might be ascribed to easier diffusion of yttrium out of the dendritic nanostructures. Furthermore, the dendritic structure might modify the extent of the Pt lattice strain, thereby affecting the activity.

Besides morphology and chemical composition of the particle, one should also concentrate on monodispersity. The peaks in the trimodal distribution showed in Fig. 3 are located at particle diameters which have ratios of $(11.2/8.75) = 1.28$ and $(13/8.75) = 1.48$, respectively. These values are remarkably close, within the error bar, to the cube root of 2 (~ 1.26), and to the cube root of 3 (~ 1.45). This suggests that particles with mass double or triple of the intended mass were also deposited. TEM images shown in Fig. 3 and 4 confirm that double or triple mass particles were deposited.

This is a serious problem which can occur while depositing clusters and nanoparticles synthesized using sputtering and aggregation techniques. The presence of significant amounts of nanoparticles with double or triple masses may completely compromise the result of a catalytic experiment.

Masses are effectively filtered through a Von Issendorff type Time of Flight (TOF) mass filter, however, the chance for the deposition of undesired masses is not zero. Masses which are multiples according to an integer n of the intended mass M can

also be filtered; all that is needed is that their charge e is a multiple according to the same integer n , so that the mass to charge ratio is equal to the desired one. The relevant quantity here is the mass to charge ratio: $\frac{nM}{ne}$.

The presence of multiple negative charges (particularly with $n < 4$) is not unlikely for nanoparticles with diameter in the range 1–10 nm. This is due to the presence of a Coulomb barrier inhibiting the loss of electrons, as discussed by other authors.^{60,61} However, it seems that charges higher than $3e$ do not represent a serious threat for the deposition. This is corroborated by the fact that, in Fig. 3, the quadruple mass peak at $9 \times 1.59 = 14.3$ nm is really negligible compared to the other peaks.

Nanoparticles with a charge higher than $3e$ would probably rapidly discharge through the electron tunnelling mechanism. However, double ($n = 2$) or even triple negative charges ($n = 3$) can be retained by the nanoparticle for time intervals long enough to represent a serious problem in the particle mass selection process.

The case presented in Fig. 4a–c represents an acceptable case of deposition.

The deposition starts at 0.76 $M/2M$. This would be a disastrous ratio to start with, and a majority of $2M$ should be deposited. However, the ratio changes during the deposition, and the final ratio is 4.75. This prevents a large quantity of $2M$ from passing through the mass filter.

The reference case presented in Fig. 4d–f represents the ideal case of deposition. The $M/2M$ ratio is very high (>20) compared to Fig. 4a, and remains high throughout the deposition. As a consequence, very few $2M$ are filtered through the time of flight analyzer. The particles filtered are of a different element (Ru) compared to the ones shown in Fig. 4a–c, to stress the generality of the concept.

In summary, great care should be taken in choosing deposition profiles (deposition current *versus* deposited mass curves) which present an $M/2M$ ratio as high as possible. The outcome of the deposition should be checked at the end of the deposition, to ensure that such a ratio has not changed significantly, compared to the starting curve.

Deposition curves offer a fast and reliable diagnostic method to ensure that the deposition was performed correctly.

If the ratio of $M/2M$ stays at high values (>20 at least) throughout the deposition, one can be confident the amount of multiple masses will be minimized. This threshold value is expected to vary with particle size, resulting in larger particles (diameter > 5 nm) being the most exposed to this kind of problem.

To achieve a high $M/2M$ ratio, two phenomena should be avoided: (i) the shift of deposition minima and (ii) the appearance of new minima, compared to the pre-deposition curves. These two phenomena can mar the deposition outcome by changing the $M/2M$ ratio beyond the allowed threshold.

Interestingly, we have noticed that in the cluster source we use, a potentially dangerous shift in the deposition minimum can occur as a result of a variation in pressure in the aggregation chamber. In Fig. 5b, three deposition curves taken at 15 minutes

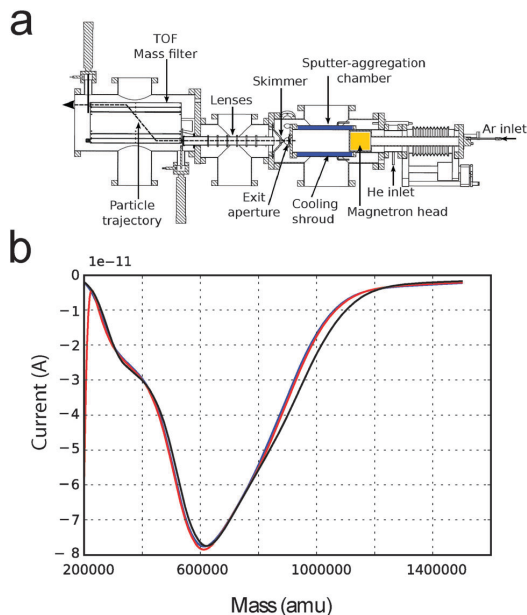


Fig. 5 (a) Scheme of the Birmingham cluster source used to deposit size selected nanoparticles. (b) Current *versus* mass deposition curves taken keeping the pressure in the sputter-aggregation chamber constant. The three deposition curves were collected at time intervals of 15 minutes.

time from each other are shown. In this case, the pressure at the “Exit Aperture” (Fig. 5a) was kept constant by regulating the flow of He/Ar sputter gas with a feedback loop. The deposition curves show no significant change over a time that is comparable with a typical deposition time. Therefore, we can conclude that by keeping the pressure constant, depositions which are more reliable can be achieved.

We note that the double or triple mass problem presented here might be, in rare cases, caused by other factors such as sudden changes in the plasma state or abrupt change in the temperature of the sputter-aggregation chamber.

Conclusions

Using the magnetron sputtering and gas aggregation technique, we have shown how composition and morphology influence the catalytic activity of Pt_xY nanoparticles. The interplay between microscopic, spectroscopic techniques and nanoparticle production is of paramount importance, if the catalytic properties of nanoparticles are to be correctly understood and predicted.

We have analysed the deposition curves (deposition current *versus* deposited mass) for size-selected nanoparticles produced using magnetron sputtering techniques. We proposed a simple protocol to gain feedback regarding whether the depositions contain negligible or intolerable amounts of double/triple mass. Although here we have focussed on Pt_xY nanoparticles,

our approach is general and could be applied to any particle produced using this method.

Acknowledgements

The authors gratefully acknowledge financial support from the Danish Ministry of Science's UNIK initiative, Catalysis for Sustainable Energy. The Center for Individual Nanoparticle Functionality is supported by the Danish National Research Foundation (DNRF54). The A. P. Møller and Chastine Mc-Kinney Møller Foundation is gratefully acknowledged for its contribution towards the establishment of the Centre for Electron Nanoscopy in the Technical University of Denmark. The Interdisciplinary Centre for Electron Microscopy (CIME) at EPFL is gratefully acknowledged for the use of the FEI Tecnai Osiris TEM. Support for this work was received from the Danish Council for Strategic Research's project NACORR (12-133817) and MEDLYS (10-093906). I.E.L.S. was supported by the ForskEL programme's project CATBOOSTER (2001-1-10669). D.N.M. is the recipient of a HC Ørsted postdoctoral fellowship.

References

- S. Vajda, M. J. Pellin, J. P. Greeley, C. L. Marshall, L. A. Curtiss, G. A. Ballentine, J. W. Elam, S. Catillon-Mucherie, P. C. Redfern, F. Mehmood and P. Zapol, *Nat. Mater.*, 2009, **8**, 213–216.
- Y. Lei, F. Mehmood, S. Lee, J. Greeley, B. Lee, S. Seifert, R. E. Winans, J. W. Elam, R. J. Meyer, P. C. Redfern, D. Teschner, R. Schlögl, M. J. Pellin, L. A. Curtiss and S. Vajda, *Science*, 2010, **328**, 224–228.
- J. A. van Bokhoven, C. Louis, J. T. Miller, M. Tromp, O. V. Safonova and P. Glatzel, *Angew. Chem., Int. Ed.*, 2006, **45**, 4651–4654.
- J. T. Miller, A. J. Kropf, Y. Zha, J. R. Regalbuto, L. Delannoy, C. Louis, E. Bus and J. A. van Bokhoven, *J. Catal.*, 2006, **240**, 222–234.
- A. Tuxen, S. Carencio, M. Chintapalli, C.-H. Chuang, C. Escudero, E. Pach, P. Jiang, F. Borondics, B. Beberwyck, A. P. Alivisatos, G. Thornton, W.-F. Pong, J. Guo, R. Perez, F. Besenbacher and M. Salmeron, *J. Am. Chem. Soc.*, 2013, **135**, 2273–2278.
- H. M. Torres Galvis, J. H. Bitter, C. B. Khare, M. Ruitenbeek, A. I. Dugulan and K. P. de Jong, *Science*, 2012, **335**, 835–838.
- G. Prieto, J. Zečević, H. Friedrich, K. P. de Jong and P. E. de Jongh, *Nat. Mater.*, 2013, **303**, 31–40.
- M. Nesselberger, M. Roefzaad, R. Faysal Hamou, P. Ulrich Biedermann, F. F. Schweinberger, S. Kunz, K. Schloegl, G. K. H. Wiberg, S. Ashton, U. Heiz, K. J. J. Mayrhofer and M. Arenz, *Nat. Mater.*, 2013, **3712**, 1–6.
- S. Kunz, K. Hartl, M. Nesselberger, F. F. Schweinberger, G. Kwon, M. Hanzlik, K. J. J. Mayrhofer, U. Heiz and M. Arenz, *Phys. Chem. Chem. Phys.*, 2010, **12**, 10288–10291.
- J. Gavnholt and J. Schiøtz, *Phys. Rev. B: Condens. Matter Mater. Phys.*, 2008, **77**, 035404.
- F. Masini, C. E. Strebel, D. N. McCarthy, A. U. F. Nierhoff, J. Kehres, E. M. Fiordaliso, J. H. Nielsen and I. Chorkendorff, *J. Catal.*, 2013, **308**, 282–290.
- F. J. Perez-Alonso, D. N. McCarthy, A. Nierhoff, P. Hernandez-Fernandez, C. Strebel, I. E. L. Stephens, J. H. Nielsen and I. Chorkendorff, *Angew. Chem., Int. Ed.*, 2012, **51**, 4641–4643.
- C. Chen, Y. Kang, Z. Huo, Z. Zhu, W. Huang, H. L. Xin, J. D. Snyder, D. Li, J. A. Herron, M. Mavrikakis, M. Chi, K. L. More, Y. Li, N. M. Markovic, G. A. Somorjai, P. Yang and V. R. Stamenkovic, *Science*, 2014, **343**, 1339–1343.
- S. Mostafa, F. Behafarid, J. R. Croy, L. K. Ono, L. Li, J. C. Yang, A. I. Frenkel and B. R. Cuenya, *J. Am. Chem. Soc.*, 2010, **132**, 15714–15719.
- F. Behafarid, L. K. Ono, S. Mostafa, J. R. Croy, G. Shafai, S. Hong, T. S. Rahman, S. R. Bareb and B. Roldan Cuenya, *Phys. Chem. Chem. Phys.*, 2012, **14**, 11766–11779.
- G. L. Bezemer, J. H. Bitter, H. P. C. E. Kuipers, H. Oosterbeek, J. E. Holewijn, X. Xu, F. Kapteijn, A. J. van Dillen and K. P. de Jong, *J. Am. Chem. Soc.*, 2006, **128**, 3956–3964.
- M. Haruta, *Catal. Today*, 1997, **36**, 153–166.
- S. H. Joo, J. Y. Park, J. R. Renzas, D. R. Butcher, W. Huang and G. A. Somorjai, *Nano Lett.*, 2010, **10**, 2709–2713.
- N. Dahl, A. Logadottir, R. C. Egeberg, J. H. Larsen, I. Chorkendorff, E. Törnqvist and J. K. Nørskov, *Phys. Rev. Lett.*, 1999, **83**, 1814–1817.
- S. B. Vendelbo, M. Johansson, J. H. Nielsen and I. Chorkendorff, *Phys. Chem. Chem. Phys.*, 2011, **13**, 4486–4493.
- S. B. Vendelbo, M. Johansson, D. J. Mowbray, M. P. Andersson, F. Abild-Pedersen, J. H. Nielsen, J. K. Nørskov and I. Chorkendorff, *Top. Catal.*, 2010, **53**, 357–364.
- H. A. Gasteiger, S. S. Kocha, B. Sompalli and F. T. Wagner, *Appl. Catal., B*, 2005, **56**, 9–35.
- K. J. J. Mayrhofer, D. Strmcnik, B. B. Blizanac, V. Stamenkovic, M. Arenz and N. M. Markovic, *Electrochim. Acta*, 2008, **53**, 3181–3188.
- S. W. Lee, S. Chen, W. Sheng, N. Yabuuchi, Y.-T. Kim, T. Mitani, E. Vescovo and Y. Shao-Horn, *J. Am. Chem. Soc.*, 2009, **131**, 15669–15677.
- J. P. Greeley, J. Rossmeisl, A. Hellman and J. K. Nørskov, *Z. Phys. Chem.*, 2007, **221**, 1209–1220.
- G. A. Tritsarlis, J. Greeley, J. Rossmeisl and J. K. Nørskov, *Catal. Lett.*, 2011, **141**, 909–913.
- M. Nesselberger, S. Ashton, J. C. Meier, I. Katsounaros, K. J. J. Mayrhofer and M. Arenz, *J. Am. Chem. Soc.*, 2011, **133**, 17428–17433.
- W. Sheng, S. Chen, E. Vescovo and Y. Shao-Horn, *J. Electrochem. Soc.*, 2012, **159**, B96–B103.
- A. Kuzume, E. Herrero and J. M. Feliu, *J. Electroanal. Chem.*, 2007, **599**, 333–343.
- A. Hitotsuyanagi, M. Nakamura and N. Hoshi, *Electrochim. Acta*, 2012, **82**, 512–516.
- A. S. Bandarenka, H. A. Hansen, J. Rossmeisl and I. E. L. Stephens, *Phys. Chem. Chem. Phys.*, 2014, **16**, 13625–13629.
- H. A. Gasteiger and N. M. Markovic, *Science*, 2009, **324**, 48–49.
- I. E. L. Stephens, A. S. Bondarenko, U. Grønbjerg, J. Rossmeisl and I. Chorkendorff, *Energy Environ. Sci.*, 2012, **5**, 6744–6762.

- 34 T. Toda, H. Igarashi, H. Uchida and M. Watanabe, *J. Electrochem. Soc.*, 1999, **146**, 3750–3756.
- 35 V. R. Stamenkovic, B. Fowler, B. S. Mun, G. Wang, P. N. Ross, C. A. Lucas and N. M. Markovic, *Science*, 2007, **315**, 493–497.
- 36 V. R. Stamenkovic, B. S. Mun, M. Arenz, K. J. J. Mayrhofer, C. A. Lucas, G. Wang, P. N. Ross and N. M. Markovic, *Nat. Mater.*, 2007, **6**, 241–247.
- 37 D. L. Wang, H. L. L. Xin, R. Hovden, H. S. Wang, Y. C. Yu, D. A. Muller, F. J. DiSalvo and H. D. Abruna, *Nat. Mater.*, 2013, **12**, 81–87.
- 38 C. H. Cui, L. Gan, M. Heggen, S. Rudi and P. Strasser, *Nat. Mater.*, 2013, **12**, 765–771.
- 39 H. L. Xin, J. A. Mundy, Z. Liu, R. Cabezas, R. Hovden, L. F. Kourkoutis, J. Zhang, N. P. Subramanian, R. Makharia, F. T. Wagner and D. A. Muller, *Nano Lett.*, 2011, **12**, 490–497.
- 40 S. Chen, H. A. Gasteiger, K. Hayakawa, T. Tada and Y. Shao-Horn, *J. Electrochem. Soc.*, 2010, **157**, A82–A97.
- 41 L. Dubau, F. Maillard, M. Chatenet, J. André and E. Rossinot, *Electrochim. Acta*, 2010, **56**, 776–783.
- 42 J. Greeley, I. E. L. Stephens, A. S. Bondarenko, T. P. Johansson, H. A. Hansen, T. F. Jaramillo, J. Rossmeisl, I. Chorkendorff and J. K. Nørskov, *Nat. Chem.*, 2009, **1**, 552–556.
- 43 M. Escudero-Escribano, A. Verdager-Casadevall, P. Malacrida, U. Grønbyjerg, B. P. Knudsen, A. K. Jepsen, J. Rossmeisl, I. E. L. Stephens and I. Chorkendorff, *J. Am. Chem. Soc.*, 2012, **134**, 16476–16479.
- 44 I. E. L. Stephens, A. S. Bondarenko, L. Bech and I. Chorkendorff, *ChemCatChem*, 2012, **4**, 341–349.
- 45 T. P. Johansson, E. T. Ulrikkeholm, P. Hernandez-Fernandez, P. Malacrida, H. A. Hansen, A. S. Bandarenka, J. K. Nørskov, J. Rossmeisl, I. E. L. Stephens and I. Chorkendorff, *Top. Catal.*, 2014, **57**, 245–254.
- 46 P. Malacrida, M. Escudero-Escribano, A. Verdager-Casadevall, I. E. L. Stephens and I. Chorkendorff, *J. Mater. Chem. A*, 2014, **2**, 4234–4243.
- 47 T. P. Johansson, E. T. Ulrikkeholm, P. Hernandez-Fernandez, M. Escudero-Escribano, P. Malacrida, I. E. L. Stephens and I. Chorkendorff, *Phys. Chem. Chem. Phys.*, 2014, **16**, 13718–13725.
- 48 P. Hernandez-Fernandez, F. Masini, D. N. McCarthy, C. E. Strebøl, D. Friebeł, D. Deiana, P. Malacrida, A. Nierhoff, A. Bodin, A. M. Wise, J. H. Nielsen, T. W. Hansen, A. Nilsson, I. E. L. Stephens and I. Chorkendorff, *Nat. Chem.*, 2014, DOI: 10.1038/nchem.2001.
- 49 V. Komanicky, H. Iddir, K.-C. Chang, A. Menzel, G. Karapetrov, D. Hennessy, P. Zapol and H. You, *J. Am. Chem. Soc.*, 2009, **131**, 5732–5733.
- 50 C. Wang, H. Daimon, T. Onodera, T. Koda and S. Sun, *Angew. Chem., Int. Ed.*, 2008, **47**, 3588–3591.
- 51 J. Wu, J. Zhang, Z. Peng, S. Yang, F. T. Wagner and H. Yang, *J. Am. Chem. Soc.*, 2010, **132**, 4984–4985.
- 52 J. X. Wang, C. Ma, Y. Choi, D. Su, Y. Zhu, P. Liu, R. Si, M. B. Vukmirovic, Y. Zhang and R. R. Adzic, *J. Am. Chem. Soc.*, 2011, **133**, 13551–13557.
- 53 L. Dubau, M. Lopez-Haro, L. Castanheira, J. Durst, M. Chatenet, P. Bayle-Guillemaud, L. Guétaz, N. Caqué, E. Rossinot and F. Maillard, *Appl. Catal., B*, 2013, **142–143**, 801–808.
- 54 H. Haberland, M. Karrais, M. Mall and Y. Thurner, *J. Vac. Sci. Technol., A*, 1992, **10**, 3266–3271.
- 55 B. von Issendorff and R. E. Palmer, *Rev. Sci. Instrum.*, 1999, **70**, 4497–4501.
- 56 F. Maillard, E. R. Savinova and U. Stimming, *J. Electroanal. Chem.*, 2007, **599**, 221–232.
- 57 M. P. S. D. Briggs, *Practical Surface Analysis, Auger and X-ray Photoelectron Spectroscopy*, 1996.
- 58 L. Gan, M. Heggen, S. Rudi and P. Strasser, *Nano Lett.*, 2012, **12**, 5423–5430.
- 59 R. Alayan, L. Arnaud, M. Broyer, E. Cottancin, J. Lermé, J. L. Vialle and M. Pellarin, *Phys. Rev. B: Condens. Matter Mater. Phys.*, 2006, **73**, 125444.
- 60 R. N. Compton, A. A. Tuinman, C. E. Klots, M. R. Pederson and D. C. Patton, *Phys. Rev. Lett.*, 1997, **78**, 4367–4370.
- 61 C. Yannouleas and U. Landman, *Chem. Phys. Lett.*, 1994, **217**, 175–185.

The enhanced activity of mass-selected Pt_xGd nanoparticles for oxygen electroreduction

Amado Velázquez-Palenzuela^a, Federico Masini^a, Anders F. Pedersen^a, María Escudero-Escribano^a, Davide Deiana^b, Paolo Malacrida^a, Thomas W. Hansen^b, Daniel Friebel^c, Anders Nilsson^c, Ifan E.L. Stephens^a, Ib Chorkendorff^a

a Center for Individual Nanoparticle Functionality (CINF), Department of Physics, Technical University of Denmark, Kongens Lyngby DK-2800, Denmark

b Center for Electron Nanoscopy (CEN), Technical University of Denmark, Kgs Lyngby DK-2800, Denmark

c SLAC National Accelerator Laboratory, 2575 Sand Hill Road, MS31, Menlo Park CA 94025, USA

Abstract

Mass-selected platinum-gadolinium alloy nanoparticles (Pt_xGd NPs) are synthesized for the first time as oxygen reduction reaction (ORR) electrocatalysts using the gas aggregation technique, under ultra-high vacuum (UHV) conditions. The morphology of the Pt_xGd catalysts is characterized and their catalytic performance towards the ORR is assessed in acidic media using a half-cell configuration. The Pt_xGd 8 nm catalyst shows a high activity (3.6 A (mg Pt)⁻¹), surpassing the highest activity reached so far with Pt_xY NP catalysts. In addition, the optimum Pt_xGd catalyst also presents high stability, as suggested by the accelerated stability tests under ORR potential cycling. Extended X-ray Absorption Fine Structure (EXAFS) spectroscopy measurements confirm

that as-prepared Pt_xGd NPs are compressively strained, relative to pure Pt and that a Pt_xGd core/Pt-rich shell structure is adopted after partial Gd leaching. The activity correlates strongly with the compressive strain. On that basis, we propose that the ORR enhancement is due to the compressive strain within the Pt shell induced by the alloy core. The results herein confirm the suitability of Pt_xGd NPs as cathode nanocatalysts for proton exchange membrane fuel cells (PEMFCs).

Keywords: Electrocatalysis - Fuel cells - Oxygen reduction reaction – Nanoparticles - Platinum-gadolinium alloy – Core/shell - Strain effect

1. Introduction

This research article is dedicated to the memory of Haldor Topsøe (1913-2013), who was always a strong proponent of fundamental research towards improved catalysis.

Both electrocatalysis and traditional heterogeneous catalysis focus on surface reactions that involve multistep reaction pathways, with sequential breaking and/or creation of chemical bonds. The catalyst consists of supported nanoparticles whose atomic and electronic structure are analyzed by means of common characterization techniques, such as X-ray photoelectron spectroscopy (XPS), transmission electron microscopy (TEM), or X-ray absorption spectroscopy (XAS) [1]. The main difference between the fields is that in electrocatalysis, the structure of the electrified metal/solution interface needs to be taken into account, which contains solvent molecules and other charged species. Despite these inherent challenges, it turns out that the factors that control the reactivity of surfaces towards gas/solid catalytic reactions are largely the same as for electrocatalytic reactions, i.e. the binding to the reaction intermediates [2]. Sabatier's principle states that the optimum catalyst should bind neither too weakly or too strongly to the reaction intermediates [3]. According to the density functional theory (DFT) calculations of Nørskov, Rossmeisl and coworkers, the binding energies of the reaction intermediates in multi-electron reactions tend to scale linearly together [4,5]. Consequently, the binding energy of just one reaction intermediate can be used as descriptor to predict the trends in activity for electrocatalytic reactions; plotting the activity as a function of such a descriptor then results in a Sabatier volcano. This model has been able to describe trends for a number of electrocatalytic reactions [6–15], in particular the oxygen reduction reaction (ORR) [4,13,16–22]. It turns out that proton exchange membrane fuel cells (PEMFCs) are limited by the ORR. Consequently, large loadings of Pt nanoparticle catalysts are required at the cathode to limit potential losses, as Pt is the most active pure metal catalyst for the reaction. [23]. Typically, the Pt loading at the PEMFC cathode, where the ORR takes place, is around one order of magnitude higher than the Pt loading at the anode (0.4 mg Pt cm⁻² vs. 0.05 mg Pt cm⁻²) where the hydrogen oxidation reaction (HOR), which is far more facile, occurs [23–27]. As a result, the high cost and short supply of Pt hinders the large scale uptake of PEMFC's, despite their promise as efficient, potentially zero-emission source of power for automotive vehicles and portable devices [28].

A suitable strategy in order to improve the ORR activity, and hence reduce the Pt loading at the cathode, is to use Pt alloys instead of pure Pt [16,23,28–30]. The effect of alloying is to weaken the binding of the surface to the

hydroxyl intermediates. In accordance to the volcano model [4], the overpotential on pure Pt catalysts is due to the reduction of *OH (where *OH is an adsorbed hydroxyl intermediate) [4,16,31–34]. The optimum catalyst for the ORR should have an *OH binding energy 0.1 eV weaker than Pt(111), or an O* binding 0.2 eV weaker; excessive weakening of HO* will cause the reaction to be limited by the formation of the superhydroxyl intermediate, HOO* [35]. Typically, the surface atoms of a Pt alloy will consist of pure Pt, as most other metals will be unstable at the oxidising, acidic, conditions of a PEMFC cathode. Thereby, the introduction of a second metal in the Pt structure induces a change in the electronic structure of the Pt surface atoms; this can either be induced because of direct interactions with the second metal, i.e. the *ligand effect* [19,36,37] and/or the existence of lattice compression (*strain effect*), as result of a decrease of the Pt-Pt interatomic distances [38–40].

In recent years, efforts have been focused on Pt-alloys with late transition metals (LTM), such as Fe, Ni, Cu and Co; they have shown considerably greater activity compared to pure Pt [41–51]. The active phase in these alloys is a Pt overlayer whose thickness strongly depends on the catalyst pre-treatment [46]. Thus, the Pt overlayer is typically one monolayer thick when the Pt-LTM alloy is subjected to annealing in ultra-high vacuum (UHV) conditions prior to the electrochemical characterization ("Pt-skin" surface) [46]. In contrast, a considerably thicker, ~1 nm Pt overlayer, equivalent to 3-4 monoatomic Pt layers, is achieved when the alloy is exposed to the acidic electrolyte, because of leaching of the less noble metal from the outermost atomic layers of the surface (denoted by Markovic, Stamenkovic and coworkers as a "Pt-skeleton" surface) [46,52]. On such a thick Pt overlayer, ligand effects can be excluded, and hence the ORR enhancement should be due to surface strain effects.

Although these Pt alloy catalysts show significant initial enhancements in activity, relative to pure Pt, over time their performance tends to degrade: the second element will segregate to the surface and dissolve into the electrolyte, via a process known as dealloying [43,48,53–58].

As a result of the instability of alloys of Pt and late transition metals, we, in collaboration with theory group of Nørskov and Rossmeisl, screened for a more stable class of Pt alloy ORR catalysts, using computational DFT based screening methods [18]. We searched for alloys that were not only predicted to be active, on the basis of the O* binding, but also stable, as predicted by the alloying energy; the output of the screening was that both Pt₃Y and Pt₃Sc should be active and stable. Subsequent experiments on sputter-cleaned polycrystalline Pt₃Y showed that it exhibited exceptionally high activity for the ORR, only surpassed by single-crystal Pt₃Ni(111) with an annealed "Pt-skin" structure [50]. The considerable negative alloying energy (or heats of

formation) of Pt₃Y and Pt₃Sc ($\Delta H_{f(\text{alloy})} \approx -4$ eV/formula unit), is also shared by other Pt alloys with early transition metals and lanthanides, such as Pt₅La, Pt₅Ce and Pt₅Gd; this contrasts with the negligible heat of formation of the Pt-LTM intermetallic compounds (LTM = Fe, Co, Cu, Ni; $\Delta H_{f(\text{alloy})} > -1$ eV) [59,60] (we note that, despite their denomination as “rare earths”, the lanthanide metals are much more abundant and more inexpensive than Pt [61]). We are aware that, despite the significant heat of formation of the Pt-lanthanides alloys, there is still an immense driving force for the dealloying of the solute metal under the corrosive environment of a PEMFC cathode. Nevertheless, we expect that the dealloying mechanism ultimately involves an energy barrier for diffusion determined at least partially driven by the heat of formation of the bulk alloy, hence its use as a descriptor of the kinetic stability [18]. This notion is consistent with surface science experiments performed at our laboratory: a Cu monolayer on Pt(111) will diffuse subsurface at ~500 K [62]; under the same conditions, a Y monolayer on Pt(111) will diffuse subsurface at ~800 K [63]. This is likely due to the stronger interaction between Pt and Y than between Pt and Cu, ($\Delta H_{f(\text{Pt}_3\text{Y})} \approx -4.04$ eV/formula unit than $\Delta H_{f(\text{Pt}_3\text{Cu})} \approx -0.56$ eV/formula unit) [18]. On the other hand, adsorbed O* or subsurface oxide may induce the segregation of the solute element [64], but only when the oxygen atom is in close vicinity to the solute metal.

Our subsequent electrochemical experiments also revealed that other Pt-lanthanide alloys show superior activity for the ORR in the bulk polycrystalline form, in particular Pt₅Gd, which shows a similar activity to Pt₃Y [30,59,60,65]. We must emphasise that sputter-cleaned polycrystalline Pt₅Gd and Pt₃Y alloys have displayed the highest ORR activities ever reported in the literature, to the best of our knowledge the highest for samples prepared in this manner (5-fold increase at 0.9 V, compared to polycrystalline Pt) [60,65]. Furthermore, these intermetallic compounds exhibit a high stability under ORR conditions. For example, Pt₅Gd only exhibits 15% activity loss after 10,000 cycles between 0.6 and 1.0 V in O₂-saturated electrolyte [59,60]. In comparison, Todoroki and coworkers demonstrated that Pt-enriched Ni/Pt(111) lost 75% of its initial activity under similar experimental conditions [48]. Moreover, the great stability of Pt-early transition metal alloys has been also confirmed by Lim and coworkers through analysis of sputtered thin-film electrodes [66].

It turns out that the origin of activity of Pt₃Y was somewhat more complicated than we originally anticipated [63,65]. Angle-resolved X-ray photoelectron spectroscopy (AR-XPS) analysis of the sputter-cleaned alloyed electrodes showed that a Pt-skeleton structure is developed after the electrochemical experiment, the Pt overlayer being around 1 nm thick. A similar structure was also found for Pt₅Gd alloy after the electrochemical

measurement [60] and, consequently, the ORR enhancement in both cases was attributed to compressive strain imposed onto the Pt overlayer by the alloy bulk. Such behavior seems counterintuitive, given that Y and Gd has a larger covalent radius than Pt [67]; one could expect that the resulting alloy would induce surface tensile strain, leading to a stronger adsorption of *OH and a higher overpotential for the ORR. Nevertheless, we explain the superior ORR activity of Pt_xY and Pt₅Gd compared to pure Pt by considering the inherent structural characteristics of such alloys. In order to accommodate the different Pt and second metal atomic radii most of the Pt atoms are arranged in *kagomé* nets with a very short Pt–Pt nearest-neighbour distance (< 2.7 Å) and with larger voids in which the solute atoms reside with bond lengths greater than 3 Å to their neighbor atoms (see Figure S1 in the Supplementary Information for an illustrative example of such arrangement). On the basis of the described structure, we proposed that Pt_xY and Pt₅Gd alloys impose compressive strain onto the Pt overlayer [60,65], resulting in weaker *OH adsorption and enhanced oxygen reduction activity.

In the light of our results with extended surfaces of Pt_xY and Pt₅Gd, we aimed to synthesise the catalysts in the more technologically relevant nanoparticulate form. Nevertheless, this task is not trivial, because of the difficulties of synthesizing the non-noble metal in the metallic state, due to the particularly negative standard reduction potential of Gd or Y ($U^0(\text{Gd}^{3+}/\text{Gd}) = -2.28$ V and $U^0(\text{Y}^{3+}/\text{Y}) = -2.37$ V); in comparison, late transition metals, such as Ni, have a much more positive dissolution potential ($U^0(\text{Ni}^{2+}/\text{Ni}) = -0.25$ V) [68]. This drawback makes it highly challenging to synthesise Pt_xGd and Pt_xY alloy nanoparticles by means of traditional wet chemical methods, which would involve the exposure of the non-noble metal to oxygen or water [69]. Consequently, in order to prove that nanoparticles of this class of catalysts could be worthy of further investigation, and eventual chemical synthesis, we resorted to a physical method for producing Pt_xY nanoparticles [70]. Our chosen route was the gas aggregation method, combined with time-of-flight separation after sputtering of a primary alloy target [70–75]. Apart from providing a proof-of-concept, this method also produces catalysts with a well-defined size, shape, morphology and composition, providing significant scientific insight. The corresponding ORR activities displayed in the electrochemical experiments, avoid typical secondary factors, such as possible interactions of the nanoparticles with a high surface area carbon substrate or the influence of the metal precursors/solvents employed in the synthesis [76–80]. Our work showed that the ORR activity of Pt_xY nanoparticles supported on a planar glassy carbon support showed a marked size-dependence; the 9 nm catalyst showing an exceptionally high mass activity of 3.05 A (mg Pt)⁻¹, only surpassed by the performance of annealed Pt₃Ni nanoframes [41]. In addition, the Pt_xY

catalyst retained 63% of the activity after accomplishing the long-term stability test under ORR conditions. These results confirmed that the high ORR activity of the sputter-cleaned Pt₃Y alloy [18] could be extended to the nanoparticulate form and that they show moderate stability.

Herein, we extend this approach to perform structural and electrochemical characterization of Pt_xGd alloy nanoparticles synthesized by the gas aggregation method, following the same procedure used for the production of Pt_xY nanoparticles. The activity of the Pt_xGd nanoparticles towards the ORR was evaluated in half-cell configuration by use of the rotating ring-disk electrode (RRDE) technique. In addition, the composition and morphology changes of the catalysts before and after the electrochemical test were characterized by means of XPS, transmission electron microscopy (TEM) and extended X-ray absorption fine structure (EXAFS) spectroscopy measurements.

2. Materials and Methods

2.1. Synthesis of mass-selected Pt_xGd nanoparticles

The nanoparticles were prepared using a magnetron sputter gas aggregation source (Birmingham Instruments Inc.), combined with time-of-flight mass filtering, and deposited onto glassy carbon electrodes mounted in a multichamber ultrahigh vacuum (UHV) system (Omicron, Multiscan Lab) with a base pressure in the 10⁻¹¹ mbar region. The gas aggregation technique involves Ar⁺ sputtering of an alloy target (in this study a Pt 9:1 Gd alloy target from Kurt J. Lesker Inc.), to produce an atomic vapor that is condensed into nanoparticles through collisions with cooled Ar and He gas. It must be noted that the composition of the target determines the atomic ratio of the mass-selected nanoparticles, as demonstrated with Pt_xY nanoparticles in our preceding publications [70,81]. It turns out the use of a target with the same composition than the corresponding extended, polycrystalline alloy of interest leads to nanoparticles with high solute content that would corrode in excess [65,70,81]. Consequently, in the present study we used the same 9:1 ratio for the synthesis of Pt-rich Pt_xGd nanocatalysts.

The gas aggregation method is particularly useful in the context of metallic formation of nanoparticles from metals such as gadolinium that have high affinities for oxygen, as it is an ultrahigh vacuum compatible method: oxygen is present in extremely low levels and therefore it can entirely be avoided in the as-deposited Pt-Gd alloy particles. The second major advantage arises from the fact that many of the nanoparticles produced via aggregation of Ar⁺ sputtering atoms are ionized [82], thus the particles can be filtered based on their mass-to-charge ratio, which in turn allows the

deposition of particles with narrow size distributions. In our experiments, the Pt-Gd nanoparticles are filtered using a time-of-flight mass filter [83].

Following the particle production and filtering stages, the ionized nanoparticles were directed using Einzel lenses onto glassy carbon electrode supports mounted in the vacuum chamber. The Einzel lenses can be used to control the breadth and position of the particle beam, which gives control of the total number of particles that are deposited onto the electrode surface, as well as the density of the nanoparticles. The combination of particle counting and mass selection allow us to accurately estimate the amount of catalyst deposited onto the glassy carbon substrate. The mass which was used for the calculation of the mass activity was the mass calculated from the deposition current.

Assuming spherical and singly charged particles, the total deposited mass was calculated from the formula $M_{\text{dep}} = m_p I_{\text{dep}} t$, where m_p is the single particle mass, set using the mass filter, I_{dep} the deposition current and t the deposition time. This mass, from the deposition current, combined with the Pt:Gd ratio estimated from the XPS measurements of the as-prepared catalysts, was used to determine the mass activity for the ORR.

Elemental characterization of the as-prepared glassy carbon supported Pt-Gd nanoparticles was performed in-situ for each nanoparticles size, i.e. without breaking the vacuum, using X-ray photoelectron spectroscopy (XPS). The X-ray source was an XR-50 from Specs GmbH., with Aluminum and Magnesium anodes. XPS and ISS measurements after air exposure and after electrochemical testing were conducted in a different UHV system.

2.2. X-ray photoelectron spectroscopy (XPS)

X-ray photoelectron spectroscopy (XPS) measurements were acquired in two different UHV chambers. A preliminary analysis of the as-prepared nanoparticles was performed in-situ, soon after deposition. In this first experimental setup the X-ray source (XR-50 manufactured by SPECS GmbH) consisted of a Mg anode (Mg K α emission line at 1253.6 eV). The XPS spectra were measured with an Omicron hemispherical analyzer with a pass energy of 25 eV. Ex-situ measurements of the samples after air-exposure, after ORR activity tests and after stability tests were instead performed in a Theta-Probe instrument (Thermo Scientific). This instrument is equipped with a monochromatized Al K α source (emission line at 1486.7 eV), and XPS spectra were obtained at an analyzer pass energy of 100 eV. In all cases the atomic concentrations were quantified by integration of the Pt 4f, Gd 4d, O 1s, C 1s peaks after removal of a Shirley-type background. The resulting XPS intensities were corrected for the transmission function of the

analyzers, Wagner sensitivity factors [84] and electron mean free path estimated from the TPP-2M formula [85].

2.3. Transmission electron microscopy (TEM) analysis

Bright-field transmission electron microscopy (TEM) and high angle annular dark field scanning transmission electron microscopy (HAADF-STEM) was performed in a FEI Titan Analytical 80-300 equipped with a CEOS C_s probe aberration corrector on the condenser lens. Identical Location (IL) studies were carried out in bright-field TEM at 300 kV accelerating voltage. The particle size distributions (PSD) were extracted from HAADF-STEM micrographs acquired at 300 kV accelerating voltage. Within each specimen, the HAADF-STEM images were analyzed with the same microscope condition, constant acquisition dwell time as well as the HAADF detector settings. For the TEM measurements, the nanoparticles were deposited directly onto lacey carbon-coated Au TEM grids. The setup for the electrochemical stability test under ORR conditions was adapted from the procedure developed from an earlier study at our laboratory [86].

2.4. Electrochemical measurements

The electrochemical testing of the Pt_xGd nanoparticles was carried out in a custom-made three-electrode glass cell provided with an external jacket attached to a water bath with temperature control. The counter electrode was a Pt wire and the reference was a Hg|Hg₂SO₄ electrode, both separated from the working electrode compartment using ceramic frits. The electrolyte, 0.1 M HClO₄, was prepared using high-purity 70% HClO₄ (Merck, Suprapur) and ultrapure water (Millipore Milli-Q, resistivity > 18.2 MΩ cm⁻¹), whereas all the gases used in the electrochemical tests were grade 5N5 (AGA). All the measurements were accomplished at 23 ± 1 °C.

The electrochemical experiments were performed with a VMP2 multi-channel potentiostat (Bio-Logic Instruments) computer-controlled using EC-Lab software. The rotating ring-disk electrode (RRDE) assemblies and the glassy carbon (GC) substrates (5 mm diameter) were acquired from Pine Instruments Corporations and HTW, respectively. All the potentials indicated in the text are referred to the reversible hydrogen electrode (RHE) measured in the same electrolyte and corrected for Ohmic losses.

In each experiment, the GC disk containing the as-prepared Pt_xGd nanoparticles was inserted into a RRDE Teflon holder and used as working electrode for the electrochemical test. Subsequently, the electrode was immersed into the electrochemical cell under potential control at 0.10 V in N₂-saturated 0.1 M HClO₄ electrolyte and subjected to potential cycling

between 0.05 V and 1.00 V at 50 mV s⁻¹ until a stable cyclic voltammogram was achieved. Following this, the ORR performance of the Pt_xGd nanoparticles was evaluated by means of hydrodynamic voltammetry in O₂-saturated solution. After the ORR experiment, CO-stripping analysis was carried out for determining the electrochemical surface area (ECSA) of the Pt_xGd nanoparticles. For this purpose, CO gas was first bubbled into the electrolyte for 2 min, while the working electrode potential was kept at 0.05 V; and then the remaining CO dissolved in solution was removed by sparging Ar for 15 min whereas keeping the potential control. Afterwards, the potential was scanned up to 1.00 V in CO-free Ar purged solution at 50 mV s⁻¹. The corresponding electrochemical active surface area (ECSA) of the Pt_xGd catalysts was estimated assuming a ratio of 420 μC cm⁻² [87].

The long-term stability of the Pt_xGd nanoparticles was subjected to analysis by cycling between 0.60 and 1.00 V at 100 mV s⁻¹ in quiescent O₂-saturated 0.1 M HClO₄ solution for a total of 10,000 potential cycles. The ORR activity was evaluated after 1,000 and 10,000 potential cycles. A second CO stripping experiment was performed in order to probe the possible change of the electrochemical area after the stability test.

2.5. Extended X-ray absorption fine structure (EXAFS) analysis

Grazing incidence x-ray absorption spectroscopy (GI-XAS) measurements were carried out at beam line 11-2 at the Stanford Synchrotron Radiation Lightsource (SSRL). An absorption spectrum around the Pt L₃ edge (11,564 eV) was acquired for each sample, and the energy range was 11,334-12,273 eV, which corresponds to an EXAFS range up to a photoelectron wavenumber of 13.6 Å⁻¹. The samples were aligned in grazing incidence geometry near the critical angle of total external reflection in order to maximize the fluorescence yield. The fluorescence photons from the Pt atoms in the nanoparticles were captured using a 100 element Ge solid state detector. Several spectra were recorded for each sample, and subsequently averaged to increase the signal-to-noise ratio. The data analysis was done using the program SixPACK, which is based on the IFEFFIT program. EXAFS fitting was done in *R*-space using a *k*-weighting of *k*², a *k*-range of 3-11 Å⁻¹, and an *R*-range of around 1.5-3.2 Å. A detailed description of the data treatment and the fitting procedure can be found in the Supplementary Information.

3. Results

3.1. Synthesis of mass-selected Pt_xGd nanoparticles

The mass-selected Pt_xGd particles were prepared through combination of gas aggregation of a Pt₆Gd target and time of flight separation as shown in Figure 1. The charged nanoparticles were subsequently deposited directly onto a planar glassy carbon substrate under ultra-high vacuum conditions. In order to define the overall particle composition, XPS measurements were acquired in-situ after deposition. Figure S2 shows that the Pt:Gd ratios were rather similar in all cases, irrespective of the particle size, with an average value of 3.6 ± 0.8 .

3.2. X-ray photoelectron spectroscopy (XPS)

Further XPS characterization was carried out ex-situ after exposure of the samples to air and after electrochemical ORR activity testing. Figure 2 reports the XPS spectra of the Gd 4d core-level region for a 9 nm sample in different conditions: very similar spectra were also taken for different particle sizes indicating that the following considerations can be extended to all Pt_xGd nanoparticles. As typical for the lanthanide metals, the XPS features of Gd are in general quite complex due to presence of localized electrons in the 4f shell. The localized f electrons couples through Russell-Saunders and spin-orbit coupling and result in a complex broad multiplet structure see Figure 2 [88]. In principle this could be fitted using the multiplet structure but we have here chosen to perform a careful analysis of the peak position and a comparison with the reference spectrum of a sputter-cleaned Pt₅Gd polycrystalline alloy where Gd atoms are in a completely metallic state, allows us to monitor the chemical state of Gd. In the case of the as-deposited 9 nm Pt_xGd nanoparticles, the position of the Gd 4d spectrum is very similar to the polycrystalline sample, demonstrating that the synthesis of alloyed nanoparticles was successful and that no Gd oxidation occurred. However, as soon as the nanoparticles are taken out of the deposition chamber and exposed to air, a clear shift of the Gd 4d features and a change of shape can be observed, the new peak position agrees with the formation of Gd oxide on the surface [88]. Notably, these oxidized components are completely removed after electrochemical measurements, suggesting that the oxide is not stable in acid and dissolves in the electrolyte, in agreement with the Pourbaix diagram for Gd [68]. The remaining Gd signal resembles closely that of the as-prepared nanoparticles and that of clean polycrystalline Pt₅Gd; this indicates that a Pt overlayer is formed during the acid leaching of surface Gd and this Pt shell protects the alloyed Gd in the core from further oxidation or dissolution [60]. The formation of such core-shell structure is also supported by the measured Pt:Gd ratios in Figure S2: for all particle sizes and in particular for the small nanoparticles the relative amount of Pt after electrochemistry is considerably higher than for the as-

prepared or air-exposed nanoparticles. It should be noticed that analogous XPS evidences were found for Pt_xY nanoparticles in our previous study, supporting the notion that a similar core-shell structure is formed [70].

3.3. Transmission electron microscopy (TEM) analysis

Figure 3 shows the particle size distribution (PSD) histograms of the different particles determined by HAAD-STEM. As seen, nanoparticulate catalysts with mean particle sizes ranging between ~3 and ~9 nm were synthesized. For simplicity, the particle sizes are rounded up to the closest integer to denominate the different catalysts; however, when plotting electrochemical or morphological parameters as a function of the size, the actual measured value and the corresponding standard deviation are employed, as indicated in Table S1 in the Supplementary Information. The PSDs present narrow peaks at the selected sizes indicating the successful mass selection. The satellite peaks at higher diameters correspond to double-charge nanoparticles, with a mass twice the intended one. This undesired effect is minimized by optimizing the synthesis conditions, namely by stabilization of the deposition current during the nanoparticles deposition [81]. IL-Bright-field TEM of the 8 nm sample is shown in Figure 4. The images of the as-prepared Pt_xGd catalyst and following the stability test under ORR conditions indicate the high stability of the nanoparticles on the carbon film support. A closer inspection of the exact same nanoparticles at high magnification reveals an amorphous shell covering the particles on the untreated sample that disappears after ORR catalytic test. In light of the XPS results, the amorphous shell can be ascribed to an oxide formed during air exposure. Presumably, the oxide would be dissolved in the electrolyte in the early stages of the electrochemical experiments.

3.4. ORR measurements of Pt_xGd catalysts

Following the sample preparation and the preliminary morphological characterization, the alloyed nanoparticles supported on glassy carbon were electrochemically tested in 0.1 M HClO₄ using a rotating ring-disk assembly. As a first step, the catalysts were electrochemically activated by means of potential cycling between 0.05 V and 1.00 V in N₂-saturated electrolyte until a stable voltammogram was achieved, as indicated in the Figure S3 of the Supplementary Information, and subsequently the ORR experiment was carried out in O₂-saturated electrolyte under hydrodynamic conditions. The activity of the Pt-alloy catalysts at 0.9 V, expressed in terms of specific activity and mass activity (normalized by Pt loading), is presented in Figure 5 as a function of the nanoparticle size. For comparison purposes, our previous

results obtained with mass-selected Pt_xY and Pt nanoparticles are also included [70,71]. The activities of sputter-cleaned, polycrystalline Pt₃Gd and Pt₃Y extended surfaces, as well as sputter-cleaned, polycrystalline Pt are also presented in Figure 5. The obtained size-dependence of the specific activity for the Pt_xGd nanoparticles is in agreement with the trend found for both mass-selected Pt_xY and Pt nanoparticulate catalysts, namely the ORR specific activity increases with the nanoparticle size, with the activity of the larger nanoparticles approaching the result reported for the corresponding extended, polycrystalline surface. From Figure 5 it is manifest the superior activity of the Pt_xGd nanoparticles compared to pure Pt catalysts, with the only exception of the analyzed smallest size (3 nm), similarly to the performance achieved with the Pt_xY nanoparticles of a comparable particle size (4 nm) [70]. Additionally, the enhanced activity factor of the Pt_xGd catalysts is similar to that observed for Pt_xY nanoparticles, indicating that the equivalent promotional effect for the ORR found with Pt₃Y and Pt₃Gd bulk alloys is also attained in the nanoparticulate form. This is a subject of special interest regarding the potential application of Pt_xY and Pt_xGd electrocatalysts in PEMFC cathodes. Moreover, the specific activity of the 9 nm samples of each alloy (13.5 mA cm⁻² and 10.7 mA cm⁻² for Pt_xY and Pt_xGd, respectively) are comparable, or marginally higher, than that reported for carbon-supported annealed Pt₃Ni nanoframes (~20 nm), synthesized by Stamenkovic and co-workers (8.5 mA cm⁻²) [41].

On the other hand, the mass activity evaluated as a function of the size reveals, not only the greater mass activity of the Pt_xGd catalysts compared to pure Pt nanoparticles, but also the higher performance versus the Pt_xY catalysts. In the case of the Pt_xGd nanoparticles, the size-dependence of the mass activity originates a volcano-plot with the highest mass activity achieved with the 8 nm size and being equal to 3.6 A (mg Pt)⁻¹, which is significantly higher than the optimum mass activity reported for the Pt_xY nanoparticles in our previous work (3.0 A (mg Pt)⁻¹, with 9 nm as set particle size). Moreover, the maximum mass activity is ~3.6 times higher than the optimum result found with the pure Pt nanoparticles synthesized using the same size-selection experimental procedure [71] and roughly 6.5 times higher than the most-active carbon-supported pure Pt electrocatalyst (0.55 A (mg Pt)⁻¹) [89]. The remarkable mass activity peak of the Pt_xGd nanoparticles also represents *the highest ORR activity reported in the literature for solid nanoparticles* (opposed to hollow or porous nanocatalysts) *based on an acid-leached structure*; it is only overtaken in overall by the performance of Pt₃Ni nanoframes (5.7 A (mg Pt)⁻¹) [41].

In order to investigate the stability of the Pt_xGd nanoparticles, long-term potential cycling experiments under ORR conditions were carried out. For this purpose, the alloyed electrodes were cycled between 0.6 V and 1.0 V for

10,000 cycles in O₂-saturated 0.1 M HClO₄ [53,55]. Figure 6 displays the results of the stability test in terms of the evolution of the mass activity with the extended cycling treatment for mass-selected Pt_xGd nanoparticles with average particle size of 5 nm, 8 nm and 9 nm. For comparison purpose, the stability test results obtained with the most active Pt_xY catalyst (9 nm), as well as the initial activity of Pt 3 nm nanoparticles, are included in the Figure 6. It can be seen that for the three analyzed sizes the magnitude of the ORR activity losses is similar to that found with the Pt_xY nanoparticles, i.e. 30-55% [70], and that most of the activity decrease occurs in the early stages of the stability test (first 1,000 cycles). According to the CO stripping analysis data, the electrochemical active surface area remains invariable after the stability test, indicating that a possible decrease of the available surface area (e.g. nanoparticles sintering, agglomeration or detachment) cannot be accounted for the ORR activity losses. A similar conclusion could be extracted from the results of the IL-TEM analysis, shown in the Figure 4 for the case of the Pt_xGd 8 nm catalyst. As seen, no significant changes were detected in the catalyst general morphology after the stability test, with the exception of the dissolution of the oxide layer covering the as-prepared nanoparticles. The most active Pt_xGd nanoparticles (8 nm) retain 70% of the initial activity after 10,000 cycles, indicating that their stability is comparable (or slightly better) than that of Pt_xY nanoparticles of the optimum size (9 nm) [70]. Consequently, even after the extended potential cycling treatment, the Pt_xGd nanoparticles of 8 nm are still ~5 times more active than pure Pt nanoparticles with a comparable size and ~2.8 times more active than the maximum mass activity achieved with the mass-selected Pt nanoparticles (3 nm).

3.5. EXAFS analysis of Pt_xGd catalysts

Motivated by our previous investigation on polycrystalline Pt₃Gd, that revealed that the compressive strain was the main cause of the superior performance of the alloy compared to pure Pt [60], we carried out grazing-incident extended X-ray absorption fine structure measurements (GI-EXAFS) for the quantification of the strain in the Pt_xGd nanoparticles. For that purpose, samples as-prepared, after the standard electrochemical experiment and after the long-term stability test were considered. The average nearest-neighbour distances between the Pt atoms were calculated through fitting of the EXAFS spectra. Details of the fitting procedure are described in detail in the Supplementary Information. The result of the analysis is summarized in Figure 7 (a), where the Pt-Pt interatomic distance and the consequent compressive strain are plotted versus the average nanoparticle size for the three different experimental conditions. The EXAFS

results obtained for as-prepared and electrochemically tested mass-selected Pt nanoparticles, reported in our preceding publication [70] are also presented. The average Pt-Pt distance for bulk Pt (Pt foil) is included in the plot for comparison and used for the estimation of the relative strain. In general, the as-prepared Pt_xGd nanoparticles exhibit a smaller Pt-Pt distance than bulk Pt, indicating the existence of a compressive strain before the electrochemical analysis. The magnitude of such strain slightly decreases with the nanoparticle size, changing from -3.8% to -3.4% (compared to bulk Pt) for the 5 nm and the 9 nm nanoparticles, respectively. In the case of the catalysts after ORR test, they show significant larger Pt-Pt distances compared to the as-prepared samples but still lower compared to bulk Pt. The Pt-Pt distances after the standard electrochemical test are remarkably size-dependent, varying smoothly from -0.7% to -2.2% for the 3 nm and the 9 nm size catalysts, respectively. In addition, the 9 nm Pt_xGd sample subjected to the stability test exhibits less compressive strain than the counterpart after the conventional electrochemical measurement (-1.7% vs. -2.2%, respectively), demonstrating that the accelerated stability test produces some relaxation in the Pt_xGd nanoparticles. On the other hand, the average Pt-Pt distance/strain estimated by EXAFS measurements can be also associated to the XPS atomic Gd:Pt ratio of the Pt_xGd nanoparticles under different conditions, being the corresponding relationship displayed in Figure 7 (b) (the data for mass-selected Pt nanoparticles and Pt foil presented for comparative purpose). The obtained trend reveals that the compressive strain in the Pt_xGd nanoparticles is strongly related to the Gd content in the catalyst, increasing with the fraction of solute atoms.

4. Discussion

The interpretation of the XPS spectra shown in Figure 2 combined with the angle-resolved XPS results of polycrystalline Pt₅Gd from our previous research (see Introduction) [60], strongly supports the formation of a core/shell structure after acid leaching of Gd atoms from the outermost layers of the nanoparticles. Therefore, such model can be also used for explaining the trends derived from the EXAFS analysis, shown in Figure 7. We could rationalize the obtained findings considering that the as-prepared Pt_xGd nanoparticles are under compressive strain as a result of the alloying; this is to be expected, given that the closest nearest-neighbour Pt-Pt distance in Pt₅Gd hexagonal structure is 2.65 Å, or ~5% compressive strain relative to pure Pt (2.77 Å) [60,90] (see Figure S1 in the Supplementary Information). We take the view that a *kagomé* arrangement with a shorter Pt-Pt nearest-neighbour distance, similar to that shown by polycrystalline Pt_xY and Pt₅Gd, is attained by the as-prepared Pt_xGd nanoparticulate catalysts. Nevertheless,

we are aware that some degree of deviation from the bulk structure may occur in the case of the smaller nanoparticles. Considering that the lattice parameter *c* (2.6 nm [90]) of the orthorhombic Pt₅Gd phase is comparable to the average particle size of the smallest nanoparticles (3 nm); we anticipate some distortion of the orthorhombic structure when adopting a spherical morphology. Once the Pt_xGd nanoparticles are exposed to the electrolyte and subjected to the electrochemical characterization, the Gd atoms are leached out from the outermost atomic layers of the nanoparticles, leading to the formation of a pure Pt overlayer; this overlayer would be under compressive strain, induced by the underlying Pt_xGd alloy core, resembling the structure of polycrystalline Pt₅Gd after electrochemical characterization [60]. Similarly, the scanning transmission electron microscopy energy-dispersive X-ray spectroscopy (STEM-EDS) mapping of mass-selected Pt_xY nanoparticles revealed that a core/shell structure was developed after the ORR test, the Pt-rich being shell ~1 nm thick, in agreement with the thickness of ~3 monoatomic layers estimated for polycrystalline Pt-lanthanides alloys [70]. Logically, some strain relief could occur in the pure Pt shell of the Pt_xGd nanoparticles in the absence of the Gd atoms. However, previous investigations with single crystal surfaces have revealed that some degree of compression would still be retained in the outermost surface of the layer Pt shell [39]. Additionally, the size-dependence for the strain after the ORR presented in Figure 7 (a) is due to the smaller pure alloy core for smaller nanoparticles, as also evidenced by the size dependence of Gd:Pt ratio in Figure 7(b).

It is interesting to note that the strain in the 9 nm nanoparticles relaxes further, following the stability test. To some degree, this is only to be accepted; once the Gd is removed from the overlayer, there will be a driving force for it to relax towards pure Pt. It is curious, however, to note that in the case of the 9 nm particle, this relaxation is accompanied by a slight increase in the Pt:Gd XPS ratio, as shown on Figure 7(b); this is analogous to the behavior of extended surfaces of polycrystalline Pt₅La and Pt₅Ce alloys following extended cycling [59]. Since Gd diffusion is likely to be very slow at room temperature through the Pt overlayer (see Introduction), we speculate that the dealloying occurs via an alternative mechanism, perhaps involving subsurface oxide formation [91]. Nonetheless, the majority of the activity losses occur during the first 1,000 cycles, as shown on Figure 6. This suggests that the rate of degradation slows significantly after 1,000 cycles, at which point the catalyst has reached some kind of metastable state.

In order to gain some insight into the role of the strain in the ORR activity of the Pt_xGd nanoparticles, the specific activity is plotted as a function of the corresponding strain relative to Pt foil after ORR and after stability test in Figure 8. In addition, the previous results of activity vs. strain after ORR for

Pt_xY NPs and for Pt NPs are included for comparison. *As result, it is manifest that the ORR activity of Pt, Pt_xY and Pt_xGd all follow the same trend, i.e. the activity enhancement is largely controlled by the strain in the nanoparticles.*

This is also consistent with Strasser and co-workers' investigations of dealloyed Pt_xCu nanoparticles [39]. It should be noted that the strain dependence of the ORR activity reported in ref. [39] was found significantly less intense than that presented in this work, most likely due to excessive relaxation of the compressive strain in the Pt overlayer of the dealloyed Pt_xCu nanoparticles [39]. Moreover, the trend displayed in Figure 8 also resembles the relationship established in our previous work focused on polycrystalline Pt-lanthanides alloys [59], where the specific activity of polycrystalline Pt₅Gd, Pt₅Ce and Pt₅La was correlated with the interatomic Pt-distance in the bulk, based on X-ray diffraction (XRD) measurements. Consequently, we conjecture that the compressive strain causes the weakening of the oxygenated-intermediates adsorption, leading to the consequent enhancement of the ORR activity. According to DFT calculations, the necessary strain for optimizing the ORR performance is -2% (relative to an unstrained Pt(111) surface) [39]. This value is reached by the bulk compressive strain of the most active Pt_xGd nanoparticles (-2.2%), without reaching a maximum in activity. We expect that the local strain within the outermost layer of the Pt shell, which is responsible of the ORR activity, would be somewhat reduced compared to the overall strain plotted in Figure 8, because of strain relaxation. This would result in an unknown shift of the plot to the right and, subsequently, we propose that the trend exhibited in Figure 8 represents *the strong *OH binding side of a volcano plot. Accordingly, should a slightly greater degree of strain be imposed onto the surface, by refining the atomic ratio of the second metal or increasing the nanoparticle size, it might be possible to reach the peak of the volcano.*

5. Conclusions

We have shown in the present work that the excellent catalytic properties of polycrystalline Pt₅Gd (enhanced ORR activity compared to pure Pt and stability upon cycling) also extends to nanoparticles. The maximum mass activity reached with the Pt_xGd nanoparticles (8 nm, 3.6 A (mg Pt)⁻¹ at 0.9 V) represents a notable improvement compared to our preceding results obtained with Pt_xY nanoparticles; in the literature and is only surpassed by Pt₃Ni nanoframes. [41]. Additionally, the optimum Pt_xGd catalyst exhibits similar, albeit very slightly improved stability versus the most active Pt_xY nanoparticles previously reported (70% retention of the initial activity versus 63% for Pt_xY).

In addition, we have also confirmed that the mechanism for the ORR enhancement accounts for the compressive strain within the Pt shell induced by the Pt_xGd core. As a result, a direct relationship between the ORR activity of the Pt_xGd nanoparticles and their compressive strain can be established. We have also shown that the activity of pure Pt nanoparticles, Pt_xY and Pt₅Gd can all be correlated to the lattice strain.

Our work confirms that Pt_xGd alloy nanoparticles are of great interest for applications in PEMFC cathodes. Nevertheless, we are aware that the ultra-high vacuum procedure used in this research is not valid for catalyst mass production; eventually low-priced chemical methods should be employed for such purpose. Therefore, our efforts are currently directed to the development of suitable chemical procedures to obtain Pt_xGd alloy in nanoparticle form; using such as methods we may have control over both particle size and Gd content, and ultimately the strain, which controls the oxygen reduction activity.

Acknowledgments

We thankfully acknowledge the EU PF7's initiative Fuel Cell and Hydrogen Joint Undertaking's project CathCat (GA 303492), the Danish National Research Foundation's Center for Individual Nanoparticle Functionality (DNRF54), and the Danish Ministry of Science's UNIK initiative Catalysis for Sustainable Energy (CASE) for providing the funding for this research. We also thank the Danish Council For Strategic Research's project NACORR. The A.P. Møller and Chastine Mc-Kinney Møller Foundation is gratefully acknowledged for its contribution towards the establishment of the Centre for Electron Nanoscopy in the Technical University of Denmark. This research was partly carried out at the Stanford Synchrotron Radiation Lightsource, a National User Facility operated by Stanford University on behalf of the U.S. Department of Energy, Office of Basic Energy Sciences. We thank John R. Bargar, Apurva Mehta, Ryan C. Davis, Matthew Latimer and Erik J. Nelson for their support with the GI-EXAFS setup and helpful discussions.

References

- [1] A. Wieckowski, M. Neurock, *Adv. Phys. Chem.* 2011 (2011) 1.
- [2] J.K. Nørskov, T. Bligaard, J. Rossmeisl, C.H. Christensen, *Nat. Chem.* 1 (2009) 37.
- [3] P. Sabatier, *Ber. Dtsch. Chem. Ges.* 44 (1911) 1984.
- [4] J.K. Nørskov, J. Rossmeisl, A. Logadottir, L. Lindqvist, J.R. Kitchin, T. Bligaard, H. Jónsson, *J. Phys. Chem. B.* 108 (2004) 17886.

- [5] J. Rossmeisl, A. Logadottir, J.K. Nørskov, *Chem. Phys.* 319 (2005) 178.
- [6] J. Greeley, T.F. Jaramillo, J. Bonde, I.B. Chorkendorff, J.K. Nørskov, *Nat. Mater.* 5 (2006) 909.
- [7] J.K. Nørskov, T. Bligaard, A. Logadottir, J.R. Kitchin, J.G. Chen, S. Pandalov, U. Stimming, *J. Electrochem. Soc.* 152 (2005) J23.
- [8] A.A. Peterson, J.K. Nørskov, *J. Phys. Chem. Lett.* 3 (2012) 251.
- [9] H.A. Hansen, I.C. Man, F. Studt, F. Abild-Pedersen, T. Bligaard, J. Rossmeisl, *Phys. Chem. Chem. Phys.* 12 (2010) 283.
- [10] I.C. Man, H.Y. Su, F. Calle-Vallejo, H.A. Hansen, J.I. Martínez, N.G. Inoglu, J. Kitchin, T.F. Jaramillo, J.K. Nørskov, J. Rossmeisl, *Chem. Cat. Chem.* 3 (2011) 1159.
- [11] H. Dau, C. Limberg, T. Reier, M. Risch, S. Roggan, P. Strasser, *Chem. Cat. Chem.* 2 (2010) 724.
- [12] M.T.M. Koper, *J. Electroanal. Chem.* 660 (2011) 254.
- [13] S. Siahrostami, A. Verdager-Casadevall, M. Karamad, D. Deiana, P. Malacrida, B. Wickman, M. Escudero-Escribano, E.A. Paoli, R. Frydendal, T.W. Hansen, I. Chorkendorff, I.E.L. Stephens, J. Rossmeisl, *Nat. Mater.* 12 (2013) 1137.
- [14] T.F. Jaramillo, K.P. Jørgensen, J. Bonde, J.H. Nielsen, S. Horch, I. Chorkendorff, *Science* 317 (2007) 100.
- [15] A.A. Peterson, F. Abild-Pedersen, F. Studt, J. Rossmeisl, J.K. Nørskov, *Energy Environ. Sci.* 3 (2010) 1311.
- [16] V. Stamenkovic, B.S. Mun, K.J.J. Mayrhofer, P.N. Ross, N.M. Markovic, J. Rossmeisl, J. Greeley, J.K. Nørskov, *Angew. Chem. Int. Ed.* 45 (2006) 2897.
- [17] A.U. Nilekar, M. Mavrikakis, *Surf. Sci.* 602 (2008) L89.
- [18] J. Greeley, I.E.L. Stephens, A.S. Bondarenko, T.P. Johansson, H.A. Hansen, T.F. Jaramillo, J. Rossmeisl, I. Chorkendorff, J.K. Nørskov, *Nat. Chem.* 1 (2009) 552.
- [19] I.E.L. Stephens, A.S. Bondarenko, F.J. Perez-Alonso, F. Calle-Vallejo, L. Bech, T.P. Johansson, A.K. Jepsen, R. Frydendal, B.P. Knudsen, J. Rossmeisl, I. Chorkendorff, *J. Am. Chem. Soc.* 133 (2011) 5485.
- [20] V. Viswanathan, H.A. Hansen, J. Rossmeisl, J.K. Nørskov, *J. Phys. Chem. Lett.* 3 (2012) 2948.
- [21] A. Verdager-Casadevall, D. Deiana, M. Karamad, S. Siahrostami, P. Malacrida, T.W. Hansen, J. Rossmeisl, I. Chorkendorff, I.E.L. Stephens, *Nano Lett.* 14 (2014) 1603.
- [22] A.S. Bandarenka, H.A. Hansen, J. Rossmeisl, I.E.L. Stephens, *Phys. Chem. Chem. Phys.* 16 (2014) 13625.
- [23] H.A. Gasteiger, S.S. Kocha, B. Sompalli, F.T. Wagner, *Appl. Catal. B Environ.* 56 (2005) 9.
- [24] K.C. Neyerlin, W. Gu, J. Jorne, H.A. Gasteiger, *J. Electrochem. Soc.* 154 (2007) B631.
- [25] K.E. Swider-Lyons, S.A. Campbell, *J. Phys. Chem. Lett.* 4 (2013) 393.
- [26] C.M. Zaltis, D. Kramer, A.R. Kucernak, *Phys. Chem. Chem. Phys.* 15 (2013) 4329.
- [27] M. Wesselmark, B. Wickman, C. Lagergren, G. Lindbergh, *Electrochem. Commun.* 12 (2010) 1585.
- [28] F.T. Wagner, B. Lakshmanan, M.F. Mathias, *J. Phys. Chem. Lett.* 1 (2010) 2204.
- [29] A. Rabis, P. Rodriguez, T.J. Schmidt, *ACS Catal.* 2 (2012) 864.
- [30] I.E.L. Stephens, A.S. Bondarenko, U. Grønberg, J. Rossmeisl, I. Chorkendorff, *Energy Environ. Sci.* 5 (2012) 6744.
- [31] A.S. Bondarenko, I.E.L. Stephens, H.A. Hansen, F.J. Pérez-Alonso, V. Tripkovic, T.P. Johansson, J. Rossmeisl, J.K. Nørskov, I. Chorkendorff, *Langmuir* 27 (2011) 2058.
- [32] D. Friebe, V. Viswanathan, D.J. Miller, T. Anniyev, H. Ogasawara, A.H. Larsen, C.P. O'Grady, J.K. Nørskov, A. Nilsson, *J. Am. Chem. Soc.* 134 (2012) 9664.
- [33] V. Viswanathan, H.A. Hansen, J. Rossmeisl, J.K. Nørskov, *ACS Catal.* 2 (2012) 1654.
- [34] H.S. Casalongue, S. Kaya, V. Viswanathan, D. J. Miller, D. Friebe, H. A. Hansen, J. K. Nørskov, A. Nilsson, H. Ogasawara, *Nat. Commun.* 4 (2013) 2817.
- [35] J. Rossmeisl, G.S. Karlberg, T. Jaramillo, J.K. Nørskov, *Faraday Discuss.* 140 (2008) 337.
- [36] J.R. Kitchin, J.K. Nørskov, M.A. Barteau, J.G. Chen, *J. Chem. Phys.* 120 (2004) 10240.
- [37] F. Calle-Vallejo, J.I. Martínez, J.M. García-Lastra, J. Rossmeisl, M.T.M. Koper, *Phys. Rev. Lett.* 108 (2012) 116103.
- [38] M. Mavrikakis, B. Hammer, J. Nørskov, *Phys. Rev. Lett.* 81 (1998) 2819.
- [39] P. Strasser, S. Koh, T. Anniyev, J. Greeley, K. More, C. Yu, Z. Liu, S. Kaya, D. Nordlund, H. Ogasawara, M.F. Toney, A. Nilsson, *Nat. Chem.* 2 (2010) 454.
- [40] S. Mukerjee, S. Srinivasan, M.P. Soriaga, J. McBreen, *J. Electrochem. Soc.* 142 (1995) 1409.
- [41] C. Chen, Y. Kang, Z. Huo, Z. Zhu, W. Huang, H.L. Xin, J.D. Snyder, D. Li, J.A. Herron, M. Mavrikakis, M. Chi, K.L. More, Y. Li, N.M.

- Markovic, G.A. Somorjai, P. Yang, V.R. Stamenkovic, *Science* 343 (2014) 1339.
- [42] S. Chen, P.J. Ferreira, W. Sheng, N. Yabuuchi, L.F. Allard, Y. Shao-Horn, *J. Am. Chem. Soc.* 130 (2008) 13818.
- [43] S.I. Choi, S. Xie, M. Shao, J.H. Odell, N. Lu, H.C. Peng, L. Protsailo, S. Guerrero, J. Park, X. Xia, J. Wang, M.J. Kim, Y. Xia, *Nano Lett.* 13 (2013) 3420.
- [44] L. Gan, M. Heggen, S. Rudi, P. Strasser, *Nano Lett.* 12 (2012) 5423.
- [45] I. Spanos, J.J.K. Kirkensgaard, K. Mortensen, M. Arenz, *J. Power Sources.* 245 (2014) 908.
- [46] V.R. Stamenkovic, B.S. Mun, K.J.J. Mayrhofer, P.N. Ross, N.M. Markovic, *J. Am. Chem. Soc.* 128 (2006) 8813.
- [47] T. Wadayama, N. Todoroki, Y. Yamada, T. Sugawara, K. Miyamoto, Y. Iijima, *Electrochem. Commun.* 12 (2010) 1112.
- [48] N. Todoroki, Y. Iijima, R. Takahashi, Y. Asakimori, T. Wadayama, *J. Electrochem. Soc.* 160 (2013) F591.
- [49] C. Wang, M. Chi, D. Li, D. Stmcnik, D. van der Vliet, G. Wang, V. Komanicky, K.C. Chang, A.P. Paulikas, D. Tripkovic, J. Pearson, K.L. More, N.M. Markovic, V.R. Stamenkovic, *J. Am. Chem. Soc.* 133 (2011) 14396.
- [50] V.R. Stamenkovic, B. Fowler, B.S. Mun, G. Wang, P.N. Ross, C.A. Lucas, N.M. Markovic, *Science* 315 (2007) 493.
- [51] T. Toda, H. Igarashi, H. Uchida, M. Watanabe, *J. Electrochem. Soc.* 146 (1999) 3750.
- [52] M. Watanabe, K. Tsurumi, T. Mizukami, T. Nakamura, P. Stonehart, *J. Electrochem. Soc.* 141 (1994) 2659.
- [53] A. Ohma, K. Shinohara, A. Iiyama, T. Yoshida, A. Daimaru, *ECS Trans.* 41 (2011) 775.
- [54] H.L. Xin, J.A. Mundy, Z. Liu, R. Cabezas, R. Hovden, L.F. Kourkoutis, J. Zhang, N.P. Subramanian, R. Makharia, F.T. Wagner, D.A. Muller, *Nano Lett.* 12 (2012) 490.
- [55] The US Department of Energy (DOE), Energy Efficiency and Renewable Energy, http://www.eere.energy.gov/hydrogenandfuelcells/mypp/pdfs/fuel_cells.pdf; and the US DRIVE Fuel Cell Technical Team Technology Roadmap, <http://www.uscar.org/guest/teams/17/Fuel-Cell-Tech-Team>, 2013.
- [56] S. Chen, H.A. Gasteiger, K. Hayakawa, T. Tada, Y. Shao-Horn, *J. Electrochem. Soc.* 157 (2010) A82.
- [57] K.C. Neyerlin, R. Srivastava, C. Yu, P. Strasser, *J. Power Sources* 186 (2009) 261.
- [58] L. Dubau, M. López-Haro, L. Castanheira, J. Durst, M. Chatenet, P. Bayle-Guillemaud, L. Guétaz, N. Caqué, E. Rossinot, F. Maillard, *Appl. Catal. B Environ.* 142-143 (2013) 801.
- [59] P. Malacrida, M. Escudero-Escribano, A. Verdaguier-Casadevall, I.E.L. Stephens, I. Chorkendorff, *J. Mater. Chem. A.* 2 (2014) 4234.
- [60] M. Escudero-Escribano, A. Verdaguier-Casadevall, P. Malacrida, U. Grønbjerg, B.P. Knudsen, A.K. Jepsen, J. Rossmeisl, I.E.L. Stephens, I. Chorkendorff, *J. Am. Chem. Soc.* 134 (2012) 16476.
- [61] P.C.K. Vesborg, T.F. Jaramillo, *RSC Adv.* 2 (2012) 7933.
- [62] N. Schumacher, K. Andersson, L.C. Grabow, M. Mavrikakis, J. Nerlov, I. Chorkendorff, *Surf. Sci.* 602 (2008) 702.
- [63] T.P. Johansson, E.T. Ulrikkeholm, P. Hernández-Fernández, M. Escudero-Escribano, P. Malacrida, I.E.L. Stephens, I. Chorkendorff, *Phys. Chem. Chem. Phys.* 16 (2014) 13718.
- [64] C.A. Menning, J.G. Chen, *Top. Catal.* 53 (2010) 338.
- [65] I.E.L. Stephens, A.S. Bondarenko, L. Bech, I. Chorkendorff, *Chem. Cat. Chem.* 4 (2012) 341.
- [66] S.J. Yoo, S.K. Kim, T.Y. Jeon, S.J. Hwang, J.G. Lee, S.C. Lee, K.S. Lee, Y.H. Cho, Y.E. Sung, T.H. Lim, *Chem. Commun.* 47 (2011) 11414.
- [67] B. Cordero, V. Gómez, A.E. Platero-Prats, M. Revés, J. Echeverría, E. Cremades, F. Barragán, S. Alvarez, *Dalton Trans.* (2008) 2832.
- [68] M. Pourbaix, *Atlas of Electrochemical Equilibria in Aqueous Solutions*, Pergamon Press, Bristol, 1966, pp. 177-197, p. 330.
- [69] Y. Luo, A. Habrioux, L. Calvillo, G. Granozzi, N. Alonso-Vante, *Chem. Phys. Chem.* 15 (2014) 2136.
- [70] P. Hernández-Fernández, F. Masini, D.N. McCarthy, C.E. Streb, D. Friebel, D. Deiana, P. Malacrida, A. Nierhoff, A. Bodin, A.M. Wise, J.H. Nielsen, T.W. Hansen, A. Nilsson, I.E.L. Stephens, I. Chorkendorff, *Nat. Chem.* 6 (2014) 732.
- [71] F.J. Pérez-Alonso, D.N. McCarthy, A. Nierhoff, P. Hernández-Fernández, C. Streb, I.E.L. Stephens, J.H. Nielsen, I. Chorkendorff, *Angew. Chem. Int. Ed.* 51 (2012) 4641.
- [72] D.N. McCarthy, C.E. Streb, T.P. Johansson, A. den Dunnen, J.H. Nielsen, I. Chorkendorff, *J. Phys. Chem. C* 116 (2012) 15353.
- [73] M. Nesselberger, M. Roefzaad, R.F. Hamou, P.U. Biedermann, F.F. Schweinberger, S. Kunz, K. Schloegl, G.K.H. Wiberg, S. Ashton, U. Heiz, K.J.J. Mayrhofer, M. Arenz, *Nat. Mater.* 12 (2013) 919.
- [74] F. Yin, Z.W. Wang, R.E. Palmer, *J. Am. Chem. Soc.* 133 (2011) 10325.

- [75] F. Masini, C.E. Strebler, D.N. McCarthy, A.U.F. Nierhoff, J. Kehres, E.M. Fiordaliso, J.H. Nielsen, I. Chorkendorff, *J. Catal.* 308 (2013) 282.
- [76] C. Galeano, J.C. Meier, V. Peinecke, H. Bongard, I. Katsounaros, A.A. Topalov, A. Lu, K.J.J. Mayrhofer, F. Schüth, *J. Am. Chem. Soc.* 134 (2012) 20457.
- [77] Z.Y. Li, J.P. Wilcoxon, F. Yin, Y. Chen, R.E. Palmer, R.L. Johnston, *Faraday Discuss.* 138 (2008) 363.
- [78] J. Speder, L. Altmann, M. Bäumer, J.J.K. Kirkensgaard, K. Mortensen, M. Arenz, *RSC Adv.* 4 (2014) 14971.
- [79] A. Zana, J. Speder, N.E.A. Reeler, T. Vosch, M. Arenz, *Electrochim. Acta.* 114 (2013) 455.
- [80] R.A. Martínez-Rodríguez, F.J. Vidal-Iglesias, J. Solla-Gullón, C.R. Cabrera, J.M. Feliu, *J. Am. Chem. Soc.* 136 (2014) 1280.
- [81] F. Masini, P. Hernández-Fernández, D. Deiana, C.E. Strebler, D.N. McCarthy, A. Bodin, P. Malacrida, I. Stephens, I. Chorkendorff, *Phys. Chem. Chem. Phys.* (2014) DOI: 10.1039/C4CP02144D.
- [82] H. Haberland, M. Karrais, M. Mall, Y. Thurner, *J. Vac. Sci. Technol. A* 10 (1992) 3266.
- [83] B. von Issendorff, R.E. Palmer, *Rev. Sci. Instrum.* 70 (1999) 4497.
- [84] C.D. Wagner, L.E. Davis, M.V. Zeller, J.A. Taylor, R.H. Raymond, L.H. Gale, *Surf. Interface. Anal.* 3 (1981) 211.
- [85] S. Tanuma, C.J. Powell, D.R. Penn, *Surf. Interface Anal.* 17 (1991) 911.
- [86] F.J. Perez-Alonso, C.F. Elkjær, S.S. Shim, B.L. Abrams, I.E.L. Stephens, I. Chorkendorff, *J. Power Sources.* 196 (2011) 6085.
- [87] F. Maillard, E.R. Savinova, U. Stimming, *J. Electroanal. Chem.* 599 (2007) 221.
- [88] D. Raiser, J.P. Deville, *J. Electron Spectrosc. Relat. Phenomena.* 57 (1991) 91.
- [89] M. Nesselberger, S. Ashton, J.C. Meier, I. Katsounaros, K.J.J. Mayrhofer, M. Arenz, *J. Am. Chem. Soc.* 133 (2011) 17428.
- [90] W. Bronger, *J. Less Common Metals* 12 (1967) 63.
- [91] D. Friebel, D.J. Miller, C.P. O'Grady, T. Anniyev, J. Bargar, U. Bergmann, H. Ogasawara, K.T. Wikfeldt, L.G.M. Pettersson, A. Nilsson, *Phys. Chem. Chem. Phys.* 13 (2011) 262.

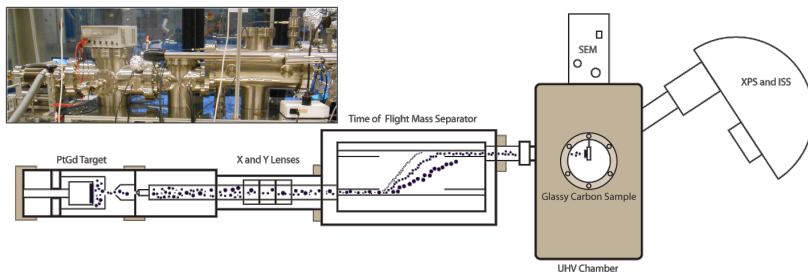


Figure 1: Schematic representation of the nanoparticle source used for the synthesis and characterization of the Pt_xGd nanoparticles in UHV conditions. The inset shows a photograph of the actual apparatus.

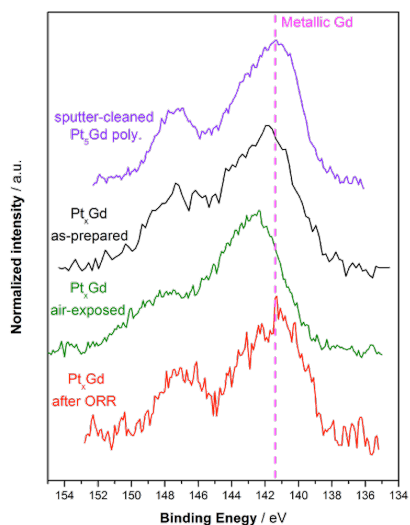


Figure 2: Detailed XPS survey of Gd 4d core-level region spectra for sputter-cleaned polycrystalline Pt_5Gd and for the Pt_xGd nanoparticles (9 nm) as-prepared (under UHV conditions), after air-exposure and after the ORR measurement.

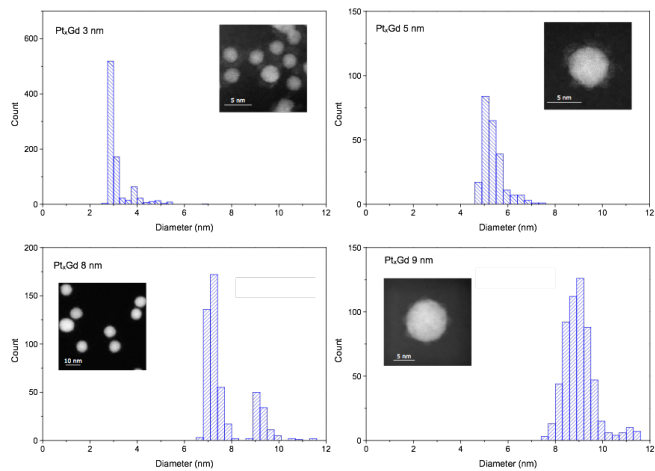


Figure 3: Particle size distributions and representative HAADF-STEM micrographs of the different Pt_xGd nanoparticle catalysts.

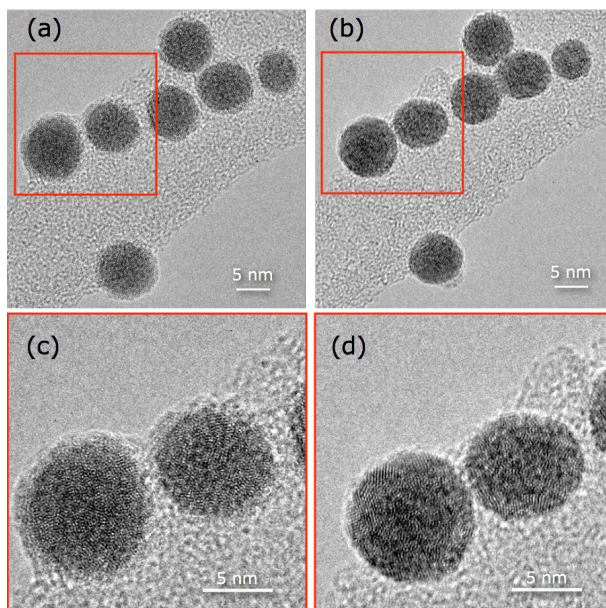


Figure 4: Bright-field IL-TEM micrographs of 8 nm Pt_xGd nanoparticles before (a) and after (b) stability test. The (c) and (d) images are a magnification of the red squares drawn in (a) and (b), respectively.

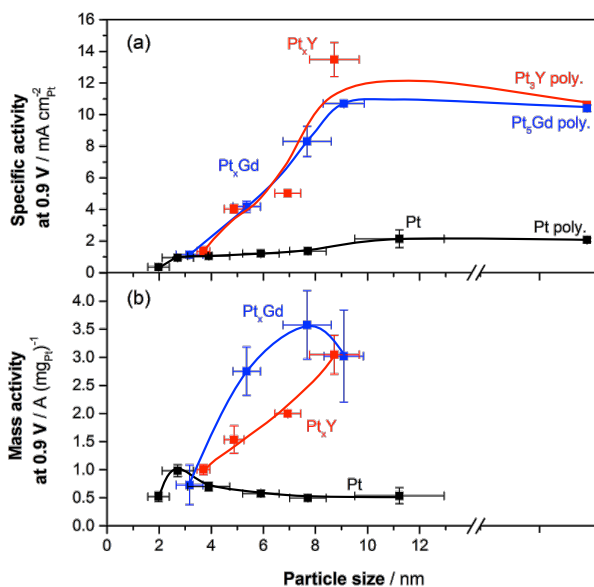


Figure 5: (a) Specific activity and (b) mass activity of Pt_xGd nanoparticles (blue). Data taken at 0.9 V from cyclic voltammetry recorded at 50 mV s⁻¹, 1,600 rpm and 23 ± 1 °C in O₂-saturated 0.1 M HClO₄. For comparison, the previously published mass and specific activities of mass-selected Pt_xY (red) and pure Pt nanoparticles (black) are also plotted [70,71]. Additionally, the specific activities obtained under the same conditions of sputter-cleaned polycrystalline Pt₅Gd and Pt₃Y extended surface electrodes, as well as sputter-cleaned polycrystalline Pt, are presented [60]. Each data point corresponds to the mean value from at least two independent electrochemical tests. The horizontal error bars show the standard deviation in the particle size distribution (PSD) whereas the vertical error bars show the standard deviation in electrochemical measurements. The lines serve as a guide for the eye. The Supplementary Information contains details of the quantification of mass and surface area carried out for the activity evaluation.

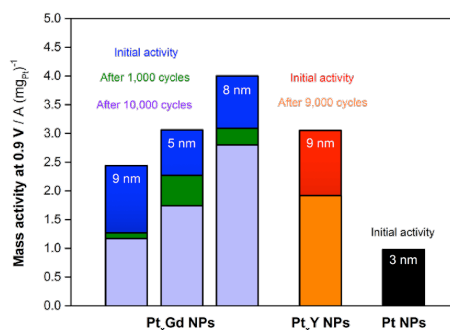


Figure 6: The initial mass activity of Pt_xGd nanoparticles (blue), and after 1,000 cycles (green) and 10,000 cycles (violet) of stability test under ORR conditions. The initial performance of the most active Pt_xY catalyst (red) and after 9,000 cycles of stability test (orange) are also displayed [70]. For a suitable comparison, the maximum activity reported for mass-selected Pt NPs is also plotted (black) [71]. Data taken at 0.9 V from cyclic voltammetry recorded at 50 mV s⁻¹, 1,600 rpm and 23 ± 1 °C in O₂-saturated 0.1 M HClO₄. Stability test carried out by potential cycling between 0.6 and 1.0 V at 100 mV s⁻¹, 0 rpm and 23 ± 1 °C in O₂-saturated 0.1 M HClO₄ solution. A detailed description of the stability test procedure is found in the Supporting Information.

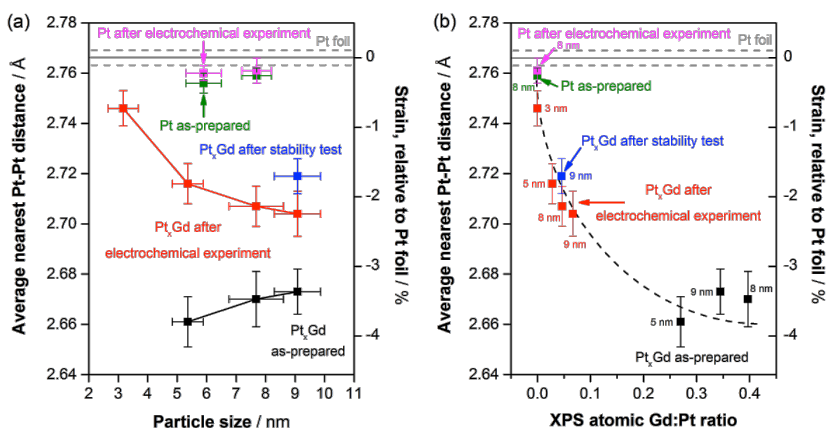


Figure 7 (a) Average nearest-neighbour Pt–Pt distance measured by EXAFS as a function of the particle size for Pt_xGd nanoparticles as-prepared (black), after electrochemical experiment (red) and after stability test (blue). For comparison purpose, the EXAFS results obtained for as-prepared (green) and electrochemically tested (pink) mass-selected Pt nanoparticles, reported in our preceding publication [70], are also shown; **(b)** average nearest-neighbour Pt–Pt distance measured by EXAFS as a function of the atomic Gd:Pt ratio estimated from XPS measurements for Pt_xGd nanoparticles as-prepared (black), after electrochemical experiment (red) and after stability test (blue). The Pt–Pt interatomic distances determined by EXAFS in our previous work for as-prepared (green) and electrochemically tested (pink) mass-selected Pt nanoparticles, with zero Gd content, are shown for comparison [70]. The corresponding average particle size is specified. Measurements were performed in situ on a Pt foil (continuous grey horizontal line in **(a)** and **(b)**); the dashed grey horizontal lines show the error from the fitting software, see details in the Supporting Information) as a reference. The left y-axis in **(a)** and **(b)** represents the nearest neighbour Pt–Pt distance, whereas the right y-axis shows the strain percentage relative to the Pt–Pt distance measured for the Pt foil. The horizontal error bars in **(a)** account for the standard deviation in the particle size distribution (PSD) and the vertical error bars in **(a)** and **(b)** represent the standard deviation from the fitting software, respectively. The dashed black line in **(b)** serves as a guide for the eye.

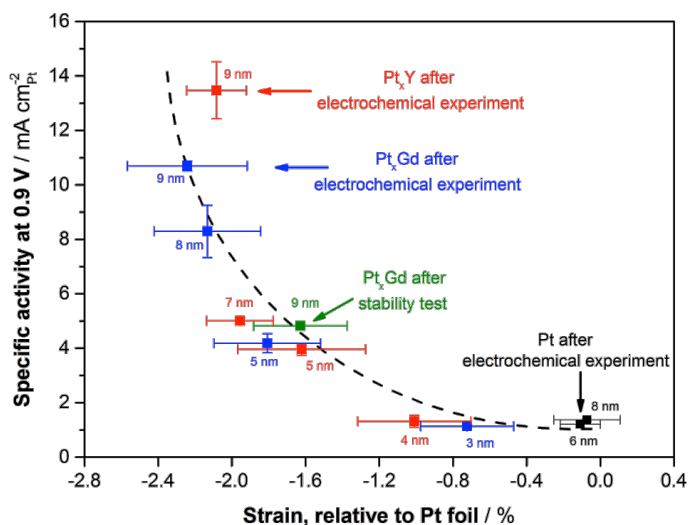


Figure 8: Specific activity results for the ORR on Pt_xGd nanoparticles as a function of the strain, relative to bulk Pt, determined through EXAFS after electrochemical experiment (blue) and after the stability test (green). Data collected from Figure 5, Figure 6 and Figure 7. The previous data reported for mass-selected Pt_xY (red) and Pt nanoparticles (black) after electrochemical experiment are included for comparison purposes [70]. The dashed black line acts as a guide for the eye. The horizontal and vertical error bars show the standard deviation in the strain estimation and in the electrochemical measurements, respectively.

Enabling direct H₂O₂ production through rational electrocatalyst design

Samira Siahrostami^{1†}, Arnau Verdager-Casadevall^{2†}, Mohammadreza Karamad¹, Davide Deiana³, Paolo Malacrida², Björn Wickman^{2,4}, María Escudero-Escribano², Elisa A. Paoli², Rasmus Frydendal², Thomas W. Hansen³, Ib Chorkendorff², Ifan E. L. Stephens^{2*} and Jan Rossmeisl^{1*}

Future generations require more efficient and localized processes for energy conversion and chemical synthesis. The continuous on-site production of hydrogen peroxide would provide an attractive alternative to the present state-of-the-art, which is based on the complex anthraquinone process. The electrochemical reduction of oxygen to hydrogen peroxide is a particularly promising means of achieving this aim. However, it would require active, selective and stable materials to catalyse the reaction. Although progress has been made in this respect, further improvements through the development of new electrocatalysts are needed. Using density functional theory calculations, we identify Pt-Hg as a promising candidate. Electrochemical measurements on Pt-Hg nanoparticles show more than an order of magnitude improvement in mass activity, that is, A g⁻¹ precious metal, for H₂O₂ production, over the best performing catalysts in the literature.

At present, the most commonly produced chemicals, such as ammonia, hydrogen, methanol and hydrogen peroxide are produced in centralized reactors on a very large scale. There is a general call^{1,2} for a more decentralized infrastructure where both energy conversion and chemical synthesis are conducted closer to the point of consumption. Electrochemical devices are set to play an increasingly important role in reaching this goal; they can be operated under ambient conditions, at variable rates and require little auxiliary plant³. They can also be coupled with intermittent renewable power sources, such as solar or wind, providing a means to store electricity and level out demand. Herein, we focus on the electrochemical production of hydrogen peroxide.

Copious amounts of H₂O₂ are produced globally; its annual production exceeds 3 million tons (ref. 4). It is both an environmentally benign chemical oxidant, used for chemical synthesis, the pulp and paper industry and in water treatment^{5,6}, and a potential energy carrier⁷. When produced from H₂ and O₂, H₂O₂ production is exergonic, with a standard Gibbs free energy of formation, $\Delta G_f^0 = -120 \text{ kJ mol}^{-1}$. At present, H₂O₂ is produced using the anthraquinone process, a batch method conducted in large-scale facilities, with an average yield of 50 thousand tons per year per plant⁴. It involves the sequential hydrogenation and oxidation of anthraquinone molecules, and it is energy intensive⁸.

The inherent complexity of the anthraquinone process has motivated many researchers towards developing a direct synthesis of H₂O₂ from its elements^{9,10} aiming at: small-scale, continuous production through a catalytic process⁶. Pd-modified Au nanoparticles (henceforth denoted as Pd/Au) are the most active catalysts for this process⁹. The electroreduction of oxygen to H₂O₂ in a fuel cell or electrolyser holds significant advantages over the above processes. It would enable on-site production of hydrogen peroxide, and unlike the direct synthesis route, it would not be constrained by the need to maintain the hydrogen and oxygen

outside the explosive regime. Moreover, when produced in a fuel cell, it should, in principle, be possible to recover most of the ΔG_f^0 , 120 kJ mol⁻¹, as electrical energy. Alternatively, one could do away with H₂ altogether, and synthesize H₂O₂ at the cathode of an electrolyser; with oxygen evolution occurring at its anode, the energy input would be ~200 kJ mol⁻¹ (see Supplementary Information). Nonetheless, industrially viable, electrochemical production of H₂O₂ requires a catalyst that is stable, active and selective for the electroreduction of oxygen^{6,11–14}.

The most active and selective catalysts found for this reaction, thus far, are based on porphyrins containing 3d transition metals such as Co (ref. 15). However, the nitrogen ligands of these catalysts degrade in the presence of H₂O₂, resulting in rapid performance losses^{16,17}. On the other hand, catalysts based on noble metals provide adequate stability under the harsh reaction conditions. Au nanoparticles have a modest activity for H₂O₂ production, ~1 mA at 0.4 V overpotential, but with a selectivity of only ~80%. On the other hand, Pd/Au nanoparticles show similar activity to Au and up to ~90% selectivity¹³. An overview of different electrocatalysts for H₂O₂ production is shown in Fig. 1, compiled from the literature.

Here, our goal is to discover new alloys for the electrochemical generation of H₂O₂, exhibiting an unprecedented combination of activity, selectivity and stability. We specifically focus our attention on catalysts that function under ambient conditions, containing elements that are stable in acidic, rather than basic electrolytes. This is because H₂O₂ decomposes at high temperatures or alkaline conditions⁶, and devices based on hydroxide-conducting polymeric electrolytes exhibit low membrane stability, poor water management and low hydrogen oxidation activity^{18,19}.

We identify the catalysts using density functional theory (DFT) calculations, synthesize and test them electrochemically and characterize their composition and structure *ex situ*.

¹Center for Atomic-scale Materials Design, Department of Physics, Technical University of Denmark, DK-2800 Kongens Lyngby, Denmark, ²Center for Individual Nanoparticle Functionality, Department of Physics, Technical University of Denmark, DK-2800 Kongens Lyngby, Denmark, ³Center for Electron Nanoscopy, Technical University of Denmark, DK-2800 Kongens Lyngby, Denmark, ⁴Department of Applied Physics, Chalmers University of Technology, SE-41296 Göteborg, Sweden. [†]These authors contributed equally to this work. *e-mail: ifan@fysik.dtu.dk; jross@fysik.dtu.dk

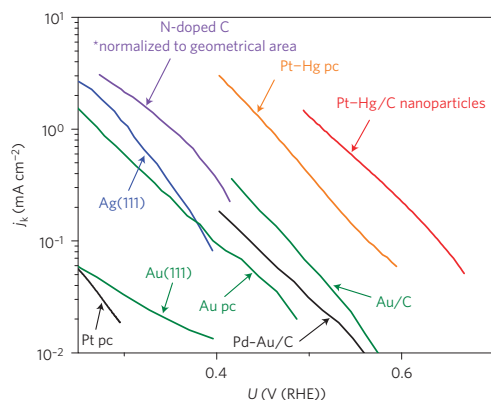
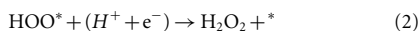


Figure 1 | Overview of different electrocatalysts for H₂O₂ production from the literature and from the present work. For the comparison, the kinetic current has been derived by correcting the partial current density for H₂O₂ production for mass transport limitations. Further details are available in the Methods and in the Supplementary Information. Data adapted from: ref. 46 for Pt polycrystalline (pc); ref. 47 for Au(111); ref. 48 for Au pc; ref. 49 for Ag(111); ref. 14 for N-doped C; ref. 13 for Pd-Au/C and Au/C. Data for Pt-Hg pc and Pt-Hg/C is from the present study.

Computational screening

The electroreduction of O₂ to H₂O₂ involves two coupled electron and proton transfers²⁰:



where * denotes an unoccupied active site, and HOO* denotes the single adsorbed intermediate for the reaction. The catalyst provides high activity, by minimizing kinetic barriers for (1) and (2), and selectivity, by maximizing the barrier for HOO* reduction or dissociation to O* and OH*, the intermediates of the four-electron reduction of O₂ to H₂O.

The catalytic activity and selectivity, in turn, are determined by an interplay between two effects: ensemble effects and electronic effects. The binding of the reaction intermediates is controlled by electronic effects^{21,22}. Varying the catalyst material allows one to tune the binding of HOO* to the surface. This means that the key parameter, or descriptor, in controlling the catalyst activity is the HOO* binding energy, ΔG_{HOO^*} . As the binding energy of HOO* scales linearly with that of HO*, ΔG_{HO^*} , by a constant amount of 3.2 ± 0.2 eV (ref. 23), ΔG_{HO^*} can also be used as a descriptor. In Fig. 2e, the thermodynamic limiting potential, U_{T} , which is the most positive potential at which both (1) and (2) are downhill in free energy, is plotted, in blue, as a function of ΔG_{HO^*} ; the HOO* binding energy is also shown on the upper horizontal axis for comparison. The thermodynamic overpotential for the two-electron reaction, $\eta_{\text{O}_2/\text{H}_2\text{O}_2}$, is denoted by the blue arrow, and is defined as the distance from the Nernstian potential for H₂O₂ production, $U_{\text{O}_2/\text{H}_2\text{O}_2}^0 = 0.7$ V, to the U_{T} . Applying a bias equivalent to $\eta_{\text{O}_2/\text{H}_2\text{O}_2}$ would allow the catalyst to sustain appreciable kinetic rates for H₂O₂ production, due to low charge transfer barriers^{24–26}.

Figure 2e establishes that there is a volcano-type relationship between $\eta_{\text{O}_2/\text{H}_2\text{O}_2}$ (and hence the catalytic activity), and ΔG_{HO^*} . Catalysts on the right-hand side of the volcano are limited by HOO* formation. For Au(211) it is 0.41 eV uphill to form HOO* at $U_{\text{O}_2/\text{H}_2\text{O}_2}^0$, as shown in the free-energy diagram in Fig. 2b. Accordingly, a thermodynamic overpotential of 0.41 V is required to drive the reaction. Catalysts on the left-hand side, such as Pt or Pd,

bind HOO* too strongly, and the overpotential for the two-electron pathway is due to the reduction of HOO* to H₂O₂. The ideal catalyst, at the peak of the volcano, has a $\Delta G_{\text{HOO}^*} \sim 4.2 \pm 0.2$ eV and $\eta_{\text{O}_2/\text{H}_2\text{O}_2} = 0$; its free-energy diagram is flat at the equilibrium potential, as shown in Fig. 2b. This means that the ideal catalyst would exhibit high current densities at negligible overpotentials.

In Fig. 2e, the U_{T} for the four-electron reduction of O₂ to H₂O is also plotted, in red, as a function of ΔG_{HO^*} and ΔG_{HOO^*} . In this case, there is an extra step contributing to the overpotential for the reaction, HO* reduction (where HO* is an adsorbed hydroxyl group, formed from the dissociation or reduction of HOO*; ref. 27):



The thermodynamic overpotential for equation (3), H₂O formation, $\eta_{\text{O}_2/\text{H}_2\text{O}}$, is indicated by the red arrow. Strikingly, in contrast to the two-electron volcano, even on the optimal catalyst, a minimum $\eta_{\text{O}_2/\text{H}_2\text{O}}$ of ~ 0.4 V is required to drive H₂O formation.

The high value of $\eta_{\text{O}_2/\text{H}_2\text{O}}$ is typical for reactions involving more than two electrons^{20,22,23,26,28,29}; this is to overcome the large difference in adsorption energies between the intermediates, HO* and HOO*, whose binding energies scale linearly with each other²⁶. On the other hand, the negligible overpotential required to drive O₂ reduction to H₂O₂ is characteristic of two-electron reactions, where the criterion for finding the ideal catalyst is relatively trivial: the adsorption of the sole reaction intermediate should be thermoneutral at the equilibrium potential³⁰.

The selectivity towards H₂O₂ or H₂O is determined by its propensity to break the O–O bond. This is, in turn, set by the binding strengths of the intermediates of the four-electron pathway, O* and HO*. To the left side of the peak (strong HO* binding) of both the four- and two-electron volcanoes (Fig. 2e), it is more downhill in free energy to form H₂O from HO*; this means the selectivity towards the four-electron pathway will dominate over the two-electron pathway, as is the case for Pt and Pd. The right side (weak HO* binding) of both two- and four-electron volcanoes overlap each other. In other words, at the peak of the two-electron volcano, there is a high activity for both H₂O₂ and H₂O formation, and both pathways will occur in tandem. Moving further right, beyond the peak of the two-electron volcano, towards Au it becomes more difficult to break the O–O bond and form HO* and O*, either through the chemical dissociation of HOO* or its electrochemical reduction. In summary, moving rightwards from the peak of the two-electron volcano weakens the interaction with O* and HO*, increasing the selectivity, but lowering the activity.

Apart from electronic effects, selectivity can also be controlled by geometric (or ensemble) effects; these are associated with the geometric arrangement of atoms on the catalyst surface^{31,32}. On a selective catalyst, both the chemical dissociation to HO* and O* and the electrochemical reduction of HOO* to O* + H₂O should be avoided. Therefore, destabilizing O*, relative to HOO*, improves the selectivity. This can be achieved by controlling the geometry of the binding site: HOO* normally binds onto atop sites whereas O* binds onto hollow sites³³. Eliminating hollow sites will specifically destabilize O*, without necessarily changing the activity. Catalysts such as Co-porphyrins³⁴ lack hollow sites whereas catalysts such as Pd/Au (ref. 13) contain hollow sites that interact weakly with oxygen; their active sites consist of single atoms, isolated by elements, such as Au, N or C (see Supplementary Information). This explains why Pd/Au is also an effective catalyst for the direct gas-phase synthesis of H₂O₂ from H₂ and O₂ (ref. 9).

Taking into account the above trends, using DFT, we screened for new alloy catalysts for the electrochemical generation of H₂O₂, which had not previously been tested. Our main criteria are that: for optimal activity, $\Delta G_{\text{HOO}^*} \sim 4.2 \pm 0.2$ eV; each of the constituent

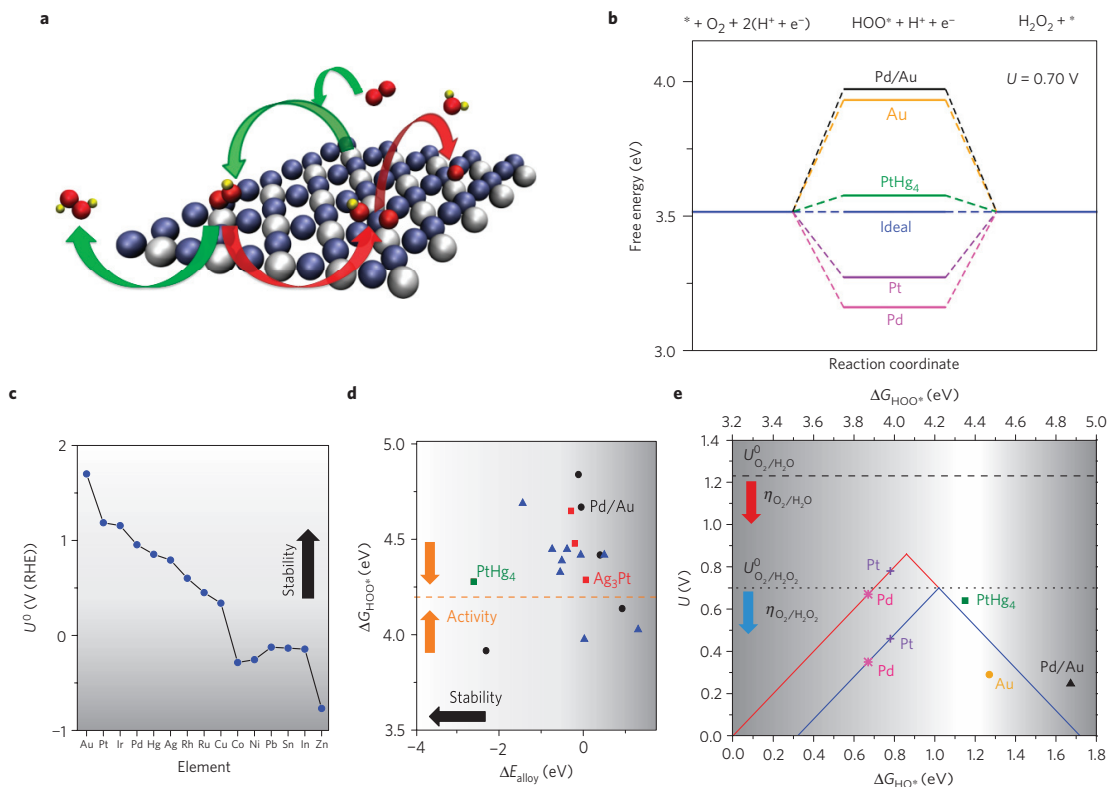


Figure 2 | Theoretical modelling of oxygen reduction to H_2O and H_2O_2 . **a**, Representation of the $\text{PtHg}_4(110)$ surface, based on the investigation of $\text{Hg}/\text{Pt}(111)$ in ref. 35. The green arrows represent the reaction path to H_2O_2 , whereas the red arrows the path to H_2O . Mercury, blue; platinum, grey; oxygen, red; hydrogen, yellow. **b**, Free-energy diagram for oxygen reduction to H_2O_2 . The ideal catalyst is compared with $\text{PtHg}_4(110)$, Pd/Au and closely packed pure metals $\text{Pd}(111)$ and $\text{Au}(211)$, all calculated for this work, and $\text{Pt}(111)$, adapted from ref. 27. **c**, Dissolution potential for various elements under standard conditions⁵⁰. **d**, Formation energy (per formula unit) ΔE_{alloy} , as a function of ΔG_{HOO^*} . The optimal value for HOO^* binding is plotted as the orange dashed line. Bulk alloys are shown by red and green squares, surface alloys with a Au substrate are shown as black circles and surface alloys with non- Au substrate are shown by blue triangles. For **c,d** the colour gradient scales with stability, with the most stable areas highlighted in white. **e**, Theoretically calculated oxygen reduction volcano plot for the two-electron (blue) and four-electron (red) reduction of O_2 , with the limiting potential plotted as a function of ΔG_{HO^*} (lower horizontal axis) and ΔG_{HOO^*} (upper horizontal axis). The equilibrium potential for the two-electron pathway, $U_{\text{O}_2/\text{H}_2\text{O}_2}^0$, is shown as the dotted line, and the equilibrium potential for the four-electron pathway, $U_{\text{O}_2/\text{H}_2\text{O}}^0$, is shown as the dashed line. The range of interesting HO^* free energy for high selectivity and activity is highlighted with the greyscale gradient at its edges, recognizing limitations to the accuracy of DFT. Extensive details of the alloys included in the DFT screening are included in the Supplementary Information.

elements should be stable against dissolution or oxidation under reaction conditions; and the alloy should have as negative a heat of formation as possible (this provides a driving force to form the required monatomic ensembles). Each of the alloys has an active site where isolated atoms of the reactive metal, for example Pt, Pd, Rh or Ir, are surrounded by more inert elements, such as Au and Hg. A total number of 30 alloys were screened. An outline for the screening process is given in Fig. 2, (further details are available in the Supplementary Information).

Our attention was focused on the use of Hg as a means of forming the isolated reactive atoms. Hg is catalytically inactive. It is stable against dissolution up to 0.80 V at pH0 (at standard conditions), and according to both our calculations (see Supplementary Information) and experiments³⁵ it forms stable alloys. The negative enthalpy of formation of the formed phase, PtHg_4 , will stabilize the Hg, relative to pure Hg, meaning that it will be stable against dissolution. Hg can be easily electrodeposited onto Pt (ref. 36); on $\text{Pt}(111)$ it forms a self-organized surface structure at room

temperature³⁵; each Pt atom is surrounded by Hg, as shown in Fig. 2a, thus forming the monatomic ensembles required for high selectivity. Figure 2b also shows that PtHg_4 has a close to optimal binding energy, with a thermodynamic overpotential smaller than 0.1 V. Alloying evidently induces electronic effects, as the binding of HOO^* is ~ 0.37 eV weaker than pure Pt. Indeed, we emphasize that PtHg_4 is the only catalyst identified in the screening that fulfils all of our criteria for activity, selectivity and stability.

Although Hg is toxic, only monolayer quantities of Hg would be required to produce the required atomic ensembles; its present industrial applications, for example, lighting or the cathode for chlorine synthesis, require much larger amounts⁴. In the following we show that PtHg_4 is indeed highly selective and active for the two-electron pathway.

Experimental results

To synthesize PtHg_4 , we modified a polycrystalline Pt disc following the procedure of ref. 35 for $\text{Hg}/\text{Pt}(111)$. About 10 monolayers

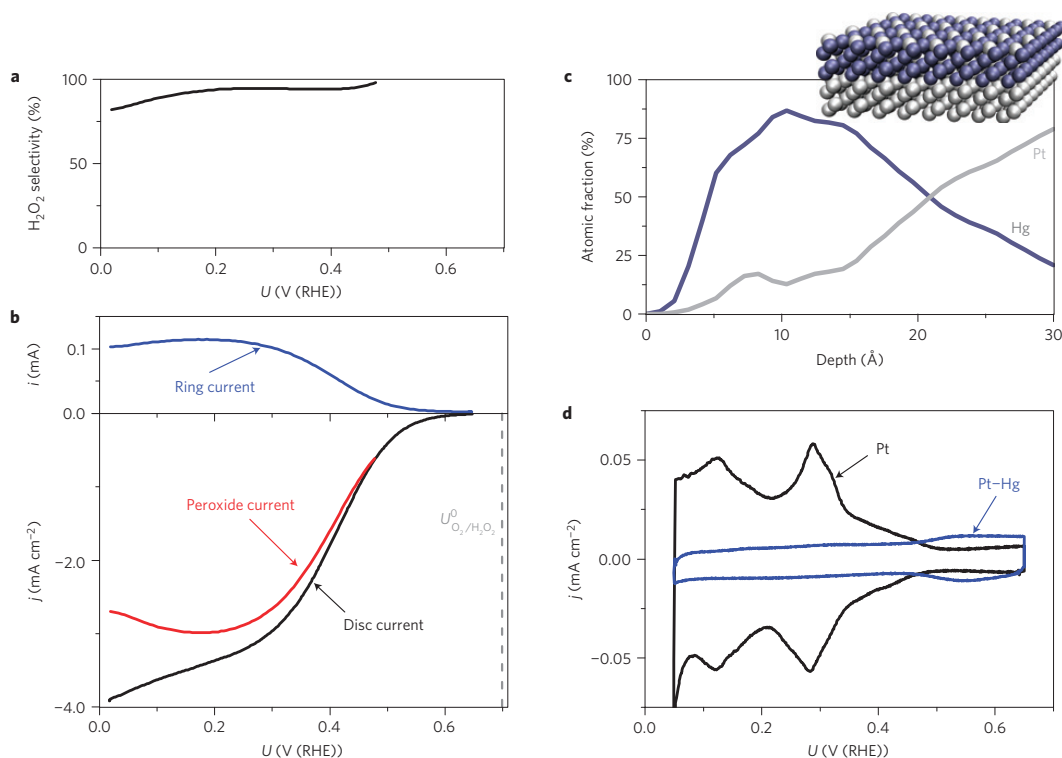


Figure 3 | Experimental characterization of Pt-Hg on extended surfaces. **a**, H_2O_2 selectivity as a function of the applied potential. **b**, RRDE voltammograms at 1,600 r.p.m. in O_2 -saturated electrolyte with the disc current, ring current and current corresponding to hydrogen peroxide obtained from the ring current (only the anodic cycle is shown). **c**, Angle-resolved XPS depth profile of Pt-Hg. The adventitious C and O traces have been omitted for clarity. The inset shows a schematic representation of the structure revealed by the angle-resolved depth profile, with a Pt-Hg alloy above a Pt substrate. **d**, Voltammograms in N_2 -saturated electrolyte of Pt and Pt-Hg. All electrochemical measurements were taken in 0.1 M HClO_4 and at 50 mV s^{-1} at room temperature.

of Hg were electrodeposited from HgClO_4 . *Ex situ* angle-resolved X-ray photoelectron spectroscopy (XPS) of the sample at this stage revealed that the surface is composed of $\sim 20\%$ Pt and $\sim 80\%$ Hg, in agreement with a PtHg_4 structure (Fig. 3c). Figure 3d shows a cyclic voltammogram in N_2 -saturated solution for Pt and Hg-modified Pt. The voltammogram for Pt shows the typical hydrogen adsorption/desorption peaks at 0.05–0.5 V, whereas Pt-Hg has a flat profile, suggesting a negligible amount of hydrogen adsorption. This is consistent with our DFT calculations (see Supplementary Information), which show that H is destabilized on $\text{PtHg}_4(110)$, relative to $\text{Pt}(111)$. Moreover, isolated Pd atoms on Au exhibit similar voltammograms¹³. We understand this phenomenon on the basis that on pure Pt and Pd, H usually adsorbs at hollow sites, with three Pt or Pd nearest neighbours³⁷; isolated Pt or Pd atoms would lack such sites. The negative alloying energy of PtHg_4 provides a driving force to maximize the coordination of Hg to Pt and minimize the number of Pt–Pt nearest neighbours. Further evidence for the surface composition can be found in the Supplementary Information. In summary, our observations support the notion that isolated Pt atoms are formed at the surface of Pt–Hg, consistent with earlier experiments on Hg/Pt(111) (ref. 35).

We measure the electrochemical activity for oxygen reduction to hydrogen peroxide, using the rotating ring disc electrode (RRDE) technique³⁸. Figure 3b shows the voltammograms in oxygen for Pt–Hg. The disc current increases exponentially with a decrease

in potential from $\sim 0.6 \text{ V}$, as kinetic barriers are lowered. To quantify the amount of hydrogen peroxide formed, the ring was potentiostated at 1.2 V, where the oxygen reduction current is negligible and H_2O_2 oxidation is mass transport limited. This gives rise to a positive current at the ring as hydrogen peroxide is produced at the disc (Fig. 3b). The onset potential at the ring and the disc coincide at $\sim 0.6 \text{ V}$, corresponding to an overpotential of $\sim 0.1 \text{ V}$. Such low overpotential is in agreement with our theoretical predictions. As the overpotential increases, most of the current in the disc can be accounted for by the amount of H_2O_2 detected at the ring; the efficiency of hydrogen peroxide production is as high as 96% in the region between 0.2 and 0.4 V (Fig. 3a). Within these potential limits, the hydrogen peroxide current density is 3 mA cm^{-2} , the theoretical mass transport limit for the two-electron reduction of oxygen. It is only at potentials below 0.2 V that both selectivity and hydrogen peroxide current start to decrease, implying that water formation is favoured.

To validate the stability criteria for our computational screening (Fig. 2), we also tested Pt–Sn and Ag_3Pt as catalysts for H_2O_2 production. As described in the Supplementary Information, we predict that both of these catalysts would, in principle, have optimal H_2O_2 activity. However, they fail to meet our stability criteria. Consequently, the less noble component, Sn or Ag, dissolved under reaction conditions. These examples illustrate the importance of stability in the corrosive electrochemical environment, which is both acidic and oxidizing.

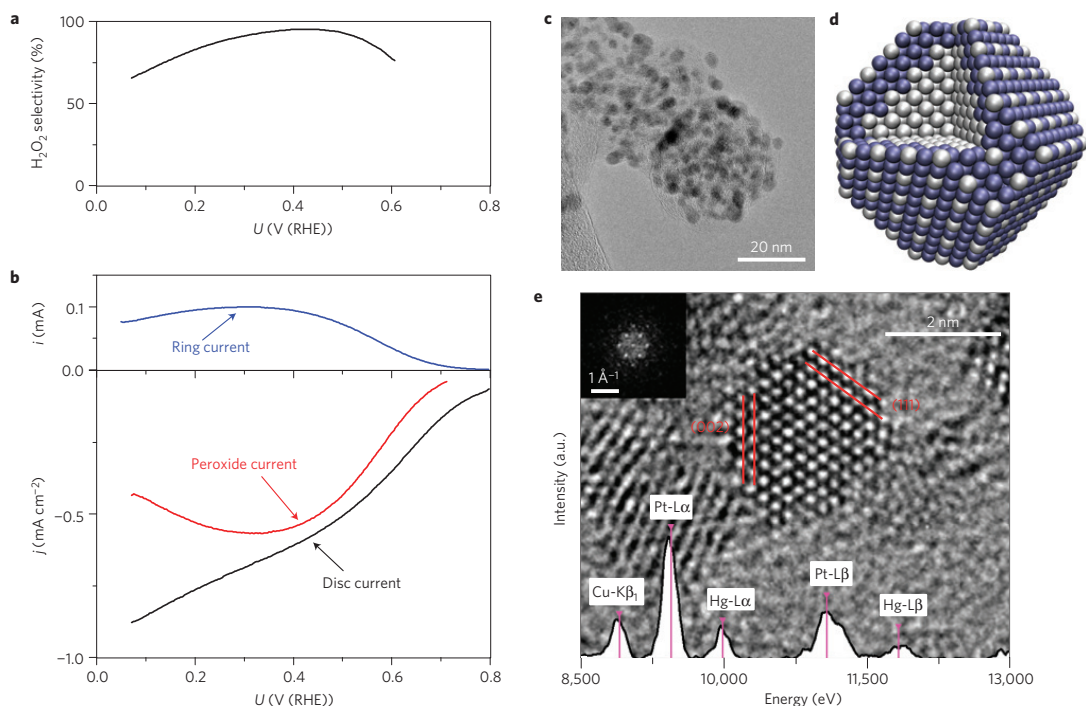


Figure 4 | Experimental characterization of Pt-Hg/C nanoparticles. **a**, H_2O_2 selectivity as a function of the applied potential. **b**, RRDE voltammograms at 1,600 r.p.m. in O_2 -saturated electrolyte with the disc current, ring current and current corresponding to hydrogen peroxide obtained from the ring current (only the anodic cycle is shown). All electrochemical measurements were taken in 0.1 M HClO_4 and at 50 mV s^{-1} at room temperature. The disc current is normalized to the surface area of Pt nanoparticles (from H-upd) before deposition of Hg. **c**, TEM image of Pt-Hg/C nanoparticles. **d**, Schematic representation of a Pt-Hg/C nanoparticle. Mercury, blue; platinum, grey. **e**, HRTEM image of a single Pt-Hg nanoparticle, with the corresponding EDS spectrum of the particle superimposed on top, with peaks corresponding to Pt and Hg from the nanoparticle, and Cu, from the TEM grid; the {111} and {002} planes are shown in red; the corresponding diffractogram is shown in the inset.

Ultimately, should electrochemical hydrogen peroxide synthesis make a technological impact, it will require high-surface-area catalysts or thin films^{26,39}. It turns out that Pt-Hg/C nanoparticles are even more active than the extended surfaces.

An ink was prepared from commercial Pt/C and drop-cast on a glassy carbon electrode (details in the Supplementary Information). To prepare the Pt-Hg alloy we followed the same electrodeposition procedure as for the polycrystalline surface. The features of the base voltammograms were similar to those of polycrystalline Pt-Hg (see Supplementary Information).

Transmission electron microscopy (TEM) analysis showed well-distributed nanoparticles on the carbon support (Fig. 4c). A high-resolution TEM (HRTEM) image of a single nanoparticle and its Fourier transform are shown in Fig. 4e. By positioning the scanning TEM probe on an individual nanoparticle, an energy-dispersive X-ray spectroscopy (EDS) spectrum as shown in Fig. 4e was acquired. Both Pt and Hg peaks are present in the spectrum. XPS analysis, which is sensitive to the first few atomic layers, confirmed the presence of both elements. However, the lattice parameters from the HRTEM are consistent with the structure of Pt. Together, the HRTEM and XPS data suggest a core of Pt and a shell of Pt-Hg (see Supplementary Information).

We then evaluated oxygen reduction on Hg-modified Pt nanoparticles (Fig. 4b), where we observed a similar current profile to the polycrystalline surfaces. The ring current proved that a high yield of hydrogen peroxide was achieved, with over 90% selectivity between 0.3 and 0.5 V (Fig. 4a). The catalyst is highly stable

under reaction conditions. When cycling the potential between 0.05 and 0.8 V for 8,000 cycles in an O_2 -saturated electrolyte, there were no measurable losses in H_2O_2 production activity (see Supplementary Information).

The viability of an electrochemical device producing H_2O_2 will require it to be efficient, safe and that the cost of its constituent materials is minimal. Given that the most viable catalysts for H_2O_2 production are based on precious metals, it is essential that the loading of these metals is minimized, that is, that the current density per gram of precious metal is maximized.

State-of-the-art fuel cells and electrolyzers are engineered to avoid losses due to the transport of oxygen. Thus, to yield a quantitative comparison of catalyst performance, we have corrected the data in Figs 3 and 4 for mass transport losses. The results are shown in Fig. 1. In terms of specific activity (normalized to the surface area of Pt), nanoparticulate Pt-Hg/C exhibits 4–5 times the activity of polycrystalline Pt-Hg. The higher activity of the nanoparticles compared with extended surfaces indicates that undercoordinated sites, which are more prevalent on nanoparticulate surfaces⁴⁰, could play an important role in the reaction. Notably, Pt-Hg/C shows more than one order of magnitude improvement in mass activity over previously reported Pd-Au/C or Au/C (ref. 13). To the best of our knowledge, Pt-Hg nanoparticles present the best activity reported in the literature for hydrogen peroxide synthesis on a metallic catalyst, with a selectivity of up to 96% and a mass activity of $26 \pm 4 \text{ A g}^{-1}_{\text{metal}}$ at 50 mV overpotential.

In this work, we have taken advantage of the isolated active site concept to tune the activity and selectivity for oxygen reduction. Our theoretical model successfully predicted Pt–Hg as an active, selective and stable catalyst for hydrogen peroxide synthesis.

Comparing the activity reported here with that reported for other two-electron reactions, we anticipate that it should be possible to discover even more active catalysts for electrochemical H₂O₂ production^{23,30,37,41,42}. Nonetheless, as our theoretical model shows, improved activity may come at the cost of selectivity. The rational approach used here to tune activity and selectivity can be extended to other, more complex reactions for sustainable energy conversion, in particular the electroreduction of CO₂ and N₂ (refs 28,29).

Methods

Computational details. The computational analysis was carried out using grid-based projector-augmented wave (GPAW) method, a DFT code based on a projected augmented wave (all-electron frozen core approximation) method integrated with the atomic simulation environment^{43,44}. The revised Perdew–Burke–Ernzerhof functional was used as an exchange correlation functional⁴⁵. An eight-layer 2 × 2 slab with 17.5 Å vacuum between successive slabs was used to model the PtHg₄(110) surface. Monkhorst–Pack grids with dimensions of 4 × 4 × 1 were used to sample the Brillouin zone. The bottom four layers were fixed in the bulk structure whereas the upper layers and adsorbates were allowed to relax in all directions until residual forces were less than 0.05 eV Å⁻¹. Further details on DFT calculations are provided in the Supplementary Information.

Extended surface electrode preparation. A platinum polycrystalline electrode was mirror polished to <0.25 μm before every experiment and prepared by flame annealing as previously reported⁴⁶. Several voltammograms in nitrogen-saturated 0.1 M HClO₄ were recorded to ensure a reproducible surface, and then the electrode was moved to an electrodeposition cell containing 0.1 M HClO₄ + 1 mM HgCl₂. The potential was swept from open circuit (about 1 V) at 50 mV s⁻¹ to 0.2 V, where the potential was stopped for 2 min to electrodeposit mercury following the procedure detailed in ref. 35. The potential was scanned to 0.65 V at 50 mV s⁻¹ and stopped there while removing the electrode from the cell. We immediately moved the Hg-modified Pt electrode back into the RRDE cell, where it was inserted under potential control of about 0.1 V in N₂-saturated 0.1 M HClO₄. Then the potential was swept between 0.05 and 0.65 V until a stable cyclic voltammogram was obtained. As we observed mercury traces at the ring, we cleaned it electrochemically by cycling it between 0.05 and 1.6 V while rotating the electrode to avoid mercury redeposition. Once the ring and disc voltammograms became stable, we saturated the cell with O₂ to record voltammograms at the disc while keeping the ring at 1.2 V to detect H₂O₂.

High-surface-area catalysts. To prepare the Pt/C nanoparticles, a simple synthesis method was employed. First, 5.75 mg of 60% wt Pt supported on C was mixed with 9.5 ml of Millipore water, 3 ml of isopropanol and 50 μl of 1:100 Nafion. To facilitate dispersion of the nanoparticles, 20 μl of 2% wt solution of polyvinylpyrrolidone was used. The nanoparticles had a nominal size of 3 nm. The mixture was sonicated for 20 min at about 25 °C and 10 μl of it was drop-casted on top of a glassy carbon disc of 0.196 cm². The sample was then left to dry before embedding into a RRDE set-up. To ensure a good dispersion of the film, oxygen reduction was carried out on the Pt/C nanoparticles (see Supplementary Information). The same procedure adopted for the polycrystalline sample was followed to electrodeposit mercury. All data relative to nanoparticles were normalized to the underpotential deposition of hydrogen (H-upd); that is, assuming that the voltammetric charge between 0.5 and 0.05 V is equivalent to 210 μC cm⁻² of Pt surface area¹⁸ before Hg deposition, and the corresponding capacitance was subtracted from all oxygen reduction measurements.

Chemicals. Concentrated HClO₄ was obtained from Merck and diluted to 0.1 M. HgClO₄ was obtained from Sigma Aldrich and diluted in 0.1 M HClO₄ to reach 1 mM HgClO₄. All gases were of 5N5 quality and purchased from AGA.

Electrochemical measurements. A typical three-electrode cell was used for the RRDE experiments. Another three-electrode cell was used to electrodeposit mercury. In both cells the counter electrodes were Pt wires and Hg/Hg₂SO₄ electrodes were used as a reference, separated from the working electrode compartment using a ceramic frit. All potentials are quoted with respect to the reversible hydrogen electrode, and are corrected for ohmic losses. All experiments were performed using a Bio-Logic Instruments' VMP2 potentiostat, controlled by a computer. The RRDE assembly was provided by Pine Instruments Corporation. The ring was made of platinum and its collection efficiency, *N*, was of 20 ± 1%. To compute H₂O₂ selectivity, η , we made use of the following equation³⁸: $\eta = 2(I_r/N/I_d + I_r/N)$, where *I_r* and *I_d* are ring and disc currents, respectively. H₂O₂ selectivity is not calculated below ~0.2 mA of disc current, owing to a poorer signal to background ratio at low currents.

To correct the current for mass transport losses, the equation $1/j = 1/j_d + 1/j_k$ was used, where *j* is the total current, *j_d* is the mass-transport-limited current to hydrogen peroxide (obtained from the ring), and *j_k* is the kinetic current to hydrogen peroxide. Further details are given in the Supplementary Information.

Received 27 June 2013; accepted 1 October 2013; published online 17 November 2013; corrected after print 21 November 2013 and 23 December 2013

References

- Perlo, P. *et al.* *Catalysis for Sustainable Energy Production* 89–105 (Wiley, 2009).
- Armaroli, N. & Balzani, V. The future of energy supply: challenges and opportunities. *Angew. Chem. Int. Ed.* **46**, 52–66 (2007).
- Kotrel, S. & Brauning, S. in *Handbook of Heterogeneous Catalysis* 2nd edn (eds Ertl, G., Knoezinger, H., Schueth, F. & Weitkamp, J.) 1963 (Wiley, 2008).
- Ullmann's Encyclopedia of Industrial Chemistry* (Wiley, 1999–2013).
- Samanta, C. Direct synthesis of hydrogen peroxide from hydrogen and oxygen: An overview of recent developments in the process. *Appl. Catal. A* **350**, 133–149 (2008).
- Campos-Martin, J. M., Blanco-Brieva, G. & Fierro, J. L. G. Hydrogen peroxide synthesis: An outlook beyond the anthraquinone process. *Angew. Chem. Int. Ed.* **45**, 6962–6984 (2006).
- Fukuzumi, S., Yamada, Y. & Karlin, K. D. Hydrogen peroxide as a sustainable energy carrier: Electrochemical production of hydrogen peroxide and the fuel cell. *Electrochim. Acta* **82**, 493–511 (2012).
- Háncu, D., Green, J. & Beckman, E. J. H₂O₂ in CO₂/H₂O biphasic systems: Green synthesis and epoxidation reactions. *Ind. Eng. Chem. Res.* **41**, 4466–4474 (2002).
- Edwards, J. K. *et al.* Switching off hydrogen peroxide hydrogenation in the direct synthesis process. *Science* **323**, 1037–1041 (2009).
- Ford, D. C., Nilekar, A. U., Xu, Y. & Mavrikakis, M. Partial and complete reduction of O₂ by hydrogen on transition metal surfaces. *Surf. Sci.* **604**, 1565–1575 (2010).
- Yamanaka, I., Hashimoto, T., Ichihashi, R. & Otsuka, K. Direct synthesis of H₂O₂ acid solutions on carbon cathode prepared from activated carbon and vapor-growing-carbon-fiber by a H₂/O₂ fuel cell. *Electrochim. Acta* **53**, 4824–4832 (2008).
- Lobytseva, E., Kallio, T., Alexeyeva, N., Tammeveski, K. & Kontturi, K. Electrochemical synthesis of hydrogen peroxide: Rotating disk electrode and fuel cell studies. *Electrochim. Acta* **52**, 7262–7269 (2007).
- Jirkovský, J. S. *et al.* Single atom hot-spots at Au–Pd nanoalloys for electrocatalytic H₂O₂ production. *J. Am. Chem. Soc.* **133**, 19432–19441 (2011).
- Fellinger, T.-P., Hasché, F., Strasser, P. & Antonietti, M. Mesoporous nitrogen-doped carbon for the electrocatalytic synthesis of hydrogen peroxide. *J. Am. Chem. Soc.* **134**, 4072–4075 (2012).
- Gouérec, P. & Savy, M. Oxygen reduction electrocatalysis: Ageing of pyrolyzed cobalt macrocycles dispersed on an active carbon. *Electrochim. Acta* **44**, 2653–2661 (1999).
- Bezerra, C. W. B. *et al.* A review of Fe–N/C and Co–N/C catalysts for the oxygen reduction reaction. *Electrochim. Acta* **53**, 4937–4951 (2008).
- Schulenburg, H. *et al.* Catalysts for the oxygen reduction from heat-treated iron(III) tetramethoxyphenylporphyrin chloride: Structure and stability of active sites. *J. Phys. Chem. B* **107**, 9034–9041 (2003).
- Sheng, W., Gasteiger, H. A. & Shao-Horn, Y. Hydrogen oxidation and evolution reaction kinetics on platinum: Acid vs alkaline electrolytes. *J. Electrochem. Soc.* **157**, B1529–B1536 (2010).
- Ayers, K. E., Dalton, L. T. & Anderson, E. B. Efficient generation of high energy density fuel from water. *ECS Trans.* **41**, 27–38 (2012).
- Viswanathan, V., Hansen, H. A., Rossmeisl, J. & Nørskov, J. K. Unifying the 2e⁻ and 4e⁻ reduction of oxygen on metal surfaces. *J. Phys. Chem. Lett.* **3**, 2948–2951 (2012).
- Nørskov, J. K., Bligaard, T., Rossmeisl, J. & Christensen, C. H. Towards the computational design of solid catalysts. *Nature Chem.* **1**, 37–46 (2009).
- Greeley, J. *et al.* Alloys of platinum and early transition metals as oxygen reduction electrocatalysts. *Nature Chem.* **1**, 552–556 (2009).
- Koper, M. T. M. Thermodynamic theory of multi-electron transfer reactions: Implications for electrocatalysis. *J. Electroanal. Chem.* **660**, 254–260 (2011).
- Janik, M. J., Taylor, C. D. & Neurock, M. First-principles analysis of the initial electroreduction steps of oxygen over Pt(111). *J. Electrochem. Soc.* **156**, B126–B135 (2009) doi:10.1149/1.3008005.
- Tripković, V., Skúlason, E., Siahrostami, S., Nørskov, J. K. & Rossmeisl, J. The oxygen reduction reaction mechanism on Pt(111) from density functional theory calculations. *Electrochim. Acta* **55**, 7975–7981 (2010).
- Stephens, I. E. L., Bondarenko, A. S., Gronbjerg, U., Rossmeisl, J. & Chorkendorff, I. Understanding the electrocatalysis of oxygen reduction on platinum and its alloys. *Energy Environ. Sci.* **5**, 6744–6762 (2012).
- Rossmeisl, J., Karlberg, G. S., Jaramillo, T. & Nørskov, J. K. Steady state oxygen reduction and cyclic voltammetry. *Faraday Discuss.* **140**, 337–346 (2009).

28. Peterson, A. A. & Nørskov, J. K. Activity descriptors for CO₂ electroreduction to methane on transition-metal catalysts. *J. Phys. Chem. Lett.* **3**, 251–258 (2012).
29. Skulason, E. *et al.* A theoretical evaluation of possible transition metal electro-catalysts for N₂ reduction. *Phys. Chem. Chem. Phys.* **14**, 1235–1245 (2012).
30. Hansen, H. A. *et al.* Electrochemical chlorine evolution at rutile oxide (110) surfaces. *Phys. Chem. Chem. Phys.* **12**, 283–290 (2010).
31. Maroun, F., Ozanam, F., Magnussen, O. M. & Behm, R. J. The role of atomic ensembles in the reactivity of bimetallic electrocatalysts. *Science* **293**, 1811–1814 (2001).
32. Strmcnik, D. *et al.* Enhanced electrocatalysis of the oxygen reduction reaction based on patterning of platinum surfaces with cyanide. *Nature Chem.* **2**, 880–885 (2010).
33. Viswanathan, V. *et al.* Simulating linear sweep voltammetry from first-principles: Application to electrochemical oxidation of water on Pt(111) and Pt₃Ni(111). *J. Phys. Chem. C* **116**, 4698–4704 (2012).
34. Siahrostami, S., Bjorketun, M. E., Strasser, P., Greeley, J. & Rossmeisl, J. Tandem cathode for proton exchange membrane fuel cells. *Phys. Chem. Chem. Phys.* **15**, 9326–9334 (2013).
35. Wu, H. L., Yau, S. & Zei, M. S. Crystalline alloys produced by mercury electrodeposition on Pt(111) electrode at room temperature. *Electrochim. Acta* **53**, 5961–5967 (2008).
36. Angerstein-Kozłowska, H., MacDougall, B. & Conway, B. E. Origin of activation effects of acetonitrile and mercury in electrocatalytic oxidation of formic acid. *J. Electrochem. Soc.* **120**, 756–766 (1973).
37. Skulason, E. *et al.* Modeling the electrochemical hydrogen oxidation and evolution reactions on the basis of density functional theory calculations. *J. Phys. Chem. C* **114**, 18182–18197 (2010).
38. Paulus, U. A., Schmidt, T. J., Gasteiger, H. A. & Behm, R. J. Oxygen reduction on a high-surface area Pt/Vulcan carbon catalyst: A thin-film rotating ring-disk electrode study. *J. Electroanal. Chem.* **495**, 134–145 (2001).
39. Van der Vliet, D. F. *et al.* Mesostuctured thin films as electrocatalysts with tunable composition and surface morphology. *Nature Mater.* **11**, 1051–1058 (2012).
40. Perez-Alonso, F. J. *et al.* The effect of size on the oxygen electroreduction activity of mass-selected platinum nanoparticles. *Angew. Chem. Intl Ed.* **51**, 4641–4643 (2012).
41. Wessellmark, M., Wickman, B., Lagergren, C. & Lindbergh, G. Hydrogen oxidation reaction on thin platinum electrodes in the polymer electrolyte fuel cell. *Electrochem. Commun.* **12**, 1585–1588 (2010).
42. Wolfschmidt, H., Weingarth, D. & Stimming, U. Enhanced reactivity for hydrogen reactions at Pt nanoislands on Au(111). *ChemPhysChem* **11**, 1533–1541 (2010).
43. Mortensen, J. J., Hansen, L. B. & Jacobsen, K. W. Real-space grid implementation of the projector augmented wave method. *Phys. Rev. B* **71**, 035109 (2005).
44. Atomic Simulation Environment (ASE), available at <https://wiki.fysik.dtu.dk/ase>, Center for Atomic Scale Material Design (CAMD), Technical University of Denmark, Lyngby.
45. Hammer, B., Hansen, L. B. & Nørskov, J. K. Improved adsorption energetics within density-functional theory using revised Perdew-Burke-Ernzerhof functionals. *Phys. Rev. B* **59**, 7413–7421 (1999).
46. Verdager-Casadevall, A., Hernandez-Fernandez, P., Stephens, I. E. L., Chorkendorff, I. & Dahl, S. The effect of ammonia upon the electrocatalysis of hydrogen oxidation and oxygen reduction on polycrystalline platinum. *J. Power Sources* **220**, 205–210 (2012).
47. Alvarez-Rizatti, M. & Jüttner, K. Electrocatalysis of oxygen reduction by UPD of lead on gold single-crystal surfaces. *J. Electroanal. Chem. Interfacial Electrochem.* **144**, 351–363 (1983).
48. Jirkovsky, J. S., Halasa, M. & Schiffrin, D. J. Kinetics of electrocatalytic reduction of oxygen and hydrogen peroxide on dispersed gold nanoparticles. *Phys. Chem. Chem. Phys.* **12**, 8042–8053 (2010).
49. Blizanac, B. B., Ross, P. N. & Markovic, N. M. Oxygen electroreduction on Ag(111): The pH effect. *Electrochim. Acta* **52**, 2264–2271 (2007).
50. *CRC Handbook of Chemistry and Physics* (CRC Press, 1996).

Acknowledgements

The authors gratefully acknowledge financial support from the Danish Ministry of Science's UNIK initiative, Catalysis for Sustainable Energy and The Danish Council for Strategic Research's project NACORR (12-132695). M.E.-E. acknowledges financial support from EU PF7's initiative Fuel Cell and Hydrogen Joint Undertaking's project CathCat (GA 303492). B.W. thanks Formas (project number 219-2011-959) for financial support. The Center for Individual Nanoparticle Functionality is supported by the Danish National Research Foundation (DNRF54).

Author contributions

J.R. and S.S. conceived the DFT calculations. S.S. and M.K. performed the DFT calculations. A.V. and I.E.L.S. designed the experiments. A.V. performed the electrochemical experiments, D.D. the TEM, P.M. the XPS and B.W. the EQCM and SEM-EDS. E.A.P. and R.F. prepared the Ag₃Pt sample and performed its XRD. S.S., A.V. and I.E.L.S. co-wrote the first draft of the paper. A.V. designed the figures. All authors discussed the results and commented on the manuscript.

Additional information

Supplementary information is available in the online version of the paper. Reprints and permissions information is available online at www.nature.com/reprints. Correspondence and requests for materials should be addressed to I.E.L.S. or J.R.

Competing financial interests

Patent application EP 13165265.3 'Alloy catalyst material' has been filed.

CORRIGENDUM

Enabling direct H₂O₂ production through rational electrocatalyst design

Samira Siahrostami, Arnau Verdaguer-Casadevall, Mohammadreza Karamad, Davide Deiana, Paolo Malacrida, Björn Wickman, María Escudero-Escribano, Elisa A. Paoli, Rasmus Frydendal, Thomas W. Hansen, Ib Chorkendorff, Ifan E. L. Stephens and Jan Rossmeisl

Nature Materials **12**, 1137–1143 (2013); published online 17 November 2013; corrected after print 21 November 2013.

In the version of this Article originally published, the middle initials of the penultimate author were missing; the name should have read Ifan E. L. Stephens. In the Author contributions and Additional information sections 'I.S.' should have read 'I.E.L.S.' These errors have now been corrected in the online versions of the Article.

ERRATUM

Enabling direct H₂O₂ production through rational electrocatalyst design

Samira Siahrostami, Arnau Verdaguer-Casadevall, Mohammadreza Karamad, Davide Deiana, Paolo Malacrida, Björn Wickman, María Escudero-Escribano, Elisa A. Paoli, Rasmus Frydendal, Thomas W. Hansen, Ib Chorkendorff, Ifan E. L. Stephens and Jan Rossmeisl

Nature Materials **12**, 1137–1143 (2013); published online 17 November 2013; corrected after print 21 November 2013 and 23 December 2013.

In the version of this Article originally published, in Fig. 1, the top two values on the *y* axis were switched. This error has now been corrected in the online versions of the Article.

Trends in the Electrochemical Synthesis of H₂O₂: Enhancing Activity and Selectivity by Electrocatalytic Site Engineering

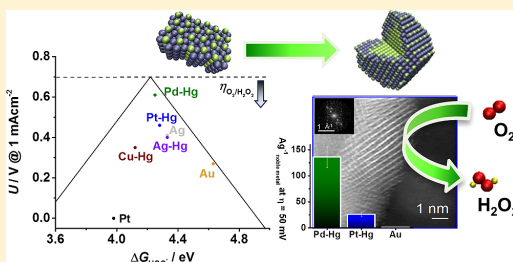
Arnau Verdaguer-Casadevall,[†] Davide Deiana,[‡] Mohammadreza Karamad,[§] Samira Siahrostami,[§] Paolo Malacrida,[†] Thomas W. Hansen,[‡] Jan Rossmeisl,[§] Ib Chorkendorff,^{*,†} and Ifan E. L. Stephens^{*,†}

[†]Center for Individual Nanoparticle Functionality, Department of Physics, [‡]Center for Electron Nanoscopy, and [§]Center for Atomic-scale Materials Design, Department of Physics, Technical University of Denmark, DK-2800 Kongens Lyngby, Denmark

S Supporting Information

ABSTRACT: The direct electrochemical synthesis of hydrogen peroxide is a promising alternative to currently used batch synthesis methods. Its industrial viability is dependent on the effective catalysis of the reduction of oxygen at the cathode. Herein, we study the factors controlling activity and selectivity for H₂O₂ production on metal surfaces. Using this approach, we discover two new catalysts for the reaction, Ag–Hg and Pd–Hg, with unique electrocatalytic properties both of which exhibit performance that far exceeds the current state-of-the-art.

KEYWORDS: H₂O₂ production, catalysis, electrochemistry, oxygen reduction, nanoparticles



Economic development and a continued increase in global population place growing pressure on our energy resources. A significant fraction of the world's total energy consumption and raw materials are employed to produce chemicals. These chemicals are typically generated on a large scale in centralized locations.¹ However, localized chemical production, closer to the point of consumption, would present significant cost and energy savings. Electrochemical devices will play a major role in the transformation, as they can be operated at ambient temperatures and pressures in small plants and require minimal capital investment.²

Herein, we focus on the electrochemical oxygen reduction to hydrogen peroxide, a chemical whose electrochemical production is particularly appealing.³ Currently, 3 M tons/year of H₂O₂ are being produced, mainly for use in the paper and chemical industry.³ It is synthesized from hydrogen and oxygen by a complex batch method, the anthraquinone process, only suitable for large scale facilities.⁴ The inherent disadvantages of batch synthesis methods and its energetic inefficiency have motivated industry and academia alike to develop an alternative. Consequently, the “direct catalytic” route to H₂O₂ synthesis has long been a dream reaction for the heterogeneous catalysis community; it involves the direct reaction of H₂ and O₂ in a liquid solvent on a Pd/Au catalyst.^{5,6} Not only would the direct method enable production in a continuous mode, but it would also permit small scale, decentralized production. However, the direct route needs to handle potentially explosive mixtures of hydrogen and oxygen and does not make use of the embedded energy released upon reacting H₂.

A growing community of researchers are proposing an electrochemical route based on catalysts that selectively reduce

oxygen to hydrogen peroxide.^{7–9} That way, the danger of explosion is avoided by keeping hydrogen and oxygen separated. Moreover, producing H₂O₂ in a fuel cell would enable recovery of the energy released during the reaction. Alternatively, by producing it in an electrolyzer, one could avoid usage of H₂ altogether and use water as a source of protons.

Crucial to the performance of electrochemical devices for H₂O₂ production is the catalyst at the electrodes. A successful electrocatalyst should have (a) high activity, operating with high current densities as close as possible to the equilibrium potential, to optimize energy efficiency and catalyst loading; (b) high selectivity, ensuring high yields of H₂O₂; and (c) high stability, enabling long-term durability.

Significant efforts have been spent in the field of electrocatalysis to find descriptors for the trends in activity for electrochemical reactions. They all lead to a Sabatier volcano, where the highest activity is achieved on the surface with a moderate interaction with the reaction intermediates.^{10–17} Most importantly, knowledge of this descriptor can lead to the discovery of new materials whose electrocatalytic performance exceeds the current state-of-the-art.^{13,14,18,19}

The activity for H₂O₂ production is a function of the binding of the sole reaction intermediate, HOO* (Figure 1a).^{20,21} For the ideal catalyst, the adsorption of HOO* should be thermoneutral at the equilibrium potential ($U_{O_2/H_2O_2}^0 = 0.7$ V),

Received: January 5, 2014

Revised: January 28, 2014

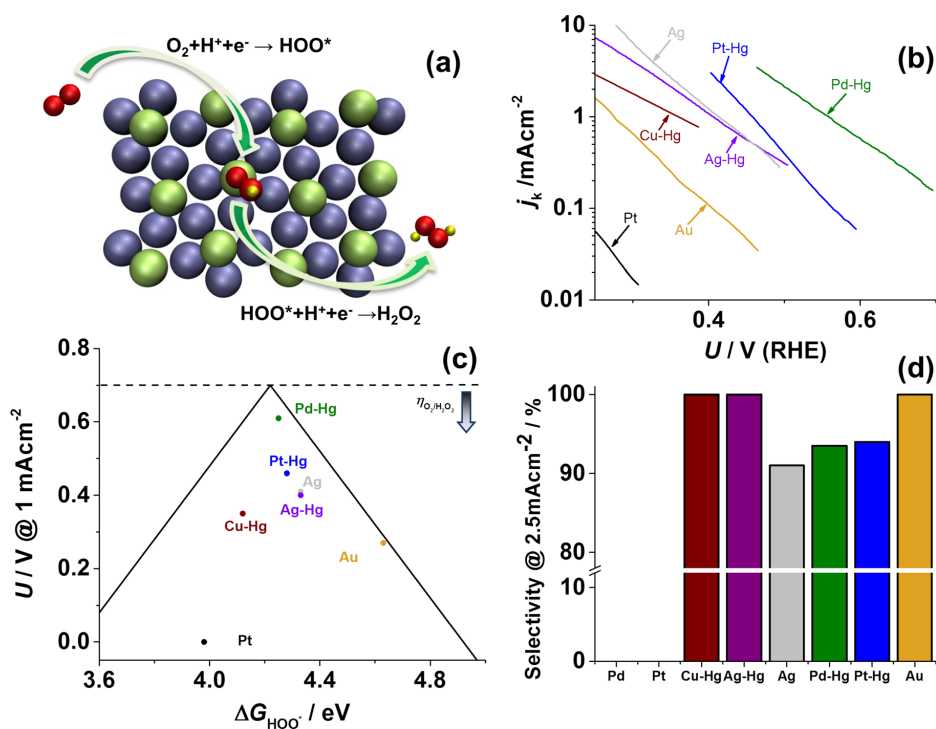


Figure 1. Trends in activity and selectivity for H₂O₂ production. (a) Schematic representation of oxygen reduction to H₂O₂ on a model Pd₂Hg₁(001) surface. Palladium atoms are represented in green, mercury in blue, oxygen in red, and hydrogen in yellow. (b) Partial kinetic current density to H₂O₂ as a function of the applied potential, corrected for mass transport losses. (c) Potential required to reach 1 mAcm⁻² of kinetic current density to H₂O₂ on polycrystalline catalysts as a function of the calculated HOO* binding energy. The solid lines represent the theoretical Sabatier volcano.²¹ The dotted line represents the thermodynamic potential for oxygen reduction to H₂O₂. (d) H₂O₂ selectivity for different catalysts at 2.5 mAcm⁻² of total current density. For this figure, data for Cu–Hg was extrapolated for ~100 mV as it is unstable above 0.25 V.²⁷ Data for Au adapted from Jirkovsky et al.,²⁸ data for Pt from Verdaguer-Casadevall et al.,⁴⁸ and data for Pt–Hg from Siahrostami et al.²⁰ All electrochemical experiments were performed at 50 mV s⁻¹ and 1600 rpm in O₂-saturated 0.1 M HClO₄ at room temperature with corrections for Ohmic drop. The surface area was normalized to the geometrical value.

so that the theoretical overpotential for the reaction, $\eta = 0$. Stronger or weaker binding to HOO* will introduce additional overpotential, or lower electrocatalytic activity. This means that the theoretical overpotential should show a Sabatier-volcano type dependence on the HOO* adsorption energy, ΔG_{HOO^*} .

Selectivity is determined by the ability of the catalyst to split the O–O bond during the oxygen reduction reaction, preventing water formation ($U_{O_2/H_2O}^0 = 1.23$ V). The most successful catalysts in this respect include Co porphyrins²² and Pd–Au.⁷ They rely on the presence of isolated sites of a reactive atom, Co or Pd, surrounded by more inert atoms, N, C, and Au. Such sites are unable to break the O–O bond, ensuring a high selectivity to H₂O₂.

On the basis of the above ideas, we recently discovered a new catalyst for H₂O₂ production. Our density functional theory calculations identified Pt–Hg as a highly active and selective catalyst for the reaction. Our experiments confirmed the theoretical predictions, showing that both extended surfaces and nanoparticles of Pt–Hg are highly active and selective for oxygen reduction to H₂O₂.²⁰ In the current study, our goal is to systematically study trends for H₂O₂ production on both pure metals and alloy surfaces. We identify the most promising

catalysts using well-characterized extended surfaces. Density functional theory (DFT) calculations are used to rationalize the observed trends. We then apply this knowledge gained from the model surfaces to produce the catalyst in a technologically relevant form, that is, nanoparticles. This approach serves as a general example of how improved catalysts can be developed via a fundamental understanding of the factors controlling their performance in an electrochemical environment.

When Hg is electrodeposited on Pt, the two metals form an ordered intermetallic at room temperature where isolated Pt atoms are surrounded by Hg.²³ The same electrodeposition procedure can be performed to modify other metals in particular Cu, Pd, and Ag. We choose these metals as they all alloy with Hg^{24–26} and they exhibit at least some stability against dissolution under the acidic conditions and potential range where O₂ reduction to H₂O₂ would take place (i.e., 0 to 0.7 V).²⁷ Further details regarding the preparation and characterization of these extended surfaces can be found in the Supporting Information.

On Figure 1b, we plot the partial current densities to hydrogen peroxide production, corrected for mass transport, on polycrystalline electrodes as a function of the applied potential.

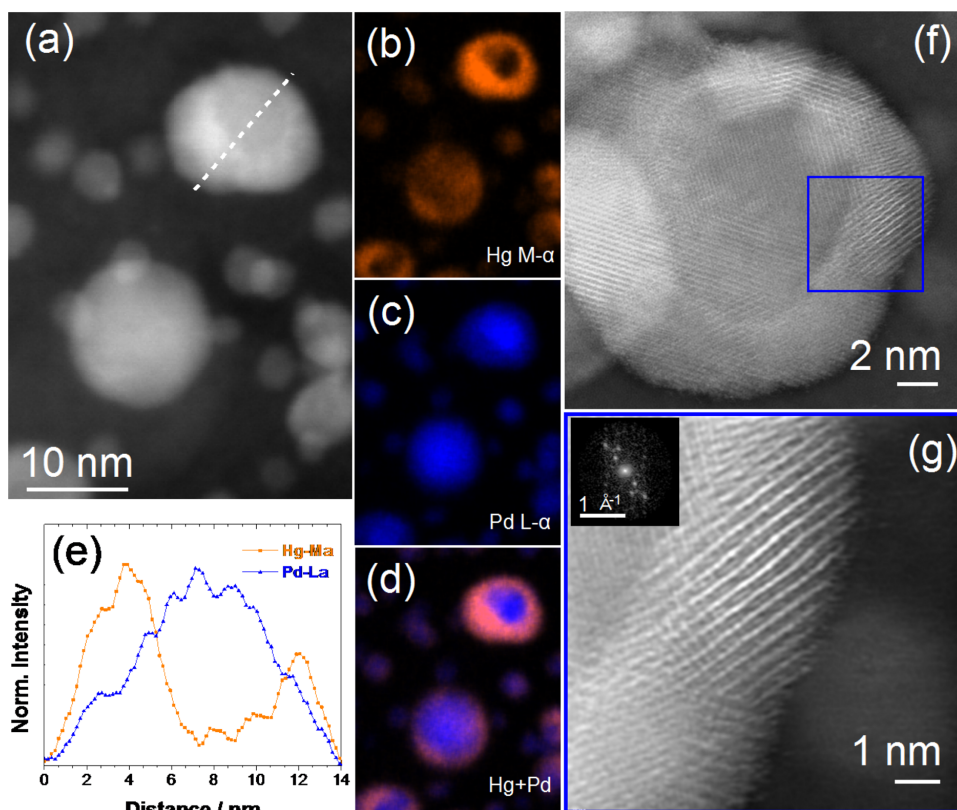


Figure 2. Electron microscopy characterization of Pd–Hg nanoparticles. (a) HAADF-STEM image of Pd–Hg nanoparticles and respective Hg, Pd, and Hg+Pd STEM-EDS elemental maps (b–d). (e) Normalized EDS Hg-M α (orange) and Pd-L α (blue) intensity line profiles extracted from the spectrum image data cube along with the white dashed line drawn on (a). (f) Fourier-filtered HAADF-STEM image of a Pd–Hg nanoparticle, showing a visible core–shell structure. (g) High-magnification HAADF-STEM image of the region enclosed in the blue square in (f); the inset shows the FFT of the bright fringes region.

Clearly, the electrode material has a decisive effect on the overpotential. In particular, the highest current at the lowest overpotential is obtained on Pd–Hg electrodes, while Pt–Hg, Ag–Hg, and Cu–Hg present increasing overpotentials. Notably, pure Ag has a high activity for this reaction, similar to that of Pt–Hg. All these materials are more active than Au-based catalysts, which have been extensively investigated in previous studies;^{7,28,29} Pt–Hg, Ag, and Ag–Hg exhibit an order of magnitude improvement over Au, whereas the activity of Pd–Hg is 2 orders of magnitude higher.

To rationalize these findings, we used DFT to calculate ΔG_{HOO^*} on the active sites for the reaction. Extensive details regarding the calculations are available in the Supporting Information. On Figure 1c, we plot the experimental overpotential required to reach 1 mAcm⁻² of current to H₂O₂ for different catalysts, as a function of ΔG_{HOO^*} . In particular, Pd–Hg exhibits the lowest overpotential, or highest activity, because it lies closest to the peak of the volcano. Catalysts such as Au or Ag bind HOO* too weakly, which means that their overpotential is due to the lack of formation of HOO* from O₂. All these catalysts lie on the right leg of the volcano and their activity follows the HOO* binding energy. On the

other hand, the left leg of the volcano is somewhat steeper than the theoretical Sabatier volcano would suggest. The reason for this is selectivity: catalysts at the left leg will tend to favor water formation over H₂O₂.^{20,21} Therefore, catalysts on the left leg will not typically produce any measurable amounts of H₂O₂. Nonetheless, H₂O₂ can be produced from such strong binding surfaces under conditions of accelerated mass transport.^{30,31} Otherwise, should the catalysts on the left leg of the volcano lack the ensembles of atoms required to dissociate the O–O bond, they will also show some selectivity to H₂O₂; this is the case on pure Pt, below ~ 0.3 V, where its surface is covered by adsorbed hydrogen,¹⁹ or on Cu–Hg, where the Cu surface atoms are isolated from each other (see Supporting Information). Despite these limitations, the volcano captures the overall trends. Moreover, to the best of our knowledge this is the first time that these trends for H₂O₂ production are confirmed experimentally.

The selectivity to H₂O₂ is much higher on Hg-modified electrodes than on pure metal surfaces. In the case of Pd–Hg and Cu–Hg, we anticipate that the structure of the active site resembles that of Pt–Hg,²³ that is, single atoms of Pd or Cu, surrounded by Hg. At least two contiguous reactive atoms are

required to dissociate HOO^* , break the O–O bond and form the intermediates of the 4-electron reduction reaction, O^* and HO^* .^{7,32} Consequently, monatomic sites are unable to break the O–O bond, making them selective for H_2O_2 production.

In the case of Ag–Hg, the cause of its high selectivity at 100% over the entire potential range is subtly different. The alloy has only a slightly negative enthalpy of formation at -0.03 eV/atom²⁶ as described in the Supporting Information. For this reason, the compound forms a solid solution, rather than an ordered intermetallic. Within such a solid solution, there will be regions close to pure Ag and other regions close to pure Hg; this would explain why the activity is equal or slightly lower to that of pure Ag. We hypothesize that the reason for the very high selectivity of Ag–Hg is due to the preferential deposition of Hg on the steps of Ag.³³ DFT calculations show that the barrier for HOO^* (or H_2O_2) dissociation is much higher on terrace sites than on step sites.³⁴ This means that steps should be inherently more selective toward the 4-electron reduction than terraces. Blocking them with Hg provides a means of ensuring high selectivity to H_2O_2 production.

The industrial implementation of electrochemical H_2O_2 production requires well dispersed catalysts with a high current density per unit mass in order to be economically competitive.^{35,36} On the basis of the results obtained for extended surfaces, Pd–Hg has an intrinsically higher activity than any other catalyst reported thus far. Below, we translate this improvement into technologically relevant Pd–Hg/C nanoparticles.

Pd/C was prepared in an ink and drop cast on a glassy carbon electrode, using the thin film rotating disk electrode technique.³⁷ The oxygen reduction activity was measured on the pure Pd catalyst and found to agree closely with literature values,³⁸ validating our experimental procedure (see Supporting Information). Following this, we electrodeposited mercury onto the electrode.

The catalyst composition was verified by scanning transmission electron microscopy (STEM) and X-ray energy dispersive spectroscopy (EDS). Figure 2f shows the high-angle annular dark-field (HAADF)-STEM image of a Pd–Hg nanoparticle. A difference in contrast between the central and outer regions of the particle is clearly visible. The HAADF signal intensity has a strong dependence with the atomic number, hence the brighter regions around the central zone of the nanoparticle indicate an Hg-rich thick surface, suggesting a core–shell structure. A closer inspection of the shell region shown in Figure 2g reveals alternating high contrast lattice fringes with spacing of 2.9 ± 0.2 Å. This is consistent with the 3.0310 Å distance separating the (001) planes of the Pd_2Hg_5 alloy structure.²⁵ Furthermore, these planes contain only Hg atoms and consequently appear brighter in the HAADF image. In order to confirm the presence of the Hg-rich shell, STEM-EDS mapping was performed. The STEM image and the corresponding EDS elemental maps of a region with different nanoparticles are shown in Figure 2a–d. The combined Hg and Pd elemental maps unmistakably show that a core–shell structure is formed with an anisotropic thickness of the shell. This can be visualized even more clearly by the EDS intensity profile linescan in Figure 2e. The anisotropy in the shell thickness can be ascribed to the different reactivity of each facet on the nanoparticle. The alloying of Pd and Hg was also confirmed by X-ray photoelectron spectroscopy (see Supporting Information). Further proof of the structure is shown in the Supporting Information. Taken as a whole, the TEM images in

Figure 2 demonstrate that the nanoparticles form a core–shell structure at room temperature. The core is Pd, whereas the shell consists of an ordered intermetallic, likely Pd_2Hg_5 . This is the same structure that was modeled in our DFT calculations, whose (001) facet we used to simulate the highly active and selective extended polycrystalline Pd–Hg surfaces described above.

Oxygen reduction on Pd–Hg/C nanoparticles shows a very similar behavior to polycrystalline Pd–Hg (Figure 3d). Upon saturation of the electrolyte with O_2 , we observed a negative current corresponding to oxygen reduction. The ring current shows that a substantial amount of the disk current is due to

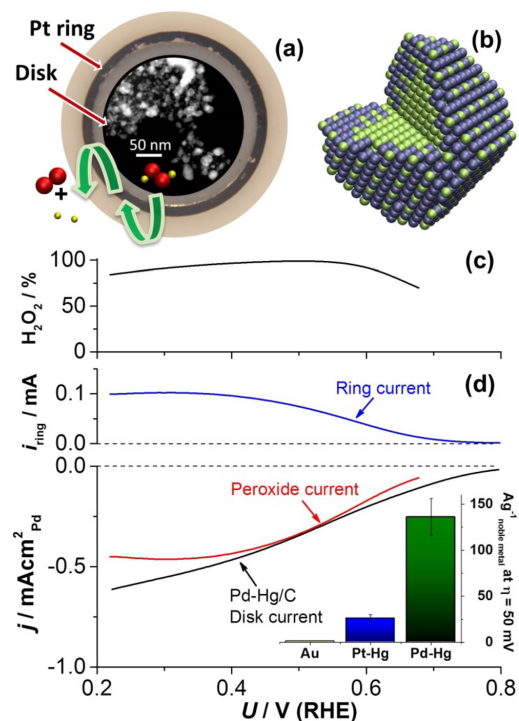


Figure 3. Electrochemical characterization of Pd–Hg/C nanoparticles. (a) Rotating ring-disk electrode with a schematic representation of H_2O_2 oxidation at the ring. The disk has been modified to show a HAADF-STEM overview of the Pd–Hg/C nanoparticles. (b) Schematic representation of a Pd–Hg nanoparticle with Pd colored in green and Hg in blue. (c) H_2O_2 selectivity as a function of the applied potential. (d) RRDE voltammograms at 1600 rpm in O_2 -saturated electrolyte with the disk current (black), ring current (blue) and corresponding current to hydrogen peroxide (red) obtained from the ring current (only the anodic cycle is shown). The disk current is normalized to the surface area of Pd nanoparticles (estimated from the oxide reduction peak before deposition of Hg). The inset shows the mass activity (A per g of noble metal) at 50 mV of overpotential for nanoparticulate catalysts. Data for Pt–Hg adapted from Siahrostami et al.²⁰ All electrochemical experiments were performed at 50 mV s^{-1} and 1600 rpm in O_2 saturated 0.1 M HClO_4 at room temperature with corrections for Ohmic drop and capacitive currents.⁴⁹ Full details on the normalization procedure and mass activity calculations are available in the Supporting Information.

hydrogen peroxide production with a selectivity higher than 95% between 0.35 and 0.55 V (Figure 3c). At 50 mV overpotential, Pd–Hg/C presents an activity per mass of precious metal five times higher than Pt–Hg/C and more than 2 orders of magnitude higher than state-of-the-art Au/C (inset of Figure 3d). In addition, Pd–Hg/C is highly stable, displaying negligible losses after 8000 potential cycles between 0.2 and 0.7 V.

In summary, we have modified different metal surfaces with Hg, as a means to tune the oxygen reduction activity and selectivity of various electrodes toward H₂O₂ production. By using a combination of theory and experiments, we have verified that the activity can be described by the *HOO binding energy, via a Sabatier-volcano. Selectivity in turn is described by the geometric arrangement of the catalyst sites. This approach led to the discovery of both Ag–Hg and Pd–Hg as catalysts for H₂O₂ production. The deployment of either catalyst could bring about significant improvements to the efficiency, selectivity, and cost³⁹ of a H₂O₂ producing device, in comparison to the current state-of-the-art.^{7,20} Fine tuning the particle shape, size, and composition should lead to an even higher activity per mass of precious metal.^{40–44} Nonetheless, future progress will be grounded on the basis of the active sites developed in this work. The concepts used here to tune oxygen reduction activity and selectivity can be extended to other reactions such as the reduction of CO₂^{45,46} or the selective oxidation of hydrocarbons.⁴⁷

■ ASSOCIATED CONTENT

Supporting Information

Detailed description of experimental and theoretical methods, as well as additional voltammetric data, characterization results, and DFT calculations. This material is available free of charge via the Internet at <http://pubs.acs.org>.

■ AUTHOR INFORMATION

Corresponding Authors

*E-mail: (I.C.) ibchork@fysik.dtu.dk.

*E-mail: (I.E.L.S.) ifan@fysik.dtu.dk.

Author Contributions

A.V. and I.E.L.S. developed the idea and designed the experiments. A.V. performed the electrochemical experiments, D.D. performed the microscopy, and P.M. performed the XPS. M.K. and S.S. performed the theoretical calculations. A.V. and I.E.L.S. wrote the first draft of the paper. A.V. and D.D. designed the figures. All authors discussed the results and commented on the manuscript.

Notes

The authors declare the following competing financial interest(s): Some of the authors of this manuscript were inventors on patent application EP 13165265.3 Alloy catalyst material. This patent includes some of the catalyst materials described here within its scope..

■ ACKNOWLEDGMENTS

The authors gratefully acknowledge financial support from the Danish Ministry of Science's UNIK initiative, Catalysis for Sustainable Energy. The Danish National Research Foundation's Center for Individual Nanoparticle Functionality is supported by the Danish National Research Foundation (DNRF54). The A.P. Møller and Chastine Mc-Kinney Møller Foundation is gratefully acknowledged for its contribution

towards the establishment of the Centre for Electron Nanoscopy in the Technical University of Denmark. The Interdisciplinary Centre for Electron Microscopy (CIME) at EPFL is gratefully acknowledged for the use of the FEI Tecnai Osiris TEM.

■ REFERENCES

- (1) Chorkendorff, I.; Niemantsverdriet, J. W. *Concepts of Modern Catalysis and Kinetics*, student ed.; Wiley-VCH Verlag GmbH & Co. KGaA: Weinheim, 2003.
- (2) Kotrel, S.; Brauning, S. *Handbook of Heterogeneous Catalysis*, 2nd ed.; Ertl, G., Knoezinger, H., Schueth, F., Weitkamp, J., Eds.; Wiley: New York, 2008.
- (3) Campos-Martin, J. M.; Blanco-Brieva, G.; Fierro, J. L. G. *Angew. Chem., Int. Ed.* **2006**, *45* (42), 6962–6984.
- (4) *Ullman's Encyclopedia of Industrial Chemistry*; Wiley: New York, 1999–2013.
- (5) Edwards, J. K.; Solsona, B.; N, E. N.; Carley, A. F.; Herzing, A. A.; Kiely, C. J.; Hutchings, G. J. *Science* **2009**, *323* (5917), 1037–1041.
- (6) Samanta, C. *Appl. Catal., A* **2008**, *350* (2), 133–149.
- (7) Jirkovský, J. S.; Panas, I.; Ahlberg, E.; Halasa, M.; Romani, S.; Schiffrin, D. J. *J. Am. Chem. Soc.* **2011**, *133* (48), 19432–19441.
- (8) Fellinger, T.-P.; Hasché, F.; Strasser, P.; Antonietti, M. *J. Am. Chem. Soc.* **2012**, *134* (9), 4072–4075.
- (9) Yamanaka, I.; Onizawa, T.; Takenaka, S.; Otsuka, K. *Angew. Chem.* **2003**, *115* (31), 3781–3783.
- (10) Parsons, R. *Trans. Faraday Soc.* **1958**, *54* (7), 1053–1063.
- (11) Trasatti, S. *J. Electroanal. Chem.* **1972**, *39* (1), 163–8.
- (12) Stamenkovic, V. R.; Mun, B. S.; Arenz, M.; Mayrhofer, K. J. J.; Lucas, C. A.; Wang, G.; Ross, P. N.; Markovic, N. M. *Nat. Mater.* **2007**, *6* (3), 241–247.
- (13) Greeley, J.; Stephens, I. E. L.; Bondarenko, A. S.; Johansson, T. P.; Hansen, H. A.; Jaramillo, T. F.; Rossmeisl, J.; Chorkendorff, I.; Nørskov, J. K. *Nature Chem.* **2009**, *1* (7), 552–556.
- (14) Suntivich, J.; May, K. J.; Gasteiger, H. A.; Goodenough, J. B.; Shao-Horn, Y. *Science* **2011**, *334* (6061), 1383–1385.
- (15) Stephens, I. E. L.; Bondarenko, A. S.; Perez-Alonso, F. J.; Calle-Vallejo, F.; Bech, L.; Johansson, T. P.; Jepsen, A. K.; Frydendal, R.; Knudsen, B. P.; Rossmeisl, J.; Chorkendorff, I. *J. Am. Chem. Soc.* **2011**, *133* (14), 5485–5491.
- (16) Subbaraman, R.; Tripkovic, D.; Chang, K.-C.; Strmcnik, D.; Paulikas, A. P.; Hirunsit, P.; Chan, M.; Greeley, J.; Stamenkovic, V.; Markovic, N. M. *Nat. Mater.* **2012**, *11* (6), 550–557.
- (17) Bandarenka, A. S.; Varela, A. S.; Karamad, M.; Calle-Vallejo, F.; Bech, L.; Perez-Alonso, F. J.; Rossmeisl, J.; Stephens, I. E. L.; Chorkendorff, I. *Angew. Chem., Int. Ed.* **2012**, *51* (47), 11845–11848.
- (18) Hinnemann, B.; Moses, P. G.; Bonde, J.; Jorgensen, K. P.; Nielsen, J. H.; Horch, S.; Chorkendorff, I.; Nørskov, J. K. *J. Am. Chem. Soc.* **2005**, *127* (15), 5308–5309.
- (19) Stamenkovic, V. R.; Fowler, B.; Mun, B. S.; Wang, G.; Ross, P. N.; Lucas, C. A.; Marković, N. M. *Science* **2007**, *315* (5811), 493–497.
- (20) Siahrostami, S.; Verdager-Casadevall, A.; Karamad, M.; Deiana, D.; Malacrida, P.; Wickman, B.; Escudero-Escribano, M.; Paoli, E. A.; Frydendal, R.; Hansen, T. W.; Chorkendorff, I.; Stephens, I. E. L.; Rossmeisl, J. *Nat. Mater.* **2013**, *12* (12), 1137–1143.
- (21) Viswanathan, V.; Hansen, H. A.; Rossmeisl, J.; Nørskov, J. K. *J. Phys. Chem. Lett.* **2012**, *3* (20), 2948–2951.
- (22) Jaouen, F.; Proietti, E.; Lefevre, M.; Chenitz, R.; Dodelet, J.-P.; Wu, G.; Chung, H. T.; Johnston, C. M.; Zelenay, P. *Energy Environ. Sci.* **2011**, *4* (1), 114–130.
- (23) Wu, H. L.; Yau, S.; Zei, M. S. *Electrochim. Acta* **2008**, *53* (20), 5961–5967.
- (24) Russell, A. S.; Kennedy, T. R.; Howitt, J.; Lyons, H. A. M. *J. Chem. Soc.* **1932**, 2340–2342.
- (25) Guminski, C. *Bull. Alloy Phase Diagrams* **1990**, *11* (1), 22–26.
- (26) Baren, M. R. *J. Phase Equilib.* **1996**, *17* (2), 122–128.
- (27) Pourbaix, M. *Atlas of electrochemical equilibria in aqueous solutions*, National Association of Corrosion Engineers, 1974.

- (28) Jirkovsky, J. S.; Halasa, M.; Schiffrin, D. J. *Phys. Chem. Chem. Phys.* **2010**, *12* (28), 8042–8053.
- (29) Erikson, H.; Jürmann, G.; Sarapu, A.; Potter, R. J.; Tammeveski, K. *Electrochim. Acta* **2009**, *54* (28), 7483–7489.
- (30) Chen, S.; Kucernak, A. *J. Phys. Chem. B* **2004**, *108* (10), 3262–3276.
- (31) Schneider, A.; Colmenares, L.; Seidel, Y. E.; Jusys, Z.; Wickman, B.; Kasemo, B.; Behm, R. J. *Phys. Chem. Chem. Phys.* **2008**, *10* (14), 1931–1943.
- (32) Siahrostami, S.; Bjorketun, M. E.; Strasser, P.; Greeley, J.; Rossmeisl, J. *Phys. Chem. Chem. Phys.* **2013**, *15* (23), 9326–9334.
- (33) Levlin, M.; Ikävalko, E.; Laitinen, T. *Fresenius J. Anal. Chem.* **1999**, *365* (7), 577–586.
- (34) Rankin, R. B.; Greeley, J. *ACS Catal.* **2012**, *2* (12), 2664–2672.
- (35) Stephens, I. E. L.; Bondarenko, A. S.; Gronbjerg, U.; Rossmeisl, J.; Chorkendorff, I. *Energy Environ. Sci.* **2012**.
- (36) Gasteiger, H. A.; Markovic, N. M. *Science* **2009**, *324* (5923), 48–49.
- (37) Schmidt, T. J.; Gasteiger, H. A.; Stab, G. D.; Urban, P. M.; Kolb, D. M.; Behm, R. J. *J. Electrochem. Soc.* **1998**, *145* (7), 2354–2358.
- (38) Shao, M.-H.; Sasaki, K.; Adzic, R. R. *J. Am. Chem. Soc.* **2006**, *128* (11), 3526–3527.
- (39) Vesborg, P. C. K.; Jaramillo, T. F. *RSC Adv.* **2012**, *2* (21), 7933–7947.
- (40) Sasaki, K.; Naohara, H.; Cai, Y.; Choi, Y. M.; Liu, P.; Vukirovic, M. B.; Wang, J. X.; Adzic, R. R. *Angew. Chem., Int. Ed.* **2010**, *49* (46), 8602–8607.
- (41) Guo, S.; Li, D.; Zhu, H.; Zhang, S.; Markovic, N. M.; Stamenkovic, V. R.; Sun, S. *Angew. Chem., Int. Ed.* **2013**, *52* (12), 3465–3468.
- (42) Cui, C.; Gan, L.; Heggen, M.; Rudi, S.; Strasser, P. *Nat. Mater.* **2013**, *12* (8), 765–771.
- (43) Mayrhofer, K. J. J.; Juhart, V.; Hartl, K.; Hanzlik, M.; Arenz, M. *Angew. Chem., Int. Ed.* **2009**, *48* (19), 3529–3531.
- (44) Wang, D. L.; Xin, H. L. L.; Hovden, R.; Wang, H. S.; Yu, Y. C.; Muller, D. A.; DiSalvo, F. J.; Abruna, H. D. *Nat. Mater.* **2013**, *12* (1), 81–87.
- (45) Kuhl, K. P.; Cave, E. R.; Abram, D. N.; Jaramillo, T. F. *Energy Environ. Sci.* **2012**, *5* (5), 7050–7059.
- (46) Li, C. W.; Kanan, M. W. *J. Am. Chem. Soc.* **2012**, *134* (17), 7231–7234.
- (47) Tomita, A.; Nakajima, J.; Hibino, T. *Angew. Chem., Int. Ed.* **2008**, *47* (8), 1462–1464.
- (48) Verdager-Casadevall, A.; Hernandez-Fernandez, P.; Stephens, I. E. L.; Chorkendorff, I.; Dahl, S. *J. Power Sources* **2012**, *220* (0), 205–210.
- (49) Nesselberger, M.; Ashton, S.; Meier, J. C.; Katsounaros, I.; Mayrhofer, K. J. J.; Arenz, M. *J. Am. Chem. Soc.* **2011**, *133* (43), 17428–17433.

